Spring 2020

EXPERIMENTAL AND NUMERICAL FAILURE ANALYSIS OF DEEP STEEL COLUMN SECTIONS

Shokoufeh zargar Zargar Shoushtari
University of New Hampshire, Durham

EXPERIMENTAL AND NUMERICAL FAILURE ANALYSIS OF
DEEP STEEL COLUMN SECTIONS

BY

SHOKOUFEH ZARGAR SHOUSHTARI

Baccalaureate Degree (BS), Shahid Chamran University of Ahvaz, 2000

Master's Degree (MS), Tehran Polytechnic (Amirkabir University of Technology), 2004

DISSERTATION

Submitted to the University of New Hampshire
in Partial Fulfillment of
the Requirements for the Degree of

Doctor of Philosophy
in
Structural Engineering

May, 2020

This thesis/dissertation was examined and approved in partial fulfillment of the requirements for the degree of Doctor of Philosophy in Structural Engineering by:

Thesis/Dissertation Director, Erin Bell, Department Chair and Professor
(Civil and Environmental Engineering, University of New Hampshire)

Ricardo A. Medina, Staff Consultant
(Simpson Gumpertz & Heger Incorporated)

Luis Ibarra, Associate Professor

(Department of Civil and Environmental. Engineering University of Utah)

Robert Henry, Associate Professor
(Civil and Environmental Engineering, University of New Hampshire)

Raymond Cook, Associate Professor
(Civil and Environmental Engineering, University of New Hampshire)

On 2-28-2020

Approval signatures are on file with the University of New Hampshire Graduate School.

Table of Contents

Appendix

Table of Figures

List of Tables

Acknowledgments

ABSTRACT

EXPERIMENTAL AND NUMERICAL FAILURE ANALYSIS OF
DEEP STEEL COLUMN SECTIONS

by

Shokoufeh Zargar Shoushtari

University of New Hampshire

The availability of reliable numerical models is essential to reduce the uncertainties present in the prediction of structural behavior. Experimental studies allow the calibration and development of numerical models capable of characterizing the realistic behavior of structural elements and components until the limit state of collapse is approached. Exterior columns in perimeter steel moment-resisting frame structures that are exposed to strong earthquakes experience bending moment demands with high levels of axial load due to overturning. Deep wide flange sections can be used as exterior columns to increase the lateral stiffness of moment frames without significantly increasing the overall weight of the structure. However, experimental data on the cyclic response of deep steel wide flange sections subjected to large drift, rotation, and axial load demands are scarce. To address this need, this research presents results from an experimental program that deals with studying and quantifying the behavior of 1:8 scaled W36X652 column sections exposed to different monotonic and cyclic loading histories consisting of large drift ratios of up to 0.1 rad, rotations at the tip of the column of up to 0.1 rad, and variable levels of axial loads up to 60% (in compression) of the column axial load carrying capacity that vary between tension and compression are used. The experiments consist of quasi-static experiments and hybrid simulations. The influence of member behavior and axial load on the parameters that control the collapse of the structure was studied. Column plastic rotations from 0.012 to 0.08 rad and post-capping rotations

1

from 0.03 to 0.37 rad were observed depending on the loading history and level of axial load. Further, numerical models of the column were calibrated utilizing the experimental results performed in this research. These models can be used for design and performance prediction of deep column section, especially valued in seismic design and assessment.

1 INTRODUCTION, BACKGROUND AND LITERATURE REVIEW

1.1 Introduction

The behavior of individual structural components is critical to preserve the structural integrity of a building and to ensure adequate building performance during service and extreme loading conditions. In tall structures whose primary lateral-load resisting system is composed of steel moment resisting frames, a column member's strength and stability are essential to avoid a building collapse during strong earthquake events. The performance assessment of these components must be conducted which requires a fundamental understanding and quantification of component behavior prior to and up to collapse. In the case of seismic events, post-event component damage assessment necessitates the availability of experimental studies. These studies should account for appropriate cyclic loading conditions and relevant boundary conditions and connection details that have a direct influence on the failure modes of components. Experimental studies are required in order to develop robust numerical models that are capable of capturing the structural response of a structure system up to collapse.

1.2 Motivation

Exterior columns in perimeter steel moment-resisting frame structures exposed to strong earthquakes experience bending moment demands with high levels of axial load due to overturning. For the design of the column, in the relationship to satisfy the "*strong column-weak beam*" criteria (in the implemented AISC Seismic Provisions for Structural Steel Buildings (AISC 341-10 (2010)), the required compressive strength of the column should include the amplified seismic load in the LRFD load combination. In previous version of the Provisions (AISC 341-05(2005)) this requirement was not considered. Further, the ASCE/SEI 7-10 (2010) design standards requires an increase in the drift by a factor which can control the member sizes to satisfy the drift and P-Delta criteria.

Deep wide flange steel sections can be used as exterior columns to increase the lateral stiffness of moment frames without significantly increasing the overall weight of the structure. Until recently, most of the available experimental data on deep wide flange steel sections has been obtained for beam members. In 2011, a research plan was proposed to emphasize the need for experimental data on deep steel column sections to better understand their seismic behavior, enable numerical simulation properties, and develop guidelines for incorporating these sections into a design (NIST, 2011). To reliably predict the behavior of a structure near the limit state of collapse, the evaluation of component behavior under a variety of loading protocols and representative boundary condition is needed. In order to have reliable numerical models for inelastic analysis and collapse simulation studies, the nonlinear behavior of deep steel columns exposed to variable drift ratios, rotation, and axial load demands should be experimentally understood and quantified.

One of the existing numerical models that has the ability to account for asymmetric component hysteretic behavior and cyclic deterioration is the model developed by Ibarra-Medina-Krawinkler (IMK model (Ibarra et al., 2005)), in which the IMK model was later modified by Lignos and Krawinkler (D. Lignos et al., 2011). In this model, the inelasticity is concentrated in certain locations in the structure while the rest of the structure remains elastic. The existing regression equations for this model at the time, did not include deep steel column sections and did not account for the existence of axial loads. However, in the recent years more experiments on and numerical simulation of deep steel column cross sections has been performed. This work provides a model for performance prediction of deep steel columns near the limit state of collapse.

1.3 Contribution of this work

This study is one of the first experimental programs consisting of various loading protocols and incorporating rotation at the tip of the deep steel column sections. The main contribution of this research to the structural engineering profession is an experimentally-verified analytical model that predicts the influence of member behavior and axial load on the parameters that control the collapse of the structure. Also, the quantification of modeling parameters such as plastic rotation capacity and post-capping rotation that are relevant for collapse simulation is defined. Another major contribution of this work is the design of an experimental testing program to capture the effect of boundary conditions, material properties, connection details, and axial load delivery on deep steel column structural behavior.

An experimental program was performed on a 1:8 scaled W36X652 cross section of an exterior column of a 20-story moment resisting frame at NEES (Network for Earthquake Engineering Simulation) @ Buffalo laboratory. Six different quasi-static tests consisting monotonic and cyclic

5

loading protocols were implemented. The developed loading protocols included lateral drift up to 0.1 rad, rotation up to 0.1 rad and axial loads up to 57% of the axial load carrying capacity of the column (constant and variable). Additionally, two hybrid simulations were conducted in which a 1:8 scaled W36X652 exterior column that is part of a 20-story steel moment resisting frame was considered as the physical substructure.

Further investigations were carried out on the 1:8 scaled W36X652 section, by testing two specimens as cantilever beams. The experimental setup was designed and fabricated at the HighBay Laboratory @ University of New Hampshire. The intent of performing these experiments was to evaluate and study of the boundary conditions, and axial loads on the column sections. Numerical models were calibrated using the experimental data obtained in the aforementioned experiments.

1.4   Literature Survey of Related Work

There is a scarcity of available experimental data on the cyclic response of deep wide steel sections subjected to large drift, rotation, and axial load demands. This issue is relevant to collapse simulation studies in which the inelastic behavior of columns up to collapse is represented by numerical models that should reliably account for column behavior. In order to address this need, the current research presents results from an experimental program that focused on studying and quantifying the behavior of deep wide flange steel column sections exposed to four different cyclic loading protocols. In this section, the current state of the research on deep column sections and the available experimental data is discussed.

1.4.1 Deep Steel Column Research

A deep steel column section is referred to herein as a section with a depth of approximately 400 mm (16 inches) or more (NIST, 2011). The focus on deep steel sections is warranted because these sections can be used as exterior columns in moment-resisting structures. During an earthquake, exterior columns carry their own tributary gravity load in addition to the axial load demands induced by overturning moments, and shear forces and bending moment demands induced by inertia forces. In 2011, a research plan was proposed to emphasize the need for experimental data on deep steel column sections to better understand their seismic behavior, enable numerical simulation properties, and develop guidelines for incorporating these sections in design (NIST, 2011).

In the recent years researchers have performed experiments on deep steel column sections. Newell and Uang (2008), tested full-scale W14 column specimens subjected to large drifts with different variable levels of axial force demands. The experimental results indicated that the predicted plastic rotation capacities by ASCE 41 (2008) equations are very conservative. In the 2017 version of ASCE 41 (2017), the modeling parameters for plastic hinges for the column have been modified. These parameters are based on the constant gravity load to axial yield capacity. The experimental results performed by Ozkula and Uang on W18, W24, and W30 deep steel column specimens (Ozkula, 2017), identified that for compact sections with low width-to-thickness ratios the failure mode changes from local buckling to lateral torsional buckling. The results reported better performance of the columns with rotation at the tip with respect to fixed boundary conditions.

1.4.2 Loading Protocols

The variability of earthquakes and different structural systems, makes it impossible to prescribe a unique and best loading history for testing structural components. The importance of loading histories that would capture the structural response behavior when a structural system is close to collapse was emphasized by Krawinkler (Krawinkler, 2009). Several loading histories have been developed and implemented for testing specimens for testing steel structure components (ATC-24 , SAC [Ref]). These loading protocols did not account for the existence of the axial load or rotation of the tip for column sections. Newell and Uang (Newell & Uang, 2006), developed a symmetric cyclic loading protocol of combined axial load and story drift. According to the NIST report published in 2011 (NIST, 2011), loading protocols should include both monotonic and cyclic flexural and axial loading, and consider the possible boundary conditions that can be experienced by deep beam-column sections.

1.4.3 Column Experiments Subjected to Drift, Rotation, and Axial Load Demands

In order to have reliable numerical models for inelastic analysis and collapse simulation studies, the nonlinear behavior of deep steel column sections exposed to variable drift ratio, rotation at the tip, and axial load demands should be experimentally understood and quantified. The ability of a column to dissipate energy via inelastic deformations is influenced by the column's bending moment gradient as well as material properties, section types, and loading condition (Gioncu & Mazzolani, 2003). In order to reliably predict damage to steel structural components, it is necessary to account for the effects of material fatigue, stress concentrations, local buckling (Fogarty & El-Tawil, 2013), and local imperfections (Krawinkler et al., 1983). In this context, damage assessment implies a fundamental understanding and quantification of component

structural behavior up to collapse. In the case of earthquakes, component damage assessment necessitates the availability of experimental studies for quantification of component response. These studies should account for appropriate cyclic loading conditions and relevant boundary conditions (Nakashima, 1994) that have direct influence on component structural behavior and failure modes.

Currently, standards for testing steel columns to quantify damage and evaluate their seismic performance are nonexistent. Factors such as the uncertainty in the seismic input due to record-to-record variability, limitations of laboratory equipment, economic constraints, and limitations associated with the number of structural components to be tested highlight the need to develop representative loading histories that can evaluate the seismic performance of steel columns. The knowledge base acquired from this type of testing will increase one's understanding of steel column structural behavior up to collapse, provide much needed data to calibrate and develop numerical models of columns, and improve seismic design provisions for steel moment-resisting frames.

At the system level, collapse assessment can be conducted efficiently based upon numerical models of structural systems. This necessitates the availability of component hysteretic models capable of representing the most relevant modes of monotonic and cyclic deterioration. In general, the aforementioned hysteretic models are characterized by parameters that are calibrated upon experimental studies. Ibarra, Medina, and Krawinkler introduced a hysteretic model, IMK model, that incorporates the most important sources of cyclic strength and stiffness deterioration (Ibarra et al., 2005). This model has been used extensively to numerically evaluate the seismic response of steel structures using a concentrated plasticity approach. Lignos and Krawinkler (D. G. Lignos & Krawinkler, 2010) compiled a comprehensive database of steel component experimental

responses. They utilized the experimental results contained in the database to develop regression equations useful to predict the parameters of the IMK model to represent the behavior of steel beams and columns. This database and its associated regression equations do not include results from the testing of deep steel column sections. In 2013, quasi-static and hybrid experiments were conducted on a 1:8 scaled W36X652 exterior column of a 20-story moment resisting frame with drift ratios of up to 0.1 rad, rotation at the tip of the column of up to 0.1 rad, and axial load up to 57% of the column axial load carrying capacity, in which these experiments are the focus of this dissertation (Zargar et al., 2014). Ozkula and Uang (2017) tested full scale deep steel column sections, which included fixed and flexible boundary conditions with constant axial ???. Only one specimen was tested under variable axial load. Elkady & Lignos (2018) have tested full scale deep steel column sections, considering the rotation at the tip of the column, tested under constant axial load.

1.4.4 Hybrid testing

Hybrid simulation has been conducted since the 1970's (Takanashi et al., 1975). Hybrid testing involves the interaction between a numerical (finite element) model and experimental specimens (physical substructures) during a test. In hybrid testing, the part of the structure that can reliably be modeled is considered as the numerical substructure, and the parts and regions that are the interest are fabricated and constructed in the lab as the experimental substructure. Hybrid simulation is more economical, safe, and provides the flexibility to test specimens of various scales (Schellenberg et al., 2009). Throughout the years the implementation of this testing approach has been facilitated by improvements associated with its accuracy and efficiency (Chen et al., 2012; Shing & Mahin, 1983). Further enhancements in sub-structuring techniques (Nakashima et al.,

1988; Shao et al., 2011), their implementation, and control strategies (Kwon et al., 2005; Nakashima & Masaoka, 1999) have also been conducted.

In the past, experiments have been performed with similar experimental setups to predict the inelastic response of reinforced concrete columns (Y Yamada et al., 1990) and steel box sections (Yoshikazu Yamada et al., 1992) without necessarily approaching the limit state of collapse. The need for experiments up to limit state of collapse with representative loading histories arises from the scarcity of experimental data on the behavior of deep steel columns. The data and information obtained through experiments are important for the calibration of numerical models of column elements necessary to have a more accurate and reliable prediction of the structural behavior up to the limit state of collapse. Lignos and Krawinkler (D. G. Lignos & Krawinkler, 2010) developed a database of more than 300 experiments on steel wide flange sections and calibrated deterioration parameters that could be used in the modified Ibarra-Medina-Krawinkler hysteretic model (IMK) (Ibarra et al., 2005). However, the amount of experimental data on the response of wide flange column sections was limited. Most of the available experiments were conducted considering that columns behaved as cantilevers or in perfect double curvature (Nakashima et al., 1991; Newell & Uang, 2006). Cantilevers do not account for realistic boundary conditions at the free end of the beam. Forcing the column to deflect in perfect double curvature does not provide a realistic representation of the rotation associated with the column/panel zone/beam interface, and hence, may not provide a reliable representation of changes in the moment gradient along the height of the column element during a response history analysis.

The hybrid simulations in this study were performed at the NEES lab @ Buffalo. The Open System of Earthquake Engineering Simulation Platform software (OpenSees, 2007), was used for the numerical modeling and OpenFresco was used as the interface between the finite element

software and the control of physical actuators and data acquisition software. OpenFresco is an object-oriented based software that was developed by Takashashi and Fenves (Takahashi & Fenves, 2006) and was further modified and extended by Schellenbrg (Schellenberg & Mahin, 2006). In this study, the implicit Newmark method with fixed number of iterations was used for the integration scheme during the hybrid simulations. A predictor corrector algorithm was used to provide synchronization between the integration approach and the actuator control. A discussion on the substructuring technique used for these tests to impose appropriate demands at the tip of the column is presented.

1.4.5 Numerical Simulation

In the absence of experimental data, high fidelity numerical models are the best alternative tool to investigate and understand the behavior of structural components. Newell and Uang (Newell & Uang, 2006), performed a parametric study of commonly used column cross sections (W12, W14), and deep column section (W18, and W24). They observed, a prompt strength degradation for the deep steel column sections due to flange and web local buckling, and interaction of buckling modes, which resulted in a decreased inter-story drift capacity. Elkady and Lignos (Elkady & Lignos, 2015), analytically investigated deep steel column sections which included W36 sections. The simulations consisted of symmetric cyclic lateral loads combined with compressive axial load levels up to 50% of the axial strength. A flexible beam with a pre-defined moment of inertia was attached to the upper side of the column, to account for tip rotation which kept the inflection point of the column at a distance of 75% of the length. Further study was carried out by Fogarity and El-tawil (Fogarty & El-Tawil, 2014), on deep and slender sections under

combined axial and lateral loading (simulated as perfect double curvature). The results indicated that due to local buckling as well as lateral torsional buckling, there was a considerable reduction in column ductility.

1.5   Organization of this Dissertation

This dissertation presents an experimental program using hybrid testing for mode verification of near collapse performance prediction of deep steel sections used as columns. Each chapter is briefly described below.

- *Chapter One: Introduction*

Introduction and a literature review of previous work. A review of previous and current state of experiments performed on deep steel column sections.

- *Chapter Two: Non-Linear Static Analysis of the Scaled 20-Story Building*

The first part of this chapter consists of a description of the most relevant structural properties and modeling assumptions of an exterior column of the 20-story structure used for this research. The second part includes a summary of modal and nonlinear static analysis results.

- *Chapter Three: Experimental Studies on a Deep Steel Column Section Subjected to Variable Drift, Rotation and Axial Load Demands.*

This chapter focuses on the experimental testing program of an exterior column of a 20-story moment resisting frame, and the loading protocols that were utilized for the testing. The test setup and the controls are described. In this chapter the influence of the member structural behavior and axial load on the parameters that control the collapse of the structure are studied. This material was submitted and presented at the 10th National Conference in Earthquake Engineering, "Cyclic

Behavior of Deep Steel Columns Subjected to Large Drifts, Rotations, and Axial Loads", Zargar S, Medina RA, and Miranda E (2014). There is a paper in preparation for submission to the EERI journal; "Experimental Studies on a Deep Steel Column Section Subjected to Variable Drift, Rotation, and Axial Load Demands' Zargar S and Medina RA (2020). The dissertation author is the first author of these papers.

- *Chapter Four: Experimental Studies on a Deep Steel Column Section of a 20-Story Moment Resisting Frame Through Hybrid Testing*

In this chapter, the results of two hybrid simulations are presented where an exterior column that is part of a 20-story steel moment resisting frame was considered as the physical substructure are. This material was published in the proceeding of 2nd European Conference on Earthquake Engineering and Seismology; "Hybrid Simulation of an Exterior Steel Column in a 20-Story Moment Resisting Frame", with co-author Medina RA (2014). A paper is in preparation for submission to the EERI journal; "Experimental Studies on a Deep Steel Column Section of a 20-story Moment Resisting Frame through Hybrid", Zargar S and Medina RA (2020). The dissertation author is the first author of these papers.

- *Chapter Five: Experimental Studies on the Inelastic Behavior of a Cantilever Beam with Deep Steel Section Subjected to Large Drifts*

An experimental study on two cantilever beams was conducted. In this chapter, the experimental setup and the behavior of the cantilever beam under large displacements without axial load and rotation are evaluated. Based upon the material presented in this chapter a paper is in preparation for submission to a journal; "Experimental Studies on the Inelastic Behavior of a Cantilever Beam with Deep Steel Section Subjected to Large Drifts", Zargar S, Medina RA, and Bell E (2020). The

dissertation author is the first author of these papers.

- *Chapter Six: Numerical Studies of deep steel columns subjected to various loading histories*

The calibration of the finite elements models of the performed experiments considering various loading histories are discussed in this chapter. Based upon the material presented in this chapter a paper is in preparation for submission to a journal; "Numerical Studies of a Deep Steel Section Subjected to Different Loading Protocols", Zargar S, Medina RA, and Bell E (2020). The dissertation author is the first author of these papers.

- *Chapter Seven: Summary and Conclusion*

A summary of the experimental and numerical work presented in this dissertation is presented. The main outcome of the current research is discussed in the conclusion section.

1.6 References

ASCE-41-17. (2017). *ASCE Standard, ASCE/SEI, 41–17: Seismic Evaluation and Retrofit of Existing Buildings*.

ASCE. (2010). Minimum Designs Loads for Buildings and Other Structures, ASCE/SEI 7-10: American Society of Civil Engineers, Reston, Virginia.

Chen, C., Ricles, J. M., & Guo, T. (2012). Improved adaptive inverse compensation technique for real-time hybrid simulation. *Journal of Engineering Mechanics, 138*(12), 1432-1446.

Elkady, A., & Lignos, D. G. (2015). Analytical investigation of the cyclic behavior and plastic hinge formation in deep wide-flange steel beam-columns. *Bulletin of Earthquake Engineering, 13*(4), 1097-1118.

Elkady, A., & Lignos, D. G. (2018). Full-scale testing of deep wide-flange steel columns under multiaxis cyclic loading: Loading sequence, boundary effects, and lateral stability bracing force demands. *Journal of Structural Engineering, 144*(2), 04017189.

Fogarty, J., & El-Tawil, S. (2013). *Collapse Behavior of Steel Columns under Lateral Loading.* Paper presented at the Structures Congress 2013@ sBridging Your Passion with Your Profession.

Fogarty, J., & El-Tawil, S. (2014). COLLAPSE BEHAVIOR OF STEEL COLUMNS UNDER COMBINED AXIAL AND LATERAL LOADING. *Arbor, 1001*, 481059-482125.

Gioncu, V., & Mazzolani, F. (2003). *Ductility of seismic-resistant steel structures*: CRC Press.

Ibarra, L. F., Medina, R. A., & Krawinkler, H. (2005). Hysteretic models that incorporate strength and stiffness deterioration. *Earthquake engineering & structural dynamics, 34*(12), 1489-1511.

Krawinkler, H. (2009). *Loading histories for cyclic tests in support of performance assessment of structural components.* Paper presented at the The 3rd International Conference on Advances in Experimental Structural Engineering, San Francisco.

Krawinkler, H., Zohrei, M., Lashkari-Irvani, B., Cofie, N. G., & Hadidi-Tamjed, H. (1983). *Recommendations for experimental studies on the seismic behavior of steel components and materials*.

Kwon, O.-S., Nakata, N., Elnashai, A., & Spencer, B. (2005). Technical note a framework for multi-site distributed simulation and application to complex structural systems. *Journal of Earthquake Engineering, 9*(5), 741-753.

Lignos, D., Krawinkler, H., & Whittaker, A. (2011). Prediction and validation of sidesway collapse of two scale models of a 4-story steel moment frame. *Earthquake engineering & structural dynamics, 40*(7), 807-825.

Lignos, D. G., & Krawinkler, H. (2010). Deterioration modeling of steel components in support of collapse prediction of steel moment frames under earthquake loading. *Journal of Structural Engineering, 137*(11), 1291-1302.

Nakashima, M. (1994). Variation of ductility capacity of steel beam-columns. *Journal of Structural Engineering, 120*(7), 1941-1960.

Nakashima, M., Ishii, K., Kamagata, S., Tsutsumi, H., & Ando, K. (1988). Feasibility of pseudo dynamic test using substructuring techniques. *Proceeding of 9th World Conference on Earthquake Engineering. Tokyo, Japan, 4*, 47-52.

Nakashima, M., & Masaoka, N. (1999). Real-time on-line test for MDOF systems. *Earthquake engineering & structural dynamics, 28*(4), 393-420.

Nakashima, M., Morino, S., & Koba, S. (1991). Statistical evaluation of strength of steel beam columns. *Journal of Structural Engineering, 117*(11), 3375-3395.

Newell, J. D., & Uang, C.-M. (2006). *Cyclic behavior of steel columns with combined high axial load and drift demand*: Department of Structural Engineering, University of California, San Diego.

NIST. (2011). Research Plan for the Study of Seismic Behavior and Design of Deep, Slender Wide Flange Structural Steel Beam-Column Member. *prepared by the NEHRP Consultants Joint Venture, a partnership of the Applied Technology Council and the Consortium of Universities for Research in Earthquake Engineering for the National*

Institute of Standards and Technology, NIST GCR 11-917-13 2011(Gaithersburg, Maryland).

OpenSees. (2007). Open System for Earthquake Engineering Simulation: Pacific Earthquake Engineering Research Center (PEER). Retrieved from http://opensees.berkeley.edu

Ozkula, G. (2017). *Seismic behavior, modeling, and design of deep wide-flange steel columns for special moment frames*: University of California, San Diego.

Schellenberg, A., Kim, H. K., Takahashi, Y., Fenves, G. L., & Mahin, S. A. (2009). OpenFresco Command Language Manual: Version.

Schellenberg, A., & Mahin, S. (2006). *Integration of hybrid simulation within the general-purpose computational framework OpenSees.* Paper presented at the Eighth US National Conference on Earthquake Engineering.

Shao , X., Reinhorn , A. M., & Sivaselvan , M. V. (2011). *Real-Time Hybrid Simulation Using Shake Tables and Dynamic Actuators* (Vol. 137).

Shing, P., & Mahin, S. A. (1983). Experimental error propagation in pseudodynamic testing. *Earthquake Engineering Research Report UCB/EERC-83/12, University of California, Berkeley, 168*.

Takahashi, Y., & Fenves, G. L. (2006). Software framework for distributed experimental–computational simulation of structural systems. *Earthquake engineering & structural dynamics, 35*(3), 267-291.

Takanashi, K., Udagawa, K., Seki, M.-u., Okada, T., & Tanaka, H. (1975). Nonlinear earthquake response analysis of structures by a computer-actuator on-line system. *Bulletin of Earthquake Resistant Structure Research Center, 8*, 1-17.

Yamada, Y., Iemura, H., & Tanzo, W. (1992). Substructured hybrid loading tests of steel box-section columns for inelastic earthquake response of frame structures. *Earthquake Engineer 10th World, 5*, 2837.

Yamada, Y., Iemura, H., Tanzo, W., & Endo, K. (1990). Substructured hybrid loading of structural members under combined axial, shear, and bending loads. *Japanese Society of Soil Mechanics and Foundation Engineering, 251*, 1503-1508.

Zargar, S., Medina, R., & Miranda, E. (2014). Cyclic behavior of deep steel columns subjected to large drifts, rotations, and axial loads. *Proceedings of the 10th National Conference in Earthquake Engineering, Earthquake Engineering Research Institute, Anchorage, AK*.

2 NON-LINEAR STATIC ANALYSIS OF THE SCALED 20 STORY BUILDING

2.1 Introduction

The focus of this research is to gain a better understanding of the structural behavior of a deep steel column section in a 20-story office building. A previously designed building which is located in Century City (longitude 34.0564° and latitude -118.4339 °), CA was used as the full scale prototype. The lateral-load resisting system in the N-S and E-W directions is comprised of a pair of special moment resisting frames (SMRF) with fully restrained reduced beam sections (RBS) (Figure 2-1). The N-S moment resisting frame was the focus of this study.

This chapter has two main parts. The first part relates to a description of the most relevant structural properties and modeling assumptions. The second part includes a summary of modal and nonlinear static analysis results. The Open System of Earthquake Engineering Simulation Platform software (OpenSees, 2007) was used for analysis purposes.
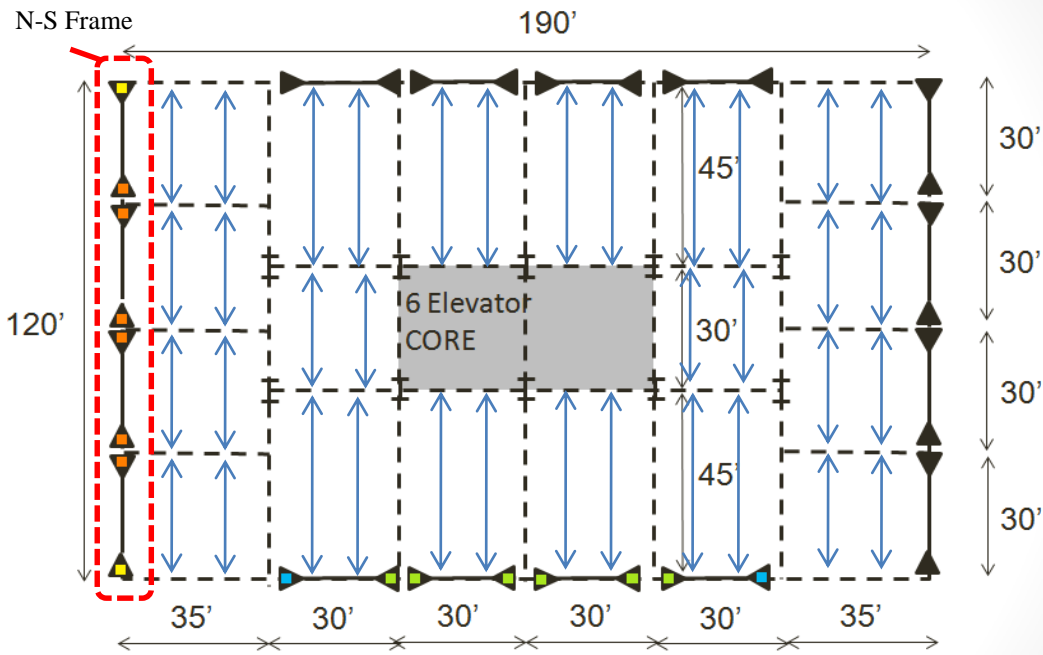
Figure 2-1. Typical plan view of the building

2.2 Building Specifications and Properties

The structure was designed according to load and resistance design specifications (LRFD) based on ASCE/SEI 7-10 (2010), *ANSI/AISC 360-10 (2010) and ANSI/AISC 341-10 (2010)*. The system design requirements including base shear and story drift limits, and strong column weak girder concept, were the bases for the design. The value of the response modification factor, R, for special steel special moment frames that was used was 8 (Table 12.2-1, ASCE/SEI 7-10). The primary geometrical and material properties of the moment resisting frame are reported in Table 2-1. Final design sections for the structure are shown in Figure 2-2 and Figure 2-3.

Table 2-1. Prototype structure specifications and properties

number of stories	20
number of frame bays	4
SMRF bay width	360 in
1st floor story height[1]	155.2 in
2nd-20th story heights[2]	156 in
Total height of the structure	3119.2 in
Distance from exterior column to leaning column	360 in
Height of splice[3]	48 in
Elastic modulus, E	29000 ksi
Yield strength[4], F_y	49.9 ksi

1. Height from top of baseplate to center of the beam girders
2. Height measured from centerline to centerline of the beam girders
3. From top of girder to the center of change in the section
3. Obtained from the tensile coupon test on the test specimens
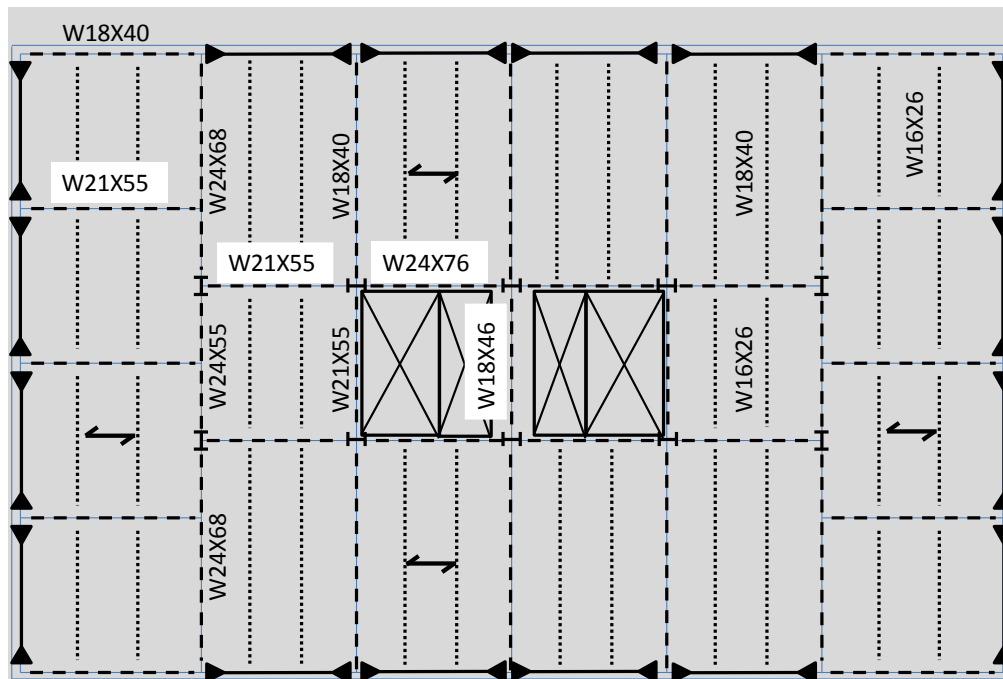
Figure 2-2. Typical girders and beam sections
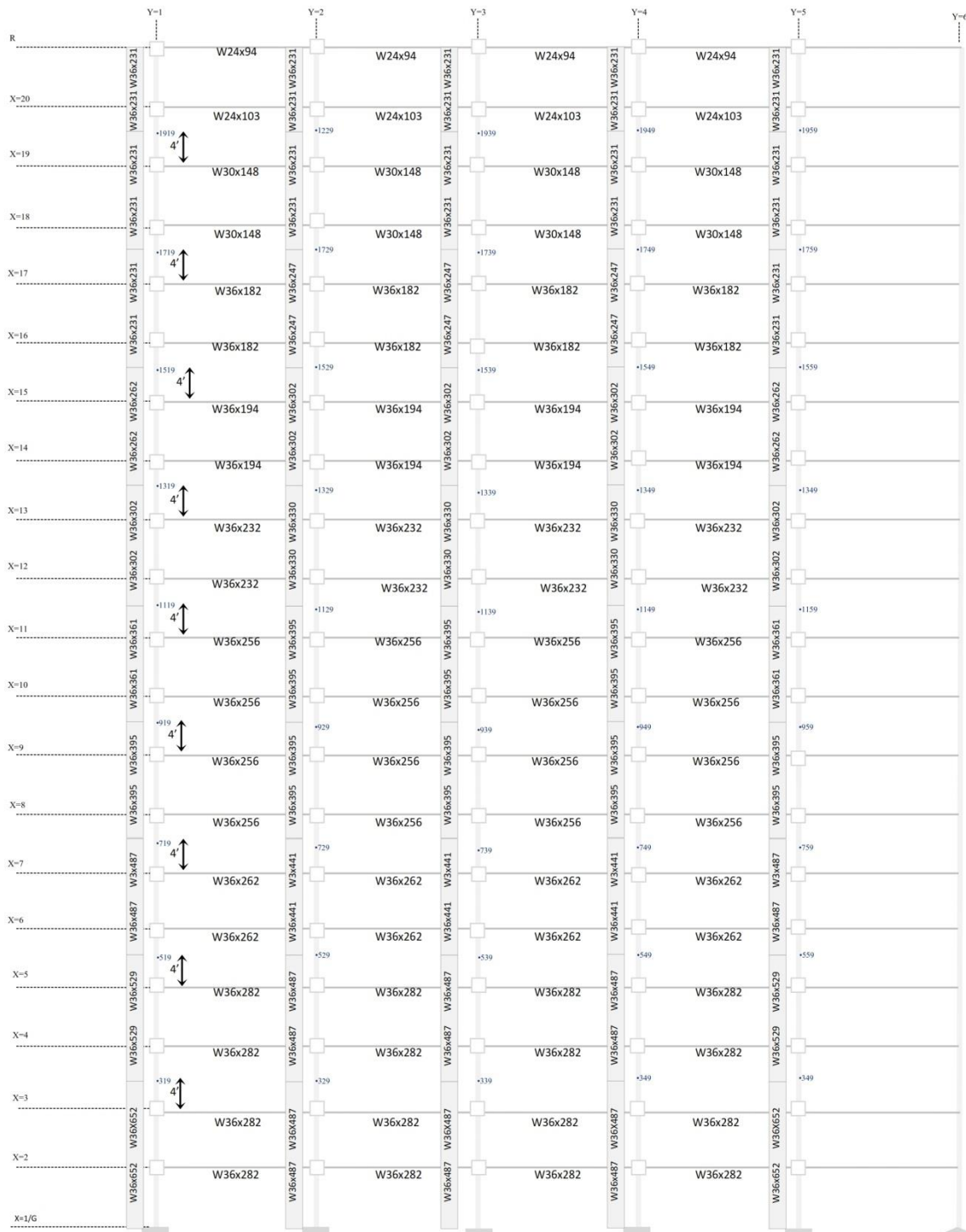
Figure 2-3. N-S Moment Resisting Frame Elevation

23

2.3 Scaled Model

To develop a scaled model of a typical N-S SMRF, the geometry and the properties of the full scale prototype structural model was developed by Annika Mathieson (Mathiasson & Medina, 2013) in OpenSees. The geometry and properties were scaled based on the scaling parameters shown in Table 2-2. Because the experimental testing of an exterior first story column was done with a 1:8 scale, the scale factor that was applied to the prototype structural model is $l_r = 1/8 = 0.125$.

Table 2-2. Summary of similitude laws (after Moncarz, 1981)

Scaling Parameters	Model Type
Length, l_r	l_r
time, t_r	$l_r^{1/2}$
Frequency, ω_r	$l_r^{-1/2}$
Velocity, v_r	$l_r^{1/2}$
Gravitational acceleration, g_r	1
Acceleration, a_r	1
Strain, ε_r	1
Stress, σ_r	E_r
Modulus of elasticity, E_r	E_r
Specific stiffness, $(E/\rho)_r$	**
Displacement, δ_r	l_r
Force, F_r	$E_r l_r^2$
Energy, $(EN)_r$	$E_r l_r^3$

** Undefined scale ratio to be selected by the investigator

2.4 Yield Strength

The prototype structure was designed using a yield strength of 50 ksi. However, the yield strength value used for modeling purposes was obtained from experimental data. A total of six steel coupons (three obtained from the web section and three obtained from the flange section used to fabricate the steel specimens) were used to evaluate the yield strength. The stress-strain relation for all tests is presented in Figure 2-4.
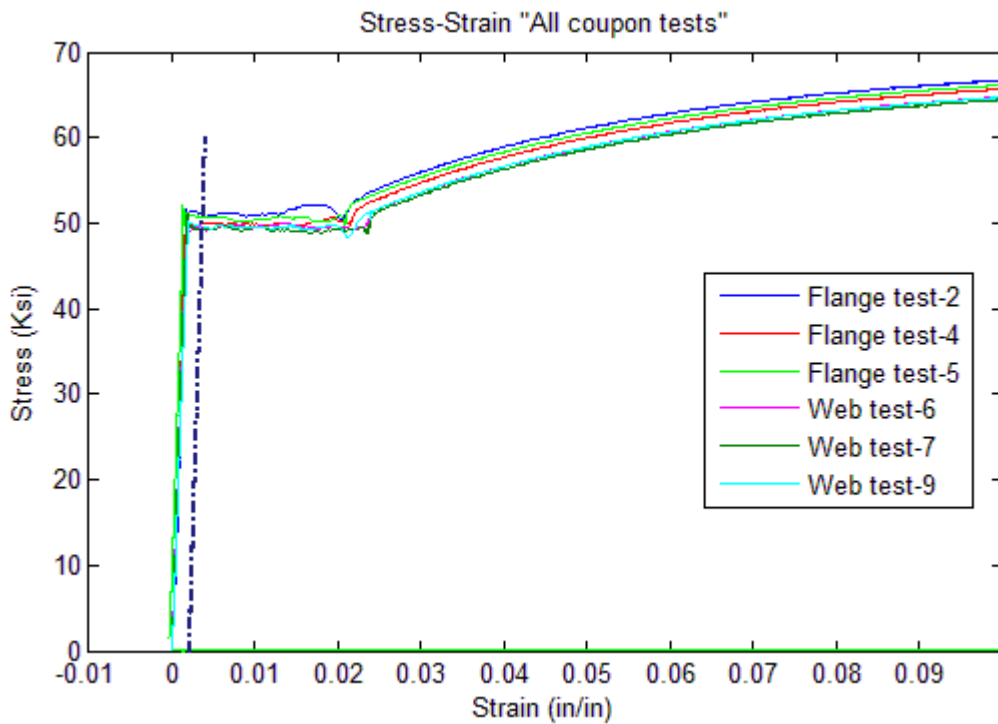
Figure 2-4. Stress-strain relation of the tensile tests for 6 coupons

The yield strength was obtained from the intersection of a straight line parallel to the initial linear portion of the stress-strain curve with the yield plateau at a strain offset of 0.2% as shown in Figure 2-4. An average value of 49.9 ksi was obtained using the estimated yield strength from the six experimental tests, Table 2-3.

Table 2-3. Estimated yield strength and the average from all six tests

Description	F_y (ksi)
Flange test-2	50.7
Flange test-4	49.9
Flange test-5	50.8
Web test-6	49.5
Web test-7	49.2
Web test-9	49.4
Flange test Average	50.5
Web test Average	49.4
Total Average	*49.9*

2.5   Reduced Beam Section Connection Design (RBS)

Considering Reduced Beam Section (RBS) moment connections in the design, forces yielding and formation of the plastic hinges at the location of the reduced section of the beam, which will limit the moment demands at the interface of the beam to the column. Using RBS will move the plastic hinge away from the welds at the direct connection of the beam to the column. The RBS connection consists of a circular radius cut in both top and bottom flanges, which results in reduced flange cross section area and consequently reducing the plastic moment capacity over a length of the beam near the ends of the beam span. The design of the RBS connection was based on prequalified connections (AISC 358 -10, (2010)). The range of *a* and *b* values based on beam flange width, b_f, and depth, *d*, of each member are *a= (.5 to .75)*bf* and *b= (65 to .85)*d*. a and *b* were rounded up from the minimum value of the equation range to the nearest quarter to create the minimum distance from the face of the column to the RBS cut, and *b* the length of the RBS cut. The parameters are illustrated in Figure 2-5 and reported in Table A 2-1 and A 2-2 in Appendix 2.
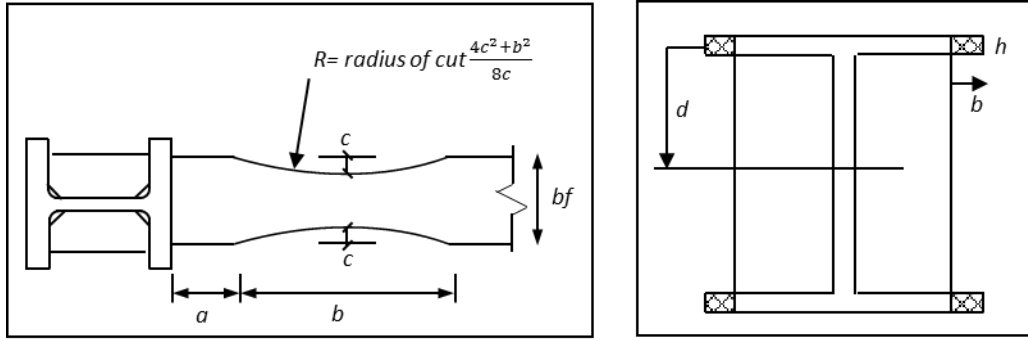
Figure 2-5. Reduced beam section (RBS) parameters

2.6 Panel Zones

Panel zone is the region where the columns and the beams intersect, Figure 2-6. The panel zone is modeled using the Gupta and Krawinkler (1999) approach. In this approach, the panel zone is modeled with eight rigid elastic beam-column elements and a zero-length rotational spring to represent shear distortions in the panel zone at a corner as shown in Figure 2-7.
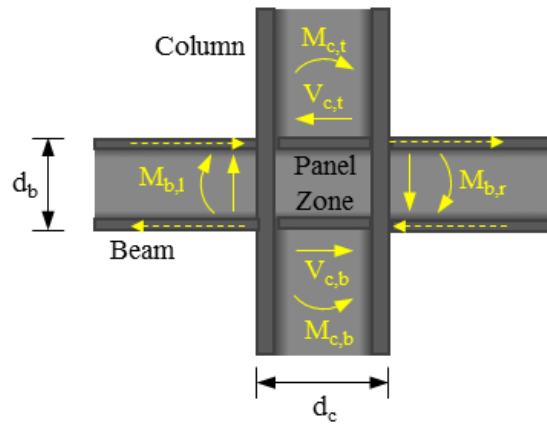
Figure 2-6. Panel zone and the corresponding demands

2.7 Stiffness Modifications to Elastic Frame Elements

The beam element that spans from the centers of the RBS sections of a girder is modeled as an elastic element connected in series with rotational springs at both ends (Figure 2-7). The rotational springs are located at the center of the RBS sections. Thus, the stiffness of these components must be adjusted so that the equivalent stiffness of the subassembly is equivalent to the stiffness of the prototype frame member. The rotational spring's stiffness *Ks* are made "*n*" times stiffer than the 6*EI/L* rotational stiffness of the elastic beam element. To ensure the equivalent stiffness of the assembly is equal to the stiffness of the prototype frame member, the stiffness of the elastic beam element I_e must be "*(n+1)/n*" times greater than the stiffness of the prototype frame member *I*. Damping is assigned only to the elastic element following the approach proposed by Zareian and Medina (2010). The rotational spring stiffness of the beams is presented in Table A 2-3 (Appendix 2).
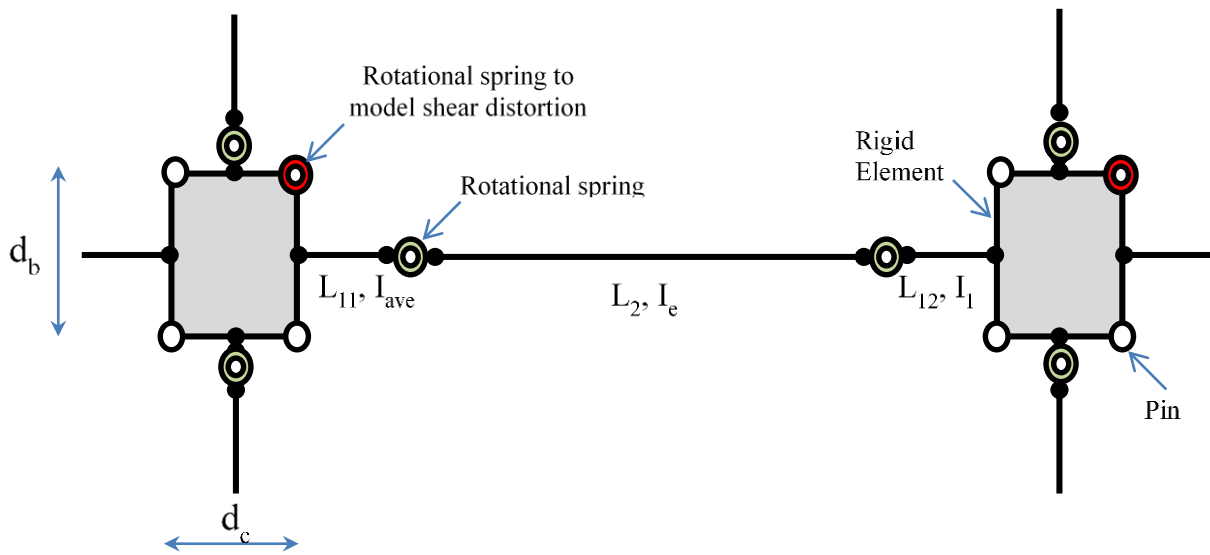
Figure 2-7. Analytical modeling for typical beam and panel zone

The rotational stiffness of the exterior and interior column sections is presented in Table A 2-4 and Table A 2-5 (Appendix 2). The length of the column is defined as the clear length between the stories (the clear distance from top of girder on the lower floor to the bottom of the girder on the following story). In stories with a splice in the column (Figure 2-3, for example above 3rd floor), the length of the column bellow the splice to the top of the girders and the length above the splice to the bottom of the following story is determined as the column's length. Each portion of the column is treated as separate element with a rotational spring located at the end of the column near the end panel zones. The stiffness of these components must be adjusted so that the equivalent stiffness of the subassembly is equivalent to the stiffness of the prototype frame member. The stiffness of the rotational spring, K_s, are made "n" times stiffer than the $6EI/L$ rotational stiffness of the elastic beam element. To ensure the equivalent stiffness of the assembly is equal to the stiffness of the prototype frame member, the stiffness of the elastic beam element I_e must be "(n+1)/n" times greater than the stiffness of the prototype frame member I. Damping is assigned only to the elastic element following the approach proposed by Zareian and Medina (2010).

2.8   Column Plastic Hinges (Modified IMK Model)

This necessitates the availability of component hysteretic models capable of representing the most relevant modes of monotonic and cyclic deterioration. In general, the aforementioned hysteretic models are characterized by parameters that are calibrated upon experimental studies. Ibarra, Medina, and Krawinkler introduced a hysteretic model, IMK model, that incorporates the most important sources of cyclic strength and stiffness deterioration (Ibarra et al., 2005). This model has been used extensively to numerically evaluate the seismic response of steel structures using a concentrated plasticity approach. Lignos and Krawinkler (D. G. Lignos & Krawinkler, 2010) compiled a comprehensive database of steel component experimental responses. They

utilized the experimental results contained in the database to develop regression equations useful to predict the parameters of the IMK model to represent the behavior of steel beams and columns.

In Figure 2-8, the modified Ibarra-Medina-Krawinkler Model (IMK) with monotonic and cyclic deterioration is shown. The plastic rotation capacity, θ_p, is the difference between yield rotation and rotation at maximum bending moment); and the post-capping rotation, θ_{pc}, is the difference between rotation at maximum moment and rotation at complete loss of strength). Moreover, additional modeling parameters such as the effective yield strength (M_p), the post-capping strength (M_{pc}, the maximum moment), as well as cyclic strength and stiffness deterioration (Λ) is defined.
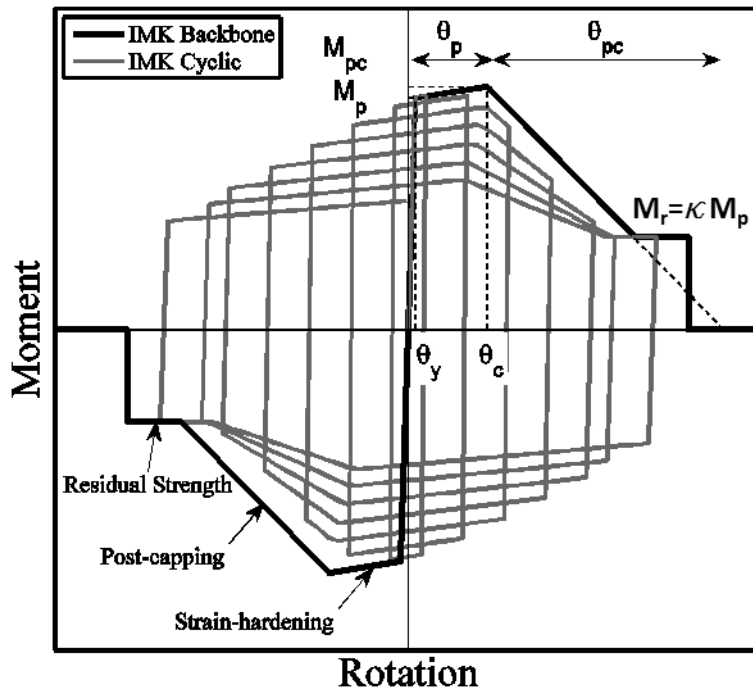
Figure 2-8. Modified Ibarra-Medina-Krawinkler Model (IMK) with monotonic and cyclic deterioration

2.8.1 Column Plastic Hinges (Modified IMK Model)

Column plastic hinge properties are estimated for the modified IMK model based on the equations develop by Lignos and Krawinkler (2010), Eq. 2-1, 2-2, and 2-3. For columns, these equations are based on the data set denoted as "other than RBS beams". In this study, these equations are utilized due to the scarcity of experimental data for columns. Furthermore, the effect of the axial load on the flexural behavior of steel columns is not accounted for in the development of the regression equations. Therefore, it should be highlighted that in these equations the effect of axial load on the plastic hinge properties has been ignored. Some of the properties predicted by these equations are approximately modified to account for the presence of axial loads as explained in Section 2-9.

Because the depths of the sections are greater than 21inches (533.4 mm) the following equations have been used:

- Pre-capping plastic rotation

$$\theta_p = 0.318 \cdot \left(\frac{h}{t_w}\right)^{-0.550} \cdot \left(\frac{b_f}{2.t_f}\right)^{-0.345} \cdot \left(\frac{L_b}{r_y}\right)^{-0.0230} \cdot \left(\frac{l}{d}\right)^{0.090} \cdot \left(\frac{c_{unit}^1 \cdot d}{533}\right)^{-0.330} \cdot \left(\frac{c_{unit}^2 \cdot F_y}{355}\right)^{-0.130}$$

(2-1)

$$R^2 = 0.457, \quad \sigma_{ln} = 0.351$$

- Post capping plastic rotation

$$\theta_{pc} = 7.50 \cdot \left(\frac{h}{t_w}\right)^{-0.610} \cdot \left(\frac{b_f}{2.t_f}\right)^{-0.710} \cdot \left(\frac{L_b}{r_y}\right)^{-0.110} \cdot \left(\frac{c_{unit}^1 \cdot d}{533}\right)^{-0.161} \cdot \left(\frac{c_{unit}^2 \cdot F_y}{355}\right)^{-0.320}$$

$$R^2 = 0.49, \quad \sigma_{ln} = 0.24$$

(2-2)

- Reference cumulative plastic rotation

$$\Lambda = \frac{E_t}{M_y} = 536 \cdot \left(\frac{h}{t_w}\right)^{-1.26} \cdot \left(\frac{b_f}{2 \cdot t_f}\right)^{-0.525} \cdot \left(\frac{L_b}{r_y}\right)^{-0.130} \cdot \left(\frac{c_{unit}^2 \cdot F_y}{355}\right)^{-0.291}$$

(2-3)

$R^2 = 0.496, \quad \sigma_{ln} = 0.34$

These equations are limited to the following parameter ranges:

- $20 \leq h/t_w \leq 55$ for other $-$ than $-$ RBS; $21 \leq h/t_w \leq 55$ for RBS;
- $20 \leq L_b/r_y \leq 80$ for other $-$ than $-$ RBS; $20 \leq L_b/r_y \leq 65$ for RBS;
- $4 \leq b_f/2t_f \leq 8$ for other $-$ than $-$ RBS; $4.5 \leq b_f/2t_f \leq 7.5$ for RBS;
- $2.5 \leq L/d \leq 7$ for other $-$ than $-$ RBS; $2.3 \leq L/d \leq 6.3$ for RBS;
- $102\ mm\ (4\ in.) \leq d \leq 914\ mm\ (36\ in.)$ for other $-$ than $-$ RBS; $533\ mm\ (21\ in.) \leq d \leq 914\ mm\ (36\ in.)$ for RBS; and
- $240\ MPa\ (35\ ksi) \leq F_y \leq 450\ MPa\ (65\ ksi)$ for other $-$ than $-$ RBS; $262\ MPa\ (38\ ksi) \leq F_y \leq 435\ MPa\ (63\ ksi)$ for RBS.

In the above equations, h/t_w is the fillet to fillet is web depth over web thickness ratio of the W-section; $b_f/2 \cdot t_f$ is the flange width to thickness ratio; L_b/r_y is the ratio between beam unbraced length L_b over radius of gyration about the weak axis of the cross-section; L/d is the ratio of shear span to depth ratio of the cross-section; F_y is the yield strength of the flange of the beam in ksi; $C_{unit}^1 = 25.4$ and $C_{unit}^2 = 6.895$ are coefficient for units conversion when units are in inches. Considering the above equations, the plastic hinge properties have been derived for exterior and interior columns as shown in Table 2-4 and Table 2-5, respectively. As mentioned before F_y is 49.9 ksi.

Table 2-4. Calculated plastic hinge properties for exterior columns

Exterior Columns: Story	h/t_w	$b_f/(2t_f)$	L_b (in)	r_y (in)	(L_b/r_y)	L (in)	d (in)	L/d	Λ	θ_P	θ_{Pc}
20	42.2	6.54	131.6	3.71	35.47	131.6	36.5	3.61	1.14	0.0184	0.1258
19	42.2	6.54	128.4	3.71	34.61	128.4	36.5	3.52	1.14	0.0183	0.1262
18	42.2	6.54	125.3	3.71	33.77	125.3	36.5	3.43	1.14	0.0183	0.1265
17	42.2	6.54	122.5	3.71	33.02	122.5	36.5	3.36	1.15	0.0183	0.1268
16	42.2	6.54	119.7	3.71	32.26	119.7	36.5	3.28	1.15	0.0183	0.1271
15	42.2	6.54	71.6	3.71	19.30	71.6	36.5	1.96	1.23	0.018	0.135
	38.2	5.75	48	3.76	12.77	48	36.9	1.30	1.57	0.019	0.164
14	38.2	5.75	119.5	3.76	31.78	119.5	36.9	3.24	1.40	0.0201	0.1480
13	38.2	5.75	71.2	3.76	18.94	71.2	36.9	1.93	1.50	0.019	0.157
	33.9	4.96	48	3.82	12.57	48	37.3	1.29	1.98	0.021	0.195
12	33.9	4.96	118.9	3.82	31.13	118.9	37.3	3.19	1.76	0.0224	0.1769
11	33.9	4.96	70.75	3.82	18.52	70.75	37.3	1.90	1.88	0.022	0.187
	28.6	4.16	48	3.85	12.47	48	38	1.26	2.70	0.024	0.245
10	28.6	4.16	118.6	3.85	30.81	118.6	38	3.12	2.40	0.0260	0.2219
9	28.6	4.16	70.6	3.85	18.34	70.6	38	1.86	2.56	0.025	0.235
	26.3	3.83	48	3.88	12.37	48	38.4	1.25	3.13	0.026	0.273
8	26.3	3.83	118.6	3.88	30.57	118.6	38.4	3.09	2.78	0.0279	0.2475
7	26.3	3.83	70.85	3.88	18.26	70.85	38.4	1.85	2.98	0.027	0.262
	21.4	3.19	48	3.96	12.12	48	39.8	1.21	4.48	0.031	0.352
6	21.4	3.19	119.1	3.96	30.08	119.1	39.8	2.99	3.98	0.0328	0.3183
5	21.4	3.19	71	3.96	17.93	71	39.8	1.78	4.26	0.032	0.337
	19.9	2.96	48	4	12.00	48	39.8	1.21	5.11	0.033	0.388
4	19.9	2.96	118.9	4	29.73	118.9	39.8	2.99	4.55	0.0350	0.3513
3	19.9	2.96	70.9	4	17.73	70.9	39.8	1.78	4.86	0.034	0.3719
	16.3	2.48	48	4.1	11.71	48	41.1	1.17	7.24	0.039	
2	16.3	2.48	118.9	4.1	29.00	118.9	41.1	2.89	6.44	0.0410	0.4488
1	16.3	2.48	136.65	4.1	33.33	136.65	41.1	3.32	6.32	0.0414	0.4420

NOTE: Shaded cells pertain to values that are outside the range of parameter values used to develop the equations.

Table 2-5. Calculated plastic hinge properties for interior columns

Interior Columns: Story	h/t_w	b_f/(2t_f)	L_b (in)	r_y (in)	(L_b/r_y)	L (in)	d (in)	L/d	Λ	θ_P	Θ_Pc
20	42.2	6.54	131.6	3.71	35.47	131.6	36.5	3.61	1.14	0.0184	0.1258
19	42.2	6.54	128.4	3.71	34.61	128.4	36.5	3.52	1.14	0.0183	0.1262
18	42.2	6.54	125.3	3.71	33.77	125.3	36.5	3.43	1.14	0.0183	0.1265
17	42.2	6.54	74.5	3.71	20.08	74.5	36.5	2.04	1.22	0.018	0.134
	40.1	6.11	48	3.74	12.83	48	36.7	1.31	1.43	0.018	0.152
16	40.1	6.11	119.7	3.74	32.01	119.7	36.7	3.26	1.27	0.0192	0.1376
15	40.1	6.11	71.6	3.74	19.14	71.6	36.7	1.95	1.36	0.019	0.146
	33.9	4.96	48	3.82	12.57	48	37.3	1.29	1.98	0.021	0.195
14	33.9	4.96	119.5	3.82	31.28	119.5	37.3	3.20	1.76	0.0225	0.1768
13	33.9	4.96	71.2	3.82	18.64	71.2	37.3	1.91	1.88	0.022	0.187
	31.4	4.49	48	3.83	12.53	48	37.7	1.27	2.30	0.023	0.220
12	31.4	4.49	118.9	3.83	31.04	118.9	37.7	3.15	2.04	0.0241	0.1987
11	31.4	4.49	70.75	3.83	18.47	70.75	37.7	1.88	2.19	0.023	0.210
	26.3	3.83	48	3.88	12.37	48	38.4	1.25	3.13	0.026	0.273
10	26.3	3.83	118.6	3.88	30.57	118.6	38.4	3.09	2.78	0.0279	0.2475
9	26.3	3.83	118.6	3.88	30.57	118.6	38.4	3.09	2.78	0.0279	0.2475
8	26.3	3.83	118.6	3.88	30.57	118.6	38.4	3.09	2.78	0.0279	0.2475
7	26.3	3.83	70.85	3.88	18.26	70.85	38.4	1.85	2.98	0.027	0.262
	23.6	3.48	48	3.92	12.24	48	38.9	1.23	3.78	0.029	0.312
6	23.6	3.48	119.1	3.92	30.38	119.1	38.9	3.06	3.36	0.0304	0.2826
5	23.6	3.48	71	3.92	18.11	71	38.9	1.83	3.59	0.029	0.299
	21.4	3.19	48	3.96	12.12	48	39.9	1.20	4.48	0.031	0.352
4	21.4	3.19	118.9	3.96	30.03	118.9	39.9	2.98	3.98	0.0328	0.3182
3	21.4	3.19	118.9	3.96	30.03	118.9	39.9	2.98	3.98	0.0328	0.3182
2	21.4	3.19	118.9	3.96	30.03	118.9	39.9	2.98	3.98	0.0328	0.3182
1	21.4	3.19	136.65	3.96	34.51	136.65	39.9	3.42	3.91	0.0331	0.3134

NOTE: Shaded cells pertain to values that are outside the range of parameter values used to develop the equations.

2.8.2 Beams Plastic Hinge (Modified IMK model)

Beam plastic hinge properties are estimated for the modified IMK model based on the equations develop by D. G. Lignos and Krawinkler (2010), Eq. 2-4, 2-5, and 2-6. Because the depths of the RBS beam sections used in the model are greater than 21inches, the following equations have been used:

- Pre-capping plastic rotation, θ_p

$$\theta_p = 0.19 \cdot \left(\frac{h}{t_w}\right)^{-0.314} \cdot \left(\frac{b_f}{2.t_f}\right)^{-0.100} \cdot \left(\frac{L_b}{r_y}\right)^{-0.185} \cdot \left(\frac{L}{d}\right)^{0.113} \cdot \left(\frac{c_{unit}^1 \cdot d}{533}\right)^{-0.760} \cdot \left(\frac{c_{unit}^2 \cdot F_y}{355}\right)^{-0.070}$$

(2-4)

$R^2 = 0.56, \quad \sigma_{1n} = 0.24$

- Post capping plastic rotation, θ_{pc}

$$\theta_{pc} = 9.52 \cdot \left(\frac{h}{t_w}\right)^{-0.513} \cdot \left(\frac{b_f}{2.t_f}\right)^{-0.863} \cdot \left(\frac{L_b}{r_y}\right)^{-0.108} \cdot \left(\frac{c_{unit}^2 \cdot F_y}{355}\right)^{-0.360}$$

(2-5)

$R^2 = 0.48, \quad \sigma_{1n} = 0.26$

- Reference cumulative plastic Rotation, Λ

$$\Lambda = \frac{E_t}{M_y} = 585 \cdot \left(\frac{h}{t_w}\right)^{-1.14} \cdot \left(\frac{b_f}{2.t_f}\right)^{-0.632} \cdot \left(\frac{L_b}{r_y}\right)^{-0.205} \cdot \left(\frac{c_{unit}^2 \cdot F_y}{355}\right)^{-0.391}$$

(2-6)

$R^2 = 0.486, \quad \sigma_{ln} = 0.35$

These equations are limited to the following parameter ranges:

- $20 \le h/t_w \le 55 \; for \; other-than-RBS; 21 \le h/t_w \le 55 \; for \; RBS;$
- $20 \le L_b/r_y \le 80 \; for \; other-than-RBS; 20 \le L_b/r_y \le 65 \; for \; RBS;$
- $4 \le b_f/2t_f \le 8 \; for \; other-than-RBS; 4.5 \le b_f/2t_f \le 7.5 \; for \; RBS;$
- $2.5 \le L/d \le 7 \; for \; other-than-RBS; 2.3 \le L/d \le 6.3 \; for \; RBS;$
- $102 \; mm \; (4 \; in.) \le d \le 914 \; mm \; (36 \; in.) for \; other-than-RBS;$
  $533 \; mm \; (21 \; in.) \le d \le 914 \; mm \; (36 \; in.) for \; RBS; and$
- $240 \; MPa \; (35 \; ksi) \le F_y \le 450 \; MPa \; (65 \; ksi) for \; other-than-RBS;$
  $262 \; MPa \; (38 \; ksi) \le F_y \le 435 \; MPa \; (63 \; ksi) for \; RBS.$

The plastic hinge properties for the beam sections have been derived and reported in Table 2-6.

In the above equations, h/t_w is the fillet to fillet is web depth over web thickness ratio of the W-section; $b_f/2.t_f$ is the flange width to thickness ratio; L_b/r_y is the ratio between beam unbraced length L_b over radius of gyration about the weak axis of the cross-section; L/d is the ratio of shear span to depth ratio of the cross-section; F_y is the yield strength of the flange of the beam in ksi; $C_{unit}^1 = 25.4$ and $C_{unit}^2 = 6.895$ are coefficient for units conversion when units are in inches. Also, as mentioned before F_y is 49.9 ksi.

Table 2-6. Calculated plastic hinge properties for beams

Beam Positions	Beam Sections	h/t_w	$b_f/(2t_f)$	$L_b = (a+b)$ (in)	r_y (in)	(L_b/r_y)	L (in)	d (in)	L/d	Λ	θ_P	θ_{Pc}
end spans	W24X94	41.9	5.18	20.75	1.98	10.48	323.5	24.3	13.31	1.83	0.0388	0.266
Interior Beams	W24X94	41.9	5.18	20.75	1.98	10.48	323.5	24.3	13.31	1.83	0.0388	0.266
end spans	W24X103	39.3	4.59	20.75	1.99	10.43	323.5	24.5	13.20	2.13	0.0398	0.305
Interior Beams	W24X103	39.3	4.59	20.75	1.99	10.43	323.5	24.5	13.20	2.13	0.0398	0.305
end spans	W30X148	41.6	4.44	25.50	2.28	11.18	323.5	30.7	10.54	2.01	0.0318	0.303
Interior Beams	W30X148	41.6	4.44	25.50	2.28	11.18	323.5	30.7	10.54	2.01	0.0318	0.303
end span	W36X182	44.8	5.12	30.25	2.55	11.86	323.4	36.3	8.91	1.67	0.0262	0.256
Interior Beams	W36X182	44.8	5.12	30.25	2.55	11.86	323.3	36.3	8.91	1.67	0.0262	0.256
end span	W36X194	42.4	4.81	30.75	2.56	12.01	322.9	36.5	8.85	1.84	0.0266	0.278
Interior Beams	W36X194	42.4	4.81	30.75	2.56	12.01	322.7	36.5	8.84	1.84	0.0266	0.278
end span	W36X232	37.3	3.86	30.75	2.62	11.74	322.5	37.1	8.69	2.46	0.0280	0.359
Interior Beams	W36X232	37.3	3.86	30.75	2.62	11.74	322.3	37.1	8.69	2.46	0.0280	0.359
end span	W36X256	33.8	3.53	30.75	2.65	11.60	321.6	37.4	8.60	2.92	0.0290	0.409
Interior Beams	W36X256	33.8	3.53	30.75	2.65	11.60	321.6	37.4	8.60	2.92	0.0290	0.409
end span	W36X262	38.2	5.75	33.00	3.76	8.78	320.65	36.9	8.69	1.97	0.0283	0.260
Interior Beams	W36X262	38.2	5.75	33.00	3.76	8.78	321.1	36.9	8.70	1.97	0.0283	0.260
end span	W36X282	36.2	5.29	33.00	3.8	8.68	319.8	37.1	8.62	2.22	0.0290	0.287
Interior Beams	W36X282	36.2	5.29	33.00	3.8	8.68	320.7	37.1	8.64	2.22	0.0290	0.287

NOTE: Shaded cells pertain to values that are outside the range of parameter values used to develop the equations.

2.8.3 Discussion on the Plastic Hinge Properties Used in the Numerical Model

One of the goals of this study is to evaluate the behavior of deep sections under the combined action of axial loads and bending moments. For this reason, W36 sections were assigned to the columns (Most of the beams are W36 sections as well). In order to define the cyclic moment-rotation relationship at plastic hinge locations, the regression equations developed by Lignos and Krawinkler (2012) were used. However, these formulations are for beam sections and do not consider the effect of axial force on the parameters that defined the IMK model. Therefore, in order to define the deterioration parameters of the plastic hinges for the columns the formulation for the non-RBS section were implemented and the moment capacity was reduced (ATC 76-2010).

In addition, the number of data points corresponding to W36 sections was scarce and many of the section parameters used in this model are outside the parameter ranges used to develop these equations. The median values of pre-capping plastic rotation (θ_p), post-capping rotation (θ_{pc}), and cumulative rotation capacity (Λ), are in an order of 0.02, 0.2 and 1.0 rad, respectively (Lignos & Krawinkler (2011)) for the available experimental data. However, for the applied sections in the current design these values have ranges according to Table 2-7.

An increase in beam depth d should associate with a decrease in the modeling parameters (Lignos & Krawinkler, 2011). However, the strong dependence of this increase has not been confirmed for large depth sections. Furthermore, for the section depth's used in this research there is a clear increase in modeling parameters due to increase in the section depth for other than RBS sections (plot (c) in Figure 2-9, Figure 2-10 and Figure 2-11).

There is linear regression trend in the data set used to develop deterioration equations for the modified IMK model (Lignos & Krawinkler, 2011). However, for the sections used in this study,

the range of the section parameters (i.e. h/t_w, $b_f/(2t_f)$ with Λ) is not included in the experimental data

range of the equations, and there is a convex relation between modeling parameters and the section

parameters.

In Table 2-4, Table 2-5 and Table 2-6, shaded cells pertain to values that are outside the range

of parameter values (Table 2-7) used to develop the equations.

Table 2-7. Summary of the range of the modified IMK parameters and the depending parameters

Type	Condition	Range	h/t_w	$b_f/(2t_f)$	(L_b/r_y)	d	L/d	Λ	θ_p	θ_{pc}
Beam	with RBS	max	44.80	5.75	12.01	37.40	13.31	2.92	0.040	0.409
		min	33.80	3.53	8.68	24.30	8.60	1.67	0.026	0.256
Exterior Column	Other than RBS	max	42.2	6.54	35.47	41.10	3.61	7.24	0.041	0.496
		min	16.3	2.48	11.71	36.50	1.17	1.14	0.018	0.126
Interior Column	Other than RBS	max	42.20	6.54	35.47	39.90	3.61	4.48	0.033	0.352
		min	21.40	3.19	12.12	36.50	1.20	1.14	0.018	0.126
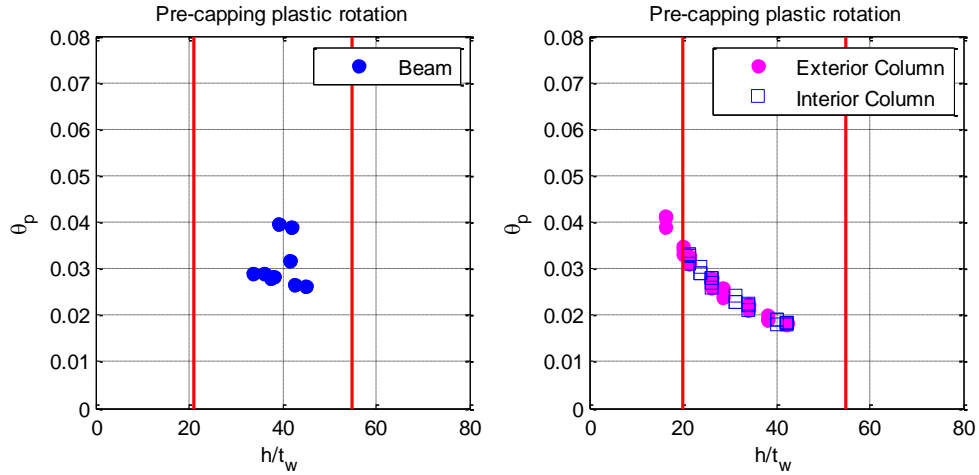
a) Dependence of pre-capping plastic rotation on h/t_w
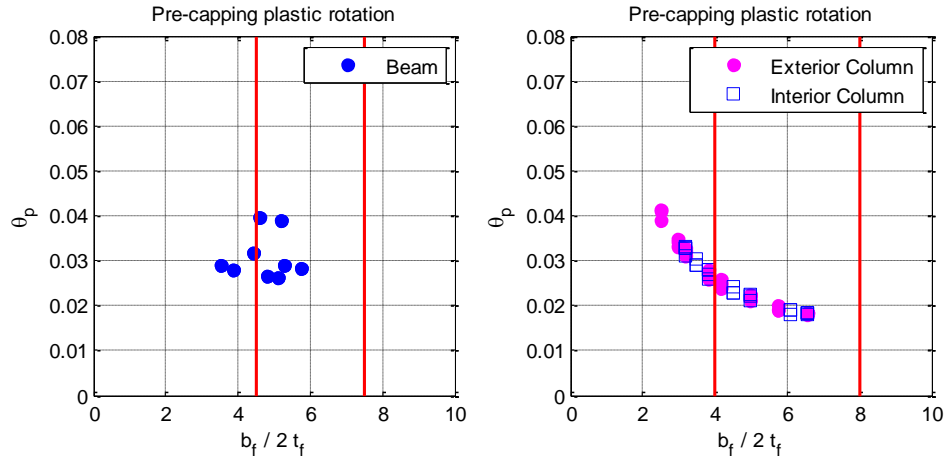
(b) Dependence of pre-capping plastic rotation on $b_f/2t_f$
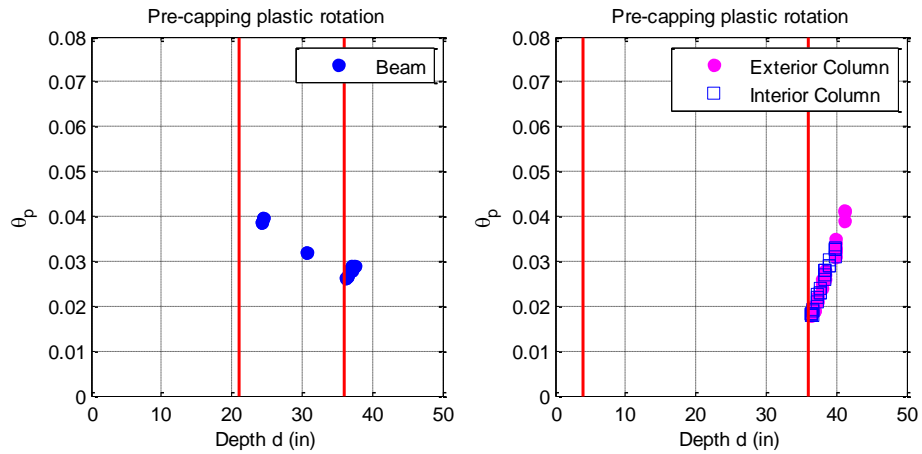
(c) Dependence of pre-capping plastic rotation on depth "d"

Figure 2-9. Dependence of pre-capping plastic rotation
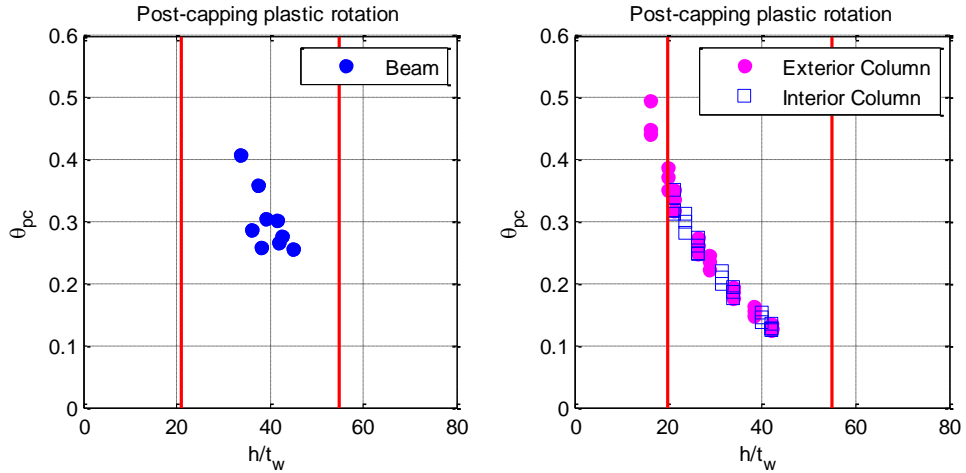
a) Dependence of post-capping plastic rotation on h/t$_w$
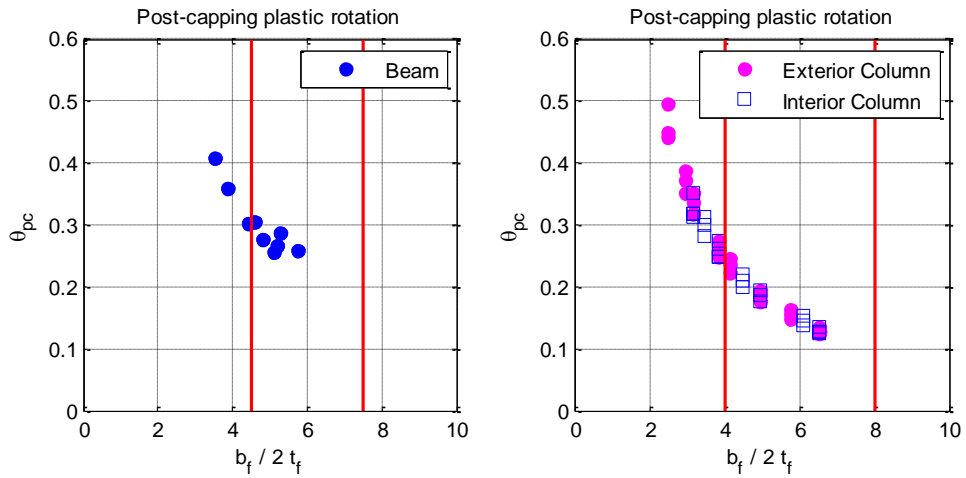
(b) Dependence of post-capping plastic rotation on b$_f$/2t$_f$
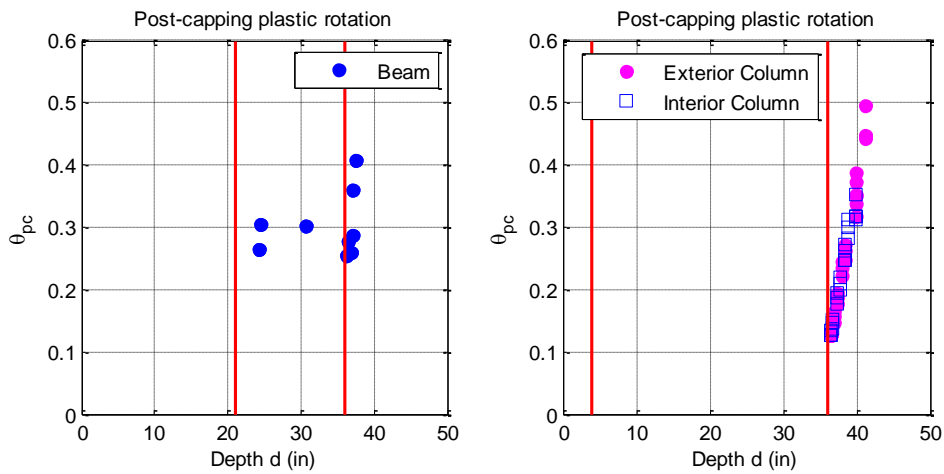
(c) Dependence of post-capping plastic rotation on depth "d"

Figure 2-10. Dependence of post-capping plastic rotation
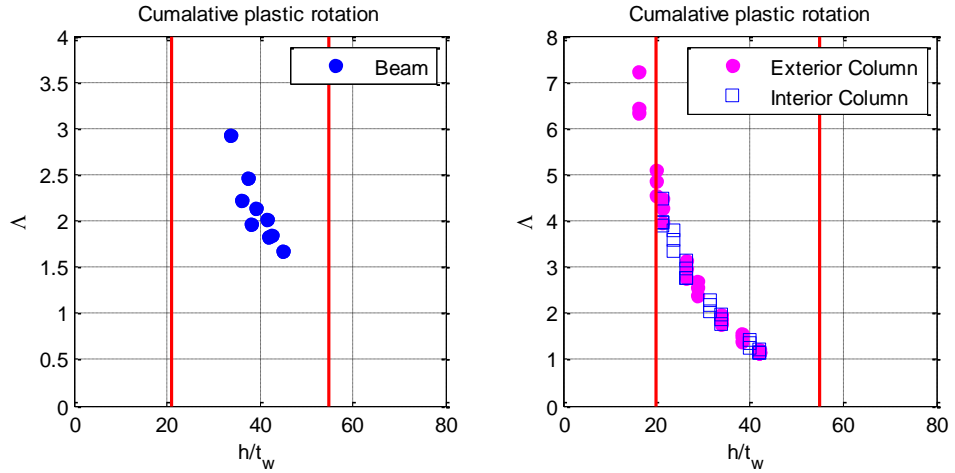
(a) Dependence of cumulative plastic rotation on h/t_w
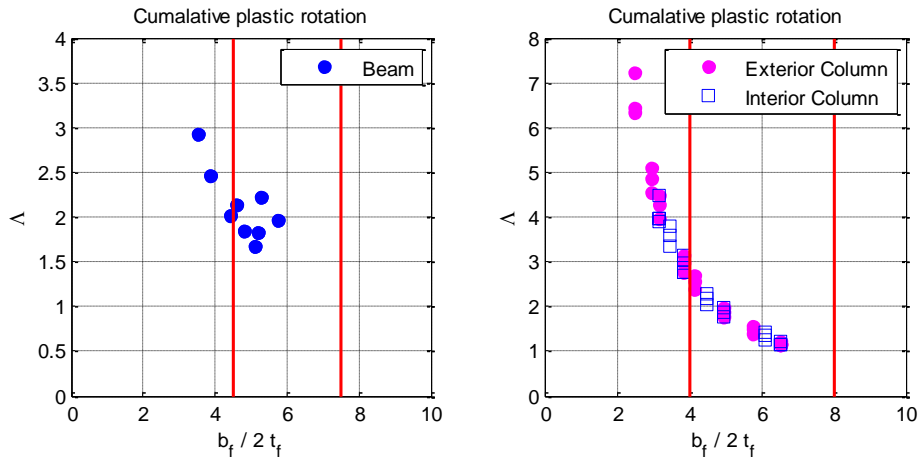
(b) Dependence of cumulative plastic rotation on b_f/2t_f
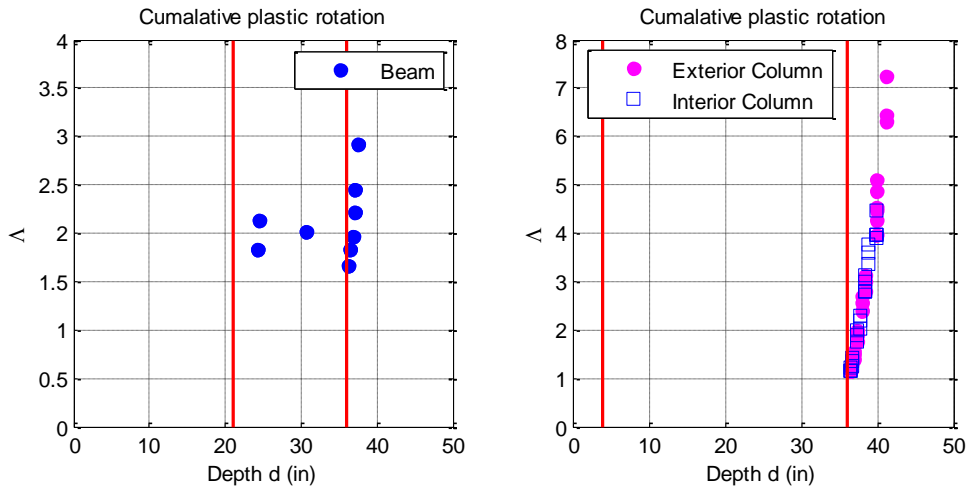
(c) Dependence of cumulative plastic rotation on depth "d"

Figure 2-11. Dependence of cumulative plastic rotation

2.9   Reduction in Estimated Plastic Rotation Capacity of Column Springs

Previous experiments on W14 sections have shown that plastic rotation capacity of the column reduces with the presence of high axial loads (Newell and Uang, 2008). However, for deep steel column sections there is a lake of experimental data. In order to represent the force (P) - moment (M) interaction, the bending strength of the column has been reduced based on an approach that uses the P-M interaction equations given in AISC-ANSI 360-10 (Chapter H). This approach has been used for the implementation of the FEMA P-695 methodology (Chapter 6, ATC 76-1, 2010).

For $\frac{P_r}{P_c} \geq 0.2$

$$\frac{P_r}{2P_c} + \frac{M_{rx}}{M_{cx}} = 1 \rightarrow \frac{M_{rx}}{M_{cx}} = \left(1 - \frac{P_r}{2P_c}\right) \rightarrow \frac{M_{rx}}{M_{nx}} = 0.9 * \left(1 - \frac{P_r}{2P_c}\right) = \alpha \qquad (2\text{-}7)$$

For $\frac{P_r}{P_c} < 0.2$

$$\frac{P_r}{P_c} + \frac{8}{9}\frac{M_{rx}}{M_{cx}} = 1 \rightarrow \frac{M_{rx}}{M_{cx}} = \frac{9}{8}\left(1 - \frac{P_r}{P_c}\right) \rightarrow \frac{M_{rx}}{M_{nx}} = 0.9 * \frac{9}{8}(1 - \frac{P_r}{P_c}) = \alpha \qquad (2\text{-}8)$$

where α is estimated reduction factor of bending strength of the column due to existing axial load demands. The available axial compressive strength P_c and available flexural strength M_{cx} (about the strong axis) are determined from the following equations:

$$P_c = \varphi_c P_n = 0.9 P_n \qquad (2\text{-}9)$$

$$M_{cx} = \varphi_c M_{nx} = 0.9 M_{nx} \qquad (2\text{-}10)$$

where P_n and M_{nx} are the nominal axial load and flexural moment.

P_r and M_{rx} are the required axial compressive load and flexural moment demand, respectively. To obtain the required axial load demand, the axial force of the column from a pushover analysis with a $k = 2$ (parabolic) ASCE-41 (ASCE, 2007) lateral load pattern was obtained. The axial load demand was estimated from combining the factored gravity axial load in the column ($P_{grav}=1.05P_D + 0.25P_L$, P_D as the dead and P_L as the live load) with 50% of the maximum axial load ($P_{E,max}$) experienced by the column due to the application of the lateral loads during the pushover analysis, $P_r=P_{grav}+0.5P_{E,max}$ (NIST, 2011). Table 2-8 and Table 2-9 present the reduction factors α, for exterior and interior columns. Table 2-10 and Table 2-11 show the reduced moment capacity for exterior and interior columns.

Table 2-8. Exterior column reduction factor (α) for bending strength

Story	Section	$P_{E,max+grav}$ (kip)	P_{grav} (kip)	$P_r=P_{grav}+$ $0.5(P_{E,max+grav}-P_{grav})$ (kip)	P_c (kip)	P_c (scaled) (kip)	P_r/P_c	$\alpha = M_r/M_n$
R	W36X231	0.89	0.56	0.72	2688	42	0.017	0.892
20	W36X231	2.36	1.51	1.93	2688	42	0.046	0.879
19	W36X231	4.61	2.52	3.57	2688	42	0.085	0.862
18	W36X231	7.24	3.54	5.39	2688	42	0.128	0.842
17	W36X231	10.84	4.62	7.73	2688	42	0.184	0.817
16	W36X231	14.49	5.71	10.10	2688	42	0.240	0.769
	W36X262	14.49	5.71	10.10	2688	42	0.240	0.798
15	W36X262	18.40	6.80	12.60	3050	48	0.264	0.745
14	W36X262	22.40	7.89	15.15	3050	48	0.318	0.691
	W36X302	22.40	7.89	15.15	3531	55	0.275	0.734
13	W36X302	27.03	9.03	18.03	3531	55	0.327	0.682
12	W36X302	31.65	10.16	20.91	3531	55	0.379	0.629
	W36X361	31.65	10.16	20.91	4223	66	0.317	0.692
11	W36X361	36.71	11.33	24.02	4223	66	0.364	0.644
10	W36X361	41.78	12.48	27.13	4223	66	0.411	0.596
	W36X395	41.78	12.48	27.13	4630	72	0.375	0.633
9	W36X395	46.86	13.63	30.25	4630	72	0.418	0.589
8	W36X395	51.97	14.77	33.37	4630	72	0.461	0.545
	W36X487	51.97	14.77	33.37	5735	90	0.372	0.635
7	W36X487	57.28	15.92	36.60	5735	90	0.408	0.599
6	W36X487	62.56	17.04	39.80	5735	90	0.444	0.563
	W36X529	62.56	17.04	39.80	6270	98	0.406	0.601
5	W36X529	68.11	18.17	43.14	6270	98	0.440	0.567
4	W36X529	73.58	19.26	46.42	6270	98	0.474	0.533
	W36X652	73.58	19.26	46.42	7758	121	0.383	0.625
3	W36X652	78.99	20.34	49.67	7758	121	0.410	0.598
2	W36X652	84.21	21.38	52.79	7767	121	0.435	0.572

Table 2-9. Interior column reduction factor (α) for bending strength

Story	Section	$P_{E,max+grav}$ (kip)	P_{grav} (kip)	$P_r=P_{grav}+$ $0.5(P_{E,max+grav}-P_{grav})$ (kip)	P_c (kip)	P_c (scaled) (kip)	P_r/P_c	$\alpha = M_r/M_n$
R	W36X231	1.12	0.84	0.98	2688	42	0.023	0.889
20	W36X231	2.88	2.28	2.58	2688	42	0.061	0.872
19	W36X231	4.81	3.69	4.25	2688	42	0.101	0.854
18	W36X231	6.57	5.10	5.84	2688	42	0.139	0.837
	W36X247	6.57	5.10	5.84	2868	45	0.130	0.841
17	W36X247	8.49	6.48	7.49	2868	45	0.167	0.825
16	W36X247	10.31	7.86	9.09	2868	45	0.203	0.807
	W36X302	10.31	7.86	9.09	3531	55	0.165	0.826
15	W36X302	12.00	9.24	10.62	3531	55	0.193	0.813
14	W36X302	13.67	10.63	12.15	3531	55	0.220	0.789
	W36X330	13.67	10.63	12.15	3860	60	0.202	0.808
13	W36X330	15.56	12.01	13.78	3860	60	0.229	0.781
12	W36X330	17.49	13.40	15.44	3860	60	0.256	0.753
	W36X395	17.49	13.40	15.44	4630	72	0.213	0.796
11	W36X395	19.41	14.78	17.09	4630	72	0.236	0.773
10	W36X395	21.27	16.17	18.72	4630	72	0.259	0.751
9	W36X395	23.01	17.56	20.28	4630	72	0.280	0.729
8	W36X395	24.72	18.97	21.85	4630	72	0.302	0.707
	W36X441	24.72	18.97	21.85	5201	81	0.269	0.740
7	W36X441	26.40	20.39	23.39	5201	81	0.288	0.721
6	W36X441	28.02	21.83	24.92	5201	81	0.307	0.702
	W36X487	28.02	21.83	24.92	5735	90	0.278	0.731
5	W36X487	29.53	23.29	26.41	5735	90	0.295	0.714
4	W36X487	30.95	24.77	27.86	5735	90	0.311	0.698
3	W36X487	32.23	26.28	29.25	5735	90	0.326	0.682
2	W36X487	33.50	27.85	30.68	5742	90	0.342	0.666

Table 2-10. Exterior column modified moment capacity

Story	Section	z (in^3)	M_n (kip)	Mr=$\alpha.M_n$ (kip)
R	W36X231	1.88	94	84
20	W36X231	1.88	94	83
19	W36X231	1.88	94	81
18	W36X231	1.88	94	79
17	W36X231	1.88	94	77
16	W36X231	1.88	94	72
	W36X262	2.15	107	86
15	W36X262	2.15	107	80
14	W36X262	2.15	107	74
	W36X302	2.50	125	92
13	W36X302	2.50	125	85
12	W36X302	2.50	125	78
	W36X361	3.03	151	104
11	W36X361	3.03	151	97
10	W36X361	3.03	151	90
	W36X395	3.34	167	105
9	W36X395	3.34	167	98
8	W36X395	3.34	167	91
	W36X487	4.16	208	132
7	W36X487	4.16	208	124
6	W36X487	4.16	208	117
	W36X529	4.55	227	137
5	W36X529	4.55	227	129
4	W36X529	4.55	227	121
	W36X652	5.68	284	177
3	W36X652	5.68	284	170
2	W36X652	5.68	284	162

Table 2-11. Interior column modified moment capacity

Story	Section	z (in^3)	M_n (kip)	Mr=$\alpha.M_n$ (kip)
R	W36X231	1.88	94	83
20	W36X231	1.88	94	82
19	W36X231	1.88	94	80
18	W36X231	1.88	94	79
	W36X247	2.01	100	84
17	W36X247	2.01	100	83
16	W36X247	2.01	100	81
	W36X302	2.50	125	103
15	W36X302	2.50	125	101
14	W36X302	2.50	125	98
	W36X330	2.75	137	111
13	W36X330	2.75	137	107
12	W36X330	2.75	137	104
	W36X395	3.34	167	133
11	W36X395	3.34	167	129
10	W36X395	3.34	167	125
9	W36X395	3.34	167	121
8	W36X395	3.34	167	118
	W36X441	3.73	186	138
7	W36X441	3.73	186	134
6	W36X441	3.73	186	131
	W36X487	4.16	208	152
5	W36X487	4.16	208	148
4	W36X487	4.16	208	145
3	W36X487	4.16	208	142
2	W36X487	4.16	208	138

2.10 Gravity Force Calculation

For the analysis of structure, nonlinear analysis procedures are performed. Therefore, the gravity loads applied on N-S frame are estimated based on the following load combination $1.05P_D + 0.25P_L$ (P_D is the dead and P_L is the live load), according to FEMA P695 (2009). A fully composite floor system was considered for the floors and roof of the structure. Based on the design, dead load of 48 psf was considered. Typical floor live loads according to ASCE/SEI 7-10 (2010), are shown in Figure 2-12. For the roof space, a uniform live load of 20 psf has been considered. Floor loads are applied to girders as distributed loads based on their tributary area. Girder self-weights are also applied as distributed loads. The loads of the floor beams based on the tributary areas and their weights (dashed lines in Figure 2-8) are applied to girders as point loads (yellow arrows indicate the floor beams loads connected to the exterior columns, and the orange arrows indicate the floor beams connected to the interior columns as shown in Figure 2-13). Column self-weights are distributed linearly over the length of the columns. The point loads on exterior and interior columns, as well as the distributed loads applied to girders the N-S frame illustrated in Figure 2-13 are reported in Table A 2-6 (Appendix 2).
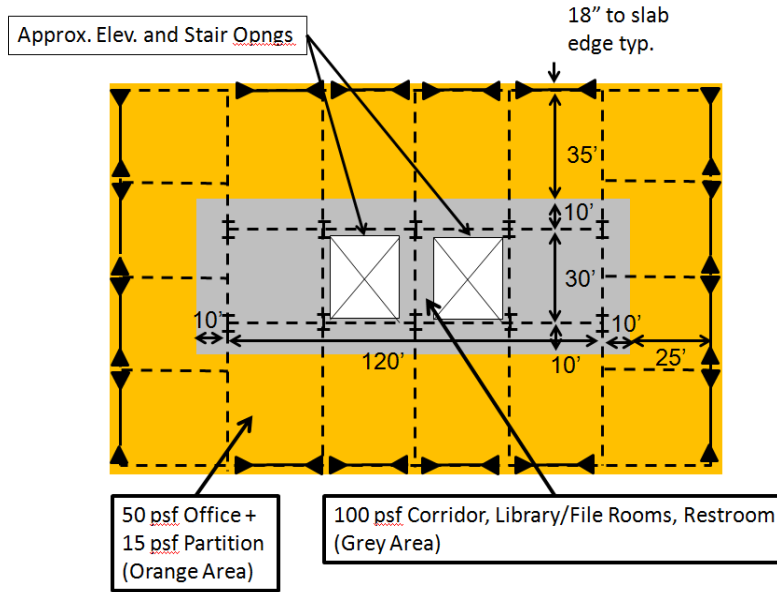
Figure 2-12. Typical office live load map
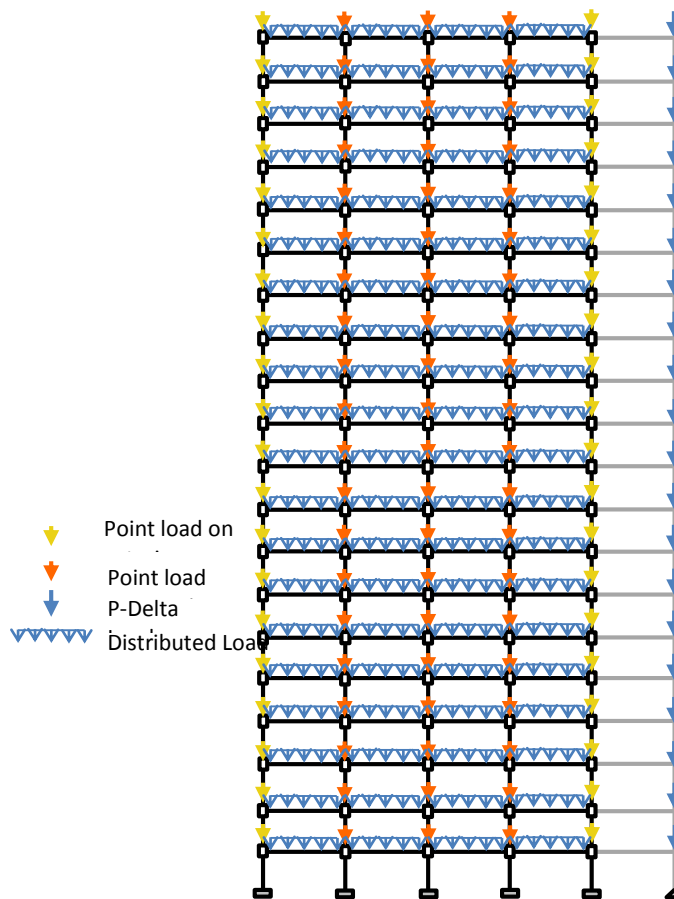
Figure 2-13. Illustration of the implemented gravity and P-Delta forces on N-S Frame Elevation

2.11 P-Delta Loads

For tall steel structures, accounting for P-Delta effect is essential to estimate the seismic collapse capacity of the structure. P-Delta is a nonlinear (second order) effect due to the total vertical load acting on the laterally deformed frame, which amplifies the story drifts. The same load combination used to calculate gravity loads for the moment-resisting frame has been used to estimate the P-Delta loads on the leaning column ($1.05P_D + 0.25P_L$, where P_D is the dead and P_L is the live load). The leaning column is an elastic column element with high axial stiffness (very large area with respect to the column members) and low lateral stiffness (very small moment of inertia with respect to the frame in order to have negligible effect on the lateral stiffness of the frame). The leaning column is supported by pin connection at the base and is linked to the N-S frame with rigid links (assigned very large area to the links as well) at each level. Because a two-dimensional frame is modeled, only half of the structure is considered when estimating P-Delta loads. The load applied to leaning column is floor gravity loads corresponding to half of the floor mass minus the tributary load of the N-S frame at each level.

The magnitude of the P-Delta loads is shown in Table 2-12. The applied P-Delta loads on the leaning column are shown as blue arrows in Figure 2-13.

Table 2-12. P-Delta loads applied on the leaning column

Floor	1.05 P_D+0.25 P_L (kips)
R	644
20	841
19	849
18	849
17	855
16	855
15	862
14	862
13	870
12	869
11	878
10	879
9	887
8	887
7	893
6	893
5	900
4	900
3	902
2	866

2.12 Effective Seismic Weight

The effective seismic weight includes the dead loads from the slab, metal deck, ceiling, flooring, beams, girders, cladding (half from stories above and below), columns (half from stories above and below), and partition loads (10 psf of floor area absed on ASCE/SEI-7-10). The values are shown in Table 2-13.

Table 2-13. Seismically effective weights and masses for each story

Floor	Seismically Effective Weight (kip)	Mass (kip-s²/in)
R	825	2.13
20	993	2.57
19	1005	2.60
18	1006	2.60
17	1015	2.63
16	1016	2.63
15	1025	2.65
14	1026	2.66
13	1039	2.69
12	1040	2.69
11	1052	2.72
10	1054	2.73
9	1062	2.75
8	1063	2.75
7	1072	2.77
6	1073	2.78
5	1083	2.80
4	1085	2.81
3	1089	2.82
2	1089	2.82

2.13 Lateral Load Pattern for Pushover Analysis

Although the structure was analyzed using the Modal Response Spectrum Analysis approach, nonlinear static analyses were conducted using the load pattern presented in the Equivalent Lateral Force procedure of ASCE/SEI-7-10. For the pushover analysis, the seismic design floor loads (F_x) according to the Equivalent Lateral Force procedure ($C_{vx}V$, where C_{vx} is the vertical distribution factor and V is the shear) are shown in Table 2-14.

Table 2-14. Seismic design floor loads for the prototype frame

Floor	Height (inches)	Height (ft)	Seismically Effective Weight (kip)	C_{vx}	F_x (kips)	Story Shear (kip)
R	3119	260	825	0.116	83.9	84
20	2963	247	993	0.126	91.1	175
19	2807	234	1005	0.114	82.8	258
18	2651	221	1006	0.102	73.9	332
17	2495	208	1015	0.091	66.1	398
16	2339	195	1016	0.080	58.1	456
15	2183	182	1025	0.070	51.1	507
14	2027	169	1026	0.061	44.1	551
13	1871	156	1039	0.052	38.0	589
12	1715	143	1040	0.044	32.0	621
11	1559	130	1052	0.037	26.7	648
10	1403	117	1054	0.030	21.7	670
9	1247	104	1062	0.024	17.3	687
8	1091	91	1063	0.018	13.2	700
7	935	78	1072	0.014	9.80	710
6	779	65	1073	0.009	6.81	717
5	623	52	1083	0.006	4.40	721
4	467	39	1085	0.003	2.48	724
3	311	26	1089	0.002	1.10	725
2	155	13	1089	0.000	0.27	725
		SUM	20711	SUM	725	

2.14 Modal Analysis

A fundamental period of 1.03 seconds was determined by performing an eigenvalue analysis of the scaled structure N-S moment resisting frame developed in OpenSees. By scaling down the corresponding fundamental period of the prototype structure which was 2.93 s (Mathiasson &

Medina, 2013) by the time scale factor of $\left(\frac{1}{8}\right)^{1/2}$, the same fundamental period of the scaled

structure is obtained; this will validate the scaling process and modeling the scaled frame in

OpenSees. The first five modal periods and mode shapes for the N-S moment resisting frame are

shown in Figure 2-14, which is consistent with the prototype structure.

Table 2-15. First five modal periods of the moment resisting frame from Eigenvalue analysis

Mode	Modal Period (s)
1	1.035
2	0.377
3	0.220
4	0.151
5	0.110
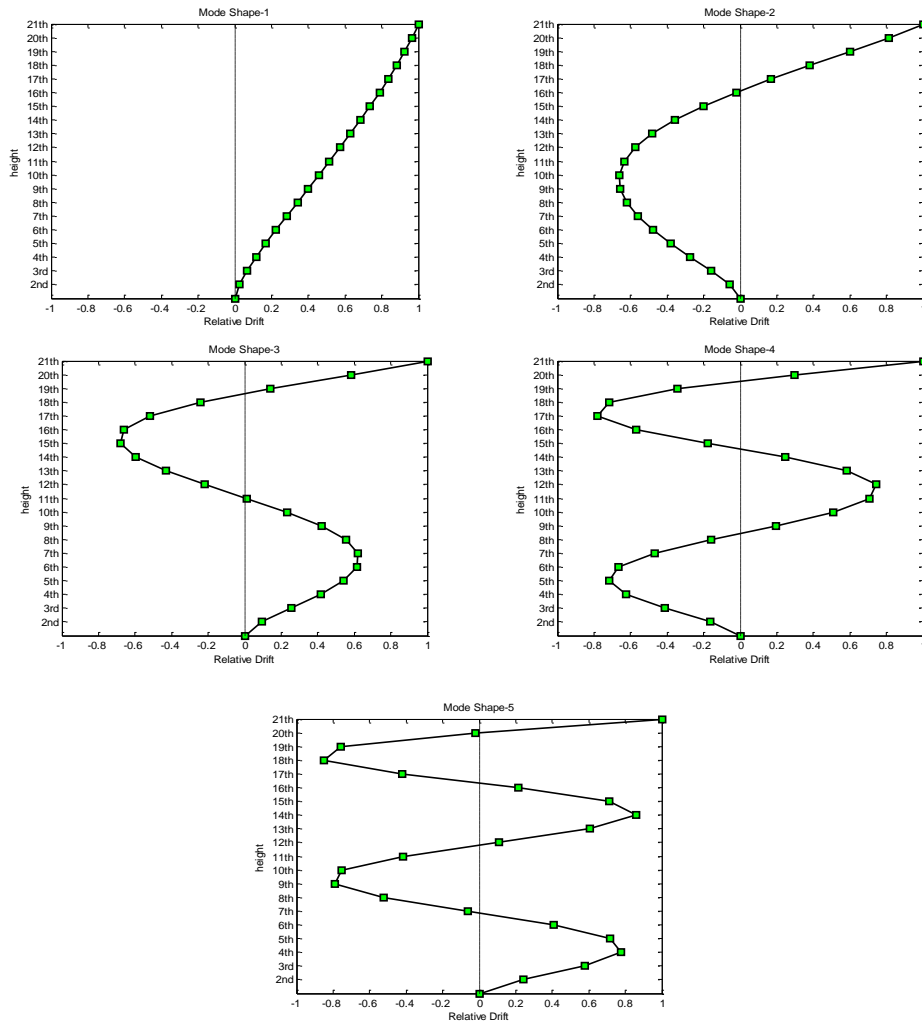
Figure 2-14. First five mode shapes of the N-S moment resisting frame model obtained by performing eigenvalue analysis in OpenSees

2.15 Non-Linear Static Pushover Analysis (Pushover) of the Scaled Model

The Non-linear static pushover analysis provides an estimate of force and deformation demands as well as the pattern of inelastic deformation throughout the structure. For the pushover analysis, an inelastic model is subjected to gravity load and followed by a monotonically increasing displacement controlled lateral load pattern. The lateral load pattern corresponding to the fundamental mode shape described in Table 2-14 was used for the pushover analysis in OpenSees.

Figure 2-15, illustrates the 1st-story pushover in which the vertical axis is the base shear normalized to the structures seismic effective weight and the horizontal axis is the first story drift ratio (first story displacement normalized by its height). The yield drift ratio of the first story is approximately 0.3%.
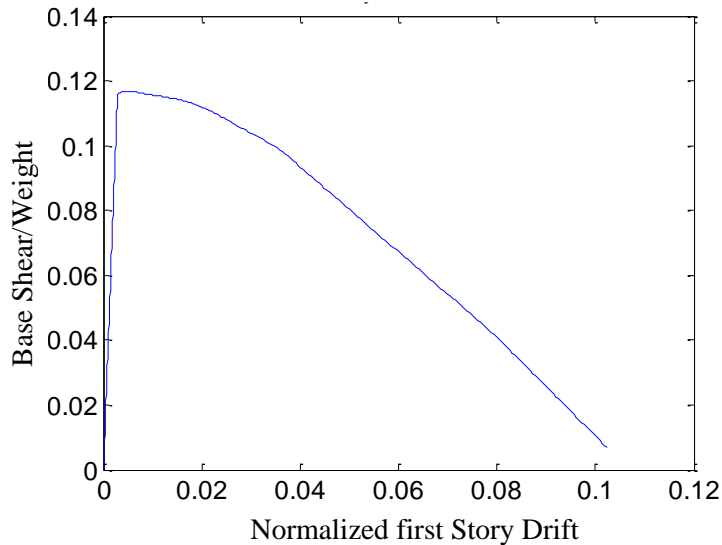
Figure 2-15. First story pushover curve

Figure 2-16, shows the global pushover curve. The vertical axis is the base shear normalized by the structure seismic effective weight (V/W) and the horizontal is the roof drift ratio (the roof displacement normalized by the structure's height). Global yielding occurs at a roof drift ratio of approximately 0.7%. After the yield and strength plateau, the P-Delta effects will take over which results in a sudden steep negative slope in the global pushover curve. The overstrength factor, Ω, in this structure is estimated as 3.9, in which is the ratio of the maximum normalized shear is $(V/W)_{max} = 0.117$ and the design normalized shear is as $(V/W)_{Design} = 0.030$.
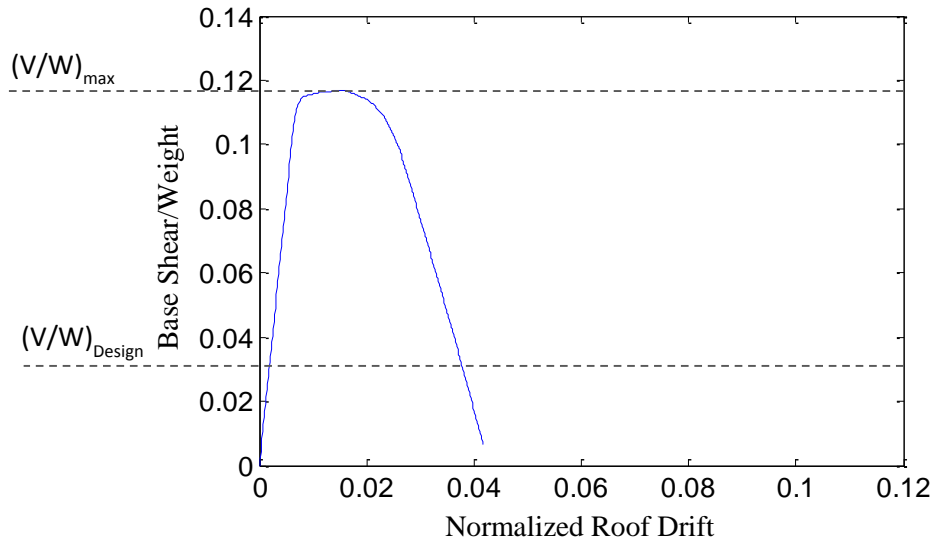
Figure 2-16. Global pushover curve

The current structure was designed based on the loading and design criteria of ASCE 7-10 (2010), AISC360-10 (2010) and AISC341-10 (2010). The over strength factor of 3.9 was estimated for the structure, which has a greater magnitude than expected value of 2 to 3 based on the previous structures which have been reported in most of the literature (ATC 76). This difference in the strength factor could be explained as follow:

- In the relationship to satisfy the "*strong column-weak beam*" criteria (in the implemented design code (eq. E3-1, AISC341-10 (2010)), the required compressive strength of the column should include the amplified seismic load in the LRFD load combination, in which in previous code (eq. 9-3, AISC341-05(2005)) this requirement was not considered. So, based on the new code design to satisfy the moment ratio a stronger column is needed.

- The modal response spectrum analysis procedure (RSA) of section 12.9 of ASCE/SEI 7-10 has been implemented as the design basis. In which, it requires an increase in the drifts by multiplying by a factor of $0.85\frac{C_sW}{V_t}$ which was not a criteria in the older versions (ASCE/SEI 7-05). Where V_t is the modal base shear, C_s is the seismic response coefficient, and W is the effective seismic weight. Figure 2-17, illustrates the influence of multiplying the factor for the interstory drifts, in which for the current design is 1.717. Moreover, the overstrength factor is controlled mostly by the drift and P-Delta stiffness criteria. In which, in the current structure the member sizes were chosen based on the drift and P-Delta criteria.
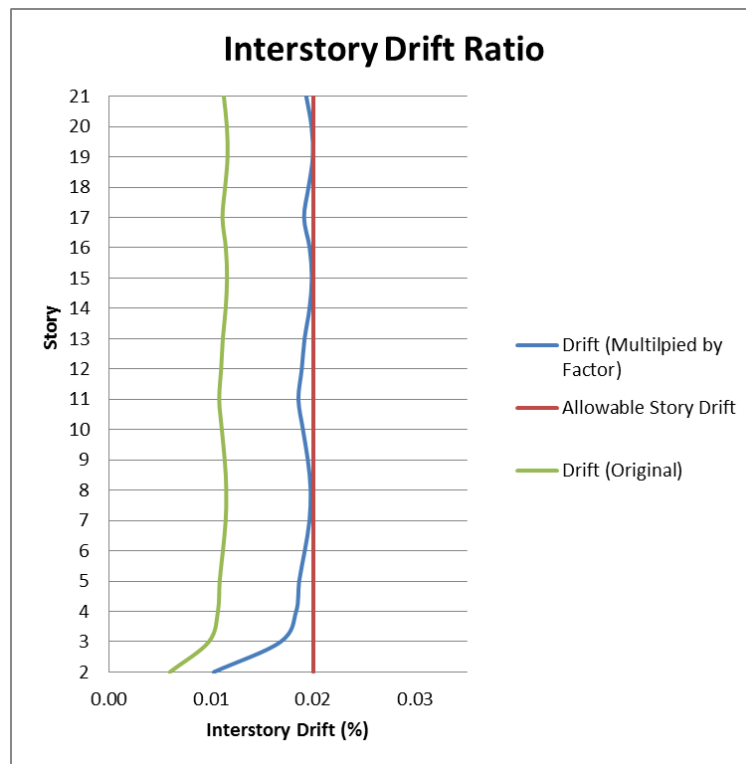
Figure 2-17. Interstory drift layout over the height of the structure

2.16 Propagation of hinging during the non-linear static analysis

The 20-story moment resisting frame is modeled with concentrated plastic hinges, during the analysis when the plastic hinges reach M_p, hining has occurred. The spread of hinging over the height of the structure is shown at the defined steps presented on the global pushover, Figure 2-18. Hinge formation at different locations in members is illustrated by the presence of red dots in the Figure 2-19. As it can be seen in Figure 2-19, in Step 47 (nt=47), hinging begins in the upper mid-height beams. As hinging in the beams and panel zones spreads through the height of the building, the base of the exterior column on the right side of the frame hinges in Step 61 (nt=61). The left side exterior column hinges in Step 68. By Step 82, all of the columns bases have hinged. In Step 108, beams on the 2nd floor begin to hinge and in Step 122, the bottom of all of the 2nd story interior columns have hinges. Hinging also occurs at the top of the interior columns in the 8th story in Step 195. In Step 318, all columns at the 7th story experience hinging at the top. The hinging mechanism of the structure before numerical instability is imminent is illustrated in Step 325. Figure 2-20, shows sample moment-rotation responses for a selected beam, column and panel zone for selected members. The selected springs have the most rotation compared to the other springs in their category in the structure. As it can be seen, the beam and column springs enter the post capping region. Moreover, the rotation in the panel zone is not significant. These location of the selected springs are shown in Figure 2-21 .
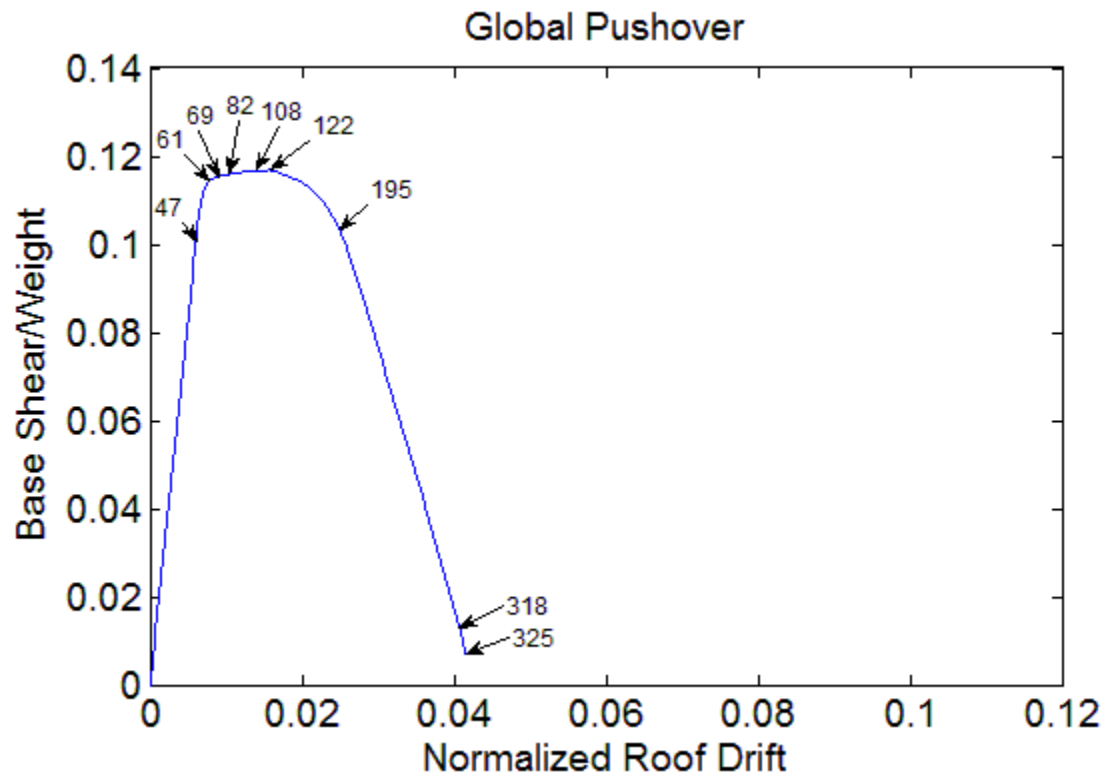
Figure 2-18. Global pushover curve of the structure mapping key points to study hinge propagation
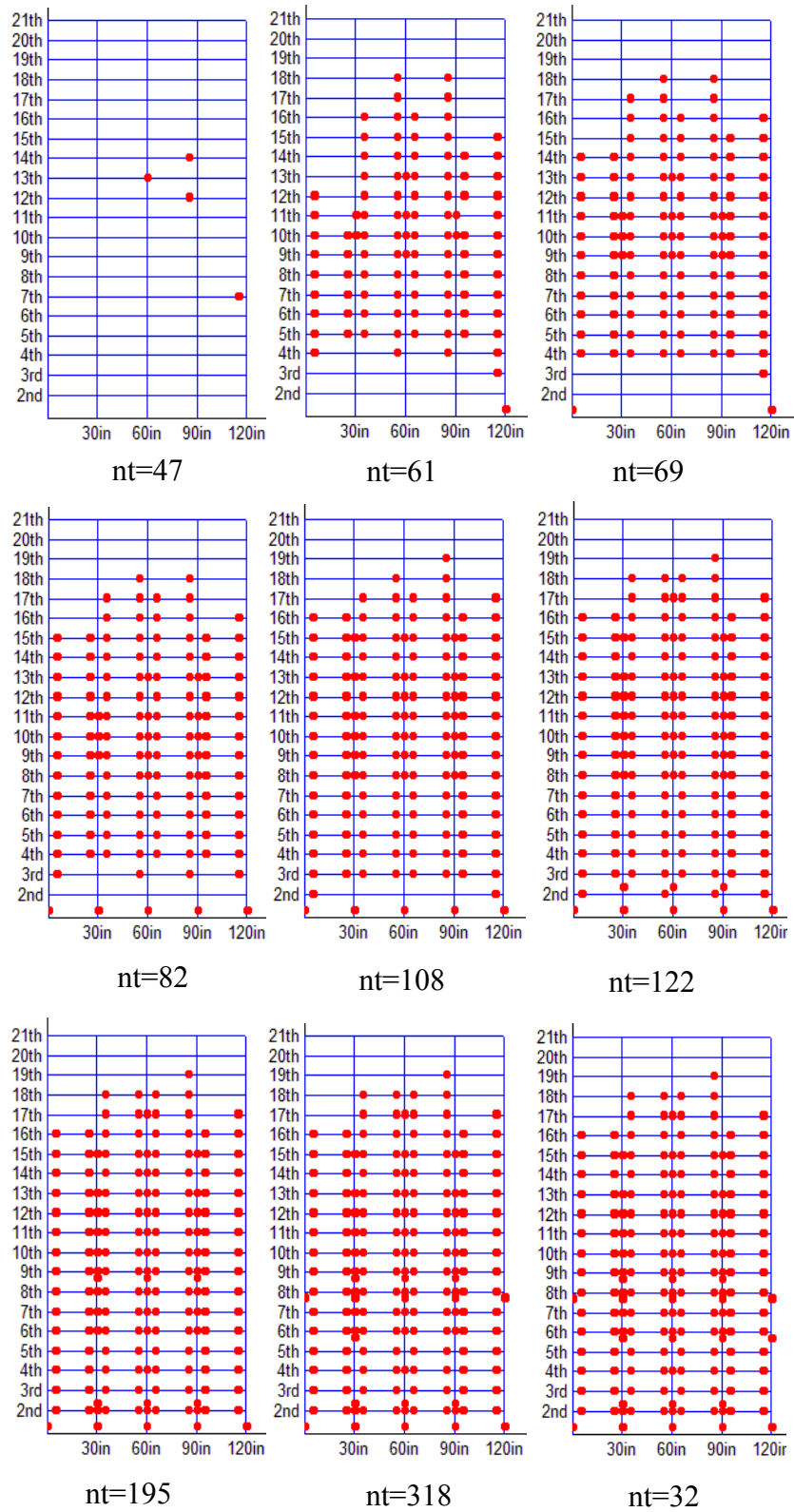
Figure 2-19. Hinge propagation in structure during non-linear static analysis in selected steps
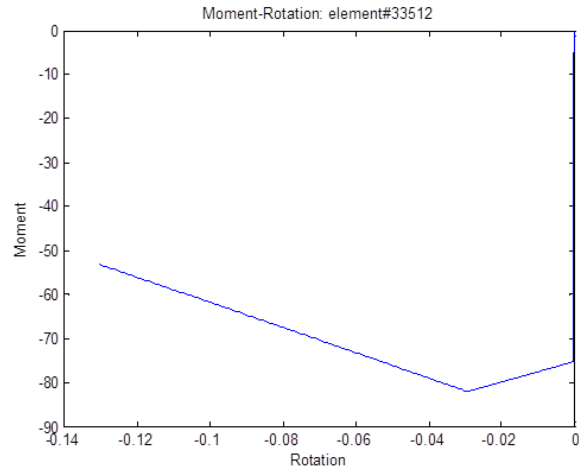
(a) Beam
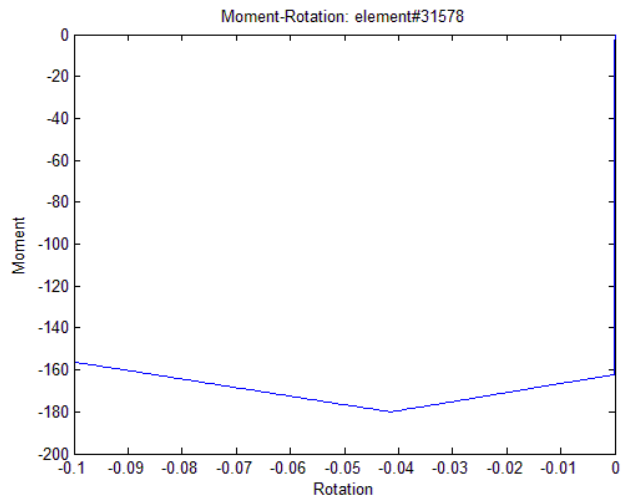
(b) Column
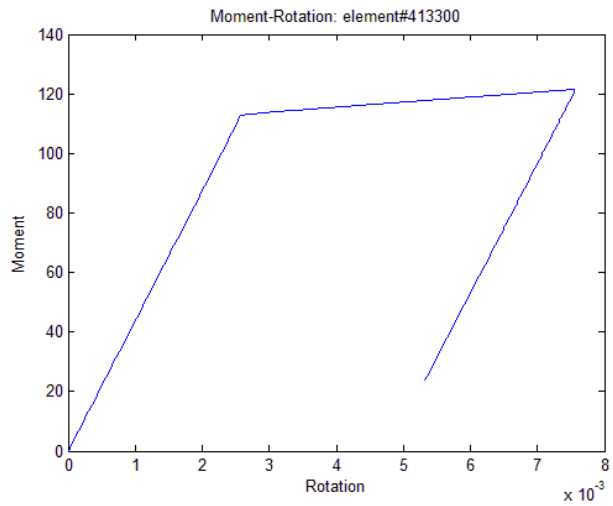
(c) Panel zone

Figure 2-20. Sample moment-rotation response of selected beam, column and panel zone

Figure 2-21. Numbering pattern used in OpenSees model of N-S frame

2.17 Structure Deformation Profiles

Deformation profiles during the pushover analysis are shown in Figure 2-22, with the corresponding drift location on the global push over curve. It is expected to have hinging earlier at the base of the columns, as well as larger drifts in the bottom stories of the structure, However, story drifts are concentrated more near the middle of the structure, except when the roof drift ratio exceeds 2.5%.
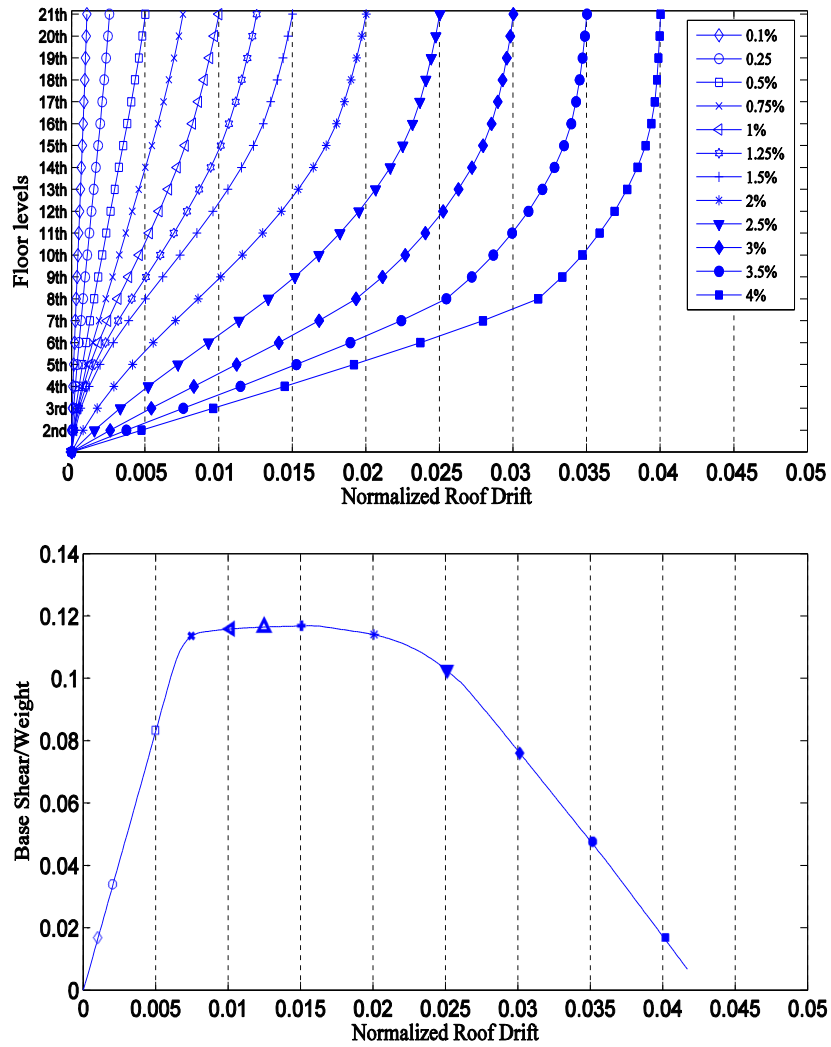
Figure 2-22. Deformation profiles (top) during the pushover analysis (bottom)

63

The process of hinging begins in the beams positioned in the mid-height of the structure and spreads out over the height. The base of the columns hinges, and then the 2nd floor beams. Furthermore, a significant number of panel zones hinge, however their corresponding rotation is small. The delay in forming a mechanism in the lower stories especially the 2nd story beams, exhibits a difference in the deformation profile of the structure corresponding (Figure 2-23) to the deformation profile for the 20-story archetype steel moment-resisting frame structures studied as part of the ATC-76 project (2010) (Figure 2-24). However, as mentioned before the current structure in this research has been designed and controlled based on the latest version of AISC and ASCE, which makes a difference in the design and drift criteria.
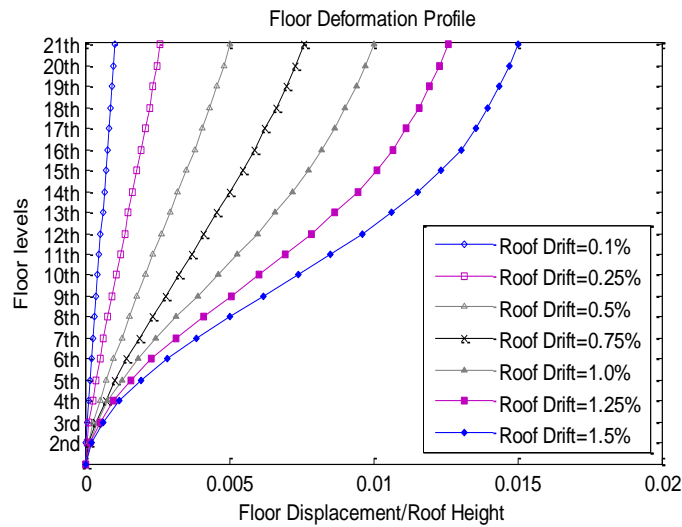
Figure 2-23. Deforming Profile of the 20-story in the current research, RSA

Floor Deformation Profile
20-story, RSA, D_{max}, First mode load pattern
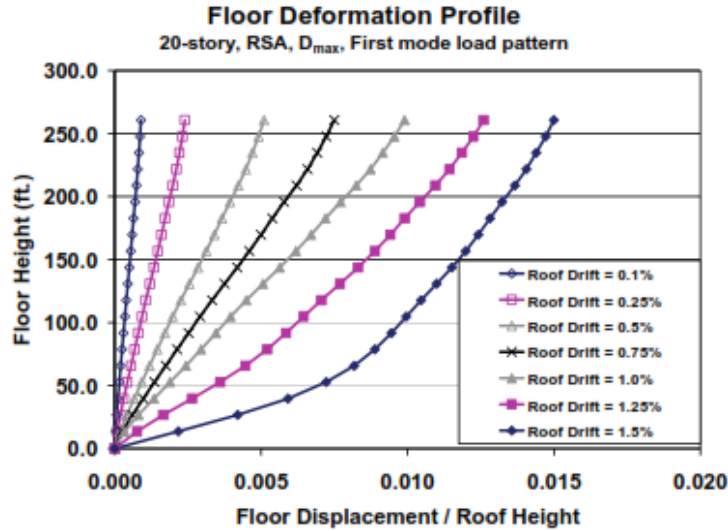
Figure 2-24. Deforming Profile of the 20-story, RSA, SDC D_{max} Archetype (ATC76-1, 2010)

2.18 Summary

In this chapter, a description of the most relevant structural properties and modeling assumptions of the 20-story moment resisting frame and the exterior column used for this research were presented. This model later was used as the numerical substructure portion of the hybrid simulation. One of the goals of this study is to evaluate the behavior of deep sections under the combined action of axial loads and bending moments. For this reason, W36 sections were assigned to the columns (Most of the beams are W36 sections as well). The member sizes in the frame were chosen based on the drift and P-Delta criteria. In order to model and capture cyclic moment-rotation relationship at plastic hinge locations (IMK), the regression equations developed by Lignos and Krawinkler (2012) were utilized. However, these equations do not account for the effect of axial force on the parameters that defines the IMK model. Therefore, in order to define the deterioration parameters of the plastic hinges for the columns the formulation for the non-RBS section were implemented and the moment capacity was reduced (ATC 76-2010). In addition, the

number of data points corresponding to W36 sections was scarce and many of the section parameters used in this model are outside the parameter ranges used to develop these equations.

2.19 References

AISC. (2010). Seismic Provisions for Structural Steel Buildings, ANSI/AISC 341-10 2010: American Institute of Steel Construction, Chicago, Illinois.

ASCE. (2007). Seismic Rehabilitation of Existing Buildings, ASCE/SEI 41-06 *American Society of Civil Engineers, Reston, VA, US*.

ASCE. (2010). Minimum Designs Loads for Buildings and Other Structures, ASCE/SEI 7-10: American Society of Civil Engineers, Reston, Virginia.

Committee, A. (2010). Specification for structural steel buildings (ANSI/AISC 360-10). *American Institute of Steel Construction, Chicago-Illinois*.

Construction, A. I. o. S. (2010). Prequalified Connections for Special and Intermediate Steel Moment Frames for Seismic Applications, ANSI/AISC 358-10.

FEMA, P. (2009). Quantification of building seismic performance factors: Washington, DC.

Ibarra, L. F., Medina, R. A., & Krawinkler, H. (2005). Hysteretic models that incorporate strength and stiffness deterioration. *Earthquake engineering & structural dynamics, 34*(12), 1489-1511.

Lignos, D. G., & Krawinkler, H. (2010). Deterioration modeling of steel components in support of collapse prediction of steel moment frames under earthquake loading. *Journal of Structural Engineering, 137*(11), 1291-1302.

Mathiasson, A., & Medina, R. A. (2013). *Seismic collapse assessment of a 20-story steel moment resisting frame structures.* (MS), University of New Hampshire, Durham, New Hampshire.

NIST. (2011). Research Plan for the Study of Seismic Behavior and Design of Deep, Slender Wide Flange Structural Steel Beam-Column Member. *prepared by the NEHRP Consultants Joint Venture, a partnership of the Applied Technology Council and the Consortium of Universities for Research in Earthquake Engineering for the National Institute of Standards and Technology, NIST GCR 11-917-13 2011*(Gaithersburg, Maryland).

OpenSees. (2007). Open System for Earthquake Engineering Simulation: Pacific Earthquake Engineering Research Center (PEER). Retrieved from http://opensees.berkeley.edu

Zareian, F., & Medina, R. A. (2010). A practical method for proper modeling of structural damping in inelastic plane structural systems. *Computers & structures, 88*(1), 45-53.

3 EXPERIMENTAL STUDIES ON A DEEP STEEL COLUMN SECTION SUBJECTED TO VARIABLE DRIFT, ROTATION, AND AXIAL LOAD DEMANDS

Shokoufeh Zargar S .M.EERI[1], Ricardo A. Medina M.EERI[2]

3.1 Abstract

Quasi-static experiments were conducted on a 1:8 scaled W36X652 exterior column of a 20-story moment resisting frame due to the scarcity of available data for calibration of existing nonlinear hysteresis models for deep steel columns. Two monotonic and four cyclic tests were implemented. The developed loading protocols included lateral column drift ratios of up to 0.1 rad, rotation at the tip of the column of up to 0.1 rad, and axial load up to 57% of the column axial load carrying capacity. The focus of this paper is on the influence of member behavior and axial

---

[1] Ph.D. Candidate, Dept. of Civil Engineering, University of New Hampshire, Durham, NH 03824,Tel : (603) 913-4578, Fax: (603)862-2364, E-mail: sxu6@unh.edu

[2] Staff Consultant, Simpson Gumpertz & Heger Inc., Waltham, MA, USA

load on the parameters that control the collapse of the structure. Column plastic rotations from 0.012 to 0.08 rad and post-capping rotations from 0.09 to 0.37 rad were observed depending on the loading history and level of axial load.

3.2 Introduction

The behavior of structural components is critical to preserve the structural integrity of a building and ensure adequate building performance during service and extreme loading conditions. In mid-rise and tall structures whose primary lateral-load resisting system is composed of steel moment resisting frames, column member's strength and stability are essential to avoid building collapse during strong earthquakes. The ability of a column to dissipate energy via inelastic deformations is influenced by the column's bending moment gradient as well as material properties, section types, and loading condition (Gioncu & Mazzolani, 2003). In order to reliably predict damage to steel structural components, it is necessary to account for the effects of material fatigue, stress concentrations, local buckling (Fogarty & El-Tawil, 2013), and local imperfections (Krawinkler et al., 1983). In this context, damage assessment implies a fundamental understanding and quantification of component behavior up to collapse. In the case of earthquakes, component damage assessment necessitates the availability of experimental studies for quantification of component response. These studies should account not only for appropriate cyclic loading conditions but also relevant boundary conditions (Nakashima, 1994) that have direct influence on component behavior and failure modes.

Currently, standards for testing steel columns to quantify damage and evaluate their seismic performance are nonexistent. In addition, factors such as the uncertainty in the seismic input due

to record-to-record variability, limitations of laboratory equipment, economic constraints, and limitations associated with the number of components to be tested highlight the need to develop representative loading histories to evaluate the seismic performance of steel columns. The knowledge base acquired from testing will increase our understanding of steel column behavior up to collapse, provide much needed data to calibrate and develop numerical models of columns, and ultimately improve seismic design provisions for steel moment-resisting frames.

At the system level, collapse assessment can be conducted efficiently based on numerical models of structural systems. This necessitates the availability of component hysteretic models capable of representing the most relevant modes of monotonic and cyclic deterioration. In general, the aforementioned hysteretic models are characterized by parameters that are calibrated upon experimental studies. Ibarra, Medina, and Krawinkler introduced a hysteretic model, IMK model, that incorporates the most important sources of cyclic strength and stiffness deterioration (Ibarra et al., 2005). This model has been used extensively to numerically evaluate the seismic response of steel structures using a concentrated plasticity approach. Lignos and Krawinkler (D. G. Lignos & Krawinkler, 2010) compiled a comprehensive database of steel component experimental responses. They utilized the experimental results contained in the database to develop regression equations useful to predict the parameters of the IMK model to represent the behavior of steel beams and columns. However, this database and its associated regression equations do not include results from testing of deep steel column sections. A deep steel column section is referred to herein as sections with a depth of approximately 400 mm (16 inches) or more (NIST, 2011). Furthermore, the effect of the axial load on the flexural behavior of steel columns is not accounted for in the development of the regression equations. The focus on deep steel sections is warranted because these sections can be used as exterior columns in moment-resisting structures. During an

70

earthquake, exterior columns carry their own tributary gravity load in addition to the axial load demands induced by overturning moments, as well as shear forces and bending moment demands induced by inertia forces. Recently, a research plan was proposed to emphasize the need for experimental data on deep steel column sections to better understand their seismic behavior, enable numerical simulation properties, and develop guidelines for incorporating these sections in design (NIST, 2011). In order to have reliable numerical models for inelastic analysis and collapse simulation studies, the nonlinear behavior of deep steel columns exposed to variable drift ratio, rotation at the top, and axial load demands should be experimentally understood and quantified. The results presented in this paper are intended to help address these needs.

As part of the research plan, a set of six quasi-static and two hybrid simulation tests were conducted until the onset of global collapse was attained for a 1:8-scale deep steel column. This column specimen corresponds to an exterior column that is part of a 20-story steel special moment-resisting frame structure. The discussion presented in this chapter focuses on the quasi-static tests.

3.3   Prototype Column

In order to develop appropriate loading protocols for an exterior column of a moment-resisting frame, a 20-story office steel building with perimeter moment resisting frames assumed to be located in Century City, CA was designed based on ASCE 7-10 (ASCE, 2010) and the 2010 Steel Seismic Provisions (AISC, 2010). Designed exterior columns correspond to a W36X652 section, which is the prototype structural element used in all tests.

Note: All units are in meters.
The height of the 1st Story is 4.42 m from top of the baseplate
to the centroidal axis of the first floor girder and the height of the
other stories is 3.96 m between the axis of two adjacent floor girders.
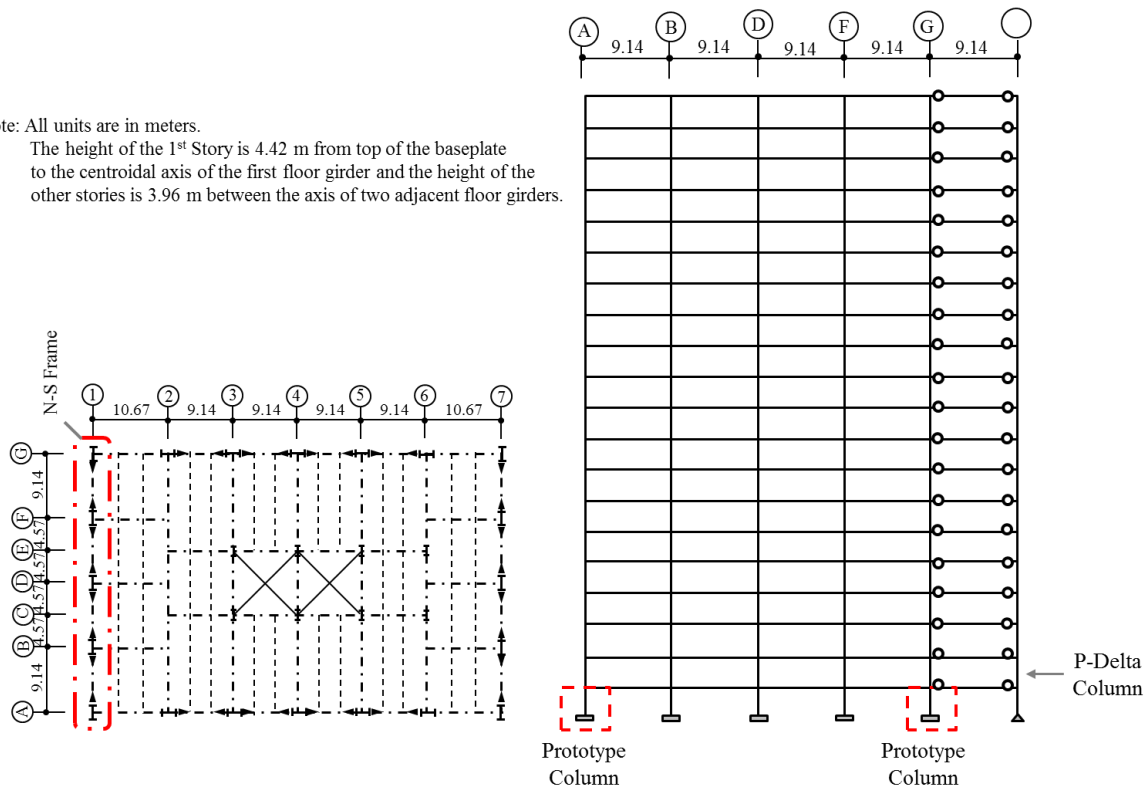
Figure 3-1. Typical floor plan and elevation of the N-S moment-resisting frame structure.

3.4 Test Setup Configuration and Specimen

The three-actuator test setup shown in Figure 3-2 was utilized for this experiment at the NEES@

Buffalo laboratory. The horizontal actuator was used to impose the lateral displacement at the tip

of the column, whereas the vertical actuators were used to impose axial force and rotation

demands. One of the vertical actuators was in force-control mode and the other one in

displacement-control mode. The drawings of the setup are presented in Appendix 3.

During the scaling process, the focus was on matching relevant parameters that control the

inelastic behavior of wide flange steel elements (t_f/t_w, h/t_w, $b_f/2t_f$ and others) within 10% of

the target values, as shown in Table 3-1. In order to fabricate the required scaled section and avoid

the need to weld a set of three plates to one another, modifications to a W8X24 section were conducted. For instance, the primary criterion was matching the ratio t_f/t_w, which is 1.6 for the W8X24 section as compared to 1.8 for the W36X652. Then, the ends of the flanges of the W8X24 section were cut along the length of the element to obtain the required $b_f/2t_f$ ratio. The web was also cut in the middle and the two remaining T-sections were welded with a groove weld. All other scaled section parameters were matched as shown in Table 3-1. The fabrication drawing of the column specimens is shown in Figure 3-3.

The height of the experimental specimen was considered as the scaled height of the prototype column from top of the base plate to bottom of the panel zone region and was equal to 493 mm (19.4 in.), which corresponds to a prototype column height of 3942 mm (155.2 in.). The column specimens were attached to 38 mm-thick (1.5 in.) base plates at both ends with fillet welds. One of the column base plates was bolted to a stiffened pedestal, and the other to the loading beam for implementing the displacements, rotations and forces at the tip of the column (Figure 3-2). The specimens were not braced over the height. An average yield strength of 344 MPa (50 ksi) was obtained from six tensile coupon tests conducted with sections of flange and web procured during fabrication of the specimens. The test configuration provides out-of-plane restraints (see lateral frames in Figure 3-2) to minimize out-of-plane displacements at the tip of the column. Furthermore, the specimen was instrumented with strain gauges at different heights on both flanges and web. In addition, a Krypton 3D coordinate tracking system and string pots were utilized to capture the three-dimensional displacement of the specimen.
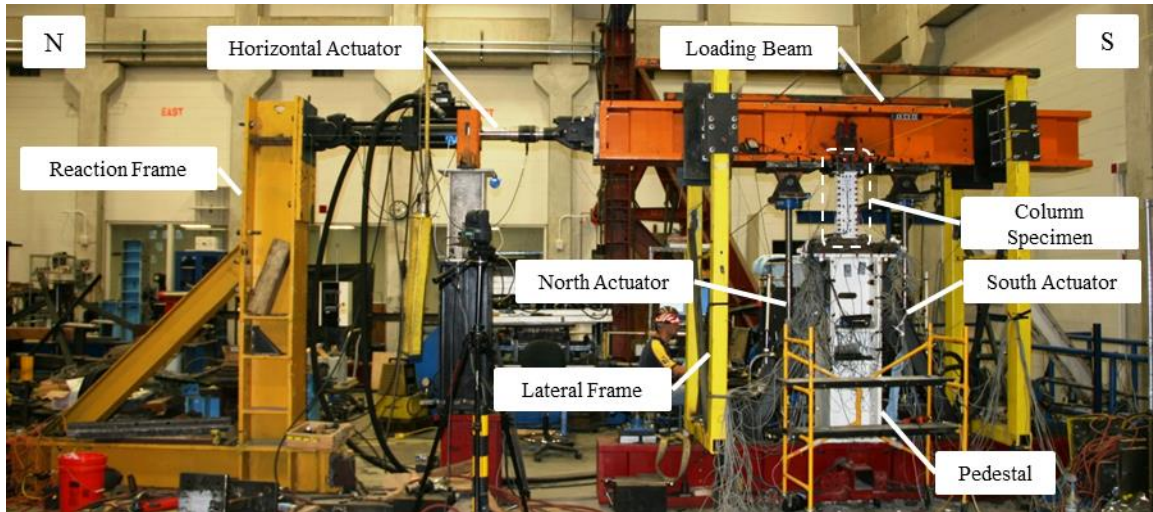
Figure 3-2. Experimental setup configuration.

Table 3-1. Cross section specification of the prototype column and test specimen

Specifications	b_f mm (in)	t_f mm (in)	$b_f/2t_f$	d mm (in)	h mm (in)	t_w mm (in)	h/t_w	t_f/t_w	L/r_y	I mm^4 (in^4)	A mm^2 (in^2)	Z mm^3 (in^3)
W36X652	447 (17.6)	90.0 (3.54)	2.49	1044 (41.10)	815 (32.1)	50.0 (1.97)	16.3	1.80	37.9	2.11E+10 (5.06E+4)	1.24E+5 (192)	4.77E+7 (2.91E+3)
Test Specimen	51 (2.0)	10 (0.40)	2.50	141 (5.56)	102 (4.02)	6.0 (0.25)	16.4	1.63		5.66E+6 (13.6)	1.88E+3 (2.91)	9.47E+4 (5.78)
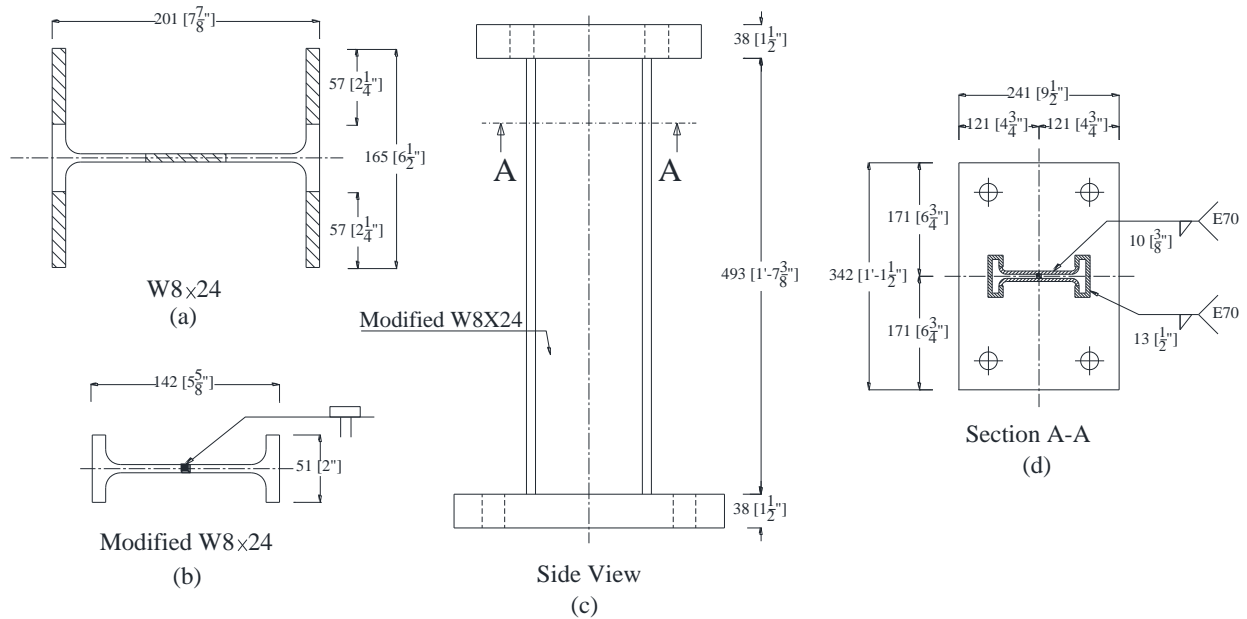
Figure 3-3. Fabrication drawing of the column specimen

3.5   Loading Protocols

To reliably predict the behavior of a structure near the limit state of collapse, the evaluation of component behavior under a variety of loading protocols is needed. Loading protocols are intended to provide (a) a reasonable representation of loading or deformation histories that a component would encounter in an earthquake, (b) a benchmark for seismic qualification tests, or (c) data for numerical model calibration. Various loading protocols are required given that demands and capacities depend on one another. The responses from specimens exposed to these loading protocols can then be used to develop and calibrate robust component deterioration models (e.g., (D. Lignos et al., 2011). James D Newell and Uang (2006), are one of the few researcher teams to study the behavior of deep steel column sections with loading protocols that account for variable axial loading. They studied the response of W27 columns and performed finite element analysis to conclude that the level of axial load has a significant effect on the strength deterioration due to

flange and web buckling. Their tests involved steel columns that did not rotate at their ends; thus, the element behaved in perfect double curvature. In order to study the behavior of a structural column element experimentally, there is a need to incorporate loading protocols that account for rotations at the top, and hence, bending moment gradients that may not be consistent with a double-curvature condition. The rotations at the tip of the column for the experiments discussed in this paper incorporate the effect of deformations of the panel zone and plastic hinging at the reduced-beam section of the beam framing into the exterior joint of the moment-resisting frame.

This study incorporates two sets of experiments with "Monotonic" and "Cyclic" loading protocols. These loading protocols were chosen to enable an increased understanding of column behavior up to collapse and a generalized calibration of the modified IMK model (Figure 3-4). By implementing monotonic loading protocols, information about the influence of axial load on the backbone curve (Figure 3-4) can be obtained. Furthermore, testing with cyclic loading protocols assists in capturing information on cyclic behavior and parameters that control the nonlinear behavior of the member. For instance, two of the parameters that are quantified and that are important to conduct collapse assessment of structures are the plastic rotation capacity (θ_p, difference between yield rotation and rotation at maximum bending moment) and the post-capping rotation (θ_{pc}, difference between rotation at maximum moment and rotation at complete loss of strength). Moreover, the quantification of additional modeling parameters such as the effective yield strength (M_p), post-capping strength (M_{pc}, maximum moment), as well as cyclic strength and stiffness deterioration is also performed (Λ). In this paper, the calibration of cyclic deterioration parameters of the IMK model is not addressed. The experimental test matrix is presented in Table 3-2.
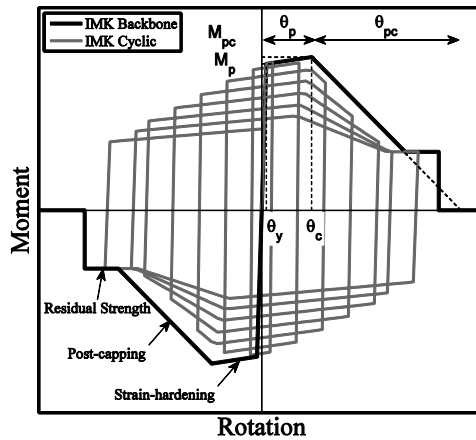
Figure 3-4. Modified Ibarra-Medina-Krawinkler Model (IMK).

Table 3-2. Test Matrix

Test Number	Lateral Displacement and Rotation	Axial Load
1	Monotonic	Constant
2	Monotonic	Variable
3	Cyclic, symmetric with trailing cycles	Cyclic
4	Cyclic, symmetric w/o trailing cycles	Cyclic
5	Cyclic, asymmetric	Cyclic
6	Cyclic, symmetric followed by monotonic	Cyclic

A two-dimensional model of the moment-resisting frame structure was developed using the Open System of Earthquake Engineering Simulation Platform (OpenSees) (Mathiasson & Medina, 2013; OpenSees, 2007a). A plan view and an elevation view of the 20-story moment resisting frame structure are shown in Figure 3-1.

The fundamental period of the scaled structural model was estimated as 1.04 s (2.93 s for the full scale prototype model). The model consisted of a combination of nonlinear rotational springs and elastic beam elements. The springs were placed at the top and bottom of the columns, as well

as at the center of the reduced beam sections. The hysteretic behavior of the springs was modeled based on the modified Ibarra-Medina-Krawinkler deterioration model (D. G. Lignos & Krawinkler, 2010). The deterioration properties for the beam and column sections were calculated using the regression equations of (D. G. Lignos & Krawinkler, 2010). Panel zones were modeled following the Gupta-Krawinkler approach (Gupta & Krawinkler, 1999). In order to account for the P-Delta effect, a leaning column with floor gravity loads corresponding to half of the floor mass minus the tributary load of the N-S frame at each level was connected to the frame with rigid links (see Figure 3-1 right). Rayleigh damping of 2% of critical was assigned to the first and fifth period of the scaled frame. The approach proposed by Zareian and Medina (Zareian & Medina, 2010) was used to model damping.

The bending moment strength of the column in the presence of axial loads was estimated based on the P-M interaction equations given in AISC-ANSI 360-10 (Design-AISC). To obtain the required axial load demand, the axial force of the column from a pushover analysis with a $k = 2$ (parabolic) ASCE-41 (ASCE, 2007) lateral load pattern was obtained. The axial load demand was estimated from combining the factored gravity axial load in the column ($P_{grav}=1.05P_D + 0.25P_L$, P_D as the dead and P_L as the live load) with 50% of the maximum axial load ($P_{E,max}$ experienced by the column due to the application of the lateral loads during the pushover analysis, $P_r=P_{grav}+0.5P_{E,max}$ (NIST, 2011). Nonlinear static and dynamic analyses were conducted with a set of 100 recorded ground motions (50 stations) to aid in the development of the testing protocols.

3.5.1 Monotonic Loading Histories

Two monotonic loading protocols were implemented to obtain a baseline for the cyclic responses of the specimens, as well as data for calibration of the backbone of the IMK model for strong-axis bending. The first monotonic test consisted of applying the drift ratio and rotation loading histories of Figure 3-5 (a) and Figure 3-5 (b) with a constant axial force of 31% of the axial load carrying capacity of the specimen (202 kN (45 kips)). The axial load carrying capacity is defined as the cross-section area times yield strength ($f_y.A$). The drift ratio (due South as positive) and rotation at the top (counterclockwise as positive) were applied out-of-phase as shown in Figure 3-5 (a) and Figure 3-5 (b).This axial force level (downwards as positive) is consistent with the gravity-load demand experienced by an interior column of the perimeter moment-resisting frame shown in Figure 3-1. The second monotonic test was similar to the first one except that a variable axial load as shown in Figure 3-5 (c) was implemented. Axial load values varied from 15 to 57% of the axial load carrying capacity of the column. These axial load ratios are consistent with the expected gravity-load level for the prototype column (15% of axial load carrying capacity, 98 kN (22 kips)) and the expected maximum axial load during an earthquake (57% of the axial load carrying capacity, 369 kN (83 kips)). As it can be seen in Figure 3-5 (c), the maximum axial load of 57% was prescribed at a column drift ratio of 0.04 rad. This drift ratio was defined to investigate the influence of variable axial load after the yield drift. During these monotonic tests, a maximum drift ratio of 0.09 rad was achieved due to limitations of the experimental setup.
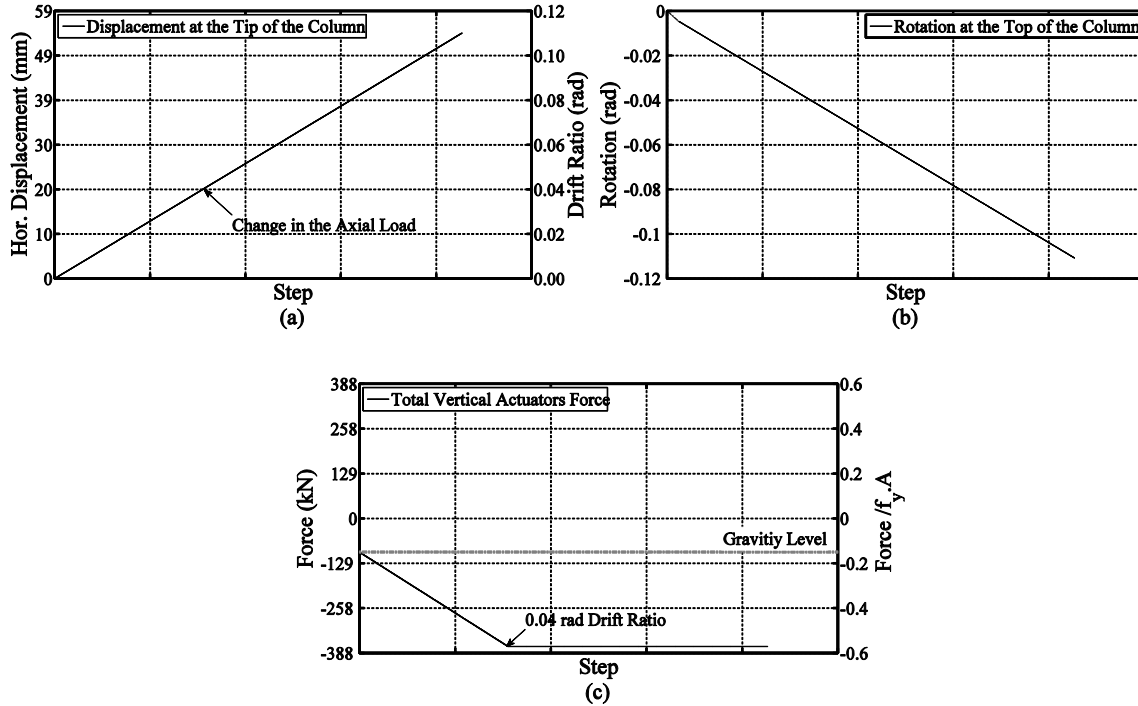
Figure 3-5. Monotonic (a) lateral displacement, (b) rotation & (c) variable axial loading protocols.

3.5.2 Cyclic Loading Histories

These tests are relevant to understand and quantify the cyclic deterioration in strength and stiffness experienced by the column when subjected to cyclic loading with the presence of variable axial load demands. A total of four cyclic tests were conducted. The loading histories were developed with the aid of numerical simulations of an exterior column in the prototype 20-story moment resisting frame.

- Symmetric Loading Histories With and Without Trailing Cycles

The cyclic loading histories of drift ratio (due south as positive) and rotation at the top (counterclockwise as positive) were applied out-of-phase as shown in Figure 3-6. In order to evaluate stiffness and strength degradation and be more consistent with the expected response time history of the column exposed to an earthquake, pairs of increasing amplitude cycles were interrupted by a pair of smaller amplitude trailing cycles as shown in Figure 3-6. Cyclic axial

80

loading is considered with a mean value of 15% of the axial load carrying capacity of the column

(98 kN (22 kips)). Increasing levels of axial force (fluctuating between tension and compression)

were applied until the yield drift value of the column was achieved. From that point on, the axial

load cycled between maximum levels of tension (27% of axial-load carrying capacity, 209 kN (47

kips)) and compression (57% of axial-load carrying capacity, 369 kN (83 kips)). The magnitudes

of drift ratio, rotation at the top, and axial load are reported in Table 3-3. To evaluate the effect of

trailing cycles, a symmetric loading history without trailing cycles (test 4) was developed as shown

in Table 3-3 without the highlighted rows.
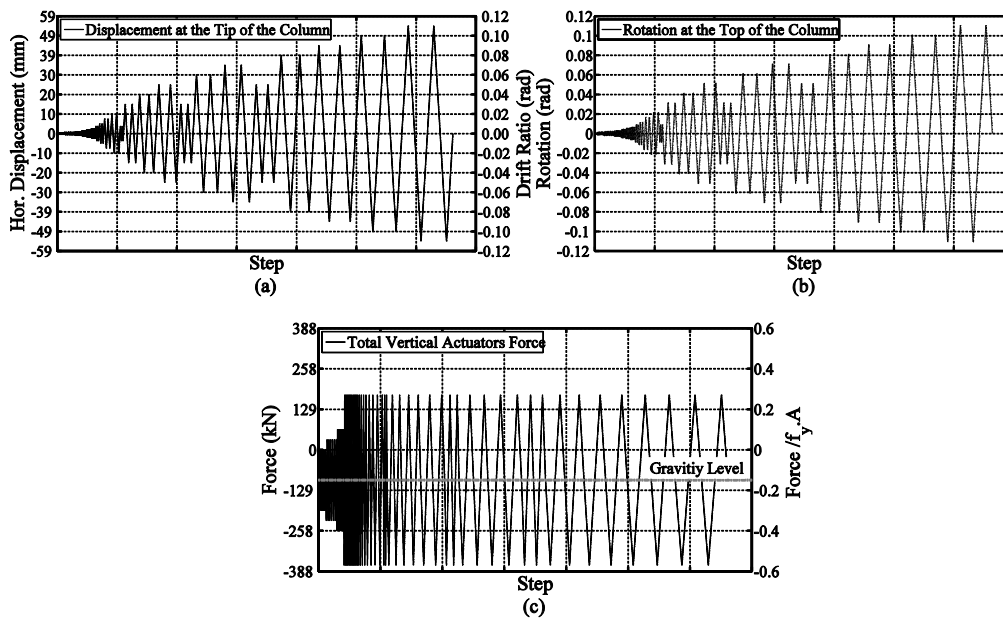
Figure 3-6. Loading protocols for Test 3; (a) lateral displacement, (b) rotation and (c) variable axial load.

Table 3-3. Symmetric loading history with trailing cycles

Sequence	# of cycles	Drift ratio (rad)	Rotation (rad)	Axial Load % Comp.	Axial Load % Ten.
1	6	0.001	0.0015	30	0
2	6	0.0015	0.0023	35	5
3	6	0.002	0.0031	40	10
4	4	0.003	0.0046	57	27
5	4	0.004	0.0056	57	27
6	4	0.005	0.0066	57	27
7	2	0.0075	0.0091	57	27
8	2	0.01	0.0116	57	27
9	2	0.015	0.0166	57	27
10	2	0.02	0.0215	57	27
11	2	0.0075	0.0091	57	27
12	2	0.03	0.0314	57	27
13	2	0.04	0.0414	57	27
14	2	0.05	0.0513	57	27
15	2	0.03	0.0314	57	27
16	2	0.06	0.0612	57	27
17	2	0.07	0.0711	57	27
18	2	0.05	0.0513	57	27
19	2	0.08	0.0810	57	27
20	2	0.09	0.0905	57	27
21	2	0.10	0.101	57	27
22	2	0.11	0.111	57	27

- Asymmetrical Loading Histories

The phenomenon of ratcheting is a common global failure mode experienced by steel structures during earthquakes, i.e., incremental sidesway collapse. Asymmetrical drift and rotation loading histories were applied to induce a ratcheting-type response in the column (Figure 3-7). These

loading histories allow for the evaluation of the effect of maximum and mean deformations on relevant deterioration parameters such as plastic rotation capacity (θ_p) and post-capping rotation (θ_{pc}).

As shown in Figure 3-7, the drift ratio loading history initiates with zero-mean symmetric cycles with drift-ratio amplitudes up to 0.01 rad (similar cycles as Tests 3 and 4). These are followed by four cycles with drift-ratio amplitudes of 0.015 rad and 0.02 rad cycling at a mean drift value of 0.02 rad and two cycles with drift-ratio amplitudes of 0.03 rad cycling at a mean drift value of 0.06 rad. This sequence is then followed by a half cycle up to a drift-ratio amplitude of 0.11 rad. The rotation loading history is applied out-of-phase with the same frequency and pattern as the drift with mean values that vary from 0, to -0.02 and -0.06 rad. The axial force history has the same pattern as that of the symmetric loading protocols (Tests 3 and 4).
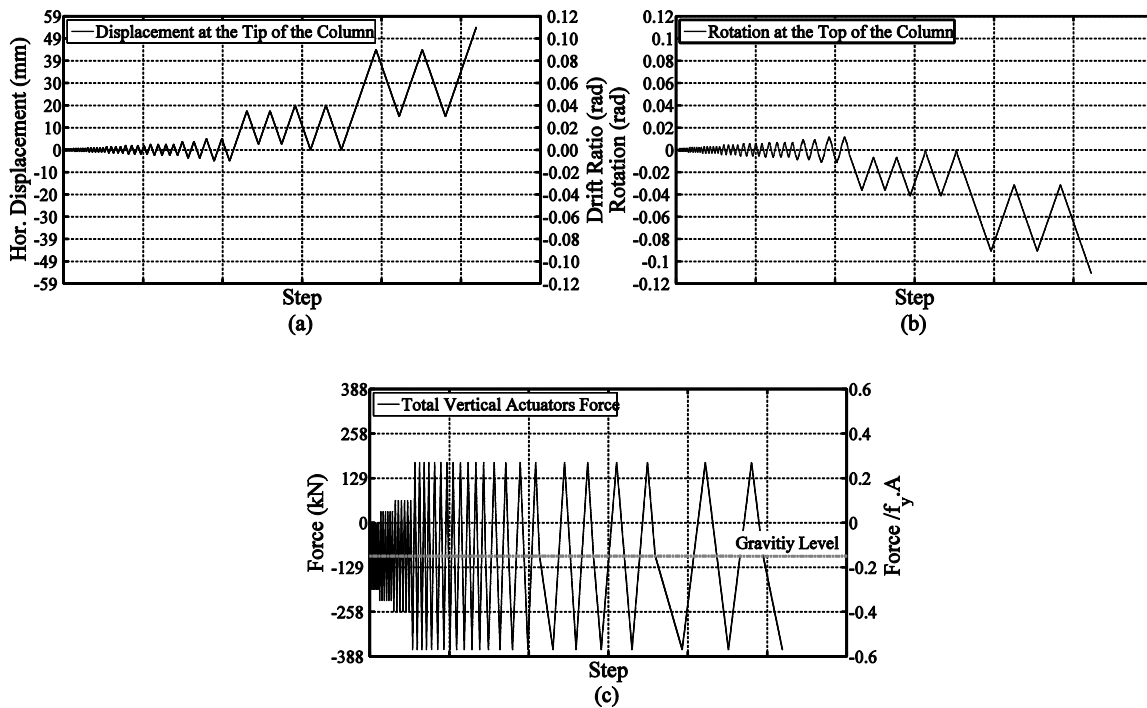
Figure 3-7. Loading protocols for Test 5; asymmetrical (a) lateral displacement, (b) rotation and (c) variable axial load.

- Symmetric Loading Histories Followed by Monotonic Histories

In this test the specimen was exposed to cyclic demands consistent with those of Test 4 up to a drift ratio of 0.06 rad. From then on, the axial load remained constant and increasingly monotonic drift ratios and rotations at the top were imposed up to a target drift ratio of 0.075 rad due to limitations of the test configuration. The objective was to examine the influence of cumulative damage on the backbone curve used to describe the hysteretic response of the column near the limit state of collapse.

3.6   Implementation of Loading Protocols

The lateral displacement is imposed via the horizontal actuator, which is displacement controlled (Figure 3-2). The axial force and rotation at the tip of the column are controlled using the vertical actuators. The vertical north actuator (slave) is displacement controlled while the vertical south actuator (master) is force controlled (Figure 3-2). This vertical-actuator setup using a master and a slave allows for an interaction between them which results in the concurrent application of the target axial load and rotation at the tip of the column at the end of a command step. The axial force command is sent to the south actuator to control the total force feedback from both actuators. The target rotation is calculated as the difference in the stroke of both vertical actuators normalized by the distance between their centerlines. This rotation is imposed by sending a displacement command to the north actuator so that the target difference in stroke is applied. In this process, in order to achieve the desired targets, both vertical actuators need to adjust their force and displacement at each step. Thus, for each step (i), the target displacement, axial force, and rotation are obtained simultaneously. A schematic representation of the control algorithm is depicted in Figure 3-8.
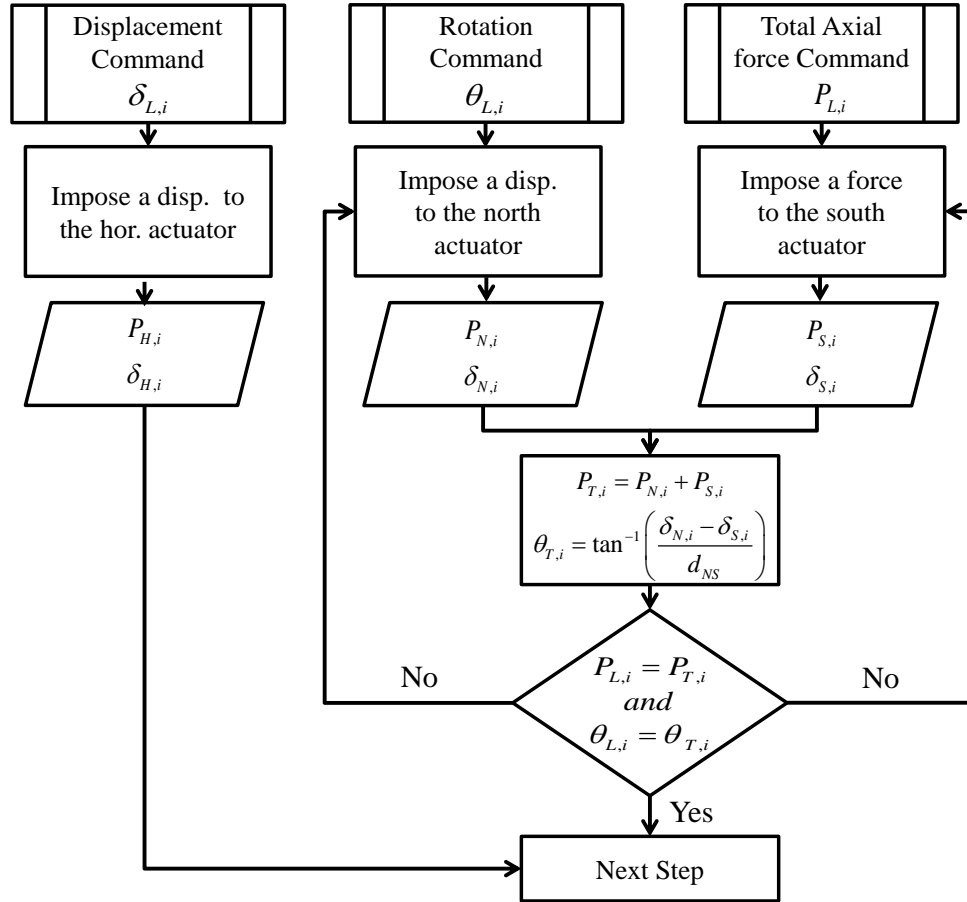
Figure 3-8. Control algorithm for test setup.

3.7 Experimental Results

The experimental results presented in this paper are in the form of column drift ratio (chord rotation) vs. strong-axis bending moment at the base of the column. The bending moment at the base of the column was determined according to the demand forces acting at the tip of the deformed configuration of the column. Horizontal and vertical components of the measured forces in the actuator load cells (horizontal and verticals) are utilized to calculate the shear force, axial load, and bending moment at the tip of the column. Eq. (3-1) shows the calculation of bending moment at base of the column.

$$M_{Tot,n} = V_n L'_n + M_{Tip,n} + P_n \Delta_{Tip-Base} \tag{3-1}$$

Where, V_n is shear force, P_n is axial load, $M_{Tip,n}$ is the bending moment at the tip of the column and $M_{Tot,n}$ is the bending moment at the base at step n. The relative lateral displacement at the top of the column with respect to its base is defined as $\Delta_{Tip-Base}$ and L'_n as the deformed vertical length of the specimen.

3.7.1 Bending Moment Strength

The bending moment-drift ratio responses for the monotonic tests are presented in Figure 3-9 (a). In Test 2 the bending-moment strength is reduced by approximately 30% with respect to the bending-moment strength of Test 1. Once the variable axial load in Test 2 reached a value of 57% of the axial load carrying capacity of the column, it remained constant for the rest of the test. During the transition of variable to constant axial load (see Figure 3-5 (c)), there is an increase in the bending-moment strength, which resembles the strain-hardening portion of a typical stress-strain curve. This increase in bending moment strength is the result of a change in column curvature (i.e., gradient of bending moment diagram) from single to double. Figure 3-10 (a) illustrates the bending moment diagram of the column at different drift levels for Test 2. At a drift level of 0.009 rad, the column is in single curvature whereas at larger drifts, it switched to double curvature. In Figure 3-10 (a), a well-defined negative slope after the point of maximum bending moment (i.e., post-capping slope) was attained when a larger variable axial load was implemented, this also demonstrated the effect of higher axial load demands on the behavior of the specimen. The loss of strength is due to the initiation of web local buckling followed by lateral torsional buckling. The change in the curvature of the column is consistent with the behavior of the first story exterior column in the pushover analysis of the case-study structure.
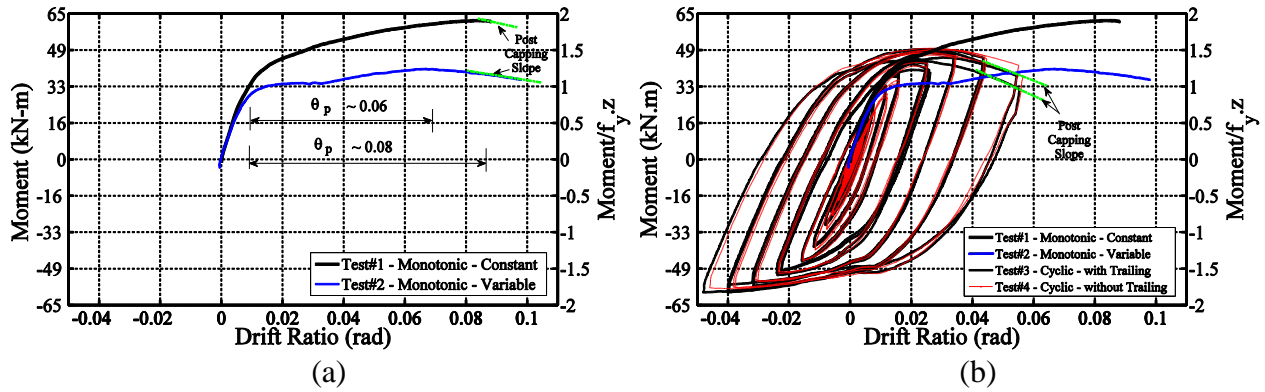
Figure 3-9. Moment-drift ratio relationship at the base of the column; (a) monotonic tests (Tests 1 and 2) and (b) cyclic tests – with and without trailing cycles (Tests 3 and 4).
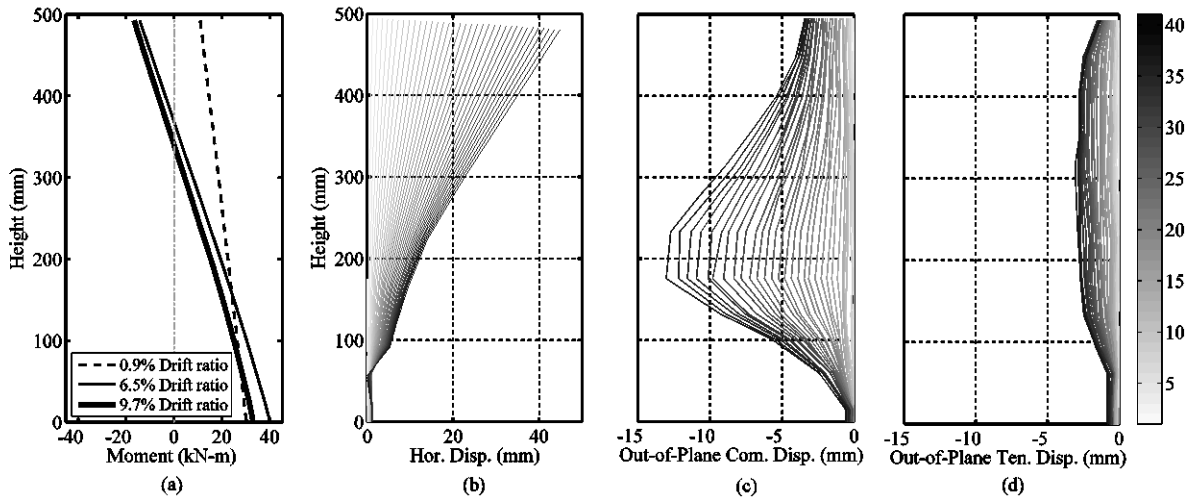
Figure 3-10. Monotonic drift and rotation with variable axial load (Test 2) (a) column bending-moment diagram (b) column displacement profile, (c) out-of-plane displacement of the south flange over the height, (d) out-of-plane displacement of the north flange.

The bending moment-drift ratio responses for Tests 3 and 4 demonstrate that the specimen exposed to additional trailing cycles experiences larger cyclic strength deterioration and stiffness degradation (Figure 3-9 (b)). For instance, in Test 3 early cycles at a drift-ratio amplitude of 0.025 rad that have been interrupted by trailing cycles exhibit an increase in post capping slope of 70% with respect to the bending moment-drift ratio response of Test 4 (without trailing cycles).

87

Quantitative information on bending moment strengths and rotation capacities are reported in Table 3-4. Unfortunately, Tests 3 and 4 were executed only to a column drift ratio of approximately 0.06 rad due to fracture in the compression flange near the base of the column about 10 mm above the weld. The rate of testing was reduced for Tests 5 and 6 from 0.025 cm/s (0.01 in/s) to 0.0051 cm/s (0.002 in/s).

Experimental results with the asymmetrical loading protocol (Test 5) show that the bending moment strength in the first inelastic hysteretic loop is greater than the monotonic strength at a consistent level of axial load (i.e., monotonic case with variable axial load) primarily because of cyclic strain hardening (Figure 3-11 (a)). However, strength deterioration is clearly observed at cycles corresponding to drift ratio levels of about 0.05 rad or more.

(a)   (b)
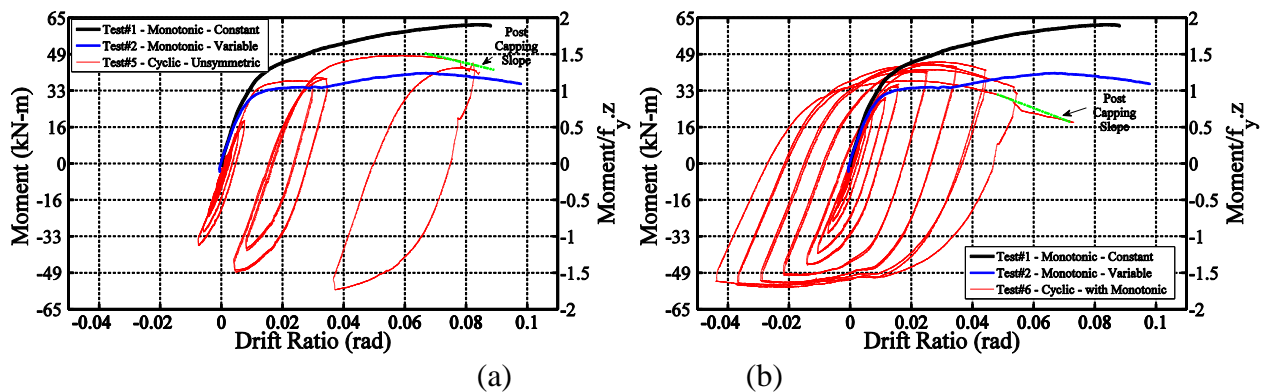
Figure 3-11. Bending moment at the base - drift ratio for (a) cyclic - asymmetrical (Test 5) and (b) cyclic, symmetric test followed by monotonic loading (Test 6).

Results for the symmetric cyclic test followed by a monotonic one (Test 6) are presented in Figure 3-11 (b). An evaluation of the last half cycle of this test shows a reduction in bending moment strength of 20% with respect to the monotonic test with constant axial load, and 63% with respect to the monotonic test with variable axial load. This demonstrates the detrimental effect of cumulative damage on the column bending moment strength. In addition, Figure 3-12 illustrates

that the spread of inelasticity is more pronounced in the specimen through approximately 75% of its height from bottom to top) when compared to Test 2. One of the reasons for the increase in maximum bending moment strength in the cyclic test as compared to the monotonic one is the presence of cyclic strain hardening in combination with the spread of inelasticity throughout the height of the column.
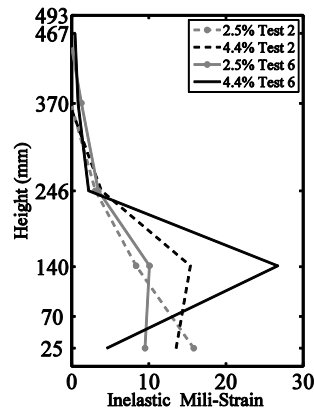
Figure 3-12. Measured inelastic strain in strain gauges in the compression flange over the height of the column in Test 2 and Test 6.

Overall, the bending moment capacity at the base of the column specimen for all the experiments is significantly larger than the estimated plastic moment capacity of the cross-section based on the product of yield strength times plastic cross-section modulus. This discrepancy emphasizes the need to account for element behavior as opposed to cross-section behavior, especially when conducting seismic collapse assessment of structures. The maximum and minimum bending moment experienced by the column specimen for the performed tests are reported in Table 3-4. At the same drift-ratio level and cycle, a 14% reduction is obtained in the maximum bending moment for axial compression in Test 6 with respect to the one observed in Test 4. This reduction is associated with the decrease in the rate of testing in which a slower rate allows comparable levels of axial load to act for a relatively longer duration at consistent drift ratio

levels. It is also observed that strength deterioration is delayed in the negative side (when a tensile load is imposed) as compared to the positive side (when a compressive load is imposed).

3.7.2 Rotation Capacity

The total elastic moment at the base ($M_{Elastic}$) is calculated according to Eq. (3-2), which accounts for the rotation at the tip and at the base of the specimen. The measured elastic stiffness of the member in the monotonic tests is approximately 15% less than the theoretical rotational stiffness.

$$M_{Elastic} = \frac{2EI}{L}\left(2\theta_{Base} + \theta_{Tip} - 3\frac{\Delta_{Tip-Base}}{L}\right) \tag{3-2}$$

In this equation, E is the modulus of elasticity, I is the moment of inertia for strong-axis bending, L is the original length of the column, and θ_{Base} and θ_{Tip} are the measured rotation at the base and the tip of the column, respectively. Theoretically, the base of the column is considered fixed; however, the flexibility of the pedestal (despite its bracing) induced a relatively small rotation (maximum 0.003 rad). Furthermore, $\Delta_{Tip-Base}$ is the measured relative lateral displacement between the tip of the column and base.

The plastic rotation capacities (θ_p, difference between yield rotation and rotation at maximum bending moment) were estimated as 0.08 and 0.06 rad for the monotonic tests under constant and variable axial load, respectively (Figure 3-9 (a)). Plastic rotations were calculated using estimates of yield drift ratios of 0.008 and 0.0075 rad obtained from the results of Tests 1 and 2 shown in Figure 3-9 (a). In this context, plastic rotations were estimated from drift ratios assuming that most of the inelasticity concentrates near the bottom of the column (Figure 3-10 (b)). For a W36X652,

ASCE-SEI 41 (2007) estimates a plastic rotation capacity of 0.009 rad when the axial force is 31% of the available axial strength and negligible plastic rotation capacity for an axial load of 57% of the available axial strength. Moreover, the plastic rotation capacity according to an extrapolation of the regression equation for W-sections for beams other-than-RBS sections developed by Lignos (D. G. Lignos & Krawinkler, 2010) would result in a value of 0.04 rad without considering the axial load effect. These results indicate that for a deep steel column such as the W36X652, the plastic rotation capacity estimated based on available equations tends to underestimate the initial value of this parameter.

On the other hand, the estimated plastic rotation capacity for the cyclic tests is shown in Table 3-4. The plastic rotation capacity in the cyclic tests is estimated from the first inelastic cycle in which a clear post-capping slope is visible (i.e., the maximum bending moment strength is achieved in that cycle). It can be observed that a significant reduction in plastic rotation capacity occurs in the symmetric cyclic tests (Tests 3, 4, 6). This reduction results in plastic rotation capacities that are on average 77% smaller than the plastic rotation capacity from the monotonic test with variable axial load. However, the plastic rotation capacity in the asymmetrical test (Test 5) is 42% smaller than the one from the monotonic test with variable axial load. Thus, when ratcheting is present in the response history, the presence of a small number of cycles followed by a larger amplitude drift has less influence on the plastic rotation and the column behavior is closer to that obtained from a monotonic test. The plastic rotation capacity is influenced by the loading history and the level of axial load.

The post-capping rotation for constant axial load (θ_{pc}, difference between rotation at maximum moment and rotation at complete loss of strength) was estimated as 0.37 rad and 0.18 rad for monotonic tests with constant and variable axial load cases, respectively (Tests 1 and 2). The

91

extrapolation of the regression for post-capping rotation for W-sections for beams developed by Lignos (D. G. Lignos & Krawinkler, 2010) estimates a value of 0.44 rad without considering the axial load effect. The estimated post-capping rotation of the last cycle of the test with and without trailing cycles (Test 3 and Test 4) is 0.09 rad and 0.11 rad, respectively (Figure 3-9 (b)). These values are smaller than the one estimated based on monotonic tests that do not account for the effects of cyclic deterioration.

Results from the asymmetrical test (Test 5) are shown in Figure 3-11 (a). The post-capping rotation of the last cycle of the asymmetrical loading is approximately 0.11 rad. Moreover, in Test 6 (Figure 3-11 (b)) the post-capping rotation for the monotonic part of the loading protocol (at the end of the cycles) was estimated as 0.09 rad, which indicates a significant reduction in the post-capping stiffness with respect to Test 2 (monotonic-variable axial load). Note that the post-capping slope, which is a consequence of lateral torsional buckling, can be clearly observed in the last few cycles. Estimate values of post-capping rotation capacity are shown in Table 3-4.

Table 3-4. Estimated parameters from quasi-static experiments

Experiments	Bending Moment /$f_y.z$		Plastic Rotation Capacity [a] (rad)	Post-capping Rotation [b] (rad)
	Maximum	Minimum		
1	1.9	-	0.08	0.37
2	1.2	-	0.06	0.18
3	1.5	1.8	0.012	0.09
4	1.6	1.7	0.014	0.11
5	1.5	1.7	0.035	0.11
6	1.4	1.7	0.015	0.09

[a] The plastic rotation capacity is calculated for the first inelastic cycles of the bending moment-drift ratio relationship in which a clear post-capping slope is visible
[b] The post-capping rotation is calculated for the last cycle of the bending moment-drift ratio relationship

3.7.3 Failure Mode

During the tests, the dominant failure modes were web buckling followed by lateral torsional buckling (see Figure 3-13). These failure modes are responsible for the instability and reduction in the load bearing capacity of the member. The web-buckling failure mode is consistent with the prediction upon the charts given for thin wall "I" sections which has been reported by Kroll et al. (Kroll et al., 1943). These charts represent which element of the cross section is responsible for the fundamental local instability. In addition, lateral-torsional buckling failure mode can be observed in Figure 3-10 (c) and (d), which depict the out-of-plane displacement throughout selected steps of the loading history for the compression and tension flanges. Subsequently, the occurrence of lateral torsional buckling affects the post capping rotation capacity of the section and also rate of cyclic deterioration.
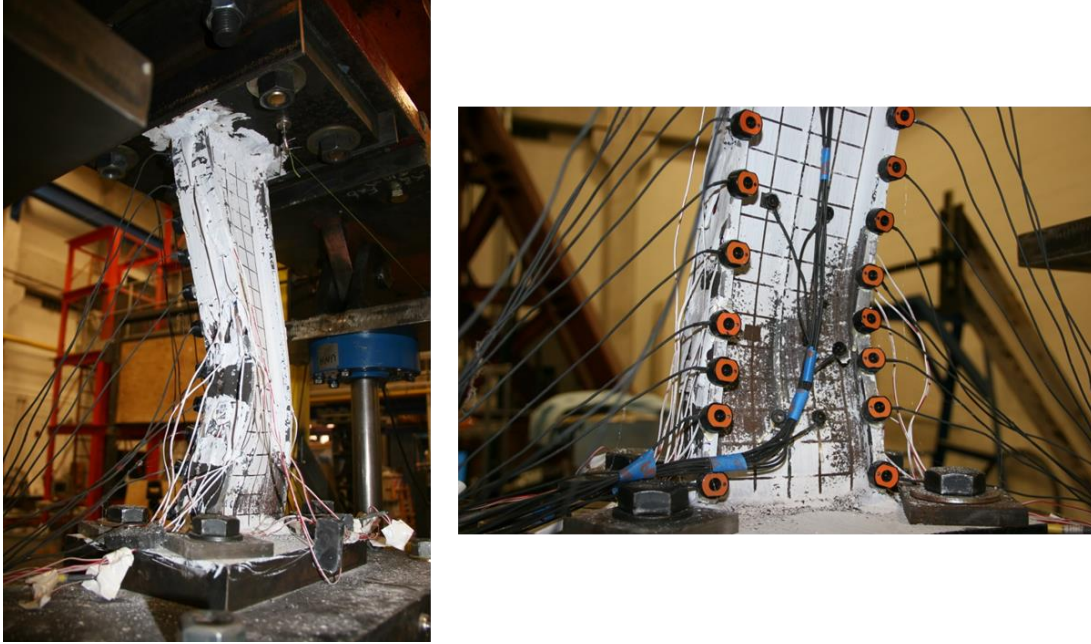
Figure 3-13. Observed lateral torsional buckling; south flange view (left), east view (right) (Test6).

3.8   Conclusions

In order to conduct reliable numerical simulations to predict collapse, an accurate evaluation of relevant modeling parameters such as plastic rotation capacity and post-capping rotation capacity is critical. First-story exterior columns experience rotation demands at the top when subjected to seismic events. Thus, in order to account for a more realistic representation of the behavior of the column, a rotation was imposed at the tip of the specimen in addition to the lateral and axial loading histories, which produced a better representation of changes in the moment gradient throughout the height of the column. Therefore, a set of loading histories were developed and applied to a column specimen to investigate the behavior of a W36 column under lateral drifts, rotation at the top, and axial loads up to the limit state of collapse.

Quasi-static (monotonic and cyclic) tests were performed on the 1:8scale W36X652 column specimen as part of this study. Monotonic tests demonstrated that the spread of inelasticity and its

associated strain hardening produced a bending moment capacity at the base of the column on the order of 1.9 and 1.2 times the estimated plastic moment capacity ($f_y.z$) for constant and variable axial load, respectively. The bending moment at the base vs. drift ratio relationship shows an increase in the maximum bending moment of the tests with cyclic loadings compared to the monotonic ones at the similar level of axial force at the initiation of the loading histories, which is caused by cyclic strain hardening (e.g., in Test 4 an increase of $1.6\,f_y.z$ was observed). Furthermore, strength and stiffness deterioration after the onset of lateral torsional buckling occurs more rapidly during cyclic loading on the compression side.

The plastic rotation capacities for this column element calculated based on ASCE-SEI 41 significantly underestimate the values obtained from the tests. However, in the symmetric cyclic tests the plastic rotation capacity measured according to the first inelastic cycle in which a post-capping slope appears (i.e., maximum bending moment strength is achieved) is smaller by approximately 77%. Furthermore, the estimated post-capping rotation values indicate that they are strongly dependent on the magnitude of drift ratios, number of cycles, levels of axial load and loading protocols.

The dominant failure modes are web buckling and lateral torsional buckling, which induced strength deterioration and stiffness degradation. The inelasticity spreads out up to about 75% of the length of the column, which depends on the moment gradient in the member and the imposed loading history.

Further investigation with a broader range of column sizes and scales including the effect of biaxial bending moment demands on deep steel column sections needs to be conducted experimentally. In addition, results with different loading protocols would be beneficial in order

to assess and calibrate numerical models to facilitate a more reliable prediction of column behavior till the limit state of collapse is approached.

3.9 Acknowledgments

3.10 Notation

A $\quad$ = $\quad$ cross section area

E $\quad$ = $\quad$ modulus of elasticity

I $\quad$ = $\quad$ moment of inertia for strong-axis bending

L $\quad$ = $\quad$ unreformed length of the specimen

L' $\quad$ = $\quad$ deformed vertical length of the specimen

$M_{Elastic}$ $\quad$ = $\quad$ bending moment in the elastic range

M_p $\quad$ = $\quad$ effective yield strength

$M_{Tip,n}$ $\quad$ = $\quad$ bending moment at the tip of the column at step n

$M_{Tot,n}$ $\quad$ = $\quad$ bending moment at the base at step n

$P_{H,i}$ $\quad$ = $\quad$ horizontal actuator force at step i

$P_{L,i}$ $\quad$ = $\quad$ axial loading protocol command at step i

$P_{N,i}$ $\quad$ = $\quad$ measured north vertical actuator force at step i

$P_{S,i}$ = measured south vertical actuator force at step i

$P_{T,i}$ = measured total vertical actuator force at step i

P_n = axial load

V_n = shear force

b_f = flange width

d = depth of the column section

d_{NS} = distance between vertical actuator centerlines

f_y = yield stress

$f_y.A$ = axial load carrying capacity of the cross section

$f_y.z$ = plastic moment capacity

h = clear distance between flanges less the fillet or corner radius

n = Step

t_f = flange thickness

t_w = web thickness

z = plastic section modulus for strong-axis bending

$\Delta_{Tip-Base}$ = relative lateral displacement at the top of the column with respect to its base

Λ = cyclic strength and stiffness deterioration

θ_{Base} = measured rotation at the base of the column

$\theta_{L,i}$ = rotation command at step i

θ_{Tip} =   measured rotation at the tip of the column

$\theta_{T,i}$ =   Measured rotation at step i

θ_p =   difference between yield rotation and rotation at maximum bending moment

θ_{pc} =   difference between rotation at maximum moment and rotation at complete loss of strength

$\delta_{H,i}$ =   measured horizontal actuator displacement at step i

$\delta_{L,i}$ =   horizontal actuator displacement command at step i

$\delta_{N,i}$ =   measured north actuator displacement at step i

$\delta_{S,i}$ =   measured south actuator displacement at step i

3.11 References

AISC. (2010). Seismic Provisions for Structural Steel Buildings, ANSI/AISC 341-10 2010: American Institute of Steel Construction, Chicago, Illinois.

ASCE. (2007). Seismic Rehabilitation of Existing Buildings, ASCE/SEI 41-06 *American Society of Civil Engineers, Reston, VA, US*.

ASCE. (2010). Minimum Designs Loads for Buildings and Other Structures, ASCE/SEI 7-10: American Society of Civil Engineers, Reston, Virginia.

Design-AISC, S. 360-10 9 Steel Design-AISC 360-10. *Steel Design per AISC*, 360-310.

Fogarty, J., & El-Tawil, S. (2013). *Collapse Behavior of Steel Columns under Lateral Loading.* Paper presented at the Structures Congress 2013@ sBridging Your Passion with Your Profession.

Gioncu, V., & Mazzolani, F. (2003). *Ductility of seismic-resistant steel structures*: CRC Press.

Gupta, A., & Krawinkler, H. (1999). *Seismic demands for the performance evaluation of steel moment resisting frame structures.* Stanford University.

Ibarra, L. F., Medina, R. A., & Krawinkler, H. (2005). Hysteretic models that incorporate strength and stiffness deterioration. *Earthquake engineering & structural dynamics, 34*(12), 1489-1511.

Krawinkler, H., Zohrei, M., Lashkari-Irvani, B., Cofie, N. G., & Hadidi-Tamjed, H. (1983). *Recommendations for experimental studies on the seismic behavior of steel components and materials*.

Kroll, W., Fisher, G. P., & Heimerl, G. J. (1943). Charts for calculation of the critical stress for local instability of columns with I-, Z-, channel, and rectangular-tube section: DTIC Document.

Lignos, D., Krawinkler, H., & Whittaker, A. (2011). Prediction and validation of sidesway collapse of two scale models of a 4-story steel moment frame. *Earthquake engineering & structural dynamics, 40*(7), 807-825.

Lignos, D. G., & Krawinkler, H. (2010). Deterioration modeling of steel components in support of collapse prediction of steel moment frames under earthquake loading. *Journal of Structural Engineering, 137*(11), 1291-1302.

Mathiasson, A., & Medina, R. A. (2013). *Seismic collapse assessment of a 20-story steel moment resisting frame structures.* (MS), University of New Hampshire, Durham, New Hampshire.

Nakashima, M. (1994). Variation of ductility capacity of steel beam-columns. *Journal of Structural Engineering, 120*(7), 1941-1960.

Newell, J. D., & Uang, C.-M. (2006). *Cyclic behavior of steel columns with combined high axial load and drift demand*: Department of Structural Engineering, University of California, San Diego.

NIST. (2011). Research Plan for the Study of Seismic Behavior and Design of Deep, Slender Wide Flange Structural Steel Beam-Column Member. *prepared by the NEHRP Consultants Joint Venture, a partnership of the Applied Technology Council and the Consortium of Universities for Research in Earthquake Engineering for the National Institute of Standards and Technology, NIST GCR 11-917-13 2011*(Gaithersburg, Maryland).

OpenSees. (2007). Open System for Earthquake Engineering Simulation: Pacific Earthquake Engineering Research Center (PEER). Retrieved from http://opensees.berkeley.edu

Zareian, F., & Medina, R. A. (2010). A practical method for proper modeling of structural damping in inelastic plane structural systems. *Computers & structures, 88*(1), 45-53.

4 EXPERIMENTAL STUDIES ON A DEEP STEEL COLUMN SECTION OF A 20-STORY MOMENT RESISTING FRAME THROUGH HYBRID TESTING

Shokoufeh ZARGAR[3] and Ricardo A. MEDINA[4]

4.1 Abstract

The availability of reliable numerical models is essential to reduce the uncertainties present in the prediction of structural behavior. Experimental studies allow the calibration and development of numerical models capable of characterizing the realistic behavior of structural elements and components until the limit state of collapse is approached. Quasi-static testing is the most commonly used experimental technique, in which the structural element or component is subjected to a predefined loading or displacement history. However, these loading histories are not consistent with the response histories experienced by structural components during an earthquake event. An

---

[3] Ph.D. Student, Dept. of Civil and Environmental Engineering, University of New Hampshire, Durham, NH 03824,Tel : (603) 913-4578, Fax: (603)862-2364, E-mail: sxu6@unh.edu

[4] Associate Professor, Dept. of Civil and Environmental Engineering, University of New Hampshire, Durham, NH 03824, Tel: (603) 862-0276, Fax: (603) 862-2364, E-mail: ricardo.a.medina@unh.edu, Proof Author

alternative method for performing experiments is hybrid simulation. This approach facilitates response-history analysis of the coupled system (physical and numerical) exposed to a ground motion. In this study, two hybrid simulations were conducted in which a 1:8 scaled W36X652 exterior column that is part of a 20-story steel moment resisting frame was considered as the physical substructure. The three-actuator setup (small bearing machine) at NEES lab @ Buffalo laboratory was utilized. The most relevant lessons learned from this study are threefold. First, the results reinforced the need to for experimental data on deep steel columns subjected to various loading histories. The influence of member behavior and axial load on the parameters that control the collapse of the structure were evaluated. Column plastic rotations of 0.07 and 0.034 rad were measured for the hybrid experiments. Second, it was demonstrated that hybrid simulations through collapse can be very sensitive to the properties assigned to the numerical portion of the structure. Third, it was shown that the proposed hybrid substructuring technique and displacement-control approach implemented in this study were successful in tracing the behavior of a tall steel structure until the onset of global instability was approached.

Keywords: Hybrid simulation, Collapse, Moment-resisting frame, Substructuring, Steel beam-column, Deep column

4.2 Introduction

Hybrid simulation has been conducted since the 1970's (Takanashi et al., 1975). Hybrid testing involves the interaction between a numerical (finite element) model and experimental specimens (physical substructures) during a test. In concept, the components of the structural system that can be modeled with a higher degree of confidence are included in the numerical model. The physical substructures are comprised of those components of the structural system that need to be studied

102

experimentally. An advantage of hybrid simulation is that the complete structural system does not need to be constructed and tested in the laboratory (e.g., shake table studies). Thus, hybrid simulation is more economical, safe, and provides more flexibility to test specimens of various scales (Schellenberg et al., 2009). Throughout the years the implementation of this testing approach has been greatly facilitated by improvements associated with its accuracy and efficiency (Chen et al., 2012; Shing & Mahin, 1983). Further enhancements in sub-structuring techniques (Nakashima et al., 1988; Shao et al., 2011), their implementation, and control strategies (Kwon et al., 2005; Nakashima & Masaoka, 1999) have also been conducted.

In this study slow hybrid simulation was performed on a 20-story moment resisting frame structure designed for Century City, California. The experimental substructure is a 1:8 scaled column specimen corresponding to a prototype W36X652 first-story exterior column. The mass, damping, and stiffness associated with the rest of the structure were part of the numerical model. One of the objectives is to provide much needed information on the behavior of deep steel column sections exposed to lateral drift, rotation at the tip, and variable axial load demands from elastic behavior to the onset of collapse. Two hybrid simulations were conducted for two levels of ground motion intensity. The second test was performed until the limit state of collapse was approached. In the past, experiments have been performed with similar experimental setups to predict the inelastic response of reinforced concrete columns (Y Yamada et al., 1990) and steel box sections (Yoshikazu Yamada et al., 1992) without necessarily approaching the limit state of collapse. The information obtained in this paper is to be used in conjunction with quasi-static tests conducted by the authors as part of the NEESR project titled *Collapse Simulation of Multi-Story Buildings Through Hybrid Testing* to calibrate numerical models of deep steel columns that account for strength and stiffness degradation in the presence of axial loads (Zargar et al., 2014).

The need for these tests arises from the scarcity of experimental data on the behavior of deep steel columns. These data are important for the calibration of numerical models of column elements necessary for a more accurate and reliable prediction of structural behavior up to the limit state of collapse. Lignos and Krawinkler (D. G. Lignos & Krawinkler, 2010) developed a database of more than 300 experiments on steel wide flange sections and calibrated deterioration parameters for the modified Ibarra-Medina-Krawinkler hysteretic model (IMK) (Ibarra et al., 2005). However, the amount of experimental data on the response of wide flange column sections was limited. Furthermore, most of the available experiments were conducted considering that columns behaved as cantilevers or in perfect double curvature (Nakashima et al., 1991; James D Newell & Uang, 2006). Cantilevers do not account for realistic boundary conditions at the free end of the beam. Forcing the column to deflect in perfect double curvature does not provide a realistic representation of the rotation associated with the column/panel zone/beam interface, and hence, may not provide a reliable representation of changes in the moment gradient along the height of the element during a response history analysis.

The hybrid simulations in this study were performed at the NEES lab @ Buffalo. The Open System of Earthquake Engineering Simulation Platform software (OpenSees, 2007a), OpenSees, was used for the numerical modeling and OpenFresco was used as the interface between the finite element software and the control of physical actuators and data acquisition software. OpenFresco is an object-oriented software that was developed by Takashashi and Fenves (2006) and was further modified and extended by Schellenbrg (Schellenberg & Mahin, 2006). In this study, the implicit Newmark method with fixed number of iterations was used for the integration scheme during the hybrid simulations. Furthermore, a predictor corrector algorithm was used to provide synchronization between the integration approach and the actuator control. A discussion on the

substructuring technique used for these tests to impose appropriate demands at the tip of the column is presented.

It is demonstrated herein that (a) there is a need to obtain additional information on the seismic response of deep steel columns; (b) hybrid simulations of moment frames can be very sensitive to assumed properties in the numerical modeling of columns; and (c) the proposed hybrid simulation approach was able to reliably characterize the response of the exterior steel column until the onset of global instability was approached, which helps validate hybrid testing as a viable testing approach to study collapse. These hybrid experiments were part of a more comprehensive research plan that included six quasi-static tests with column specimens identical to the 1:8-scale deep steel column used in the hybrid simulation studies presented herein. These quasi-static tests were conducted until the onset of global collapse was achieved. The results of the quasi-static experiments are presented in a paper titled "Experimental Studies on a Deep Steel Column Section Subjected to Variable Drift, Rotation, and Axial Load Demands".

4.3 Components of Hybrid Simulation with Substructuring

4.3.1 Numerical Model

The prototype structure for the hybrid simulations consists of a 20-story office building with perimeter moment resisting frames located in Century City, CA. A plan view of the 20-story structure is shown in Figure 4-1. This structure was designed based on ASCE 7-10 (ASCE, 2007) and the Steel Seismic Provisions (AISC 341-10 (AISC, 2010)). The exterior columns are W36X652 sections, which is the prototype structural element used in all tests. A 1:8 scaled two-dimensional model of the moment-resisting frame structure (North-South (N-S) frame) was developed using OpenSees (Mathiasson & Medina, 2013).
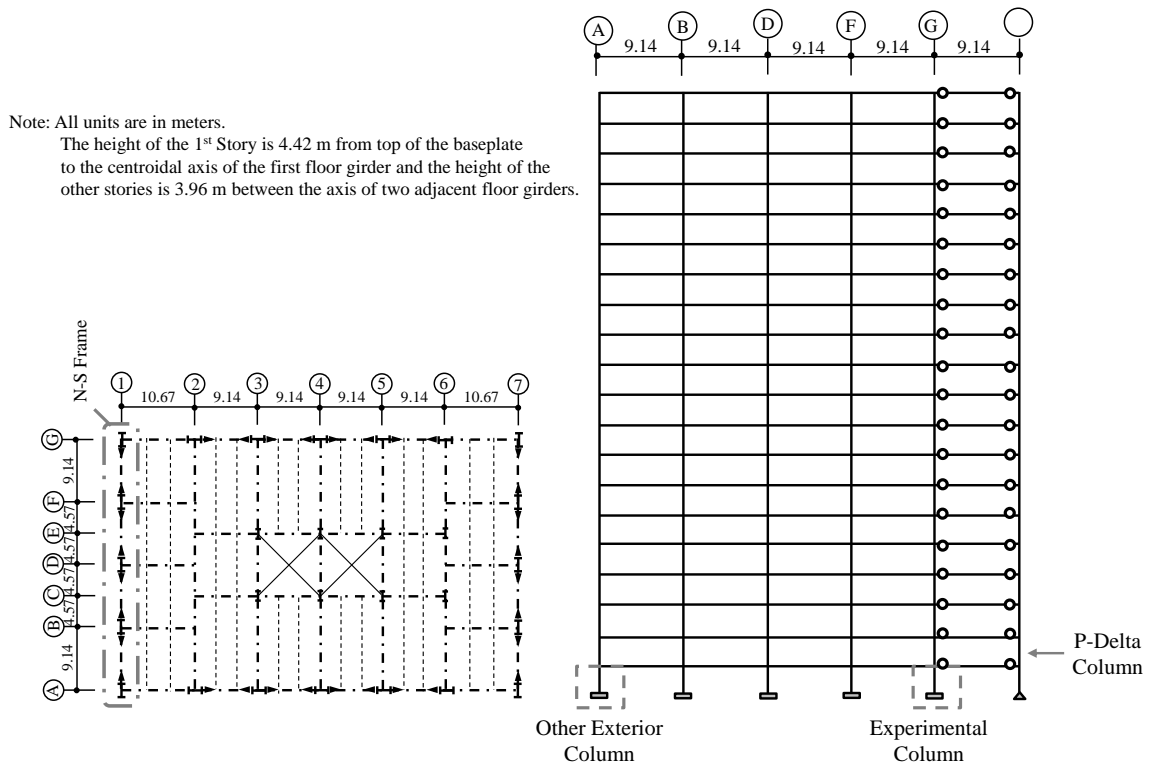
Figure 4-1. Typical floor plan of the 20-story building (left) and elevation view of

prototype model of N-S frame (right)

The fundamental period of the scaled structural model was estimated as 1.04 s (2.93 s for the

full scale prototype model). The model consisted of a combination of nonlinear rotational springs

and elastic beam elements. The springs were placed at the top and bottom of the columns, as well

as at the center of the reduced beam sections. The hysteretic behavior of the springs was modeled

based on the modified Ibarra-Medina-Krawinkler deterioration model (D. G. Lignos &

Krawinkler, 2010). The deterioration properties for the beam and column sections were calculated

using the regression equations of (D. G. Lignos & Krawinkler, 2010). Panel zones were modeled

following the Gupta-Krawinkler approach (Gupta & Krawinkler, 1999). In order to account for the

P-Delta effect, a leaning column with floor gravity loads corresponding to half of the floor mass minus the tributary load of the N-S frame at each level was connected to the frame with rigid links (see Figure 4-1-right). Rayleigh damping of 2% of critical was assigned to the first and fifth period of the scaled frame. The approach proposed by Zareian and Medina (Zareian & Medina, 2010) was used to model damping.

The bending moment strength of the column in the presence of axial loads was estimated based on the P-M interaction equations given in AISC-ANSI 360-10 (Design-AISC). To obtain the required axial load demand, the axial force of the column from a pushover analysis with a $k = 2$ (parabolic) ASCE-41 (ASCE, 2007) lateral load pattern was obtained. The axial load demand was estimated from combining the factored gravity axial load in the column ($P_{grav}=1.05P_D + 0.25P_L$, P_D as the dead and P_L as the live load) with 50% of the maximum axial load ($P_{E,max}$) experienced by the column due to the application of the lateral loads during the pushover analysis, $P_r=P_{grav}+0.5P_{E,max}$ (NIST, 2011).

Nonlinear static and dynamic analyses were conducted with a set of 100 recorded horizontal ground motions (50 stations) to facilitate the selection of the ground motion used to perform the hybrid simulations. These ground motions were from earthquakes with moment magnitudes (M_w) in the range of 6.9 to 7.62, Joyner-Boore distance and closest distance to the fault rupture area from 0 to 30 km, NEHRP site class D, and all fault mechanisms. The Duzce, Turkey 1999 horizontal ground motion record (NGA no 1605 DZS 270, Duzce Station) was selected and used to evaluate the behavior of the structure up to collapse. From here on, this ground motion record is referred to as the Duzce record. The 5%-damped 2/50 Uniform Hazard Spectrum (UHS) for Century City, CA was obtained from the Uniform Hazard Application developed by the USGS (USGS, 2008). An amplification factor of 1/0.8 was used to modify the UHS to the required 2%

damping ratio (ASCE, 2007). The 2%-damped UHS and scaled versions of the Duzce-record spectra for the ground motions used in hybrid simulations are shown in Figure 4-2.
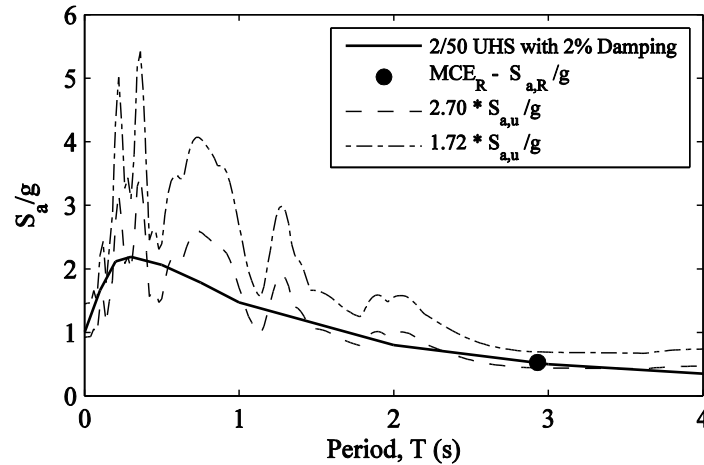
Figure 4-2. 2/50 uniform hazard spectrum (USGS, 2008) and response spectra for Duzce, Turkey 1999 horizontal ground motion (Duzce Station) with 2% damping ratio

4.3.2 Physical Specimen

The capacity (load and stroke) of the available actuators dictated the 1:8 scale used for the test specimen. The scaling process was focused on matching relevant parameters that control the inelastic behavior of wide flange steel elements (e.g., t_f/t_w, h/t_w, $b_f/2t_f$) within 10% of the target values, as shown in Table 1. The height of the experimental specimen was considered as the scaled height of the prototype column from the top of the base plate to the bottom of the panel zone region. A test specimen height equal to 493 mm (19.4 in.) was obtained, which corresponds to a prototype column height of 3942 mm (155.2 in.). An average yield strength of 344 MPa (50 ksi) and an ultimate strength of 469 MPa (68 ksi) were estimated from six tensile coupon tests conducted with coupons from sections of flange and web procured during fabrication of the specimens.

108

Table 4-1. Cross section specification of the prototype column and test specimen

	b_f	t_f	$b_f/2t_f$	d	h	t_w	h/t_w	t_f/t_w	I	A	Z
Specifications	mm	mm		mm	mm	mm			mm^4	mm^2	mm^3
	(in.)	(in.)		(in.)	(in.)	(in.)			(in.^{4})	(in.^{2})	(in.^{3})
W36X652	447	90.0	2.49	1044	815	50.0	16.3	1.80	2.11E+10	1.24E+5	4.77E+7
	(17.6)	(3.54)		(41.10)	(32.1)	(1.97)			(5.06E+4)	(192)	(2.91E+3)
Test	51	10	2.50	141	102	6.0	16.4	1.63	5.66E+6	1.88E+3	9.47E+4
Specimen	(2.0)	(0.40)		(5.56)	(4.02)	(0.25)			(13.6)	(2.91)	(5.78)

In hybrid simulation, the initial stiffness matrix should be calculated prior to the test. This system identification test was conducted and the 3×3 initial stiffness matrix of the experimental element was estimated as shown in Equation (4-1). The measured values were smaller than the theoretical stiffness values (Equation (4-2)) due to the minor lateral and axial flexibilities associated with small rotations of the loading beam, as well as small deformations of the lateral frames and the support pedestal (see Figure 4-3). The first column of the stiffness matrices shown below corresponds to the axial deformation at the tip of the column. The second and third columns refer to the lateral displacement and rotation at the tip of the column, respectively.

$$k_{i,Experimental} = \begin{bmatrix} 571 \ (kN/mm) & 0 & 0 \\ 0 & 70 \ (kN/mm) & -22010 \ (kN.mm/mm) \\ 0 & -22010 \ (kN.mm/mm) & 7231029 \ (kN.mm) \end{bmatrix} \quad (4\text{-}1)$$

$$k_{i,Theoretical} = \begin{bmatrix} 762 \ (kN/mm) & 0 & 0 \\ 0 & 113 \ (kN/mm) & -27970 \ (kN.mm/mm) \\ 0 & -27970 \ (kN.mm/mm) & 9187926 \ (kN.mm) \end{bmatrix} \quad (4\text{-}2)$$
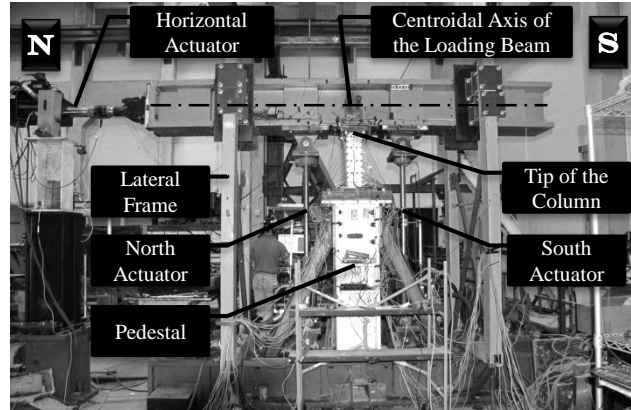
Figure 4-3. Experimental setup configuration.

4.4 Substructuring Approach and Hybrid Simulation Architecture

4.4.1 Substructuring Approach

The three-actuator test setup shown in Figure 4-3 was utilized for this experiment at the NEES@ Buffalo laboratory. This setup was used to control the two translational and rotational degrees of freedom (DOF) at the tip of the column (Figure 4-4- Left). The three actuators were in displacement-control mode. The location of the control and data acquisition DOF of the experimental setup is illustrated in Figure 4-4. The actuators were connected to a loading beam (top beam in Figure 4-3) in order to impose appropriate deformation demands at the tip of the column. The base of the horizontal actuator was connected to a reaction frame, while the base of the vertical actuators was connected to a support beam (bottom beam in Figure 4-3). The test configuration provided restraints (lateral frames in Figure 4-3) to minimize out-of-plane displacements at the tip of the column.

The ThreeActuatorJntOff Experimental Setup in OpenFresco was modified for the current study to relate and transform the displacement and forces between the tip of the actuators and the

tip of the column. In the original code the transformation of displacements and forces occurs between the pin connection of the actuator swivels and the location on the centroidal axis of the loading beam directly above the tip of the column (Figure 4-3). The tip of the prototype column is below the panel zone, which in the scaled specimen is located at the bottom face of the top base plate.

A coupled numerical model was generated to (a) test whether the hybrid substructuring technique was sound, (b) determine the appropriate ground motion scale factor to bring the structure to the onset of dynamic instability during the hybrid simulation, and (c) evaluate the required capacity (load cell and stroke) of each actuator. In this context, the term *coupled* refers to a model in which the physical specimen that forms part of the hybrid architecture is also modeled numerically using OpenSees. Thus, a virtual (purely numerical) hybrid simulation can be conducted with the numerical model of the rest of the structure (master) and the numerical model of the physical specimen (slave). An adapter element (Schellenberg et al., 2008) allowed coupling of the master and slave models through the connection of OpenFresco and OpenSees.

Nonlinear response history analyses using the coupled model showed that the onset of dynamic instability was achieved when a scale factor of 1.72 was applied to the amplitude of the Duzce record. Because these numerical analyses and subsequent hybrid simulations were conducted with 1:8 scaled structural models, the duration of the Duzce record was scaled by a time-scale ratio of $1:\sqrt{8}$. The scaled 2%-damped spectral acceleration at the first mode period of the structure was equal to 0.44g, which is less than the values corresponding to the 2%- damped 2/50 and risk-targeted maximum considered earthquake spectra at the site (both approximately equal to 0.52g) (see Figure 4-2). However, the hybrid test with this scaled ground motion had to be terminated before global collapse of the structure was attained as explained later in this paper.

The Newmark's method with a fixed number of iterations was used during the hybrid simulations to solve the equations of motion. This method does not check for convergence at the end of each step. Therefore, the unbalanced forces had to be monitored separately. Several nonlinear response history analyses with the coupled model were conducted to estimate the required number of iterations and the size of the integration time step to avoid erroneous results due to significant force unbalances. The time step sizes had to be reduced as much as possible by also taking into consideration values of incremental displacements that were appropriate for the range of the resolution of the actuator LVDTs. Thus, the ground motion was partitioned into different intervals with different time steps and different number of iterations per analysis step. The values shown in Table 2 were subsequently used in the hybrid simulations through collapse. The horizontal actuator has a force capacity of 245 kN (55 kips) and a stroke capacity of ±152 mm (±6in.). The vertical actuators each have a stroke capacity of 51 mm (±2 in.). The vertical actuator load cells used in these tests limited the vertical capacity of each actuator to 222 kN (50 kips) (34% of the axial load carrying capacity of the column). According to the drift, rotation and axial time histories, a maximum drift and rotation at the tip of the column of 0.11 rad and a maximum axial load of 444 kN (100 kips) (68% of the compressive axial load capacity of the column) can be applied given the limitations imposed primarily by the location, load-carrying capacity, and stroke of the vertical actuators.

Table 4-2. Variation in the time steps for original collapse test

Interval	Number of Ground Motion Data Points	Ground Motion Time Step (s)	Number of Iterations	Integration Time Steps (s)
1	150	$0.005*t_{sc}^{\otimes}$	4	$0.02*t_{sc}$
2	600	$0.005*t_{sc}$	4	$0.01*t_{sc}$
3	500	$0.005*t_{sc}$	6	$0.0025*t_{sc}$
4	3927	$0.005*t_{sc}$	6	$0.001*t_{sc}$

$^{\otimes}$ t_{sc} is the time scale factor for the scaled model which is $(1/8)^{0.5}$.
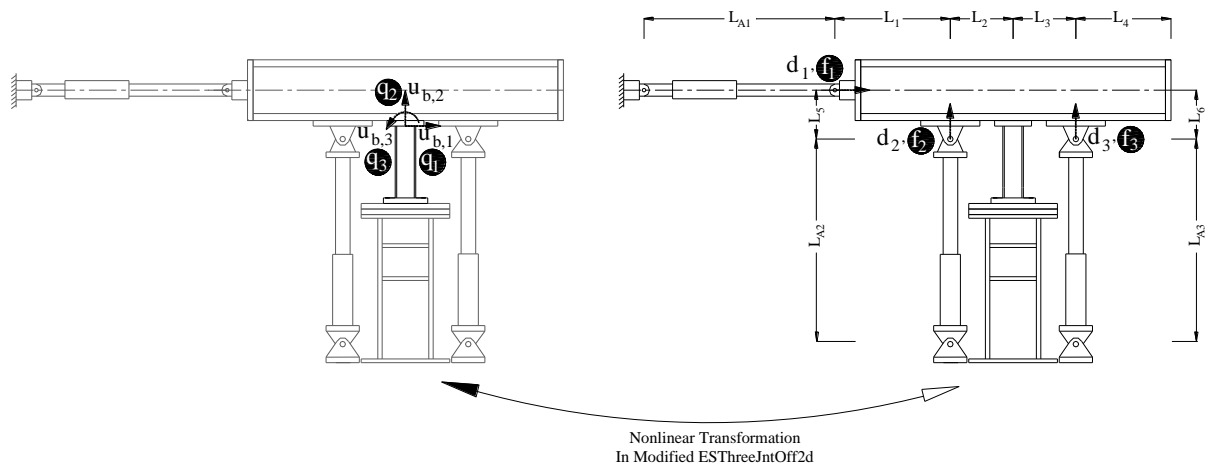
Figure 4-4. Transformation in the modified ThreeActuatorJntOff Experimental Setup

4.4.2 Hybrid Simulation Architecture

The architecture used in the hybrid simulations is shown in Figure 4-5. A hybrid laboratory had to be designed and built as part of this study because a setup for hybrid test was not available where the three-actuator test setup (small-bearing testing machine) is situated at the NEES@ Buffalo laboratory. The OpenSees finite element software was used for the modeling and analysis of the numerical structure on a host computer. OpenFresco was used to enable communication between OpenSees and the hybrid test setup. The TCP/ICP sockets connect the numerical analysis machine

(host) to the digital signal processor (target). The xPC experimental control object was employed to connect to the real-time xPC target machine, which runs the event driven predictor-corrector model. Communication between the xPC target machine and the MTS controller is provided by a National Instrument board. The MTS controller sends the command displacements to the actuators and returns back the measured forces and displacements in all actuators.
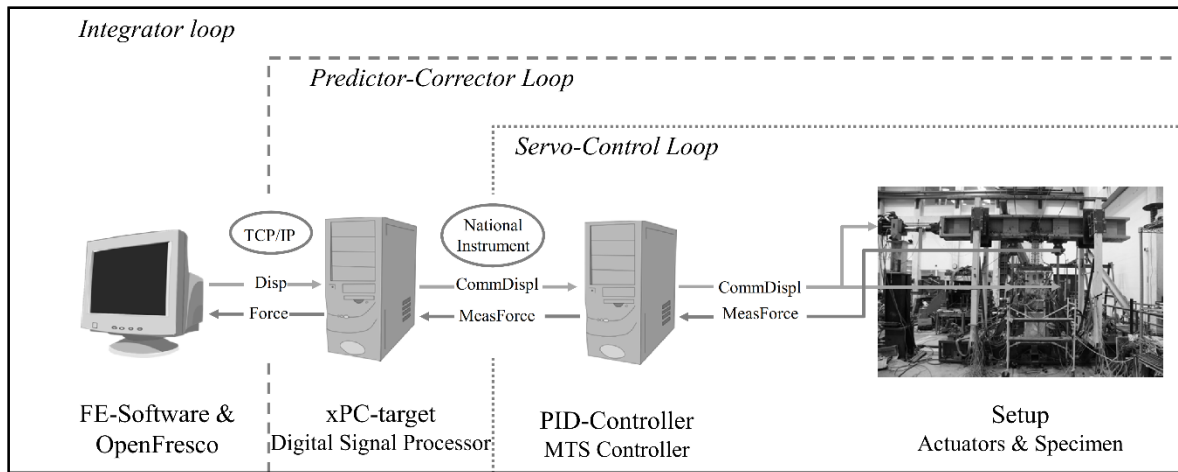
Figure 4-5. Architecture of hybrid simulation

4.5   Hybrid Simulation Results

4.5.1   Original Collapse Test

In this hybrid experiment, in order to numerically estimate and predict the response of the structure up to collapse, a coupled model (CM-56-56) was generated with a reduced moment capacity of 0.56 M_p for both exterior columns (Figure 4-6 (i)). M_p is calculated as the cross-section bending moment capacity in the absence of axial load (plastic modulus times yield strength, $f_y.z$). A reduced moment strength of 0.56 M_p was considered for the 1st story exterior columns (columns

114

on axis (A) and (G) in Figure 4-1-right) due to the presence of axial load based on the approach described in the *Numerical Model* section of this chapter.

The first-story drift ratio time history shows a good agreement between the hybrid test and the CM-56-56 model in the elastic range (time less than 2.5 s) as shown in Figure 4-7. However, once the first-story exterior column (column (b) in Figure 4-1-right) of the CM-56-56 model yields at its base, larger first-story drift ratios are obtained with respect to the ones from the hybrid simulation (at approximately 2.75 s). The moment at the base-first story drift ratio response demonstrates that the physical specimen has a higher strength ($0.95\ M_p$) as compared to the strength specified for the first-story column nonlinear springs ($0.56\ M_p$) (see Figure 4-8). The strain-hardening slope (the slope between yield rotation and rotation at maximum moment) is also steeper than the one assigned to the nonlinear spring of the numerical model. These increases are deemed to be caused by significant spread of inelasticity observed throughout the height of the test specimen (75% of the height) as shown in Figure 4-9-right. Spread of inelasticity is not appropriately captured by the concentrated plasticity approach used for the numerical model, and it is due to the moment gradient (Figure 4-10) imposed on the column from the combined effect of lateral drift and the applied rotation at its tip.

Figure 4-9-left illustrates the onset of web buckling and lateral torsional buckling that initiated soon after the column experienced a bending moment at the base approximately equal to the estimated plastic bending moment capacity in the absence of axial loads, M_p, equal to 32.5 kN-m (288 k-in.). The corresponding drift in which buckling initiates is identified with a black circular marker in Figure 4-7.
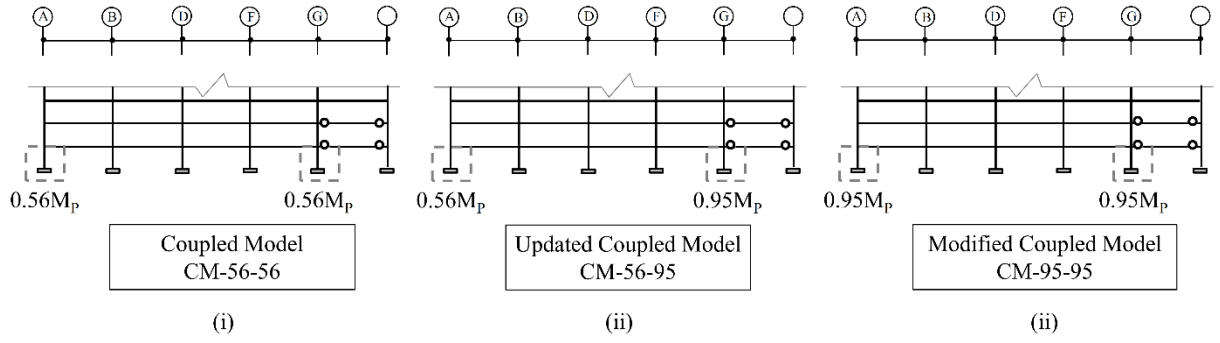
Figure 4-6. Description of coupled hybrid simulation models

Figure 4-7. First-story drift ratio time history of original collapse test and coupled models

116
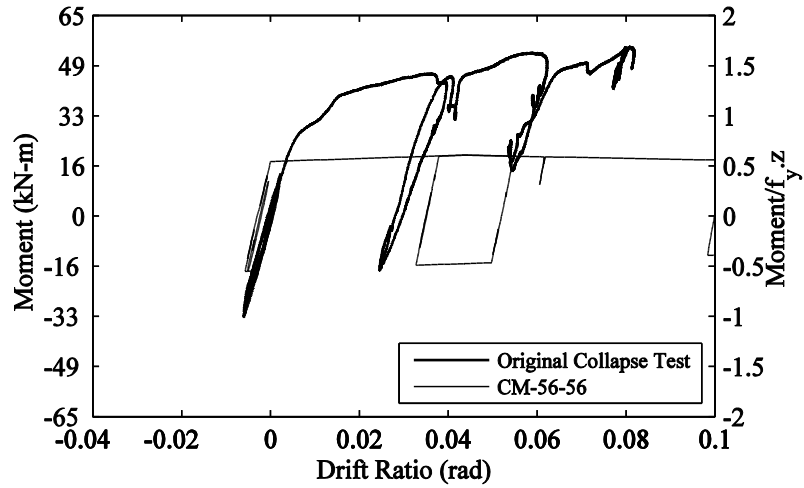
Figure 4-8. Moment-drift ratio relationship at the base of the column of original collapse

test and coupled model

Figure 4-9. Lateral torsional buckling (left), strain measurements over the height in the

south flange (right) for original collapse test

117

Figure 4-10. Column bending-moment diagram over the height for original collapse test

The maximum bending moment strength obtained experimentally was approximately equal to

0.95 M_p (Figure 4-8), primarily due to the fact that M_p was estimated based on cross-sectional

properties without taking into account the spread of inelasticity in the element. The bending

moment strength of the first-story exterior column nonlinear springs was updated accordingly in

the coupled model and a virtual hybrid simulation was conducted (this model is referred to from

here on as the updated coupled model; CM-56-95) (see Figure 4-6(ii)). The first-story drift time

history of this simulation is presented in Figure 4-7, which shows a reasonable agreement with the

performed hybrid test. This result highlights the importance of appropriate modeling of columns

in the inelastic range.

Additional results from the hybrid simulation and the numerical simulation using the updated

coupled model (CM-56-95) are presented next. The base shear hysteresis in Figure 4-11 illustrates

the contribution of global P-Delta to the response of the structure for both the hybrid simulation

and the CM-56-95 model. In the inelastic range, as the first-story drift ratio increases, the base

118

shear tends to decrease. An evaluation of the distribution of drift ratios along the height of the structure is shown in Figure 4-12. In the elastic range (time equal to 1.5s) and at a first-story drift ratio close to 0.04 (time equal to 2.65s), the story drift ratios along the height are consistent. However, at larger levels of inelastic behavior (e.g., at time equal to 4.4s) differences in the order of 10% are observed in the lower stories.
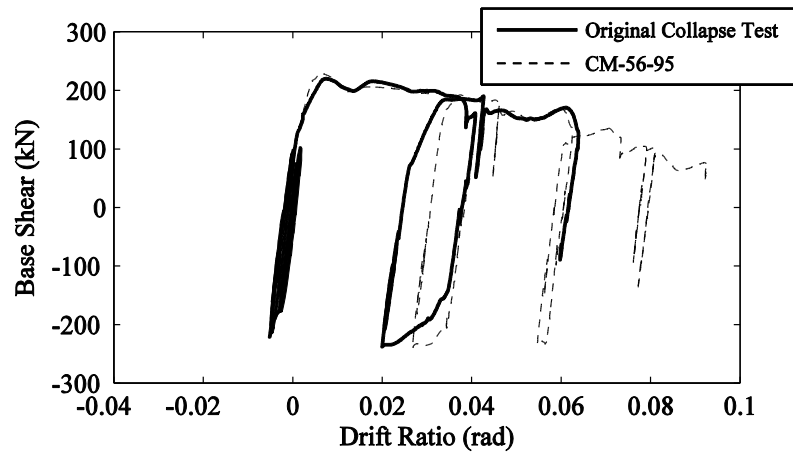
Figure 4-11. Base shear vs. first-story drift ratio of original collapse test and updated

coupled model
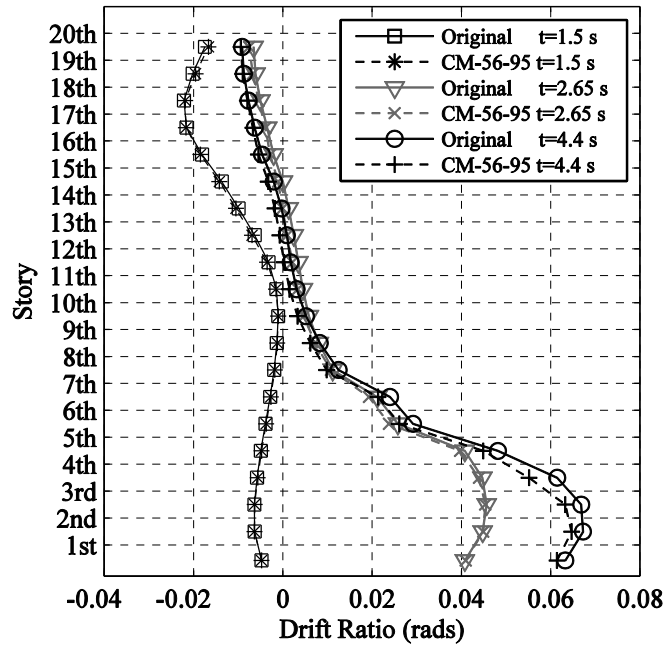
Figure 4-12. Drift ratio profiles for original collapse test and updated coupled numerical model

4.5.2 Modified Collapse Test

In the second hybrid simulation, two modifications were made with respect to the previous test. First, the bending moment capacity of the numerical model of the first-story exterior column (column on axis (A) in Figure 4-1- right) was modified from $0.56\,M_p$ to $0.95\,M_p$ based on the results from the previous hybrid simulation. Second, the Duzce record with a larger scale factor (2.7) was utilized (see Figure 4-2). Numerical simulations with the CM-95-95 model demonstrated that a larger scale factor was needed in order to approach the limit state of collapse when the aforementioned increase in bending moment strength was implemented. The time step sizes used in the various portions of this analysis are shown in Table 4-3 based on the results obtained from numerical simulations with the CM-95-95 model. The scaled 2%-damped spectral acceleration at

120

the first mode period of the structure was now equal to 0.69g which is now greater than the values

corresponding to the 2%- damped 2/50 and risk-targeted maximum considered earthquake spectra

at the site (both approximately equal to 0.52g) as seen in Figure 4-2.

Table 4-3. Variation in the time steps for modified collapse test

Interval	Number of Ground Motion Data Points	Ground Motion Time Step (s)	Number of Iterations	Integration Time Steps (s)
1	600	$0.005*t_{sc}$ $^{\otimes}$	4	$0.02*t_{sc}$
2	1800	$0.005*t_{sc}$	6	$0.001*t_{sc}$
3	2777	$0.005*t_{sc}$	6	$0.0008*t_{sc}$

$^{\otimes}$ t_{sc} is the time scale factor for the scaled model which is $(1/8)^{0.5}$.

In this case, the results from the hybrid simulation were much closer to the predicted numerical

results. For this experiment, the reduced moment capacity of $0.95Mp$ was considered for both

exterior columns (modified coupled model (CM-95-95), Figure 4-6 (iii)). For instance, the time

history of the first-story drift ratio shows reasonable agreement throughout the history up to

collapse (Figure 4-12). The moment at the base-drift ratio diagram in Figure 4-14 demonstrates

that the evaluated bending moment strength of first-story exterior columns assigned to the

numerical model was more consistent with the strength exhibited by the physical specimen.

However, the strain-hardening slope was still underestimated by the numerical model. This

discrepancy is most likely due to the spread of inelasticity through columns height. Furthermore,

the column specimen experienced a steeper negative slope after the point of maximum moment

(i.e., post-capping slope). This observation is of paramount importance for the calibration of

column hysteretic models given that very limited data on the behavior of deep steel columns are

available in the literature to evaluate the magnitude of this post-capping slope. This pronounced

deterioration in strength and stiffness is attributed to lateral torsional buckling of the column specimen at drift ratio levels greater than 0.04. Second-order, P-Delta effects are also dominant in this hybrid simulation as shown in Figure 4-15. It can also be observed that the overall prediction of base shear responses provided by the CM-95-95 model is close to that of the hybrid experiment.

An alternative way of evaluating the effect of P-Delta on the results is provided by the story drift ratio profiles shown in Figure 4-16. It can be seen that the story drift ratios of the hybrid experiment match the drift ratio profiles from the CM-95-95 model in the elastic and slightly inelastic range (time equal to 2.65s). However, once the level of inelastic behavior and the effect of P-Delta become more significant (time equal to 3.9s), P-Delta effects result in an amplification of drift ratio demands in the bottom stories. It can be seen that drift ratios obtained from the hybrid simulation are 17% larger. This difference is attributed primarily to the relative sudden drop in bending moment capacity of the test specimen after the maximum moment is attained. Figure 4-17 shows the lateral torsional bucking and web buckling experienced by the column (left) and the spread of inelasticity over the height (right). The inelasticity is more pronounced in this test compared to the previous one, which can be observed by contrasting Figure 4-9-right with Figure 4-17-right. In addition, it can be observed that there is a 66% increase in the strain measured at a height (calculated from the base of the column) equal to the depth of the column (140 mm) in the modified collapse test compared to the original test. The bending moment gradient over the height shows that the column is in single curvature at various time intervals as shown in Figure 4-18. This behavior is consistent with the strain data shown in Figure 4-17-right.
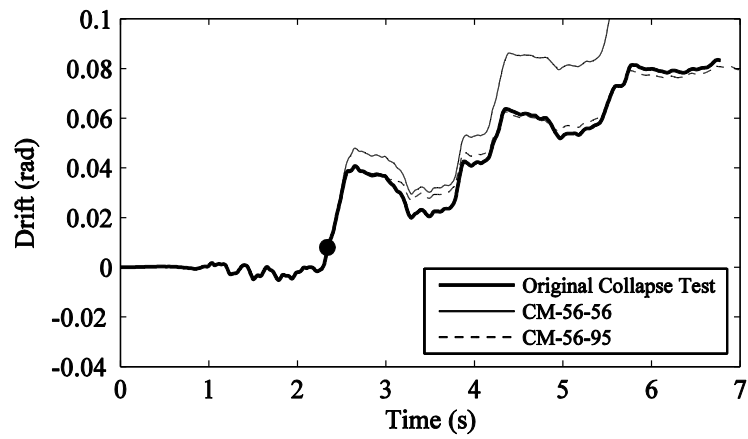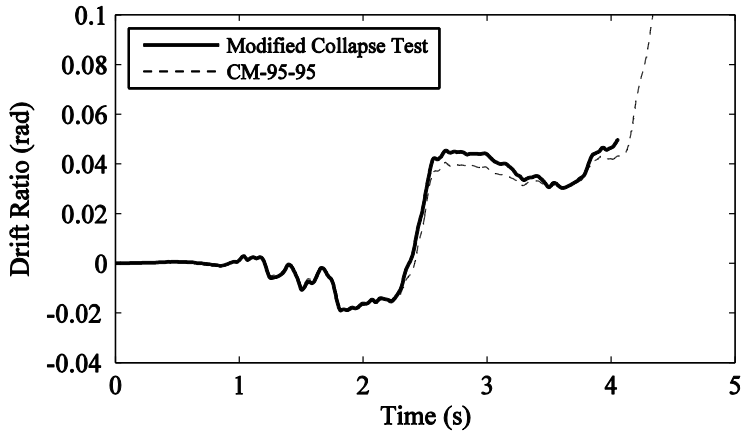
Figure 4-13. First-story drift ratio time history of modified collapse test and modified coupled model
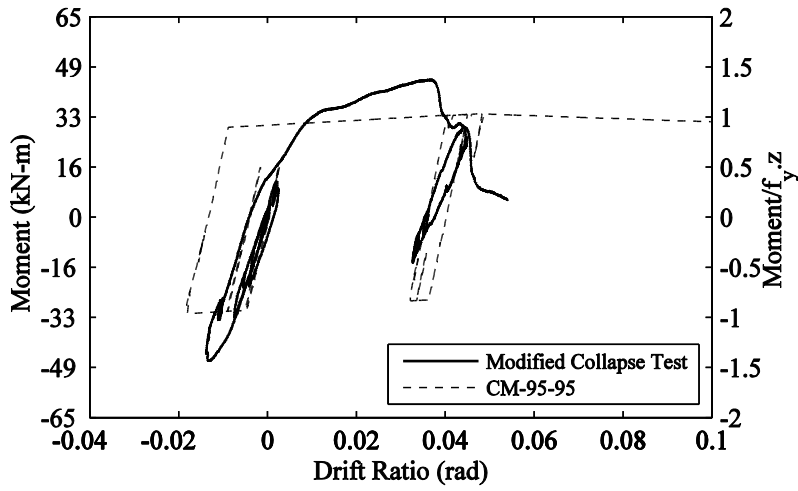
Figure 4-14. Moment- drift ratio relationship at the base of the column of modified collapse test and modified coupled model
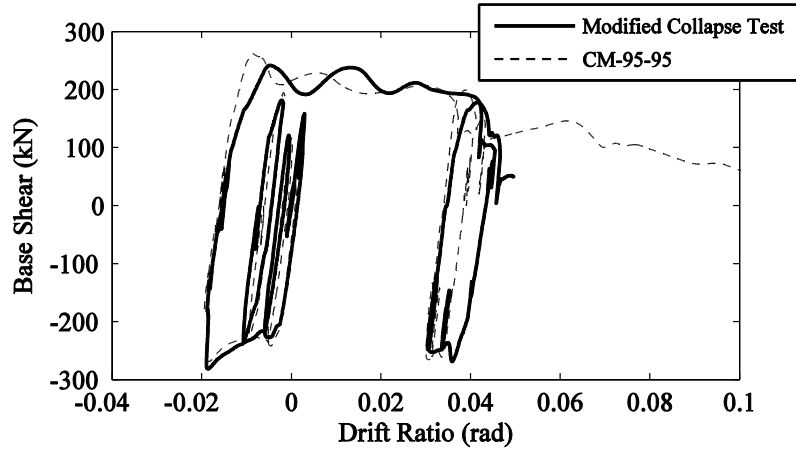
Figure 4-15. Base shear vs. first-story drift ratio of modified collapse test and the modified coupled model
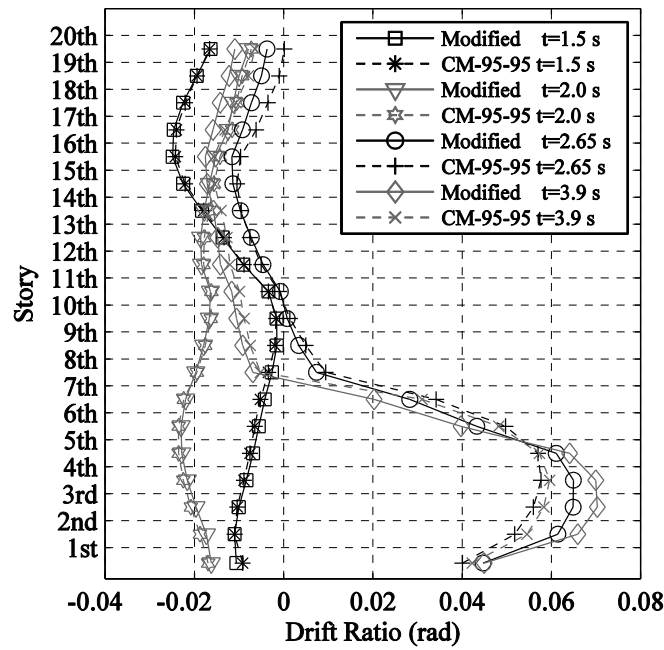
Figure 4-16. Drift ratio profiles for modified collapse test and the modified coupled model
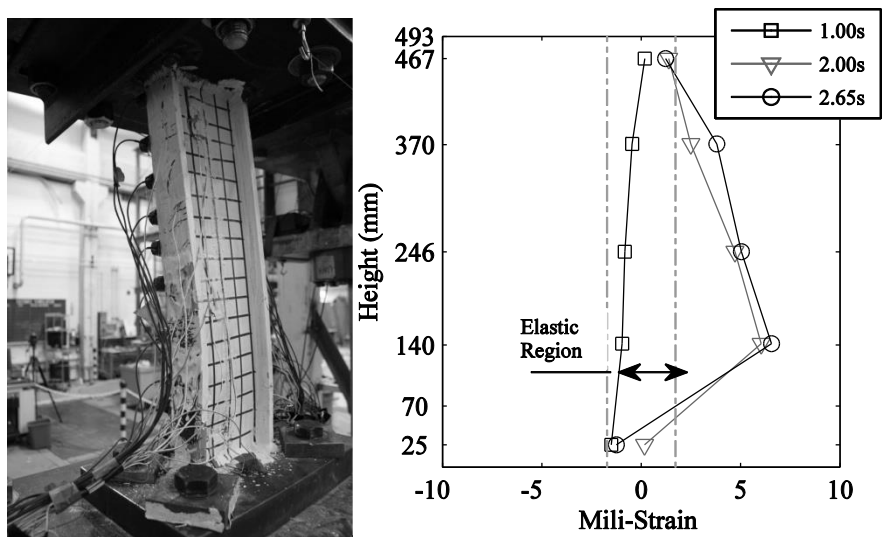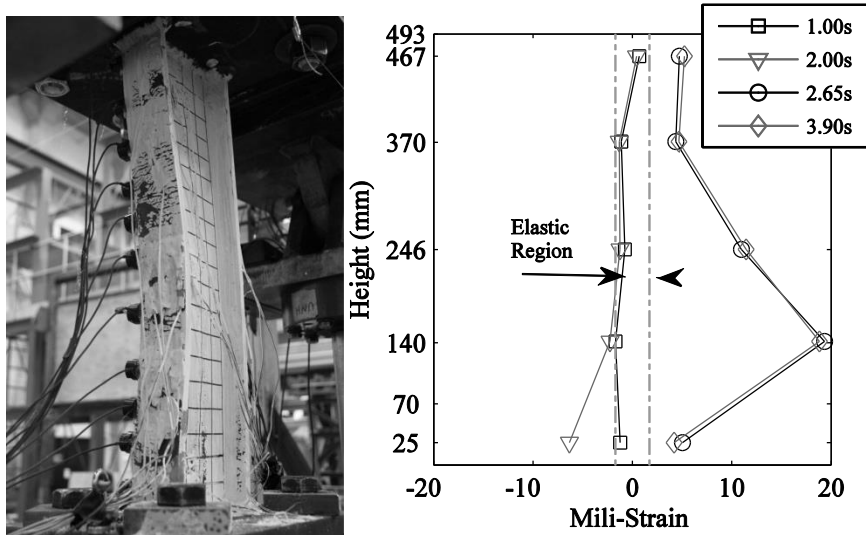
Figure 4-17. Lateral torsional buckling (left), strain measurements over the height in the south flange (right) for the modified collapse test
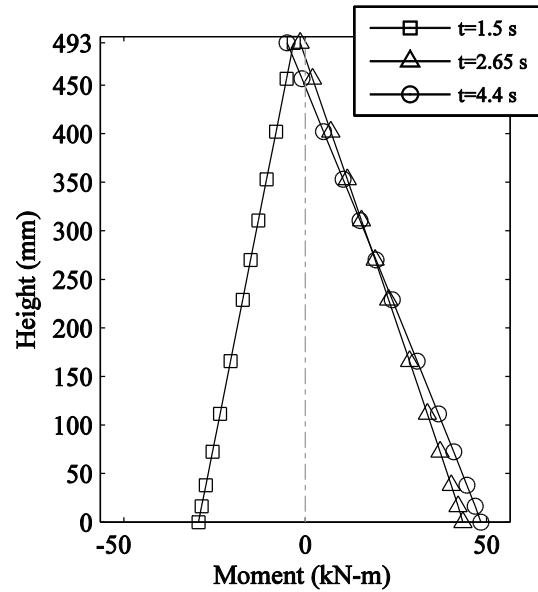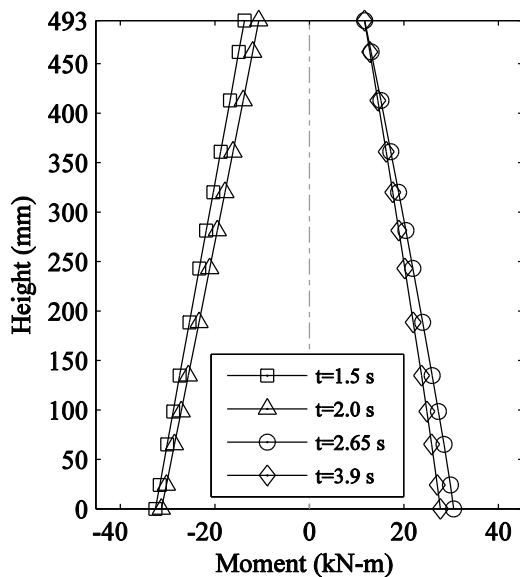

Figure 4-18. Column bending moment diagram over the height for modified collapse test

125

4.6   Quantification of the Backbone Parameters

This study incorporates testing two columns with a loading history more consistent to the actual response of an exterior column, in which it will enable an increased understanding of column behavior up to collapse and a generalized calibration of the modified IMK model (Figure 4-19). The bending moment at the base vs. drift ratio relationship shows an increase in the maximum bending moment of the columns tested through hybrid testing on the order of 1.75 and 1.4 times the plastic moment capacity (M_p) for two separate hybrid experiments with different earthquake intensities. Two of the parameters that are quantified and that are important to conduct collapse assessment of structures are the plastic rotation capacity (θ_p, difference between yield rotation and rotation at maximum bending moment) and the post-capping rotation (θ_{pc}, difference between rotation at maximum moment and rotation at complete loss of strength).
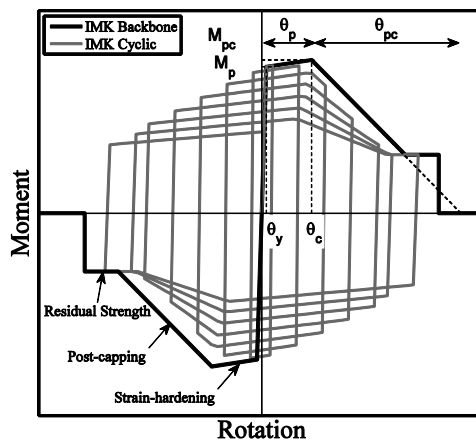
Figure 4-19. Modified Ibarra-Medina-Krawinkler Model (IMK).

126

A quantification of modeling parameters that are most relevant for collapse simulation was performed. In this section the estimated plastic rotation capacity (θ_p), and the post-capping rotation (θ_{pc}) are presented.

- Plastic rotation capacity, θ_p

The plastic rotation capacity in the cyclic tests is estimated from the first inelastic cycle in which a clear post-capping slope is visible (i.e., the maximum bending moment strength is achieved in that cycle). The plastic rotation capacities (θ_p) were estimated as 0.07 and 0.034 rad for the original and modified collapse hybrid tests, respectively. For monotonic tests under constant axial force of 31% of the available axial strength and variable axial load of 57% of the available axial strength, the estimated plastic rotation capacities were estimated as 0.08 and 0.06 rad, respectively. As shown in Figure 4-20, the modified hybrid test experiences a larger axial load compared to original and monotonic experiments, therefore there is a decrees in the plastic rotation capacity.

Additionally, the estimated plastic rotation capacity for the quasi-static asymmetrical cyclic tests performed on the similar scaled cross section subjected to large drifts, rotation, and variable axial load was estimated as 0.035 radians. On the other hand, it can be observed that a significant reduction in plastic rotation capacity occurs in the quasi static symmetric cyclic tests, which varied from 0.012 to 0.15 rad. The plastic rotation capacity is influenced by the loading history and the level of axial load.

For a W36X652, ASCE-SEI 41 (2007) estimates a plastic rotation capacity of 0.009 rad when the axial force is 31% of the available axial strength and negligible plastic rotation capacity for an axial load of 57% of the available axial strength. Moreover, the plastic rotation capacity according to an extrapolation of the regression equation for W-sections for beams other-than-RBS sections

developed by Lignos (D. G. Lignos & Krawinkler, 2010) would result in a value of 0.04 rad without considering the axial load effect. These results indicate that for a deep steel column such as the W36X652, the plastic rotation capacity is influenced by the loading history and the level of axial load.

- Post-capping rotation capacity, θ_{pc}

For the original hybrid test, a clear loss of strength after reaching the maximum strength was not observed. The post-capping rotation (θ_{pc}, difference between rotation at maximum moment and rotation at complete loss of strength) for the modified hybrid test was estimated as 0.027 rad. The extrapolation of the regression for post-capping rotation for W-sections for beams developed by Lignos (D. G. Lignos & Krawinkler, 2010) estimates a value of 0.44 rad without considering the axial load effect. For monotonic tests under constant axial force of 31% of the available axial strength and variable axial load of 57% of the available axial strength, the estimated plastic rotation capacities were estimated as 0.37 and 0.18 rad, respectively. The estimated post-capping rotation of the last cycle of the quasi-static cyclic tests performed at buffalo are in the 0.09 rad and 0.11 rad range. Results from the last cycle of the asymmetrical quasi-static loading is approximately 0.11 rad. There is significant reduction in the post-capping stiffness with respect to quasi-static monotonic and cyclic tests in the modified hybrid test. Note that the post-capping slope, which is a consequence of lateral torsional buckling, can be clearly observed after reaching the maximum axial load (60% of the available axial strength and variable axial load) in the column (Figure 4-14 and Figure 4-20).
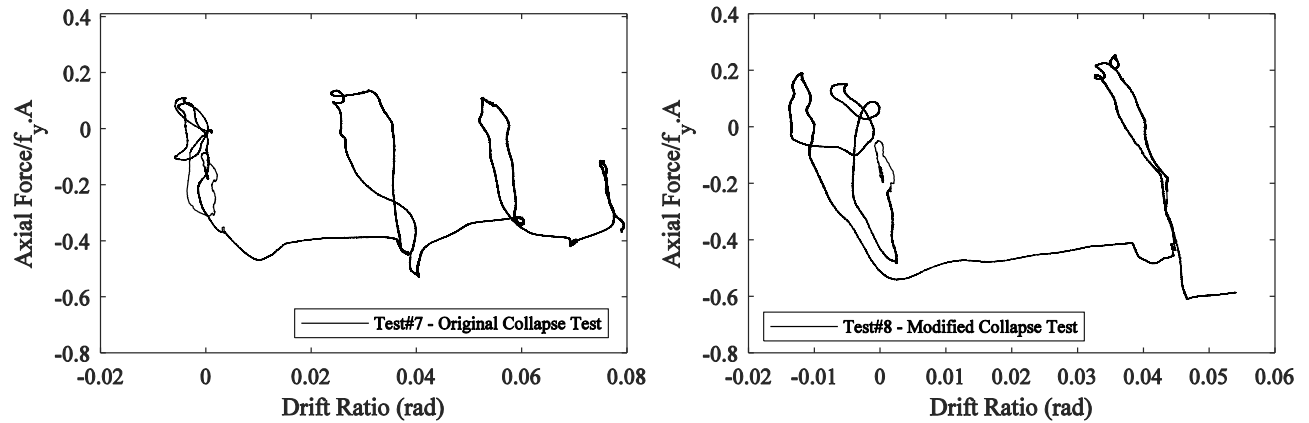
Figure 4-20. Total axial load-drift in the column for the original and modified hybrid tests

4.7 Conclusions

Two different hybrid tests were performed on a 20-story moment resisting frame with a 1:8 scaled first-story exterior deep steel column as the physical element. Lateral displacements, vertical displacements, and rotations at the tip of the column were controlled and the response of the column was evaluated from elastic behavior to the onset of global collapse. This implies that variable shear force, axial load, and bending moment demands were imposed at the tip of the column, which allowed for a more accurate simulation of changes in the bending moment gradient of an exterior column that is part of moment-resisting frame. These results are deemed to be valuable for an enhanced understanding of the behavior of steel columns, as well as an improved calibration of numerical models of deep steel columns that are exposed to significant strength and stiffness degradation in the presence of variable axial load demands.

The bending moment at the base vs. drift ratio relationship shows an increase in the maximum bending moment of the columns tested through hybrid testing on the order of 1.75 and 1.4 times the plastic moment capacity ($f_y.z$) for two separate hybrid experiments with different earthquake intensities. Further, the estimated plastic rotation capacities of 0.07 rad and 0.034 rad were

129

obtained for each of the columns (original and modified tests). One of the column specimens did not experience a noticeable loss of strength at the end of the experiment (original test). In the modified hybrid test, the post-capping rotation was estimated as 0.027 rad, in which there is significant reduction in the post-capping rotation with respect to quasi-static monotonic (0.37 rad and 0.18) and cyclic (0.9 rad and 0.11 rad) tests due to a higher axial load and a consequence of lateral torsional buckling. These results indicate that for a deep steel column such as the W36X652, the plastic rotation capacity is strongly influenced by the loading history and the level of axial load.

The primary failure mode of the column specimens was web buckling and lateral torsional buckling. This resulted in severe strength and stiffness degradation after the maximum bending moment was achieved in the second hybrid simulation through collapse. The hybrid simulations demonstrated that spread of inelasticity along 75% of the height of the column provides in this case a maximum bending moment strength 70% larger than the one predicted from *a priori* knowledge based on cross-sectional properties and available information in the literature. This discrepancy reinforces the need to further investigate the response of physical deep steel columns to provide data useful for model calibration and improved numerical collapse predictions of structural systems. In addition, these results highlight the importance of a newly developed numerical updating approach for hybrid simulation in which the properties of the numerical model can be updated during the experiment based on the knowledge obtained from the response of the physical specimen (Negrete et al., 2014).

The results presented in this paper showed that the hybrid substructuring technique and displacement-control approach implemented as part of the hybrid architecture of these tests were successful in tracing the behavior of a tall steel structure until the onset of global instability was

approached. It is important to note that these hybrid simulations referred to two-dimensional models; a single column prototype; and a single ground motion scaled to two different intensity levels. More general conclusions of deep steel column behavior relevant for numerical model calibration will necessitate additional experiments with columns of various sizes and scales that are exposed to biaxial bending moment demands, as well as ground motions with various intensities, durations, and frequency contents. The results from these tests should be interpreted within the conditions and assumptions used to conduct them. The quasi-static tests conducted with these columns as well as the hybrid tests presented herein are just initial steps geared toward characterizing the behavior of deep steel column sections more accurately.

4.8   Acknowledgements

4.9   References

AISC. (2010). Seismic Provisions for Structural Steel Buildings, ANSI/AISC 341-10 2010: American Institute of Steel Construction, Chicago, Illinois.

ASCE. (2007). Seismic Rehabilitation of Existing Buildings, ASCE/SEI 41-06 *American Society of Civil Engineers, Reston, VA, US*.

Chen, C., Ricles, J. M., & Guo, T. (2012). Improved adaptive inverse compensation technique for real-time hybrid simulation. *Journal of Engineering Mechanics, 138*(12), 1432-1446.

Design-AISC, S. 360-10 9 Steel Design-AISC 360-10. *Steel Design per AISC*, 360-310.

Gupta, A., & Krawinkler, H. (1999). *Seismic demands for the performance evaluation of steel moment resisting frame structures.* Stanford University.

Ibarra, L. F., Medina, R. A., & Krawinkler, H. (2005). Hysteretic models that incorporate strength and stiffness deterioration. *Earthquake engineering & structural dynamics, 34*(12), 1489-1511.

Kwon, O.-S., Nakata, N., Elnashai, A., & Spencer, B. (2005). Technical note a framework for multi-site distributed simulation and application to complex structural systems. *Journal of Earthquake Engineering, 9*(5), 741-753.

Lignos, D. G., & Krawinkler, H. (2010). Deterioration modeling of steel components in support of collapse prediction of steel moment frames under earthquake loading. *Journal of Structural Engineering, 137*(11), 1291-1302.

Mathiasson, A., & Medina, R. A. (2013). *Seismic collapse assessment of a 20-story steel moment resisting frame structures.* (MS), University of New Hampshire, Durham, New Hampshire.

Nakashima, M., Ishii, K., Kamagata, S., Tsutsumi, H., & Ando, K. (1988). Feasibility of pseudo dynamic test using substructuring techniques. *Proceeding of 9th World Conference on Earthquake Engineering. Tokyo, Japan, 4*, 47-52.

Nakashima, M., & Masaoka, N. (1999). Real-time on-line test for MDOF systems. *Earthquake engineering & structural dynamics, 28*(4), 393-420.

Nakashima, M., Morino, S., & Koba, S. (1991). Statistical evaluation of strength of steel beam columns. *Journal of Structural Engineering, 117*(11), 3375-3395.

Negrete, M., Medina, R., Miranda, E., Mosqueda, G., & Hashemi, M. (2014). Numerical updating on collapse simulation of a four-story building through hybrid testing. *Proceedings of the*

10th National Conference in Earthquake Engineering, Earthquake Engineering Research Institute, Anchorage, AK.

Newell, J. D., & Uang, C.-M. (2006). *Cyclic behavior of steel columns with combined high axial load and drift demand*: Department of Structural Engineering, University of California, San Diego.

NIST. (2011). Research Plan for the Study of Seismic Behavior and Design of Deep, Slender Wide Flange Structural Steel Beam-Column Member. *prepared by the NEHRP Consultants Joint Venture, a partnership of the Applied Technology Council and the Consortium of Universities for Research in Earthquake Engineering for the National Institute of Standards and Technology, NIST GCR 11-917-13 2011*(Gaithersburg, Maryland).

OpenSees. (2007). Open System for Earthquake Engineering Simulation: Pacific Earthquake Engineering Research Center (PEER). Retrieved from http://opensees.berkeley.edu

Schellenberg, A., Huang, Y., & Mahin, S. A. (2008). *Structural FE-software coupling through the experimental software framework, OpenFresco.* Paper presented at the Proceedings, 14th World Conference on Earthquake Engineering, Beijing, China.

Schellenberg, A., Kim, H. K., Takahashi, Y., Fenves, G. L., & Mahin, S. A. (2009). OpenFresco Command Language Manual: Version.

Schellenberg, A., & Mahin, S. (2006). *Integration of hybrid simulation within the general-purpose computational framework OpenSees.* Paper presented at the Eighth US National Conference on Earthquake Engineering.

Shao , X., Reinhorn , A. M., & Sivaselvan , M. V. (2011). *Real-Time Hybrid Simulation Using Shake Tables and Dynamic Actuators* (Vol. 137).

Shing, P., & Mahin, S. A. (1983). Experimental error propagation in pseudodynamic testing. *Earthquake Engineering Research Report UCB/EERC-83/12, University of California, Berkeley, 168*.

Takahashi, Y., & Fenves, G. L. (2006). Software framework for distributed experimental–computational simulation of structural systems. *Earthquake engineering & structural dynamics, 35*(3), 267-291.

Takanashi, K., Udagawa, K., Seki, M.-u., Okada, T., & Tanaka, H. (1975). Nonlinear earthquake response analysis of structures by a computer-actuator on-line system. *Bulletin of Earthquake Resistant Structure Research Center, 8*, 1-17.

USGS. (2008). Hazard Curve Application, United States Geological Survey, http://geohazards.usgs.gov/hazardtool/application.php/. Last accessed 2012.

Yamada, Y., Iemura, H., & Tanzo, W. (1992). Substructured hybrid loading tests of steel box-section columns for inelastic earthquake response of frame structures. *Earthquake Engineer 10th World, 5*, 2837.

Yamada, Y., Iemura, H., Tanzo, W., & Endo, K. (1990). Substructured hybrid loading of structural members under combined axial, shear, and bending loads. *Japanese Society of Soil Mechanics and Foundation Engineering, 251*, 1503-1508.

Zareian, F., & Medina, R. A. (2010). A practical method for proper modeling of structural damping in inelastic plane structural systems. *Computers & structures, 88*(1), 45-53.

Zargar, S., Medina, R., & Miranda, E. (2014). Cyclic behavior of deep steel columns subjected to large drifts, rotations, and axial loads. *Proceedings of the 10th National Conference in Earthquake Engineering, Earthquake Engineering Research Institute, Anchorage, AK*.

5 PERIMENTAL STUDIES ON THE INELASTIC BEHAVIOR OF A CANTILEVER BEAM WITH DEEP STEEL SECTION SUBJECTED TO LARGE DRIFTS

Shokoufeh ZARGAR[5], Ricardo A. MEDINA[6], Erin BELL[7]

5.1 Abstract

Previously a series of experiments on 1:8 scaled W36X652 column sections were performed to study the effect of boundary condition (rotation) and axial load the parameters that control the collapse of the structure. In order to evaluate the effect of member behavior and axial load, two cantilever beam sections with the same geometry as the columns were tested. For the first beam experiment, the top of the beam lost its lateral support and a plastic rotation capacity of 0.04 was measured. For the second beam experiment, in-plane displacement was enforced at the tip of the beam and did not experience post-capping slope even after a plastic rotation of 0.12 rad, in which

---

[5] Ph.D. Candidate, Dept. of Civil and Environmental Engineering, University of New Hampshire, Durham, NH 03824,Tel : (603) 913-4578, Fax: (603)862-2364, E-mail: sxu6@unh.edu

[6] Staff Consultant, Simpson Gumpertz & Heger Inc., Waltham, MA, USA

[7] Professor, Dept. of Civil and Environmental Engineering, University of New Hampshire, Durham, NH 03824, Tel: (603) 862-0276, Fax: (603) 862-2364, E-mail: Erin.Bell@unh.edu

this is 50% larger than the plastic rotation capacity obtained from the column experiment with monotonic loading with constant axial force of 31% of the axial load carrying capacity. The dominant failure mode were inelastic lateral torsional buckling for both experiments.

Keywords: Quasi-static Test, Collapse, Monotonic, Cantilever steel beam, Deep wide flange steel sections

5.2 Introduction

An experimental study on a cantilever beam with deep steel section was conducted. Deep steel sections have larger web to thickness ratios than tested W14 and stockier W-sections, therefore local buckling of flanges and web and also torsional buckling might be significant due to the loading and boundary conditions. In which, the failure mode will have an effect on inelastic properties and behavior of the member. Experimental studies on W sections with large deformations will allow us to have a better understanding of their inelastic behavior. The purpose of this project is to evaluate the behavior of a scaled W36X652 under large displacements. The overall outputs of the experimental study are addressed as follow:

- Study the dominant failure mode of the member

- Evaluating the moment-drift relationship, to capture the elastic and inelastic propertied

- Determining the plastic rotation capacity (θ_p), the rotation between yield and maximum bending moment

- Determining the negative slope or the post capping (θ_{pc}), the rotation between maximum and zero bending moment

136

The experimental program involves testing two 1:8 scaled W36X652 sections exposed to quasi-static lateral drift (monotonic). In previous tests that were performed at NEES Lab@ Buffalo, a rotation and axial load were implemented in addition to the lateral displacement (Zargar et al., 2014). It would be worthy to perform the experiments without axial and rotation in the tip to observe the change in the failure mode, and the effect of axial load and rotation on the inelastic behavior of the member.

5.3 Test Setup

The green frame at University of New Hampshire was considered for the current test setup (Figure 5-1). The base of the column is attached to a bracket and was placed tip below the piston. So, with the extension of the piston the tip of the column is going to be displaced vertically (lateral displacement for the column which bends the column about its strong axis). Also, in order to measure the implemented load, a load cell should be placed between the piston and the tip of the column. Because, the piston is not designed to carry lateral displacement, the tip of the column cannot be attached to it.

The frame and the hydraulic piston are designed to implement a downward pressure with a capacity up to 300 kips. The stroke of the hydraulic piston is 6.25 in, and it can only implement the force when it is extending (no rotation). The capacity of the scaled column section has been estimated in the following section.

In order to perform the setup following items fabricated. The drawings were developed from scratch which could be found in the Appendix 5.

- Two column specimens (modified W8X24) with baseplates

137

- Bracket

- Sleeve

- Lateral support, to prevent out-of-plane displacement at the top of the column

Figure 5-1. Green Frame Test Setup (un-bolted to the hard floor)

5.4   Test Specimen

During the scaling process, the focus was on matching relevant parameters that control the inelastic behavior of wide flange steel elements (t_f/t_w, h/t_w, $b_f/2t_f$, and others) within 10% of the target values, as shown in Table 1. The length of the experimental specimen was considered the same as the column specimen tested at Buffalo, which the height of the prototype column from top of the base plate to beginning of the panel zone region end was equal to 19.4 in. (corresponding to a prototype column height of 155.2 in.). The average yield strength of 50 ksi of a previous

experiment was considered (at NEES lab @Buffalo), which was obtained from six tensile coupon tests conducted with sections of flange and web procured during fabrication of the specimens.

For the top connection, in order to be able to impose the displacement at the tip, an end plate with a perpendicular attached plate was considered (like a T shape, Figure 5-2 (left).) In which they were stiffened with the use of triangular and rectangular plates. Also, to allow free and smooth displacement at the top of the column, roller bearings were attached to the stiffeners to be in contact with the lateral frame to prevent out-of-plane displacements (Figure 5-2 (right)).

Table 5-1. Cross section specification of the prototype column and test specimen

Specifications	b_f mm (in)	t_f mm (in)	$b_f/2t_f$	d mm (in)	h mm (in)	t_w mm (in)	h/t_w	t_f/t_w	I mm^4 (in^4)	A mm^2 (in^2)	Z mm^3 (in^3)
W36X652	447 (17.6)	90.0 (3.54)	2.49	1044 (41.10)	815 (32.1)	50.0 (1.97)	16.3	1.80	2.11E+10 (5.06E+4)	1.24E+5 (192)	4.77E+7 (2.91E+3)
Test Specimen	51 (2.0)	10 (0.40)	2.50	141 (5.56)	102 (4.02)	6.0 (0.25)	16.4	1.63	5.66E+6 (13.6)	1.88E+3 (2.91)	9.47E+4 (5.78)
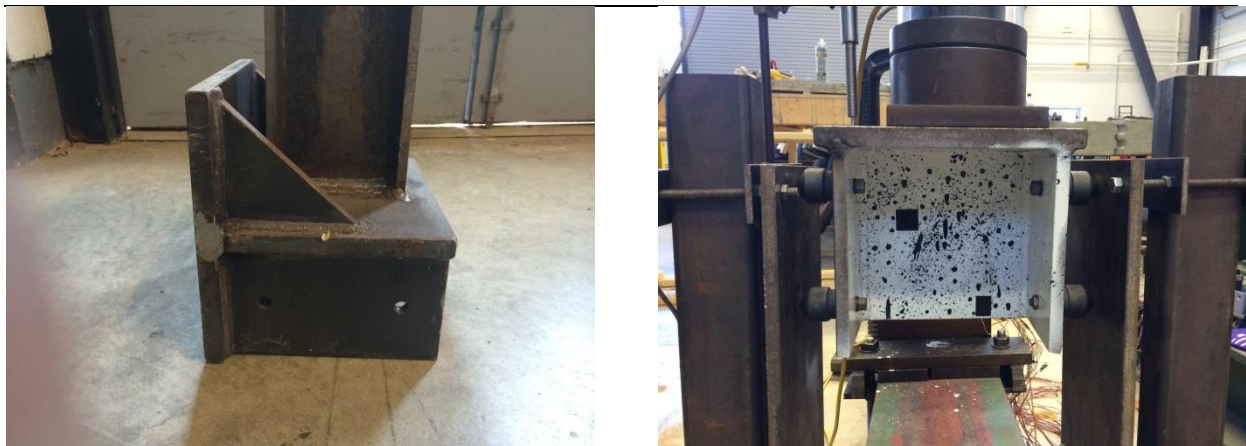
Figure 5-2. The connection of the tip of the column (left), assembled configuration in the setup

(right)

5.5   Loading protocol

A monotonic lateral displacement was applied to the tip of the beam (top beam attachment shown in Figure 5-2). The lateral displacement for the experiment is controlled with the stroke of the hydraulic piston. The available stroke of the piston is 6.25 in. If a 30% drift in the tip is considered the lateral displacement of the tip will be 5.82 in, in which is less than the stroke. This large drift will allow us to capture the inelastic parameters and behavior of the member. Also, we can observe more pronounce failure modes in the specimen.

5.6   Estimated Moment and shear capacity utilizing OpenSees

The estimated maximum plastic moment capacity can be calculated with the following Eq. 5-1.

$$M_{p,\max} = Z_x \cdot F_{u,\max} = 5.78(68) = 393 \text{ Kips} - \text{in} \tag{5-1}$$

The estimated shear capacity assuming the formation of plastic hinges at the bottom of the beam is as follow (Eq. 5-2):

$$V_{\max} = \frac{M_{p,\max}}{L} = \frac{(393)}{19.4} = 20.3 \text{ kip} \tag{5-2}$$

A numerical model of the scaled beam element was developed utilizing the Open System for Earthquake Engineering Simulation (OpenSees) Software (OpenSees, 2007b). Furthermore, a two dimensional Nonlinear Beam-Column Element with fiber sections was assigned to the member. A monotonic displacement was imposed to the tip of the numerical model. The shear and bending moment vs. drift at the base of the column are shown in Figure 5-3.
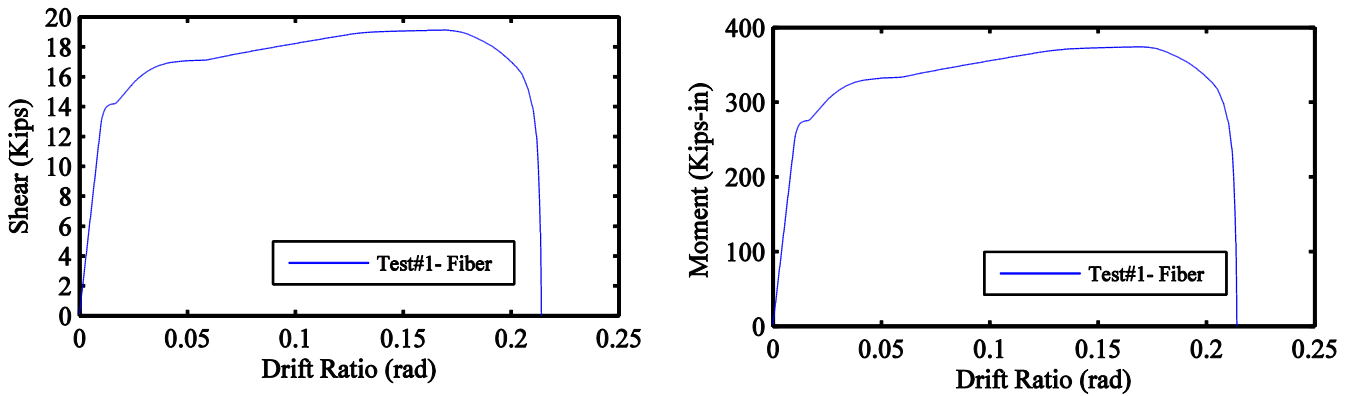
Figure 5-3. Shear-drift ratio (left) and moment-drift ratio (right) at the base of the beam from the

numerical model

5.7   Instrumentation

The displacement at the top of the column (in-plane and out of plane) was tracked with the use of Digital Image Correlation method (DIC). Two cameras where positioned, one capturing the vertical (lateral for the beam section) and out-of-plane displacement of the end plat of the tip, and the other capturing the web vertical and horizontal displacement.

Figure 5-4. Digital camera positions in the lab

Furthermore, a speckle pattern with the use of white and black paint was created on the surface of the end plate and the web (Figure 5-5). Moreover, the specimen was painted with white wash in order to detect damage. Also, to estimate the bending moment diagram and inelasticity over the length of the beam strain gauges were attached in different levels (Figure 5-6). The strain gauge layout are presented in the Appendix 5.
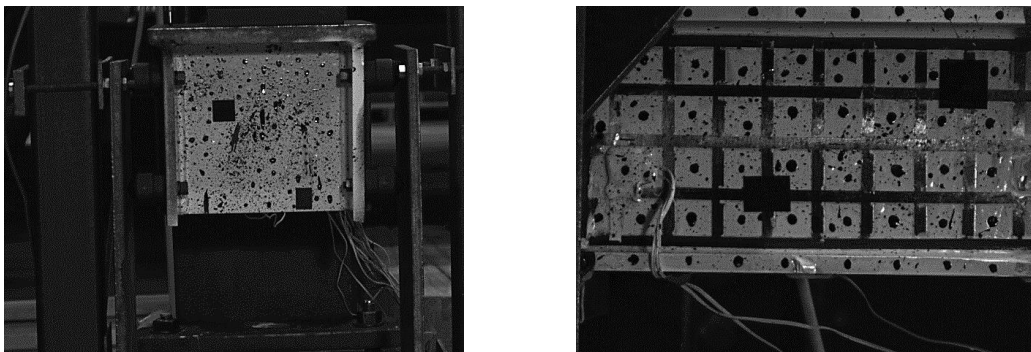
Figure 5-5. Speckle pattern of the tip end plate (left) and web (right)

Figure 5-6. Strain gauges over the length and white wash

The load is measured with the use of a load cell, which was positioned below the piston. In order to ensure the full contact during the experiment, a PVC sleeve was fabricated. An LVDT was placed at the top of the bracket to measure the out-of-plane displacement due to the imposed moment at the base of the column.

Figure 5-7. The load cell and fabricated sleeve (left), LVDT at the bracket (right)

Three video cameras were positioned in different view angles to capture the experiment during the test. The experiments videos have been upload to YouTube. The videos could be found in the following links.

https://www.youtube.com/watch?v=yVEnZpWp9-w&feature=youtu.be

https://www.youtube.com/watch?v=_8k7aKoNQrQ&feature=youtu.be

5.8   Elastic Test

The yield bending moment can be defined according to Eq. 5-3.

$$M_y = F_y S_x = 50 * 4.91 = 246 kips.in \tag{5-3}$$

If the column is assumed to deflect in perfect single-curvature bending, the yield deformation would be (Eq. 5-4)

$$\delta_y = \frac{M_y L^2}{3EI} = \frac{246 * 19.4^2}{3 * 29000 * 13.63} = 0.08 \, in$$

$$\tag{5-4}$$

So, for the elastic test a displacement about 30% of the yield displacement would be appropriate for calculating the stiffness of the specimen. Though, prior to the test a 0.025 in displacement was imposed and the force was measured with the load cell. Figure 5-8 shows the lateral stiffness of the specimen is consistent with the numerical prediction. The minor differences are due to the resolution of the load cell as it has a high capacity which it is less sensible to low magnitude forces. Also, theoretically the base of the column is considered fixed; however, the flexibility of the bracket (despite its stiffeners) may induce a relatively small rotation.

144
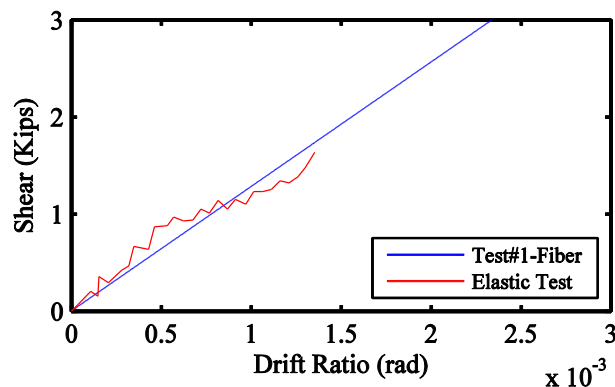
Figure 5-8. Shear-drift ratio of the elastic test and numerical model

5.9 Experiment Results for Test 1

The shear-drift ratio (left) and moment-drift ratio (right) relationship of the test is presented in Figure 5-9. The shear force is measured with the load cell in which it is positioned at the tip of the beam. Furthermore, the moment in the base of the beam is calculated in accordance to the measured force from the load cell times the distance from the tip to the base (beams height and half of the thickness of the attached plate to the tip). There is a 6% difference between the maximum shear capacity and bending moment from the experiment compared to the numerical model.
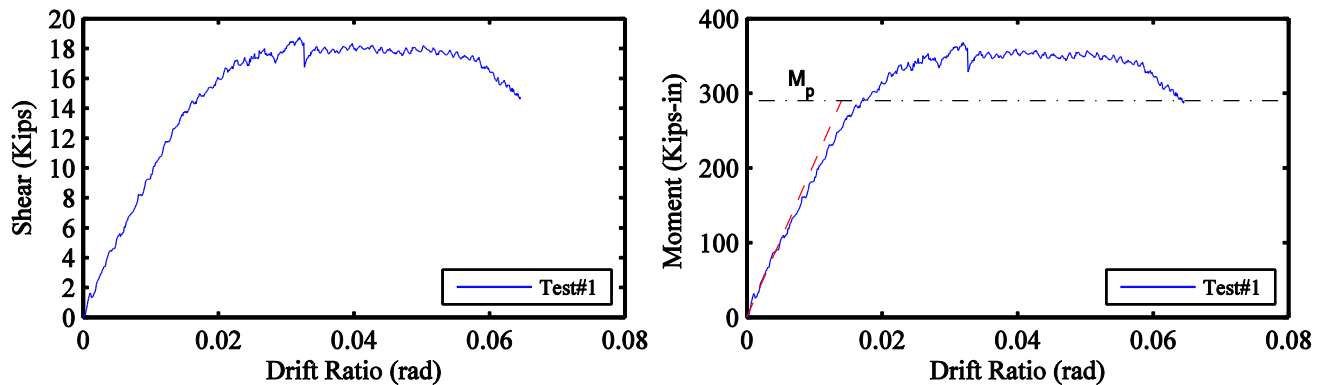
Figure 5-9. Shear-drift ratio (left) and moment-drift ratio (right) at the base of the beam

The overall shapes and the magnitude of the shear and bending moment developed from the experiment is in a good agreement with numerical simulation, but there is a difference in the rotation capacity. This difference originated from the fact that the 2D numerical model cannot capture lateral torsional buckling (Figure 5-10 (left)) which were experienced by the beam in the tests.

During the test, the dominant failure mode was lateral torsional buckling (see Figure 5-10). This failure mode is responsible for the instability and reduction in the lateral capacity of the member. A more detailed investigation on the failure more is presented in the following section. Also, the vertical and out-of-plane displacement in the tip of the column is shown in Figure 5-10 (right). The effect of out-of-plane displacement at about 3% drift could be seen as a drop in the magnitudes of shear and moment plots presented in Figure 5-9.
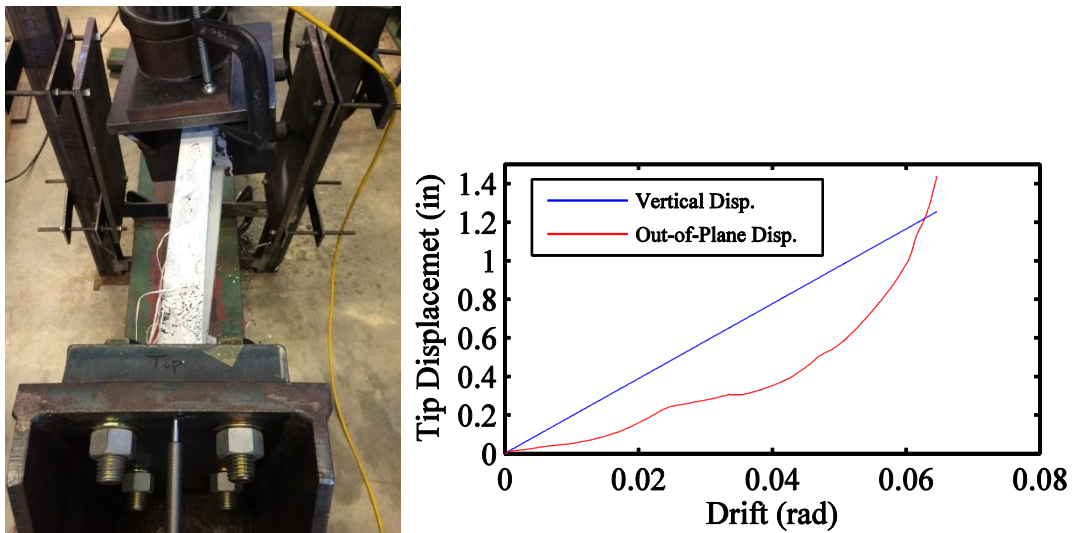
Figure 5-10. Lateral torsional buckling in the test specimen (left), displacement vs. drift at the tip (right)

The test had to be stopped before reaching the maximum stroke of the hydraulic piston due to the failure of the supporting clamp of the lateral frame Figure 5-11.

Figure 5-11. Lateral Frame (left), damaged clamp (right) at the end of the experiment

5.10 Inelastic Lateral Torsional buckling

The member was designed to be able to undergo significant plastic deformation. So, the width/thickness ratio of the flange and the height/thickness of the web were limited to the specified equations according to AISC-360-10 (TABLE B4.1) (Design-AISC) and AISC-341-10 (TABLE D1.1) (AISC, 2010) as shown in Table 5-2.

Table 5-2. Limiting width-thickness ratios

	Test Specimen	AISC-360-10 (TABLE B4.1)	AISC-341-10 (TABLE D1.1)
$b_f/2t_f$	2.5	$\lambda_p = 0.38\sqrt{E/F_y} = 9.2$	$\lambda_{hd} = 0.3\sqrt{E/F_y} = 7.2$
h/t_w	16	$\lambda_p = 3.76\sqrt{E/F_y} = 91$	$\lambda_p = 1.49\sqrt{E/F_y} = 36$

Furthermore, in order to achieve adequate strength and rotation capacity the unbraced length of the beam ($L_b = 19.4\ in$) was limited to the length of L_p (Eq.5-5) (AISC-360-10 (Eq. F2-5)).

Figure 5-12, illustrates that the nominal plastic moment (M_n) will reach the plastic moment capacity ($M_p = F_y Z_x = 50 \times 5.78 = 289 \; kip-in$) with large plastic rotation capacity ($R \geq 3$) if the lateral unbraced length does not exceed L_{pd} (Eq. 5-6) (AISC-360-10 (Eq. A-1-7)) (Salmon et al., 2009).

According to the moment-drift relationship of the experiment presented in Figure 5-9 (right), the moment exceeds the plastic moment capacity. Furthermore, the estimated plastic rotation capacity is more than 3 times of the rotation corresponding to the plastic moment capacity. Therefore, the specimen is experiencing inelastic lateral torsional buckling. The increase in the magnitude of moment in the inelastic region is due to the hardening and spread of inelasticity over a length.

$$L_p = 1.76 r_y \sqrt{\frac{E}{F_y}} = 21.5 \; in \tag{5-5}$$

$$L_{pd} = r_y \frac{3500 + 2200 \, M_1 / M_p}{F_y} = 35.9 \; in \tag{5-6}$$
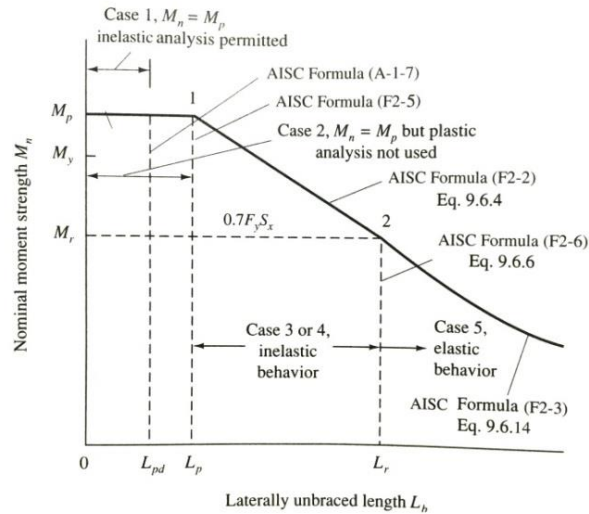
Figure 5-12. Nominal Strength M_n of "compact" sections as affected by lateral torsional buckling (Salmon et al., 2009).

5.11 Strain Data

The measured strain data in different levels of the length of the beam are plotted in Figure 5-13 (left) and Figure 5-14 (left). The inelasticity in the beam is concentrated in the bottom half of the member and mostly near the base of the beam (strain gauge T5 and B5 at 1.0 in from the base). The strain data is consistent with the observed damage in the specimen (Figure 5-18). The obtained bending moment from the strain gage data and calculated from the kinematics (measured load cell force times the distance of each level of strain gauge to the load cell) has the same trend and magnitude in the elastic range for each level. However, in the elastic range level 1 (at ¾ of the

149

height from the base) the moments are deviating. This difference could be the resultant of lateral torsional buckling and out-of-plane displacement in at the tip of the column. The strain gauges layout and positions are presented in the Appendix 5.
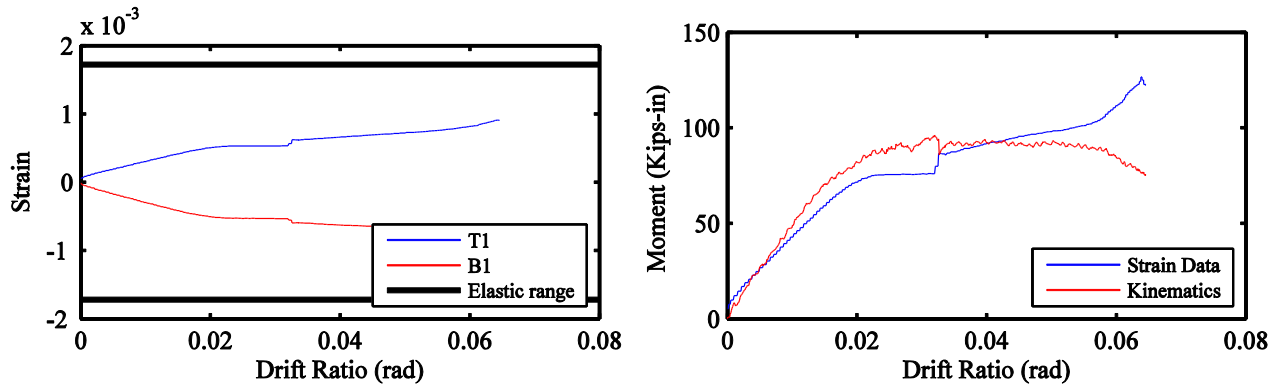
Level 1- at ¾ of the height from the base
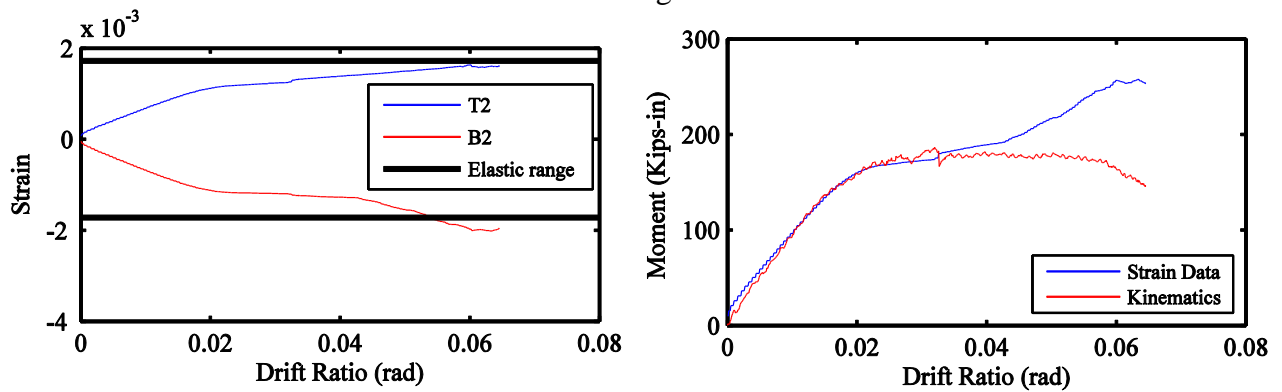
Level 2- at ½ of the height from the base
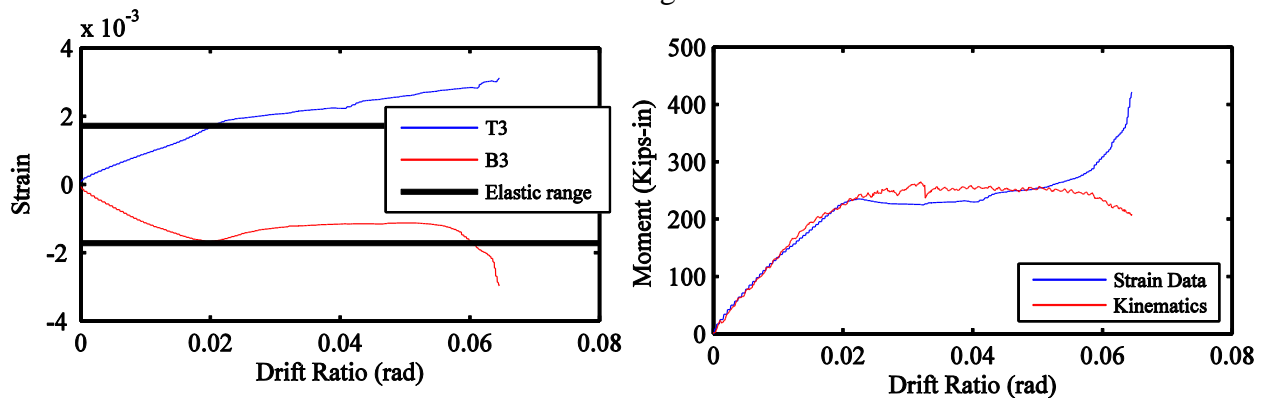
Level 3- at 5.5 in (equivalent to the depth of the beam section) from the base
Figure 5-13. Measured strain in the top (T) and bottom (B) flange strain gauges (left), calculated moment from strain gauges vs. moments calculated according to kinematics (right) in different levels of strain gauges

Level 3- at 5.5 in (equivalent to the depth of the beam section) from the base

Level 4- at 1.0 in from the base
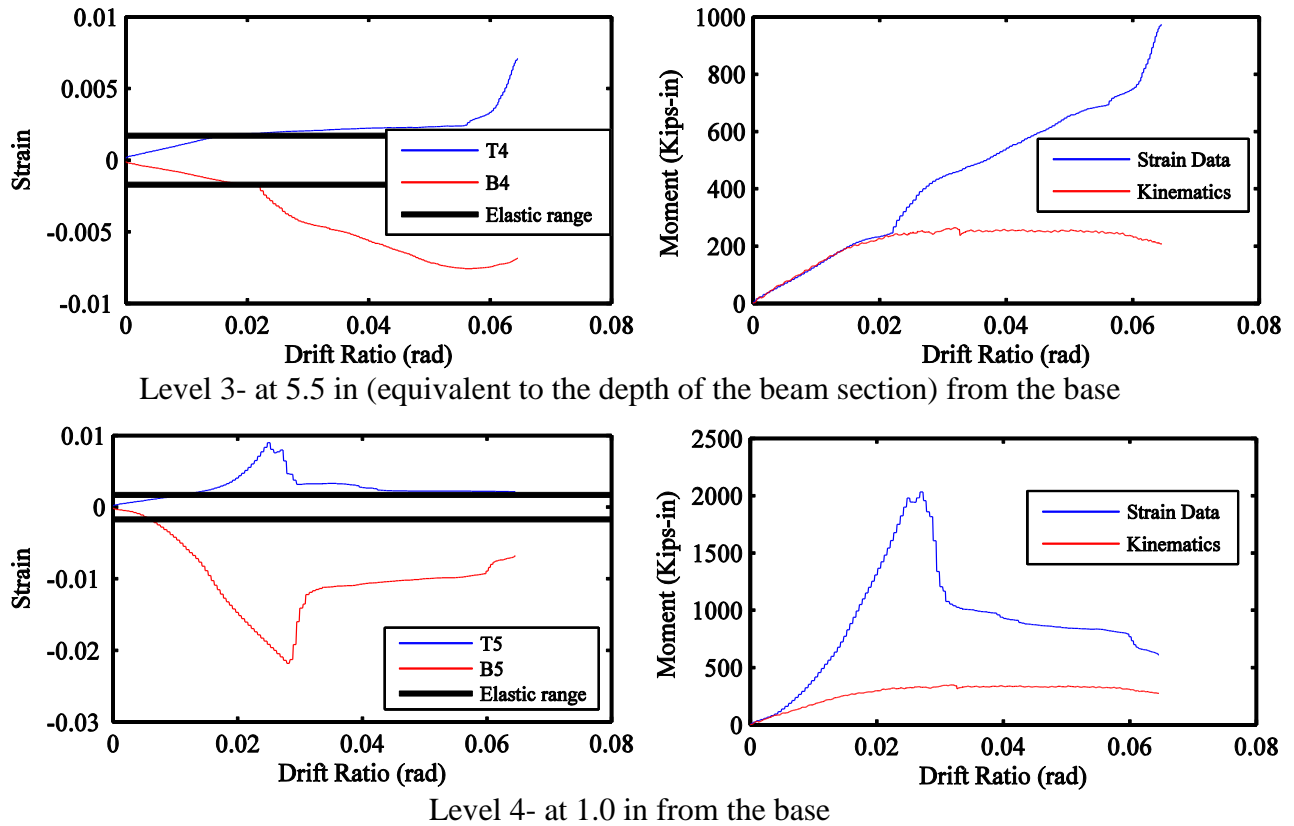
Figure 5-14. (Continued) Measured strain in the top (T) and bottom (B) flange strain gauges (left), calculated moment from strain gauges vs. moments calculated according to kinematics (right) in different levels of strain gauges

5.12 Experiment Results for Test 2

The shear-drift ratio (left) and moment-drift ratio (right) relationship of the test is presented in Figure 5-15. The setup was modified for the second experiment, by welding the lateral frame to the support beam as shown in Figure 5-17. The shear force is measured with the load cell in which it is positioned at the tip of the beam. Furthermore, the moment in the base of the beam is calculated in accordance to the measured force from the load cell times the distance from the tip to the base (beams height and half of the thickness of the attached plate to the tip). The experimental value of the effective yield strength is about 395 Kip-in which is greater than the estimated theoretical value of 289 Kip-in (Figure 5-15). This difference is due to the fact that the inelasticity in the test

151

specimen is not concentrated in only one location among the length and it spreads out throughout

a length due to the moment gradient. The spread of inelasticity and strain hardening increased the

magnitude of M_p about 36%.
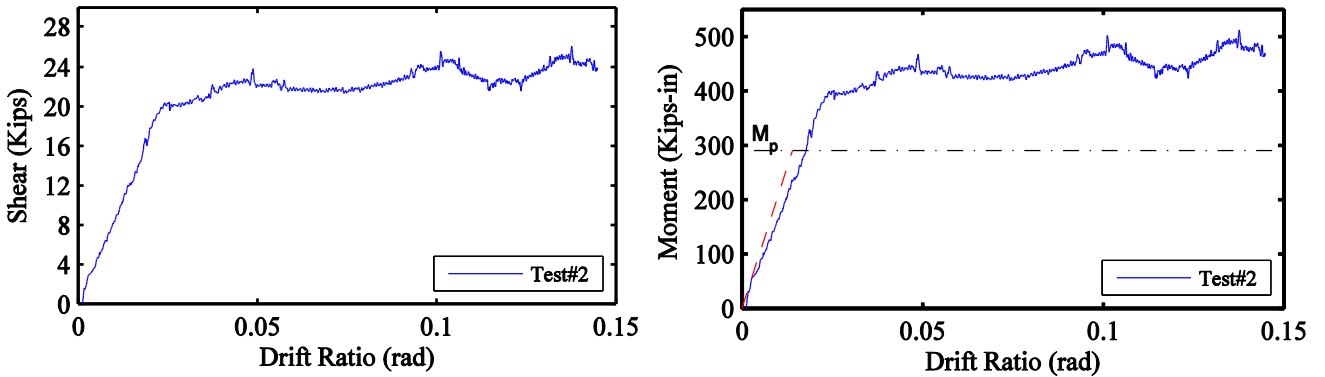
Figure 5-15. Shear-drift ratio and moment-drift ratio at the base of the beam for Test 1 and 2

During the test, the dominant failure mode was lateral torsional buckling (Figure 5-17). This

failure mode is responsible for the instability and reduction in the lateral capacity of the member.

Also, the vertical and out-of-plane displacement in the tip of the column is shown in Figure 5-17

(right).

Figure 5-16. Lateral Frame welded to the support beam (left), zoomed in (right)
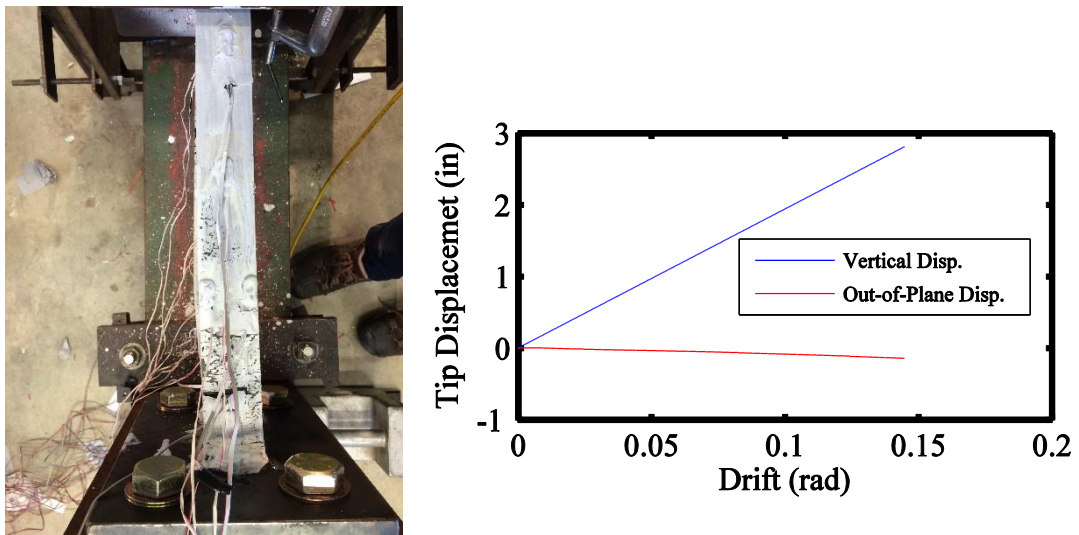
Figure 5-17. Lateral torsional buckling in the test specimen (left), displacement vs. drift at the tip

(right)

5.13 Quantification of the Backbone Parameters

Figure 5-18, shows the damage induced to the beam after performing the experiment. The flaking of the white wash and the strain data demonstrates that most of the inelasticity is concentrated in the base of the beam. In which, the beam can numerically be modeled with an elastic beam and a concentrated plastic hinge at the base. One of the existing numerical models that have the ability to account for asymmetric component hysteretic behavior and cyclic deterioration is the model developed by Ibarra-Medina-Krawinkler (IMK model) (Ibarra et al., 2005), which was modified by Lignos and Krawinkler (D. G. Lignos & Krawinkler, 2010). In this model the inelasticity is concentrated at specific locations in a structure while the rest of the structure remains elastic. Existing regression equations used to estimate the column and beam parameters that define this model do not include deep steel sections. A quantification of modeling parameters that are most relevant for collapse simulation is performed. These parameters, as they apply to local moment-rotation responses, include: elastic rotational stiffness (K_e), plastic rotation capacity (θ_p, difference between yield rotation and rotation at maximum bending moment), and the post-capping rotation (θ_{pc}, difference between rotation at maximum moment and rotation at complete loss of strength). Moreover, the quantification of additional modeling parameters such as the effective yield strength (M_{pe}) and the post-capping strength (M_{pc}, maximum moment) was also performed.
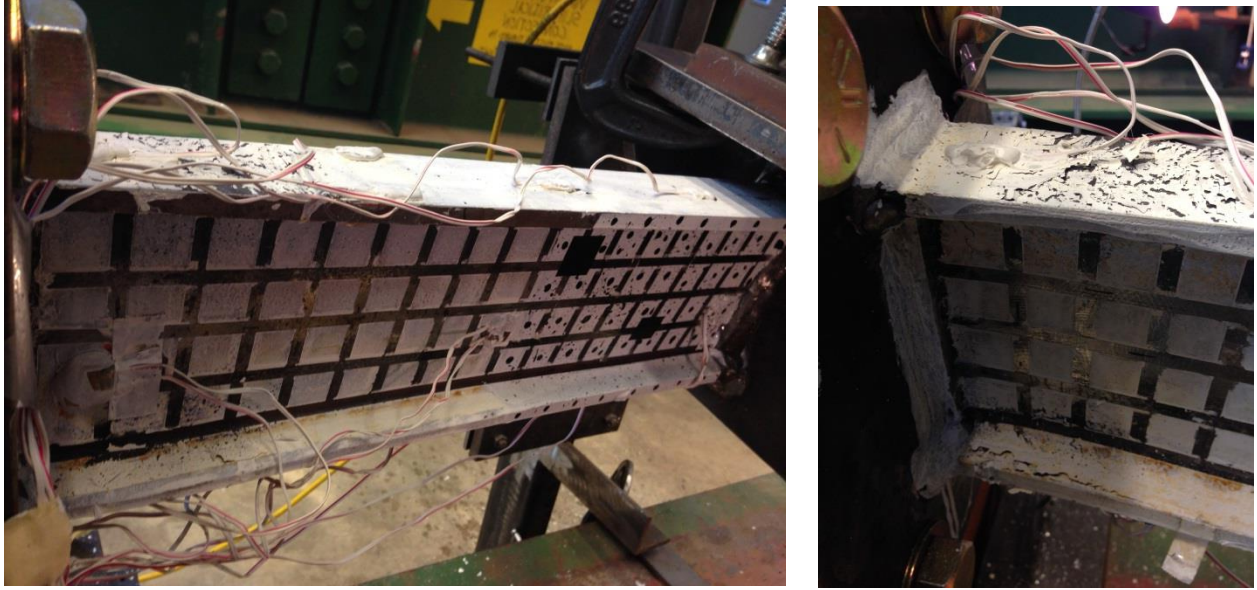
Figure 5-18. Concentrated damage in the base of the column (left), zoom in (right) (Test 1)

The moment-drift ratio response from the Test 1 is presented in Figure 5-19. The drift ratio is equivalent to the chord rotation, i.e., vertical displacement between the top and bottom of the beam divided by the length of the specimen. The elastic stiffness portion of the response was explained in section 5.8. According to the experiment moment-drift ratio, the plastic rotation capacities (θ_p, difference between yield rotation and rotation at maximum moment) of 0.04 rad is estimated. In this context, plastic rotation was estimated from drift ratios assuming that most of the inelasticity concentrates near the bottom of the column. For a W36X652, ASCE-SEI 41 (ASCE, 2007) estimates a plastic rotation capacity of 0.042 rad. Moreover, the plastic rotation capacity according to an extrapolation of the regression equation for W-sections for beams developed by Lignos (D. G. Lignos & Krawinkler, 2010) would result in a value of 0.04 rad. These results indicate that for the W36X652 beam section, the plastic rotation capacity estimated based on available equations are in a good agreement for this parameter with respect to this experiment.

The primary failure mode of the specimen is lateral torsional buckling. The onset of lateral torsional buckling takes place right at the point of maximum bending moment in the response. A well-defined negative slope after the point of maximum moment (i.e., post-capping slope) is attained, which demonstrated the effect of lateral torsional buckling on the behavior of the specimen. The post-capping rotation for constant axial load (θ_{pc}, difference between rotation at maximum moment and rotation at complete loss of strength) was estimated as 0.05 rad. The extrapolation of the regression for post-capping rotation for W-sections for beams developed by Lignos (D. G. Lignos & Krawinkler, 2010) evaluates a value of 0.44 rad. The difference in the post-capping rotation is due to the loss of support in the lateral frame and allowing out-of-plane movement in the tip of the beam for Test1 with respect to Test2.

The spread of inelasticity and strain hardening increased the magnitude of effective yield strength (M_{pe}) about 14% and 36 % compared to the plastic moment capacity (M_p=290 kip.in) for Test 1 and Test 2, respectively. Furthermore, the measured strain hardening ratio (the hardening stiffness to elastic stiffness) is 3.7% for Test 1 and Test 2, which is less than the experimented columns @Buffalo due to the fact that the spread of inelasticity is more concentrated around the base than over the length and different boundary condition, Figure 5-21.

The fitted backbone for Test 2 is shown in Figure 5-20. The elastic slope as well as hardening slope are consistent with Test1 experiment. The experiment was terminated before reaching the post-capping strength (M_{pc}, maximum moment), due to limitation of piston stroke. There is no evidence of post capping slope in Test 2 even after reaching a plastic rotation of 0.12 rad. In the column experiments, the maximum plastic rotation capacity was 0.08 rad for the monotonic test with constant axial force of 31% of the axial load carrying capacity performed @ Buffalo, which the direct effect of axial load on the plastic rotation capacity could be noticed. The applied axial

load accelerated and induced web and lateral torsional buckling mode with respect to the beam experiment (Test 2) which did not experience post-capping slope even after a plastic rotation of 0.12 rad.
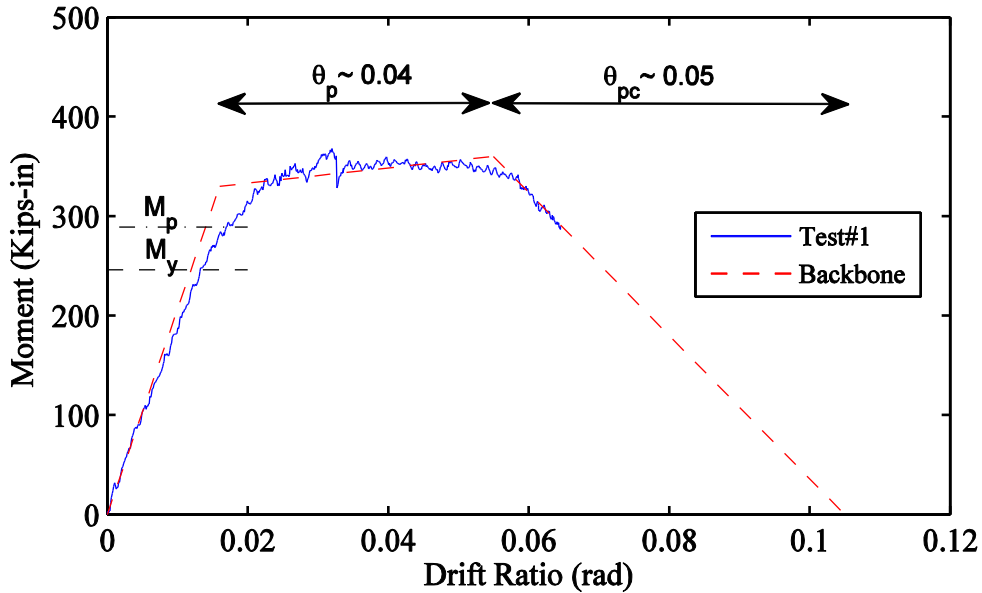
Figure 5-19. Moment- drift ratio relationship at the base of the beam (Test 1) and the backbone
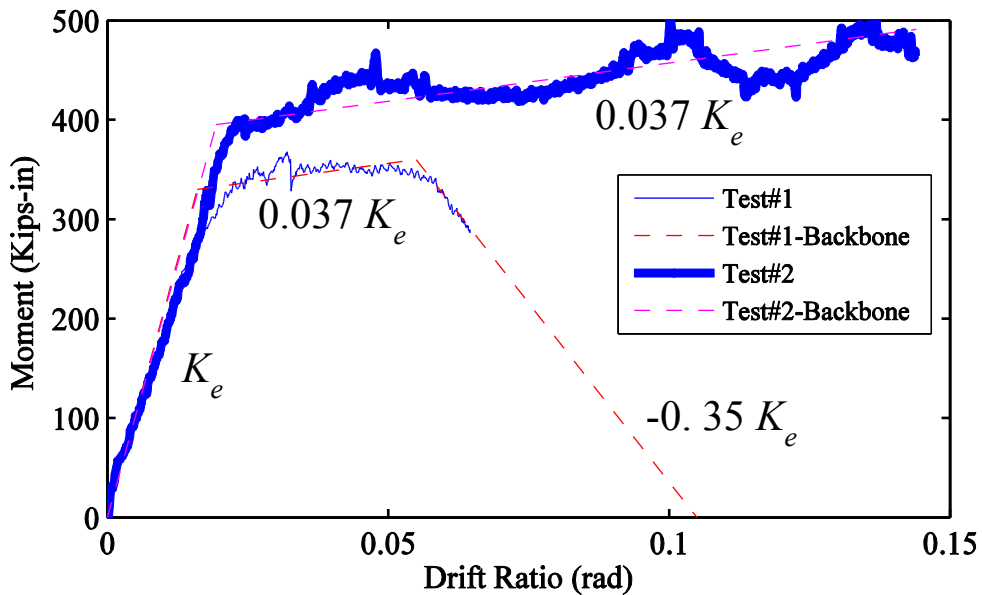
Figure 5-20. Moment- drift ratio relationship at the base of the beam (Test 1 and Test 2) and the backbone
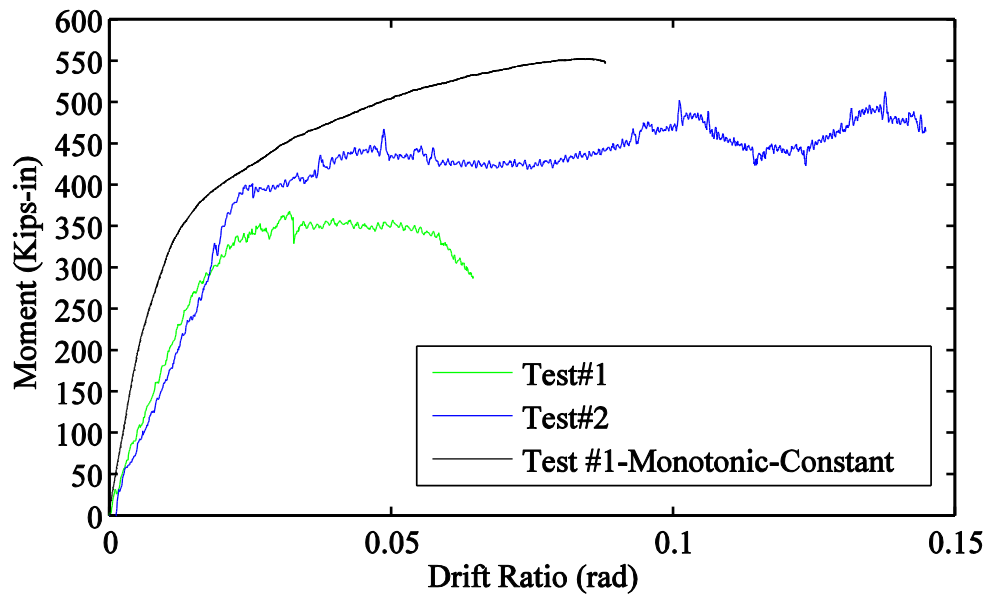
Figure 5-21. Moment- drift ratio relationship at the base of the beam (Test 1 and Test 2) and column Test 1 performed @ Buffalo

5.14 Summary and Conclusions

An experimental program was implemented in order to study the inelastic behavior of cantilever beams under lateral load. Two beam specimens with a 1:8 scaled W36X652 sections were fabricated. The setup (green frame) was modified and the required elements for the experiment were made (bracket, lateral frame and sleeve). For the first experiment (Test 1), the specimen was pushed to 0.07 rad drift, and due to the failure of the attachment of the lateral frame (clamp), the test was executed before reaching the target displacement. For Test 1, the estimated plastic rotation capacity of 0.04 rad is in a good agreement with the predicted values from the existing equations (ASCE, 2007; D. G. Lignos & Krawinkler, 2010). However, the post-capping rotation (0.05 rad) is significantly smaller than the regression equations, which is due to the damage in the lateral frame and unwanted out-of-plane displacement at the tip.

For the second experiment (Test 2), the lateral frame was welded to the supporting beam in order to prevent sideways movement at the tip of the beam (the loading of the beam is applied vertically). The measured strain hardening ratio (the hardening stiffness to elastic stiffness) is 3.7%, which is consistent with Test 1. The experiment was terminated before reaching the post-capping strength (M_{pc}, maximum moment), due to limitation of piston stroke. The plastic rotation capacity of 0.08 rad was obtained from column experiment of monotonic test with constant axial force of 31% of the axial load carrying capacity performed @ Buffalo. The applied axial load accelerated and induced web and lateral torsional buckling mode with respect to the beam experiment (Test 2) which did not experience post-capping slope even after a plastic rotation of 0.12 rad. The dominant failure mode were inelastic lateral torsional buckling for both experiments.

5.15 References

AISC. (2010). Seismic Provisions for Structural Steel Buildings, ANSI/AISC 341-10 2010: American Institute of Steel Construction, Chicago, Illinois.

ASCE. (2007). Seismic Rehabilitation of Existing Buildings, ASCE/SEI 41-06 *American Society of Civil Engineers, Reston, VA, US*.

Design-AISC, S. 360-10 9 Steel Design-AISC 360-10. *Steel Design per AISC*, 360-310.

Ibarra, L. F., Medina, R. A., & Krawinkler, H. (2005). Hysteretic models that incorporate strength and stiffness deterioration. *Earthquake engineering & structural dynamics, 34*(12), 1489-1511.

Lignos, D. G., & Krawinkler, H. (2010). Deterioration modeling of steel components in support of collapse prediction of steel moment frames under earthquake loading. *Journal of Structural Engineering, 137*(11), 1291-1302.

OpenSees. (2007). Open System for Earthquake Engineering Simulation, Pacific Earthquake Engineering Research Center (PEER), (http://opensees.berkeley.edu).

Salmon, C. G., Johnson, J. E., & Malhas, F. A. (2009). *Steel Structures: Design and Behavior : Emphasizing Load and Resistance Factor Design*: Pearson/Prentice Hall.

Zargar, S., Medina, R., & Miranda, E. (2014). Cyclic behavior of deep steel columns subjected to large drifts, rotations, and axial loads. *Proceedings of the 10th National Conference in Earthquake Engineering, Earthquake Engineering Research Institute, Anchorage, AK*.

6 NUMERICAL STUDIES OF DEEP STEEL COLUMNS SUBJECTED TO VARIOUS LOADING HISTORIES

Shokoufeh ZARGAR[1], Ricardo A. MEDINA[2], Erin BELL[3]

6.1. INTRODUCTION

Deep steel column sections could be used as exterior columns in moment-resisting structures. During an earthquake, exterior columns should carry its own tributary gravity load in addition to the axial load demands induced by overturning moments. Experimental data on deep steel column sections is limited. In the absence of experimental data, high fidelity numerical models are the best alternative tool to investigate and understand the behavior of components. The behavior of the deep steel columns can be studied by calibrating finite element models based on

[1] Ph.D. Candidate, Dept. of Civil and Environmental Engineering, University of New Hampshire, Durham, NH 03824,Tel : (603) 913-4578, Fax: (603)862-2364, E-mail: sxu6@unh.edu

[2] Staff Consultant, Simpson Gumpertz & Heger Inc., Waltham, MA, USA

[3] Professor, Dept. of Civil and Environmental Engineering, University of New Hampshire, Durham, NH 03824, Tel: (603) 862-0276, Fax: (603) 862-2364, E-mail: Erin.Bell@unh.edu

existing experimental subjected to various loading histories (various levels of axial load drift and rotation demands). The calibrated numerical models can be used for performance prediction of deep column section, especially valued in seismic design and assessment.

Newell and Uang (James D Newell & Uang, 2006), performed a parametric study of commonly used column cross sections (W12, W14), and deep column section (W18, and W24). They observed, a prompt strength degradation for the deep steep column sections due to flange and web local buckling, and interaction of buckling modes, which resulted in a decreased inter story drift capacity. Elkady and Lignos (Elkady & Lignos, 2015), analytically investigated deep steel column section which included W36 cross sections as well. The simulations consisted of symmetric cyclic lateral loads combined with compressive axial load levels up to 50% of the axial strength. A flexible beam with a pre-defined moment of inertia was included to the upper side of the column, to account for tip rotation which kept the inflection point at a distance of 0.75 of the length of the column. Further study was carried out by Fogarity and El-tawil (Fogarty & El-Tawil, 2014), on deep and slender sections under combined axial and lateral loading (simulated as perfect double curvature). The results indicated that due to local buckling as well as lateral torsional buckling, a considerable reduction in column ductility was observed. In the numerical simulation performed by Elkady and Lignos (2015), the effect of cyclic hardening on the flexural strength of the beam-column with a W36x650 section has been studied. The ratio of maximum moment, M_{max}, to the plastic flexural strength, M_p, for a symmetric cyclic lateral displacement, controlled rotation to keep the inflection point at a distance of 0.75 of the column length from the base of the column, and constant compressive axial load of 0, 20, 35, and 50% P_y, was 1.9, 1.6, 1.4, and 1.2, respectively.

In this chapter, the calibration of the numerical models simulated with Abaqus (2017) using the experiments data presented in the previous chapters are discussed. The experiments were simulated using the following modeling methods. (i) Modeling of the isolated column and applying the displacement, rotation, and loading histories with appropriate boundary conditions at the tip and base of the column. In the numerical model, for the single column model, the resultant loading and deformation histories were imposed at the boundary conditions, in which they were developed using transformation equations considering geometric nonlinearities in the setup and measured forces and displacements. (ii) Modeling of the entire three-actuator setup where the loading and displacement histories were applied through connector elements representing the actuators. The advantage of the later modeling approach is that there is no need for the transformation of the measured (or applied) actuator forces and displacements to calculate the resultant forces, moments and displacements at the tip of the column. By modeling the entire setup, the effect of geometric nonlinearities will be incorporated directly.

6.2.   Numerical Model Description

In the current study, the numerical model calibration was performed using two separate methods. First, the isolated column was modeled, and the representative boundary conditions and loading histories were applied to the tip and base of the column. Second, the entire setup consisting of all three actuators and the column was modeled numerically.

The modeling details of each of these models are discussed in the following.

- Isolated column model

The column was modeled using shell elements for the flanges and the web, Figure 6-1. The use of shell elements is computationally less expensive than solid elements. Shell elements

better account for the bending response in thin sections of the members. Shell elements are capable of carrying bending moment within the thickness of a single element while considering a single solid element through the thickness is not able to capture and resist bending (Simulia, 2017). The shell element used in this research was the general-purpose shell element type S4R which is a 4-node doubly curved general-purpose shell, reduced integration with hourglass control, finite membrane strains. This element allows transverse shear deformation.

For modeling the column cross-section, the flanges inner plate surface was modeled, and an offset towards the outer surface is considered to account for the shell thickness, shown in Figure 6-2. This method of modeling will prevent overlapping of the flanges with the web and the addition of unnecessary stiffness. For the web, the plate reference surface is modeled at the mid-thickness of the web considering thickness offset on both sides. At the intersection of the web and flanges, the thickness of the web increases. The radius where the web intersects the flanges is called the "K-region". In this study, the geometry of the K-region was assumed to be elliptical and the change of thickness of the web is considered in the numerical model, which resulted in an increase of the overall cross-section strength and the stiffness.

The top and bottom edge of the cross-section shell elements are coupled with two separate reference points (RPs), and the boundary conditions and loading histories are applied to the corresponding reference points.

- Three-actuator model

The entire experimental setup of the column test shown in Figure 6-3 was modeled in Abaqus, Figure 6-4. A similar approach as described for the isolated column was considered for modeling the column in the Three-actuator model. In order to model the connection of the

164

column to the loading beam, a rigid box using shell elements was modeled with its height equivalent to half of the loading beam depth plus the thickness of the base plate at the top of the column. The width and depth are equal to the column depth and base plate depth, respectively.

The actuators' behavior was modeled using an AXIAL connector element between the pins of the end swivels. For the loading beam, three rigid BEAM connector element was utilized through the length as follow: (i) from the horizontal actuator swivel pin (the swivel attached to the loading beam) to the intersection of the north actuator axis (left vertical actuator), (ii) from the intersection of the south actuator axis (left vertical actuator) to the top left corner (mid-depth) of the rigid box, and (ii) from the top right corner (mid-depth) of the rigid box to the intersection of the south actuator axis (right vertical actuator), see Figure 6-5. The drawing with dimensions are presented in Appendix 6.

To account for the depth of the loading beam, a rigid BEAM connector element is modeled with a length equal to half of the depth of the loading beam plus the depth of the top swivel (up to the swivel pin) of the vertical actuators. For the connection of the BEAM connector elements to the AXIAL connector elements, pin Multi Point Constraints (MPC pin) are utilized, which allows in-plane rotation. Further, for the intersection of the loading beam and the connector elements representing the beam depth and the rigid box, MPC Tie constraints are utilized to simulate a rigid connection. In the numerical model, the lateral movement at the support of the horizontal actuator due to the flexibility of the yellow frame is simulated by modeling a uniaxial spring at the base of the actuator. The stiffness of the lateral reaction frame at the location of the horizontal actuator (305 kips/in), Figure 6-6, was calibrated by the relationship of horizontal displacement of the yellow reaction frame measured by a string pot attached to it (up to 0.04 in.) and the measured force from the horizontal actuator load cell of the monotonic-constant test

165

(Test 1). The vertical and out-of-plane displacements are restraint against movement, and it is allowed to rotate in-plane. The vertical actuator supports are restrained against displacement and rotation in all directions, except they are free to rotate in-plane. Also, a uniaxial spring is modeled to account for the flexibility of the pedestal of the column in the numerical simulation. The stiffness of the spring (502 kips/in) is calibrated using the measured displacements from the KRYPTON device and calculated lateral force at the support of the column for the elastic test (before testing every specimen, a set of elastic experiments were performed) as shown in Figure 6-6.
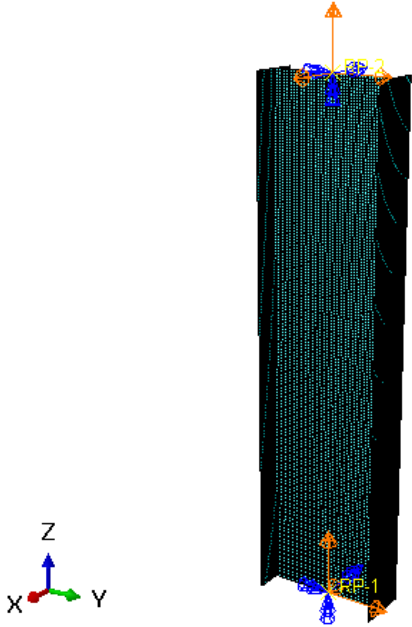
Figure 6-1. Numerical model of isolated column using shell elements

Depth 5.56 in

Ellipse K region
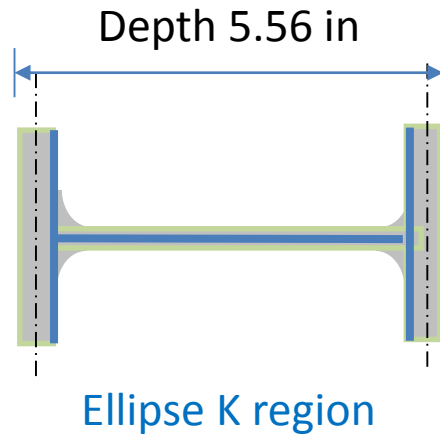
Figure 6-2. Reference surfaces considered for the shell model of the column
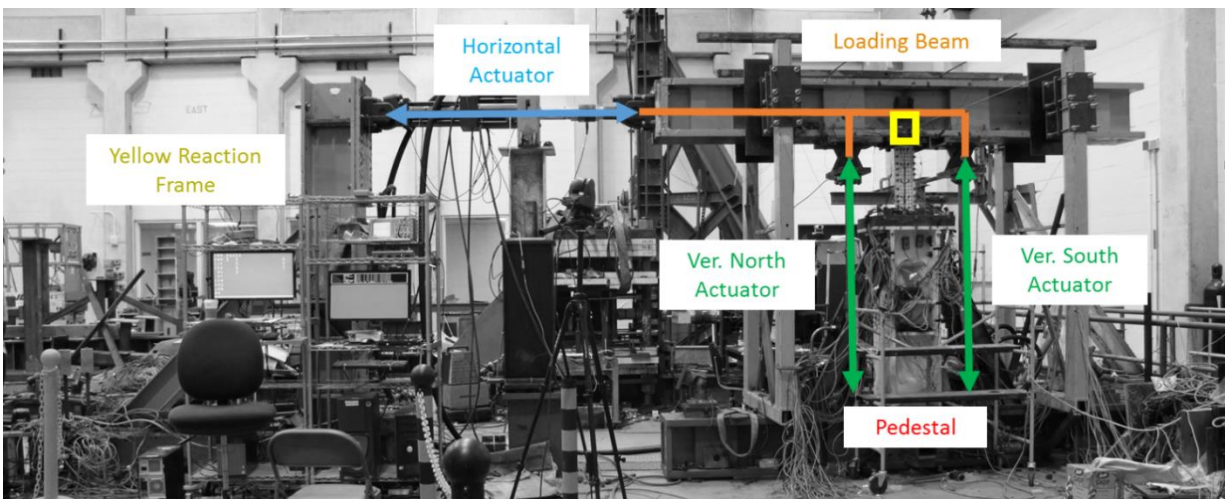
Figure 6-3. Entire experimental setup and description of components
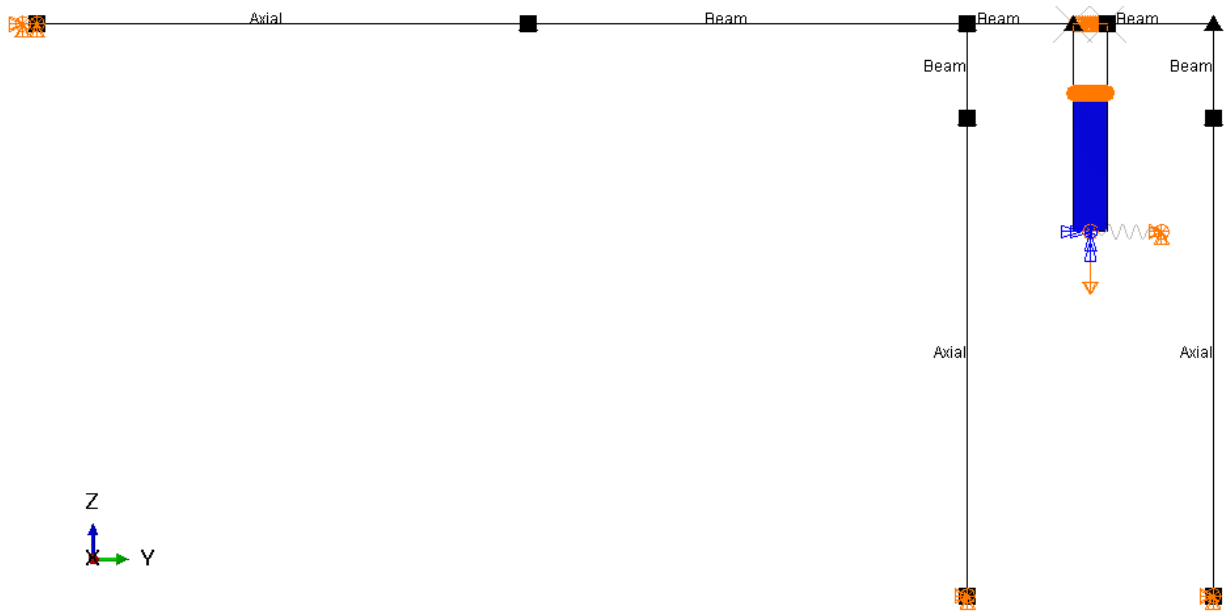
Figure 6-4. Three-actuator setup simulated in Abaqus
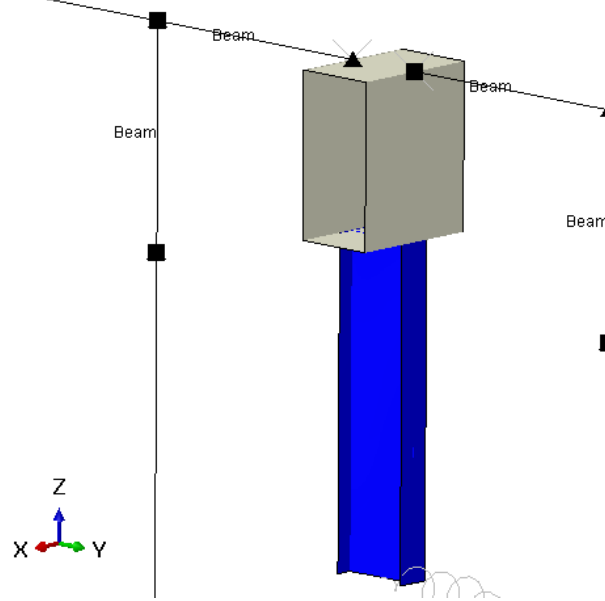
Figure 6-5. Three-actuator setup simulated in Abaqus (closer view)
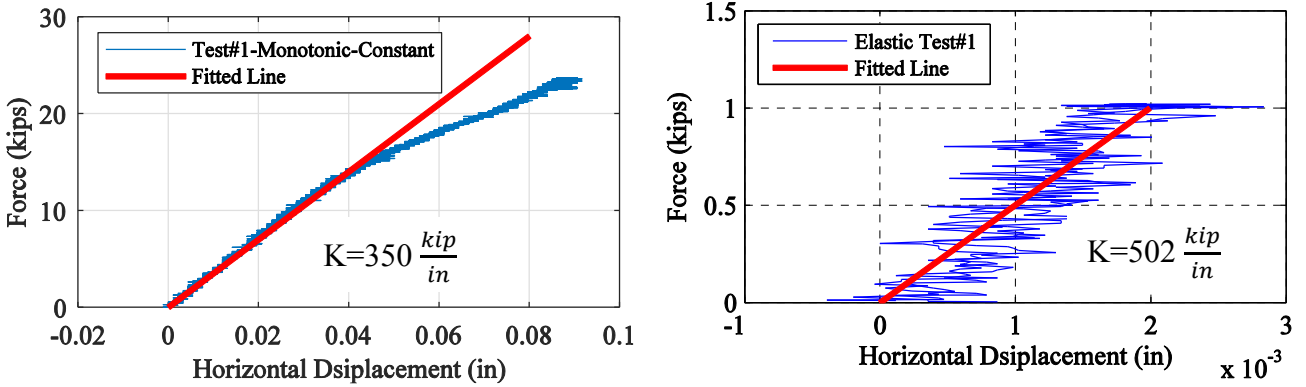
Figure 6-6. Horizontal actuator Force vs. yellow reaction frame horizontal displacement of the monotonic-constant test (Test 1, left) and Elastic test (left)

6.3. Material Properties

A total of six coupons were fabricated from the flanges and webs of the same steel section that was used to fabricate the experimental specimens. For the monotonic numerical simulations, the true stress (σ_T) vs. true strain (ε_T) curve was obtained using Eq. 6-1 and Eq. 6-2 from the engineering (nominal) stress (σ) and strain (ε) measured data of a representative tensile coupon test experiment.

$$\sigma_T = \sigma(1 + \varepsilon) \tag{6-1}$$

$$\varepsilon_T = \ln(1 + \varepsilon) \tag{6-2}$$

For the elastic region, a modulus of elasticity of 29,000 ksi, and Poisson ratio of 0.3 were considered. For defining the parameters of the plasticity model in Abaqus, the post-yield behavior was extracted from the true stress-strain curve shown in Figure 6-7.

169
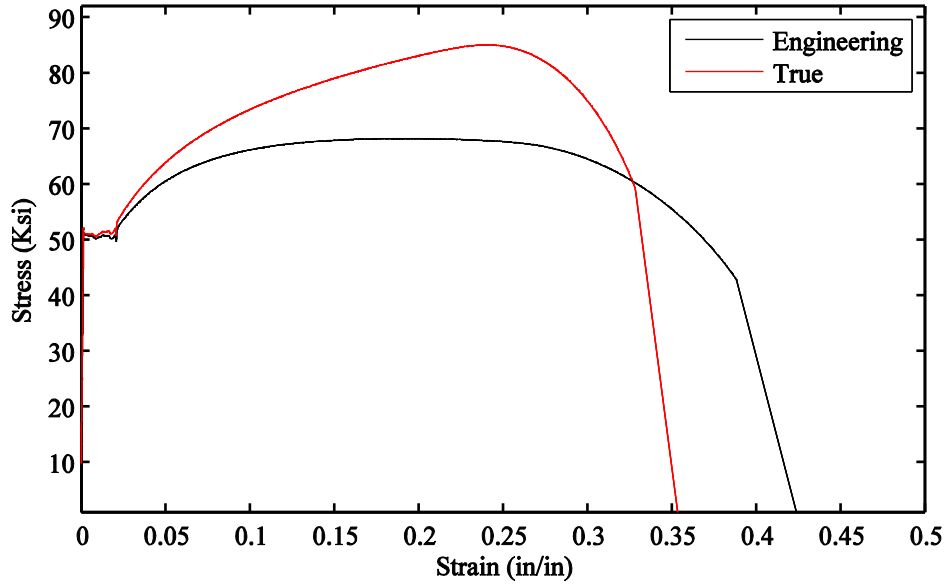
Figure 6-7. Engineering and true stress-strain curve used

For the cyclic experiments, the nonlinear isotropic/kinematic hardening Chaboche and Lemaitre (1990) model in Abaqus is used for defining the material properties. The size of the yield surface, σ^0, is defined in Eq. (6-3), which is a function of equivalent plastic strain $\bar{\varepsilon}^{pl}$. The yield surface size at zero plastic strain and the maximum change in the yield surface are defined as Q_∞ and $\sigma|_0$, respectively. The rate at which the size of yield surface changes as plastic deformation develops is controlled by the parameter b. The kinematic hardening law is shown in Eq. 6-4.

$$\sigma^0 = \sigma|_0 + Q_\infty(1 - e^{-b\bar{\varepsilon}^{pl}}) \tag{6-3}$$

$$\dot{\alpha} = C\frac{1}{\sigma^0}(\sigma - \alpha)\dot{\bar{\varepsilon}}^{pl} - \gamma\alpha\dot{\bar{\varepsilon}}^{pl} \tag{6-4}$$

where C and γ are the initial kinematic hardening modulus, and the rate at which kinematic hardening decreases with increasing plastic rotation, respectively. These parameters are calibrated based on cyclic experimental coupon test reported by Kaufmann et al. (2001) . The stress-strain

170

curve of the tensile coupon test of A913 Gr. 50 (Steel B) in the Kaufmann report were similar to the results obtained from the coupons fabricated from the specimen which were A992 Gr. 50. Therefore, the cyclic stress-strain results for Steel B were utilized for calibrating the numerical model. For the experiment reported by Kaufmann et al., a round test specimen with a 0.375 in. diameter was considered. A 1 in. gage length extensometer was used to measure deformation the strain. Four tension-compression cyclic tests were performed in 2%, 4%, 6% and 8% strain range levels consisting 10 cycles for each strain range. The combined plot of the cyclic tests is shown in Figure 6-8Figure 6-10.
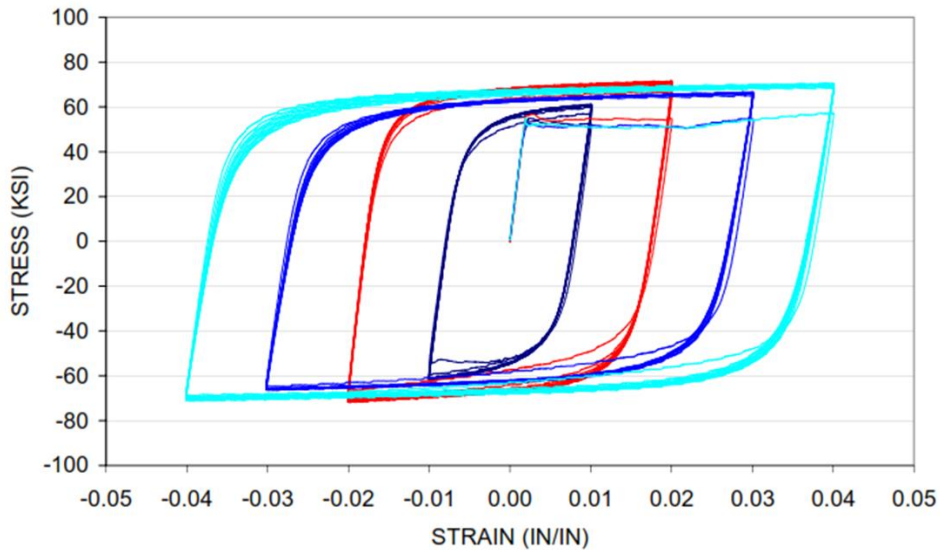
Figure 6-8. Cyclic stress-strain behavior of Steel B (10 cycles at 2%, 4%, 6% and 8% strain ranges), Kaufmann et al. (2001)

For the calibration of the numerical model, a 1 in. solid cylinder with a 0.375 in. diameter was modeled in Abaqus, shown in Figure 6-9. Both top and bottom surfaces of the cylinder were coupled with a reference point positioned at the mid-surface. For the boundary conditions, the bottom reference point was restrained in all degrees of freedom, and the top reference point was

171

restrained in all degrees of freedom except in the longitudinal direction (Y-axis), Figure 6-9. The resultant engineering stress and strain was measured by applying a displacement history at the reference point. The material properties of the combined hardening material model were calibrated using the Kaufmann stress-strain relationships. The defined parameters of the calibrated model is reported in Table 6-1. The calibrated stress-strain obtained from the numerical model is superimposed over the experimental data as shown in Figure 6-10.
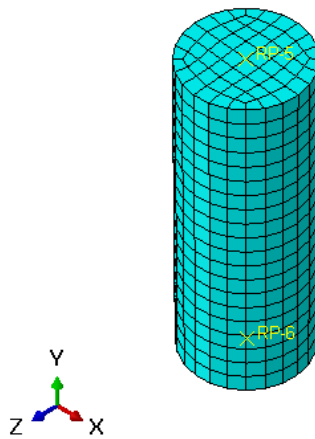
Figure 6-9. One inch. solid cylinder with a 0.375 in. diameter modeled in Abaqus

Table 6-1. Material properties for combined hardening material model

$\sigma\|_0$ (ksi)	C_1 (ksi)	γ_1	C_2 (ksi)	γ_2	Q_∞ (ksi)	b
50.66	1000	100	200	7	25	1
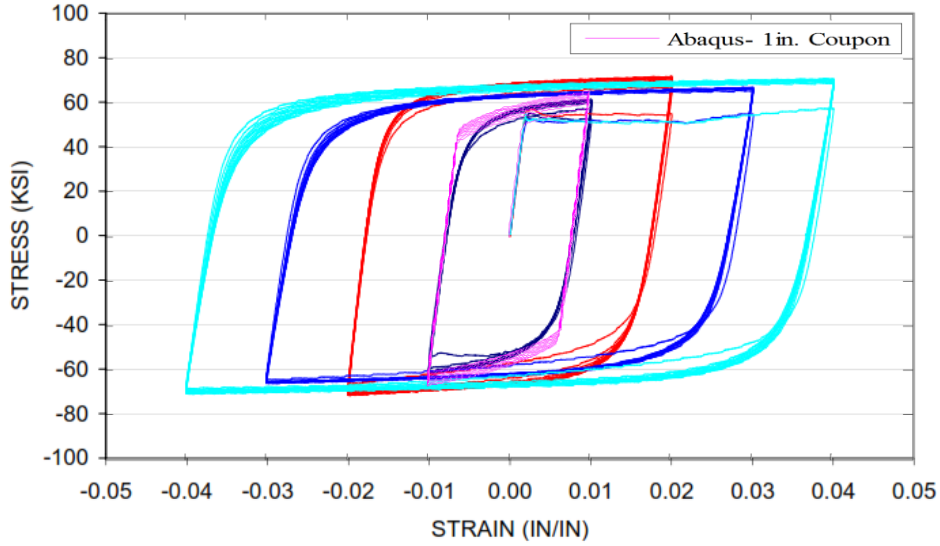
Figure 6-10. Superimposed numerical cyclic stress-strain at 1% strain with experimental cyclic behavior of Steel B (10 cycles at 2%, 4%, 6% and 8% strain ranges), Kaufmann et al. (2001)

6.4. Load and Boundary conditions

The experimental results presented are in the form of column drift ratio (chord rotation) vs. strong-axis bending moment at the base, i.e., at the interface between the bottom of the column and the top of the base plate. The bending moment at the base of the column was calculated based on the forces measured by the actuator load cells and the kinematics of the test setup as shown in Figure 6-11. Eq. 6-5 through 6-8 shows the calculation of bending moment at base of the column.

$$V_n = f_{x1} - f_{x2} - f_{x3} \tag{6-5}$$

$$P_n = f_{y1} - f_{y2} - f_{y3} \tag{6-6}$$

$$M_{Tip,n} = y_1 \cdot f_{x1} + x_1 \cdot f_{y1} + y_2 \cdot f_{x2} - x_2 \cdot f_{y2} + y_3 \cdot f_{x3} + x_3 \cdot f_{y3} \tag{6-7}$$

$$M_{Base,n} = V * l' + M_{Tip} - P * \Delta_{Tip} \tag{6-8}$$

173

Where, V_n is shear force, P_n is axial load, $M_{Tip,n}$ is the moment at the tip of the column and $M_{TBase,n}$ is the moment at the base at step n. The remaining parameters are defined in Fig. 6.

f_{xi} : Hor. component of the actuator "i" force
f_{yi} : Ver. component of the actuator "i" force
x_i : Hor. distance of the actuator "i" to the tip of the column
y_i : Ver. distance of the actuator "i" to the tip of the column
θ_c : Rotation of the tip of the column
Δ_{tip} : Hor. Displacement of the tip of the column
l' : Deformed height of the column
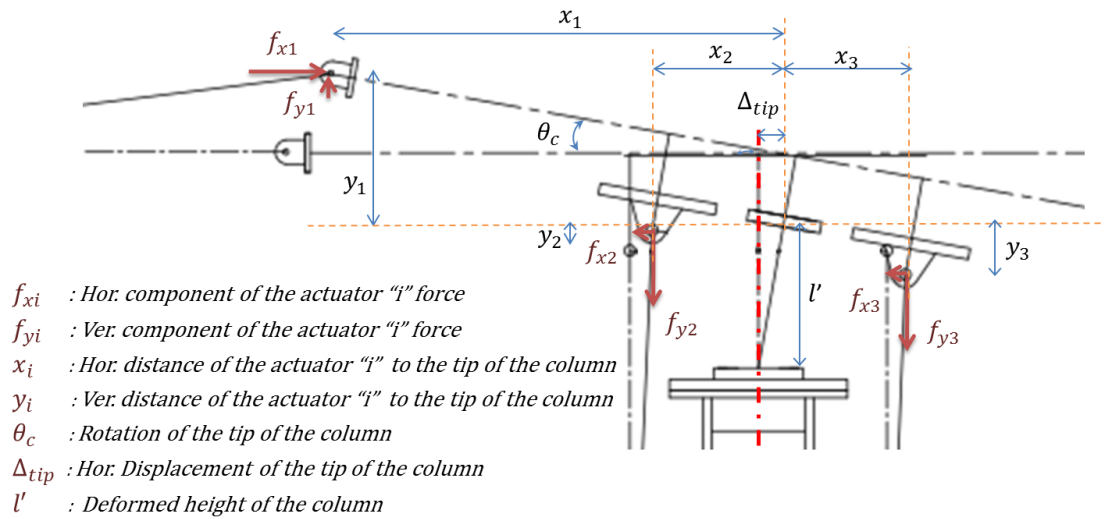
Figure 6-11. Deformed configuration of the setup and actuator force components

6.5. Initial Geometric Imperfections

Ideally, local imperfection values should be obtained from measurements of the geometry of the actual specimens. However, accurately measuring local initial deformations or imperfections is challenging given the relatively small values of such imperfections. Assumed initial geometric imperfections were included in the numerical model to have a better estimate of the capacity of the column. By superimposing scaled buckling mode shapes from Eigenvalue analyses, the global and local imperfections were introduced in the model. For the global imperfection, an out-of-straightens of $1/1000$ of the column's length according to AISC360-10 (2010) was considered. The estimated local imperfection was based on the manufacturing and fabrication tolerances and

was introduced at the base of the column where local buckling is expected to occur first. For the web, an out-of-flatness of $1/150$ of web depth and flange width were assumed based on ASTM A6/A6M (2003), respectively.

Global Imperfection   Local Imperfection
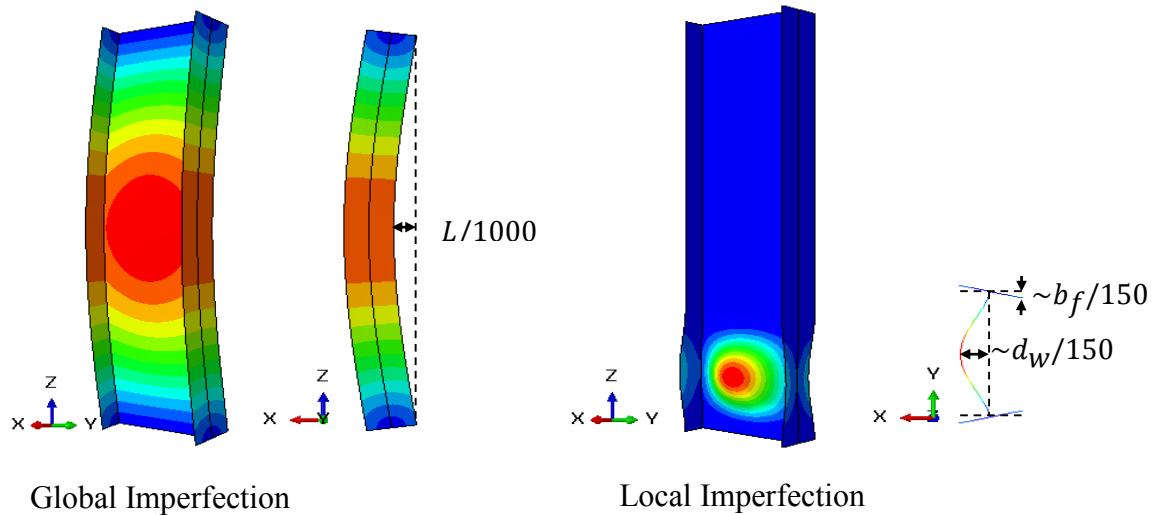
Figure 6-12. Geometric imperfection included in the numerical model

6.6.   Residual Stresses

Due to uneven cooling of hot rolled cross-sections during fabrication, cutting and welding, residual stresses are present in the modified cross-section. The residual stresses of the specimens would be different given the additional fabrication process; however, the residual stress in the fabricated specimen was assumed to be similar to the hot-rolled section due to lack of measurements.

In a previous numerical study performed by Newell (2008), it was observed that the residual stresses do not affect the ductility of the column significantly. Further numerical studies done by (Ozkula (2017)) show that considering residual stress in the model softens the transition from elastic to plastic behavior, and does not affect the global behavior of the column. In this study, the

simplified residual stress profile shown in Figure 6-13 was considered. The residual stress was included in the numerical simulation of the column as an initial stress condition in the longitudinal direction (Z direction, S22 in Figure 6-14). The stress distribution at the beginning of the simulation is shown in Figure 6-14.
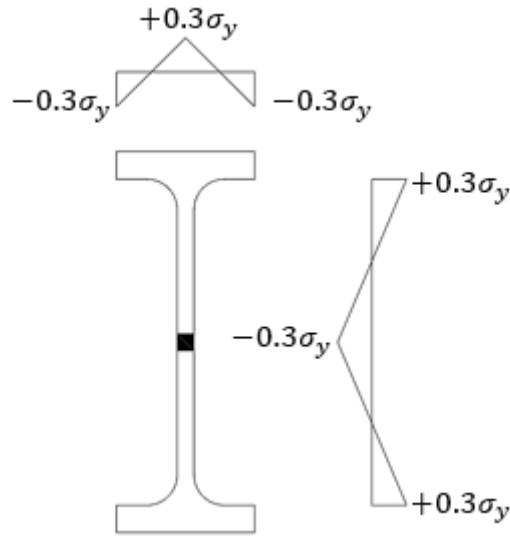
Figure 6-13. Assumed residual stress distribution of the fabricated cross section
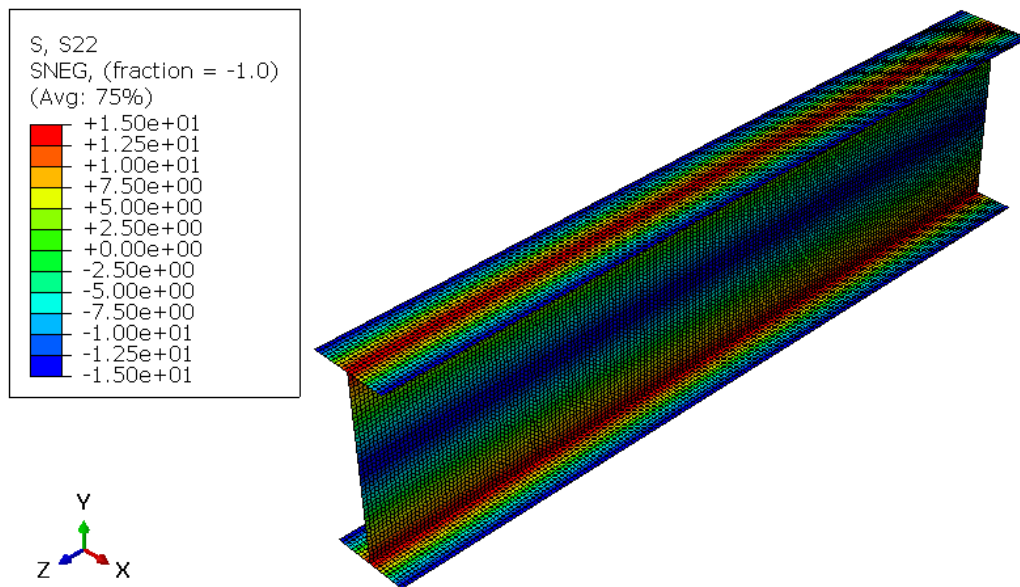
Figure 6-14. Applied residual stress as initial field stress in the Z direction (S22) in Abaqus

In Figure 6-15, the moment-drift ratio of the monotonic with variable axial load, Test 2, of the numerical simulation with and without residual stress is shown. Including residual stresses in the model as an initial stress state, has a negligible effect on the global response. Similarly, the von Mises stress distribution and deflected shape at the end of the simulation convey that considering residual stresses does not affect global behavior, Figure 6-16.
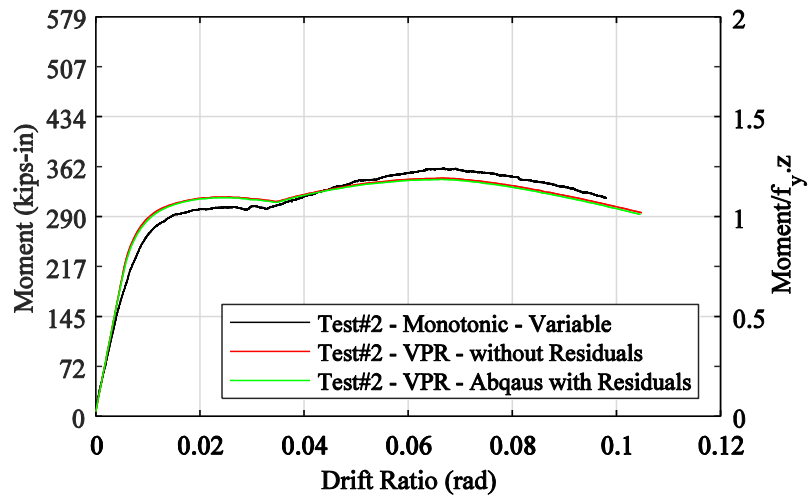
Figure 6-15. Moment-drift ratio of Test 2 and Abaqus simulation w/wo residual stress

Without Residual Stresses   With Residual Stresses
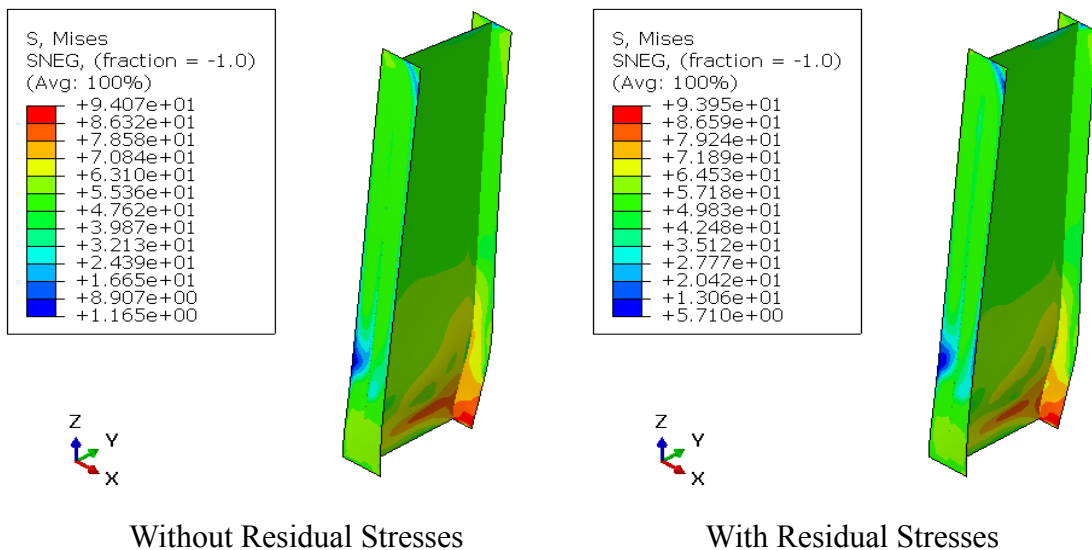
Figure 6-16. Von Mises stress distribution and deflected shape of Test 2 numerical model w/wo residuals stresses

In Figure 6-17, the moment-drift ratios of the Modified Collapse Test, Test 8, of the numerical simulation with and without residual stress are shown. Including residual stresses in the model as the initial stress state, has a negligible effect on the global response. However, the von Mises stress distribution and deflected shape at the end of the simulation when considering residual stresses is slightly different compared to the case without residual stresses, Figure 6-18.
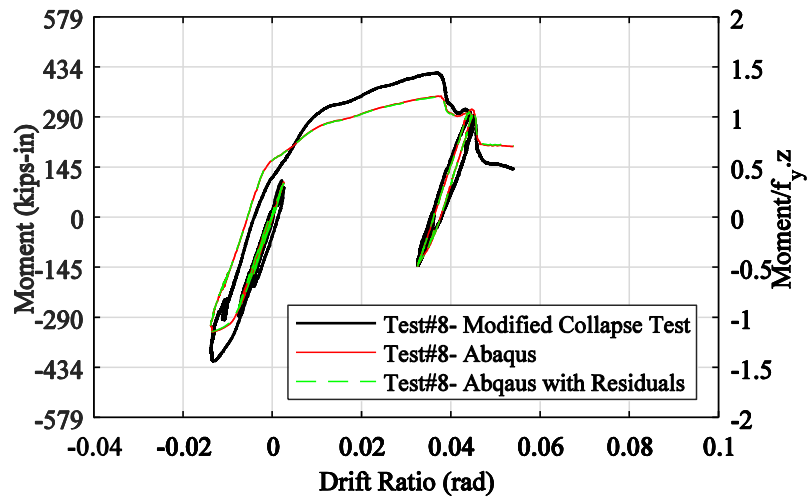
Figure 6-17. Moment-drift ratio of Test 8 and Abaqus simulation w/wo residual stress

Without Residual Stresses   With Residual Stresses
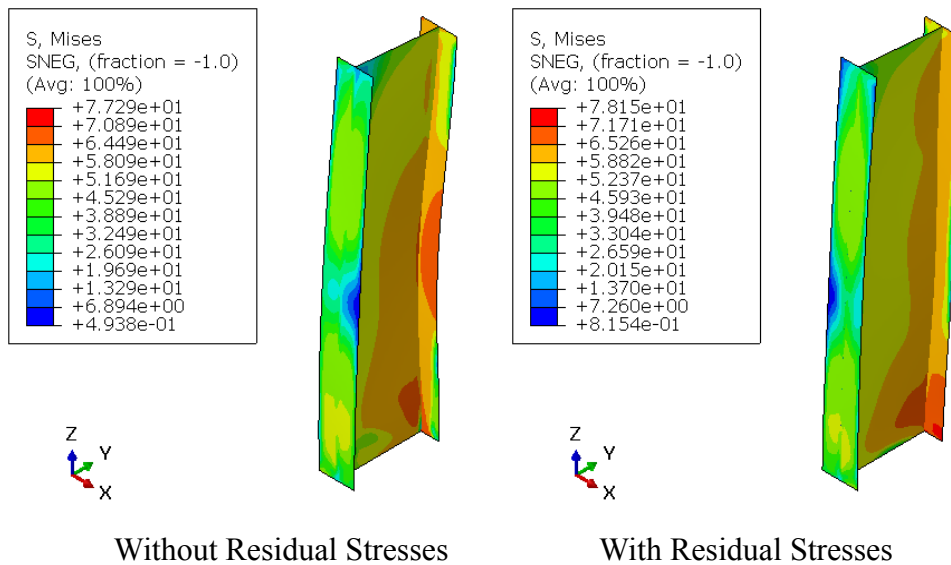
Figure 6-18. Von Mises stress distribution and deflected shape of Test 8 numerical model w/wo residuals stresses

Including residual stresses as the initial state for the numerical simulation had a negligible effect on the global response of the column.

6.7.   Simulation Results

In this section, the numerical simulation results of the column alongside the experiments are presented. In all these models, unless mentioned otherwise, the shear force (V), axial load (P), and tip rotation (R) are applied at the reference point coupled with the tip of the column.

A quantification of modeling parameters such as plastic rotation capacity (θ_p, The plastic rotation capacity is calculated for the first inelastic cycles of the bending moment-drift ratio relationship in which a clear post-capping slope is visible) and post-capping rotation (θ_{pc}, The post-capping rotation is calculated for the last cycle of the bending moment-drift ratio relationship) that are most relevant for collapse simulation of the numerical simulation are defined in this section.

- Monotonic with constant axial load, Test 1
  - Isolated column

In this simulation, the numerical column was subjected to the monotonic loading protocol with a constant axial load. The slope of the moment-drift ratio, rotational stiffness, of the simulated column in the elastic region (up to 0.08% rad) is consistent with the experimental results (Figure 6-19). However, with the initiation of yielding in which the material enters the strain hardening zone, the numerical simulation does not reach the same strength level as the experiment considering similar shear, axial and rotation histories, Figure 6-19 and Figure 6-20. At the end of the applied loading time history, the numerical model undergoes a greater drift compared to the experiment.

The plastic rotation capacities (θ_p, difference between yield rotation and rotation at maximum bending moment) were estimated as 0.08 rad and 0.09 rad for the experiment and numerical model of the monotonic test with constant axial load, respectively (Figure 6-19, moment-drift plot). Plastic rotations were calculated using estimates of yield drift ratios of 0.008 rad obtained from the results of tests 2.

The post-capping rotations for constant axial load (θ_{pc}, difference between rotation at maximum moment and rotation at complete loss of strength) were estimated both as 0.37 rad for the experiment and numerical model of monotonic test with constant axial load (tests 1).

In Figure 6-21, the numerical simulation predicts a similar trend for the vertical displacement of the column with respect to the experiment. As shown in Figure 6-22, the overall deflected shape of the column does match the experiment as well, and experiences the same failure mode of web and lateral torsional buckling.

Figure 6-19. Moment, shear, axial at the base vs. drift ratio of the Monotonic-Constant
Experiment and Abaqus (Test 1)

Figure 6-20. Rotation at the tip and base vs. drift ratio of the Monotonic-Constant Experiment and Abaqus (Test 1)

Figure 6-21. Vertical displacement of the tip vs. drift ratio of the Monotonic-Constant Experiment and Abaqus (Test 1)

Figure 6-22. Von Mises stress distribution and deflected shape (south flange view) of the numerical model and experiment at the end of the loading protocol, Test 1

o   Three-actuator setup

For this simulation, the entire setup was modeled in Abaqus, Figure 6-4. Different models were simulated, considering various cases of loading conditions. In this section, the studied case consists of having the Horizontal actuator in force-control mode (F_H), Figure 6-23, and the North and Sound actuators in displacement-control mode (D_N, and D_S), Figure 6-24. The Horizontal actuator is force control and its displacement time history obtained from the numerical simulation matches the experimental displacement history, with a slight difference towards the end of the experiment, i.e., larger experimental drifts. In Figure 6-24, applying the North and South experimental displacement histories measured by the LVDT's (Linear Variable Differential Transformers and Transducers) of the experiment to the numerical vertical actuators, did not correspond to the initial axial load and rotation at the tip of the column. This can be due to initial adjustment of the setup

and clearances in the swivels pins of the actuators. Therefore, the vertical actuator displacements were modified to match the initial axial force and rotation at the tip of the column as shown in Figure 6-24. Up to 0.005 rad drift, the total force in the vertical actuators, Figure 6-24, obtained from the numerical model is consistent with the experimental magnitudes. However, the numerical values deviate abruptly from the experimental results after 0.005 rad. In all the numerical simulation trials, the same trend is seen when using the shear time history of the experiment as input to the horizontal actuator force history in the numerical simulation.

The deflected shape of the numerical and experimental three-actuator setup is depicted in Figure 6-25.
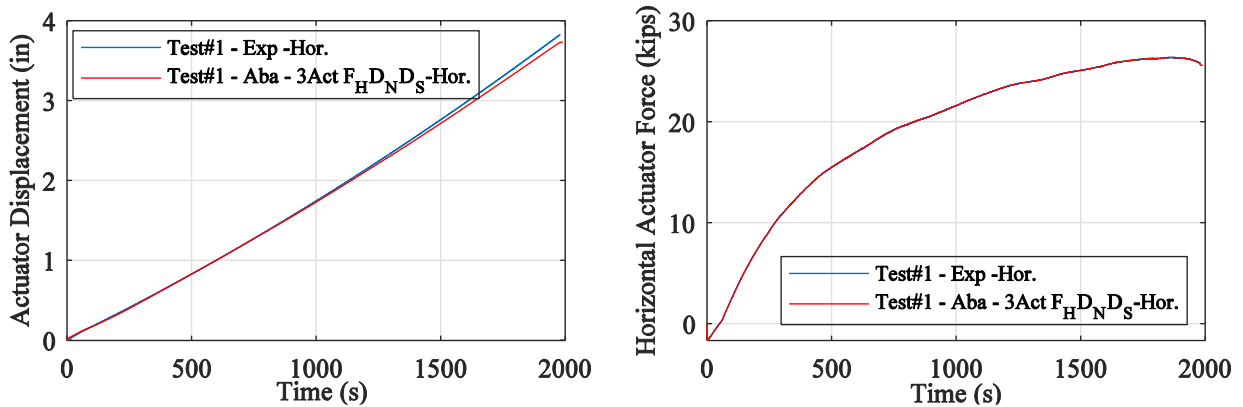
Figure 6-23. Horizontal actuator displacements and force time history of the Monotonic-Constant experiment and Abaqus three-actuator setup (Test 1)
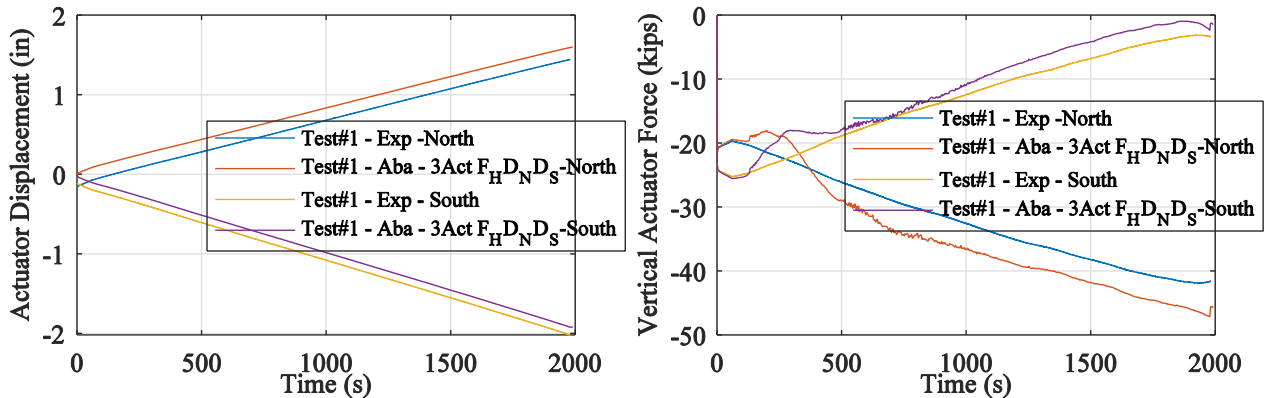
Figure 6-24. Vertical actuator displacements and force time history of the Monotonic-Constant experiment and Abaqus three-actuator setup (Test 1)
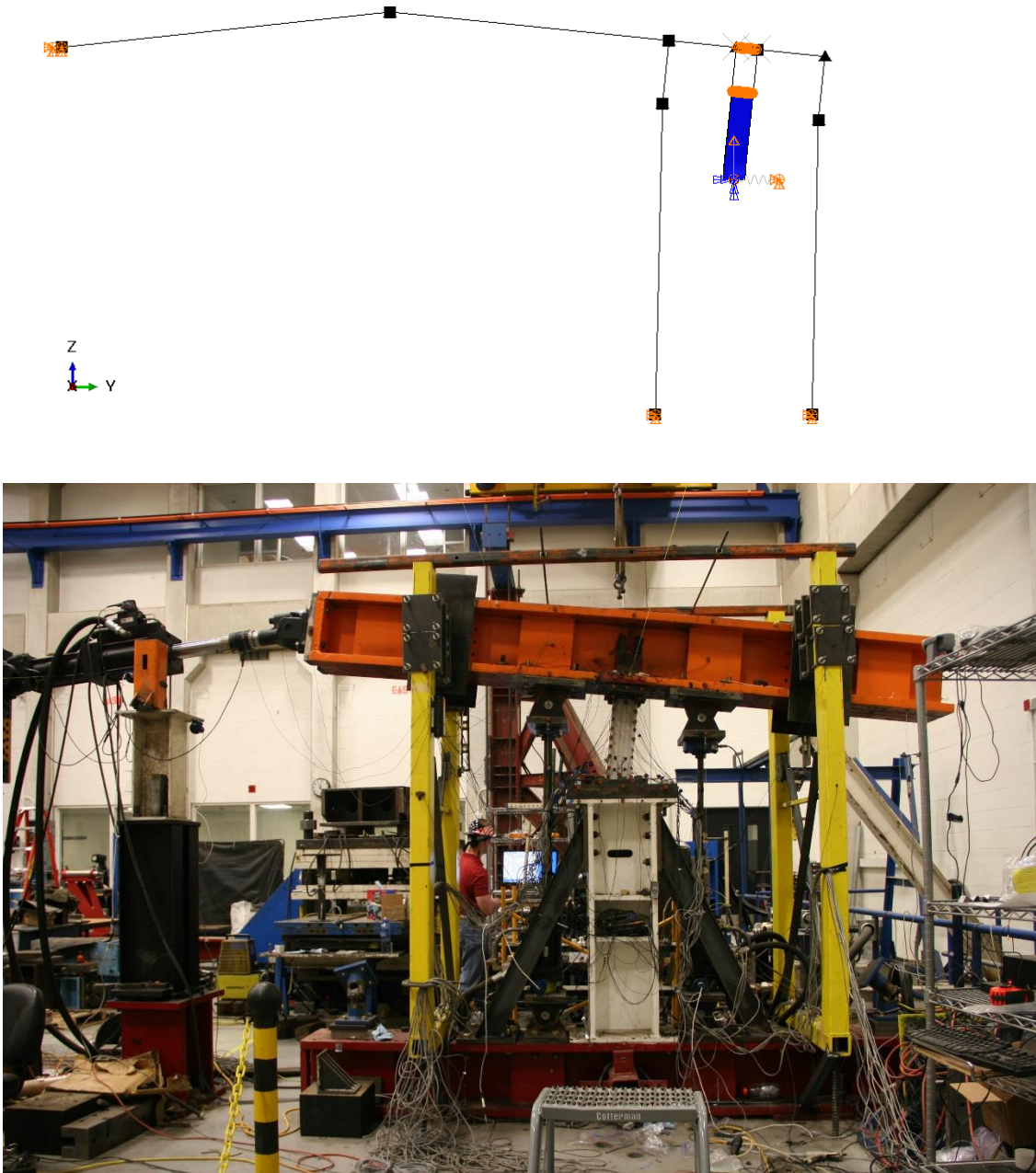
Figure 6-25. Deformed three-actuator setup at the end of the loading history of the experiment and numerical simulation, Test 1

The numerical column under FHDNDS loading histories experiences larger drift ratios with respect to the experiment, Figure 6-26. The initial slope of the moment-drift ratio, rotational stiffness, of the simulated column in the elastic region is consistent with experimental results. However, with the initiation of yielding in which the material enters the strain hardening zone, the numerical simulation does not reach the same strength level as the experiment (21% lower). The shear force in the numerical column model is consistent with the calculated shear from the experiment. However, the total axial load in the numerical column variates with respect to the experiment. The tip and base rotational loading histories are consistent with the experiment for all the numerical simulation cases, Figure 6-27.

In Figure 6-28, the numerical simulation predicts similar trends for the vertical displacement of the column with respect to the experiment. As shown in Figure 6-29, the overall deflected shape of the column does match the general-purpose, and the flaking of whitewash near the support is consistent with the maximum Von Mises stress of the numerical column layout.

During the experiment, the horizontal movement of the pedestal was measured, Figure 6-30. The displacement obtained from the calibrated spring at the base of the column in the three-actuator Abaqus model is consistent with the experiment. In addition, the shear force in the column was divided by the equivalent elastic stiffness of 502 kips/in for the pedestal which matched the displacement obtained from the calibrated spring at the base of the numerical model, Figure 6-30. The later comparison can give a verification of the equation used to calculate the shear force from all the actuators of the experiment.

Figure 6-26. Moment, shear, axial at the base vs. drift ratio of the Monotonic-Constant
Experiment and Abaqus three-actuator setup (Test 1)

Figure 6-27. Rotation at the tip and base vs. drift ratio of the Monotonic-Constant experiment and Abaqus three-actuator setup (Test 1)
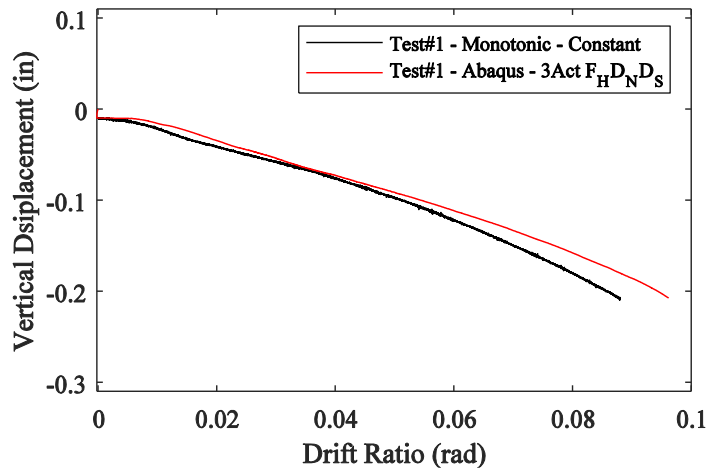
Figure 6-28. Vertical displacement of the tip vs. drift ratio of the Monotonic-Constant experiment and Abaqus three-actuator setup (Test 1)
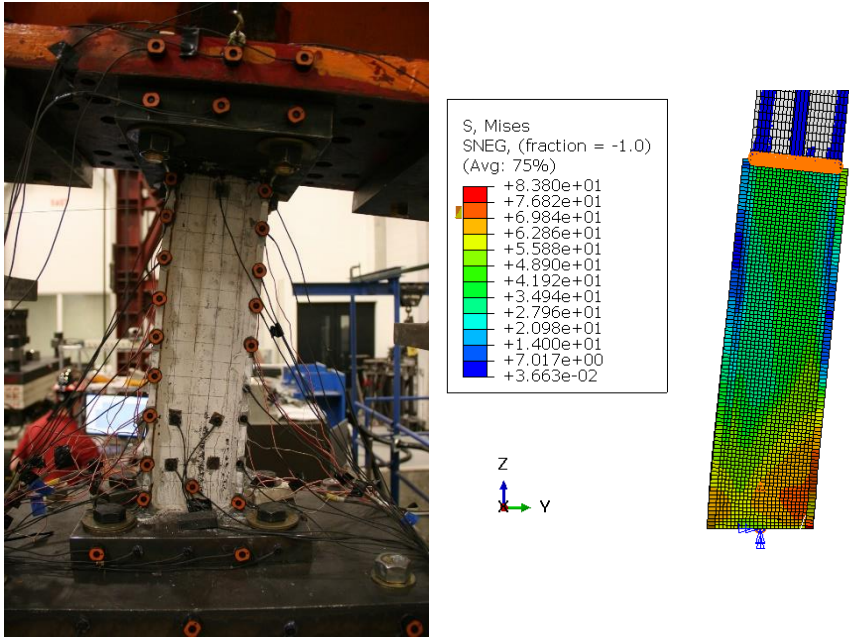
Figure 6-29. Von Mises stress distribution and deflected shape of Test 1 numerical model and experiment at the end of the loading protocol
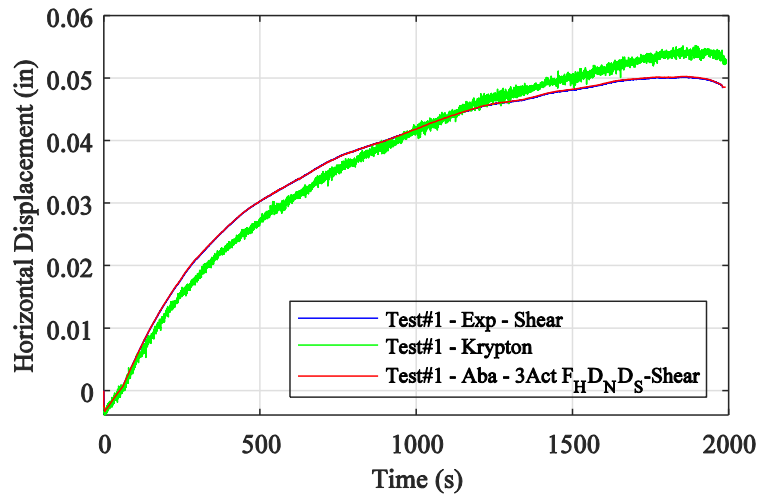
Figure 6-30. Pedestal horizontal displacement calculated from the experimental shear, measured with Krypton, and extracted from Abaqus three-actuator model

189

- Monotonic with variable axial load, Test 2

The loading protocol for this experiment was similar to test 1, with the difference of a variable axial load was applied. The slope of the moment-drift ratio, rotational stiffness, of the simulated column in the elastic region (up to ~ 0.06% rad) was consistent with experimental results, observed in the moment-drift ratio plot in Figure 6-31. The overall moment-drift ratio of the numerical simulation was similar with the experiment. The maximum strength from numerical simulation predicts 4% lower than the experiment considering similar shear, axial and rotation histories, Figure 6-19 and Figure 6-20. At the end of the applied loading time history the numerical model undergoes a greater drift compared to the experiment as well.

The plastic rotation capacities (θ_p, difference between yield rotation and rotation at maximum bending moment) were estimated as 0.06 rad for both experiment and numerical model of the monotonic with variable axial load (Figure 6-31). Plastic rotations were calculated using estimates of yield drift ratios of 0.0075 rad obtained from the results of tests 2 shown in Figure 6-31.

The post-capping rotations for constant axial load (θ_{pc}, difference between rotation at maximum moment and rotation at complete loss of strength) were estimated as 0.18 rad and 0.2 rad for the experiment and numerical model of monotonic test with variable axial load, respectively (tests 2).

In Figure 6-33, the numerical simulation predicted similar trend for the vertical displacement of the column with respect to the experiment; however, the numerical model was experiencing more axial shortening in the inelastic range. As shown in Figure 6-34, the overall deflected shape of the column does match the experiment as well, and experiences the same failure mode of web and lateral torsional buckling.
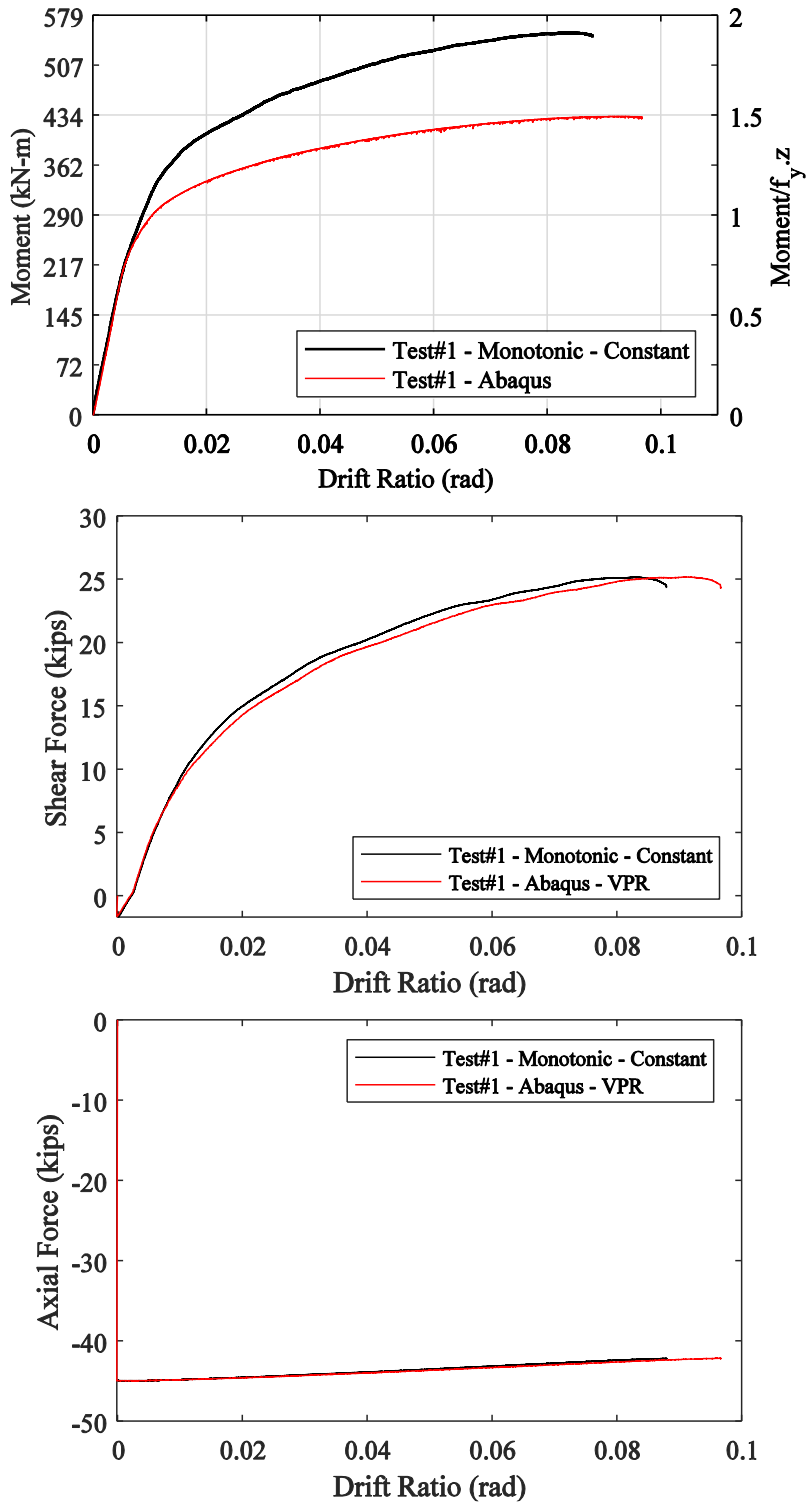
190
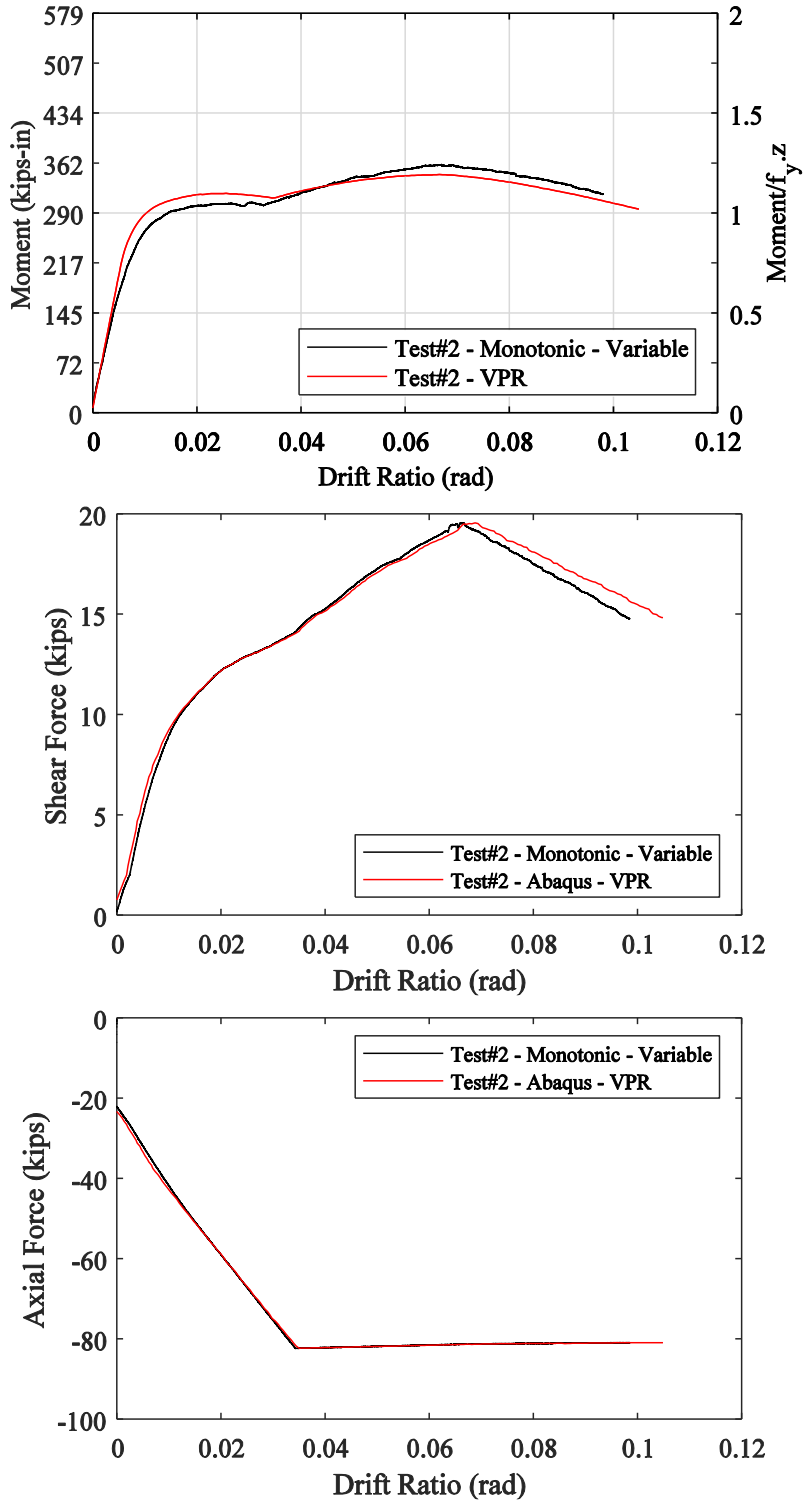
Figure 6-31. Moment, shear, axial at the base vs. drift ratio of the Monotonic-Variable Experiment and Abaqus (Test 2)
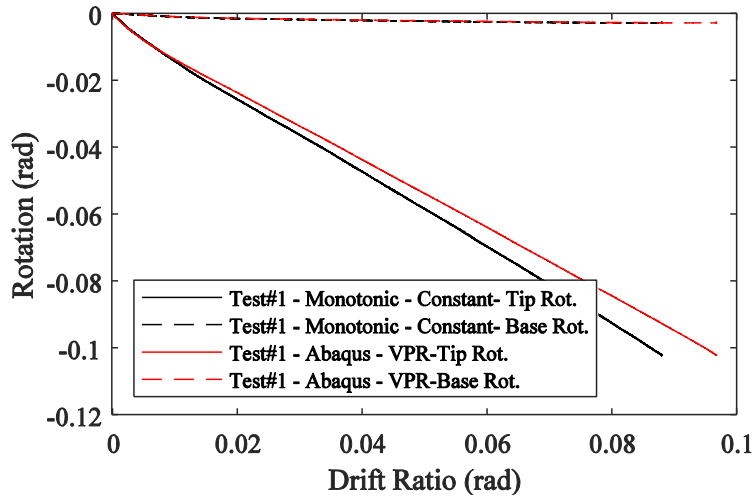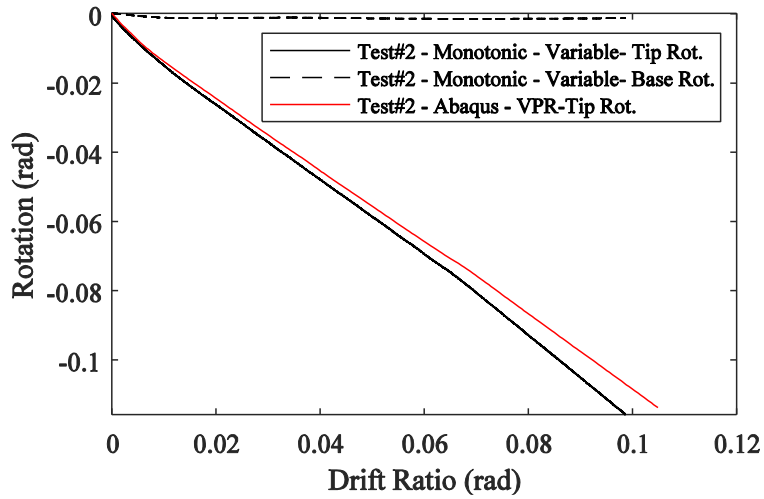
Figure 6-32. Rotation of the tip and base vs. drift ratio of the Monotonic-Variable Experiment and Abaqus (Test 2)
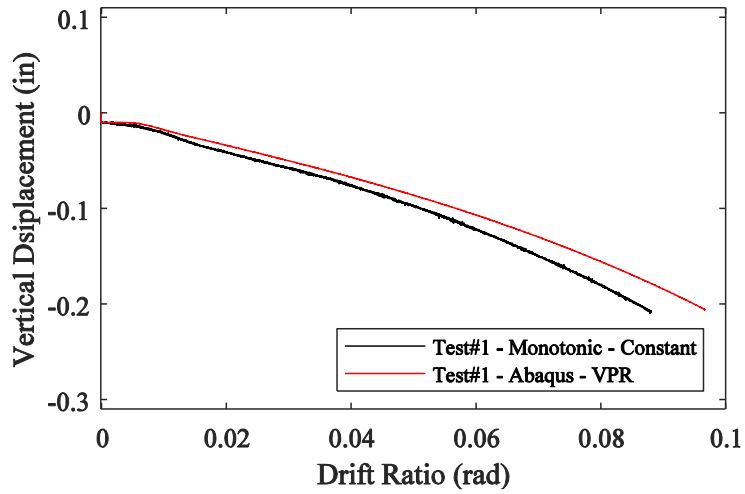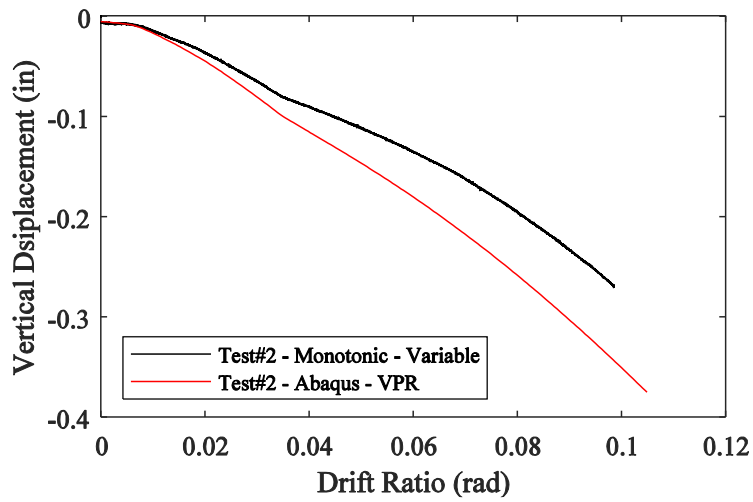

Figure 6-33. Vertical displacement of the tip vs. drift ratio of the Monotonic-Variable Experiment and Abaqus (Test 2)
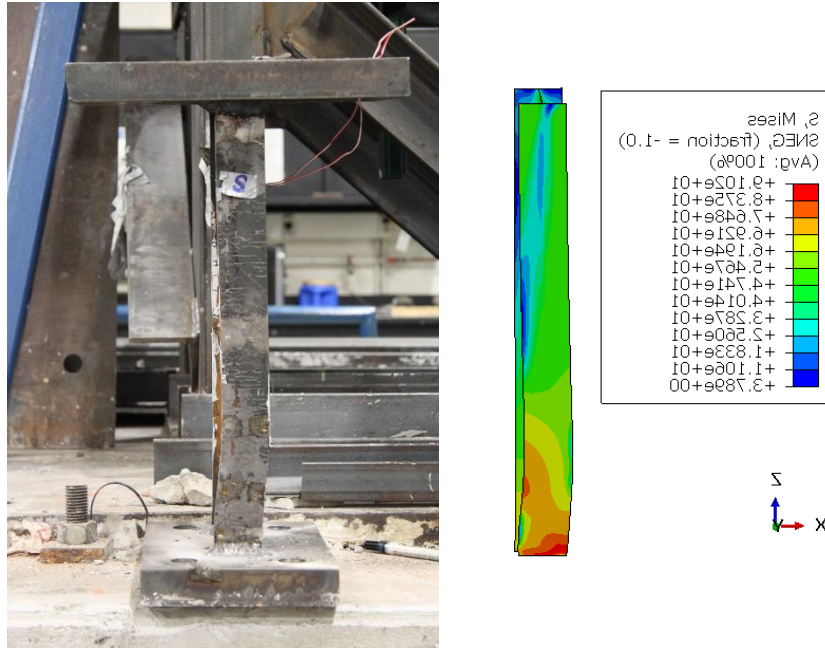
Figure 6-34. Von Mises stress distribution and deflected shape of the numerical model south flange and experiment at the end of the loading protocol, Test 2

- unsymmetrical, Test 5

In this simulation, the numerical column is subjected to the unsymmetrical cyclic loading history. The moment-drift ratio extracted from the numerical mode, in the elastic drifts matches the experiment as shown in Figure 6-35. The numerical column under VPR loading histories experiences larger drift ratios with respect to the experiment. In Figure 6-35, the slopes of the loading and unloading moment-drift ratio, rotational stiffness, of the simulated column in the elastic region is consistent with experimental results. However, with the initiation of yielding in which the material enters the strain hardening zone, and the numerical simulation does not reach the same strength level as the experiment when the axial load in the column is reaching maximum tension and compression, respectively. The tip and base rotational loading histories is consistent for all the numerical cases, Figure 6-37.

The plastic rotation capacities (θ_p, difference between yield rotation and rotation at maximum bending moment) were estimated as 0.035 rad and 0.037 rad for both experiment and numerical model of the unsymmetrical cyclic loading history (Figure 6-35).

The post-capping rotations for constant axial load (θ_{pc}, difference between rotation at maximum moment and rotation at complete loss of strength) were estimated as 0.11 rad for both the experiment and numerical model of the unsymmetrical cyclic loading history, respectively.

Figure 6-42, shows the numerical simulation has a higher rate of axial shortening with respect to the experiment, in which the axial shortening of the numerical model increases after the second set cycles (after 0.02% drift) with respect to the experiment. As shown in Figure 6-38, the overall deflected shape of the column does match the experiment as well, and experiences the same failure mode of web and lateral torsional buckling. The direction of out-of-plane deformation due buckling of the numerical model is opposite to the experiment.
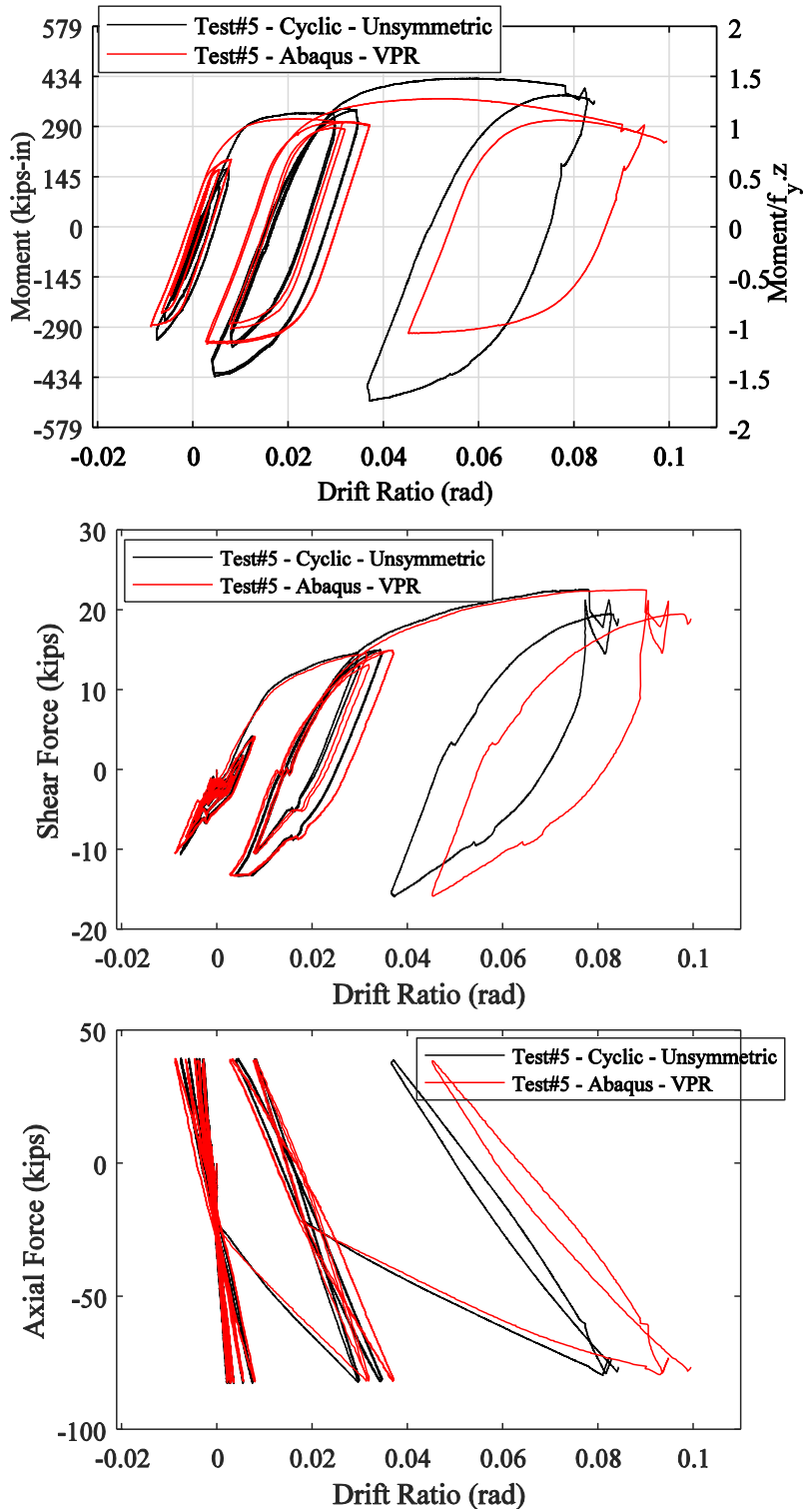
Figure 6-35. Moment, shear, axial at the base vs. drift ratio of the Cyclic-Unsymmetrical Experiment and Abaqus (Test 6)
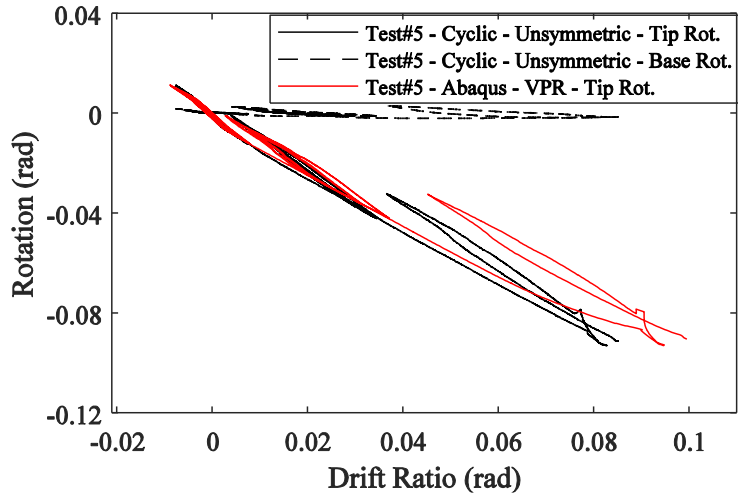
Figure 6-36. Rotation of the tip and base vs. drift ratio of the Cyclic-Unsymmetrical experiment and Abaqus (Test 6)
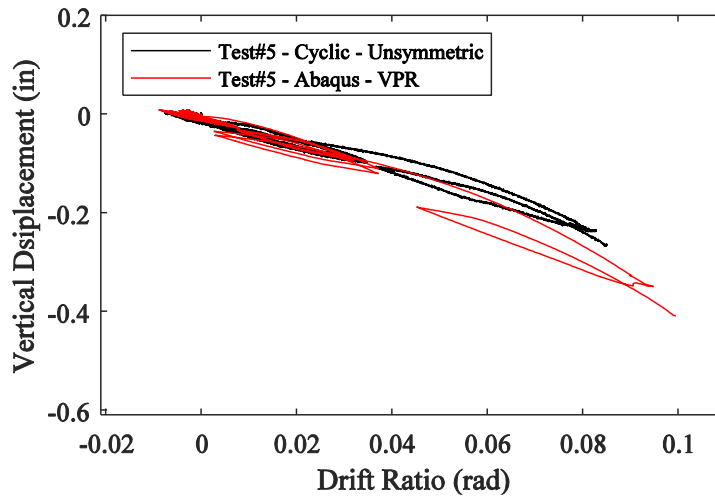
Figure 6-37. Vertical displacement of the tip vs. drift ratio of the Cyclic-Unsymmetrical experiment and Abaqus (Test 5)
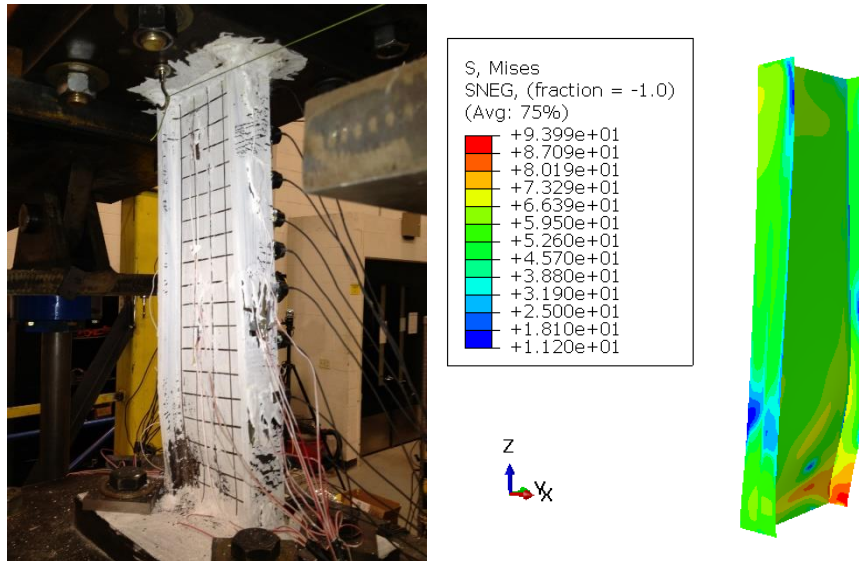
Figure 6-38. Von Mises stress distribution and deflected shape of Test 5 numerical model and experiment at the end of the loading protocol

- Cyclic with monotonic, Test 6

In this simulation, the numerical column is subjected to the cyclic followed by a monotonic loading history. The numerical simulation became unstable one cycle before reaching the end of the loading histories as shown in Figure 6-39. The numerical column under VPR loading histories experiences larger drift ratios with respect to the experiment, and the difference is larger when the axial load in the column is in tension, Figure 6-39. In Figure 6-40, the slopes of the loading and unloading moment-drift ratio, rotational stiffness, of the simulated column in the elastic region is consistent with experimental results. However, with the initiation of yielding in which the material enters the strain hardening zone, and the numerical simulation does not reach the same strength level as the experiment when the axial load in the column is reaching maximum tension and compression, respectively. The tip and base rotational loading histories is consistent for all the numerical cases, Figure 6-41.

The plastic rotation capacities (θ_p, difference between yield rotation and rotation at maximum bending moment) were estimated as 0.015 rad for both experiment and numerical model of the cyclic followed by a monotonic loading history (Figure 6-40). Plastic rotations were calculated using estimates of yield drift ratios of 0.008 rad obtained from the results of test 6.

The post-capping rotations for constant axial load (θ_{pc}, difference between rotation at maximum moment and rotation at complete loss of strength) were estimated as 0.09 rad and 0.12 rad for the experiment and numerical model of cyclic followed by a monotonic loading history, respectively (test 6). The post-capping rotation in the numerical simulation was estimated one cycle prior to the experiment, since the numerical mode became instable.

Figure 6-42, shows the numerical simulation has a higher rate of axial shortening with respect to the experiment, in which the axial shortening of the numerical model is one cycle ahead of the experiment. As shown in Figure 6-43, the overall deflected shape of the column does match the experiment as well, and experiences the same failure mode of web and lateral torsional buckling.
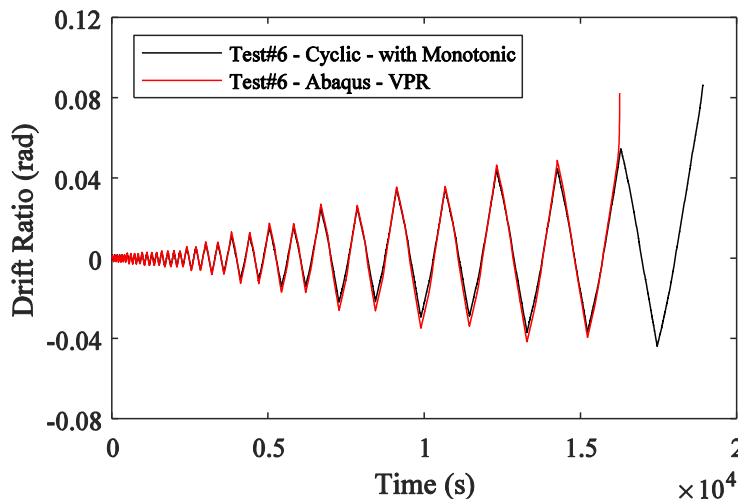
Figure 6-39. Drift ratio time history of the Cyclic-with Monotonic experiment and Abaqus (Test 6)
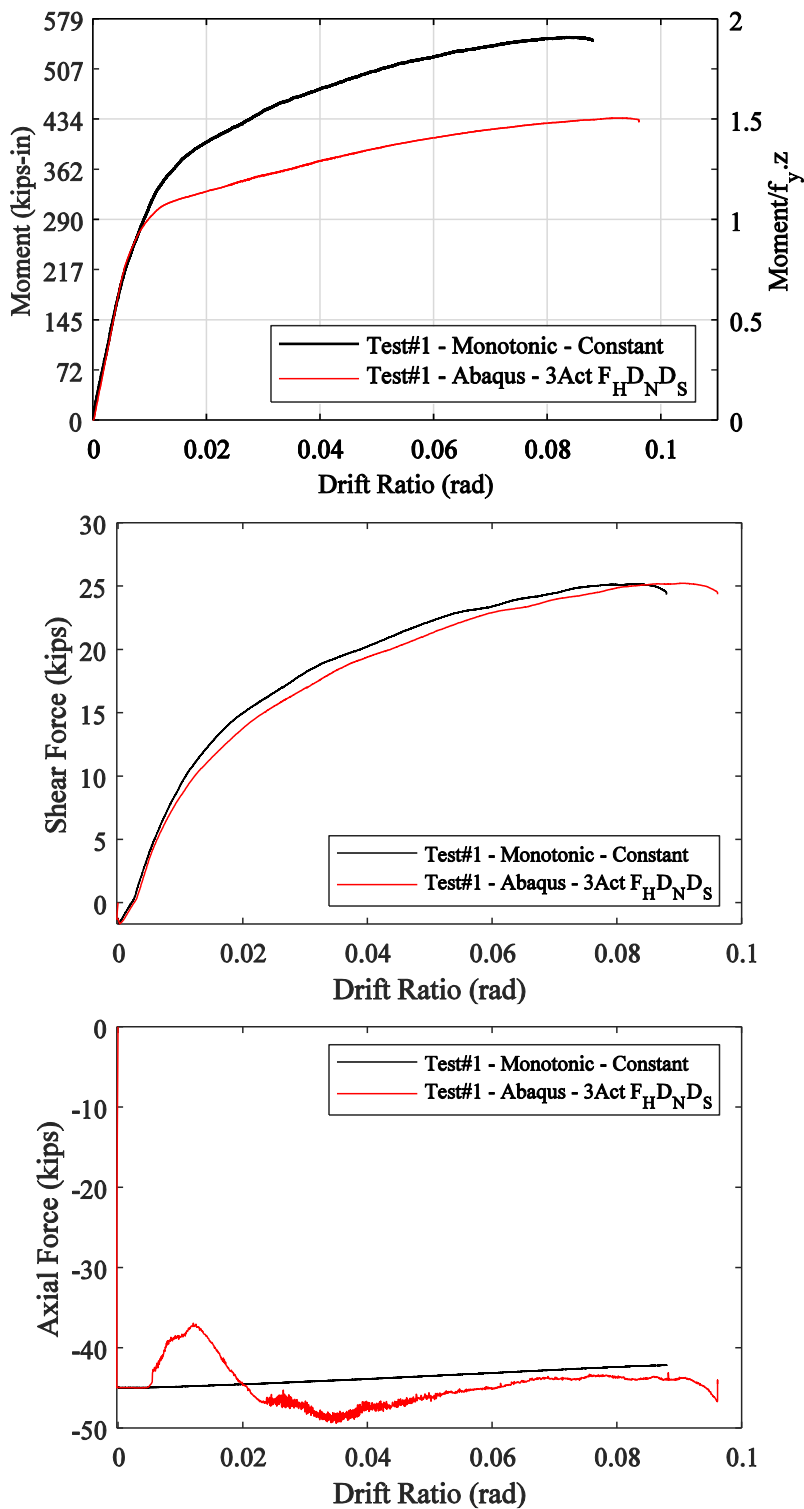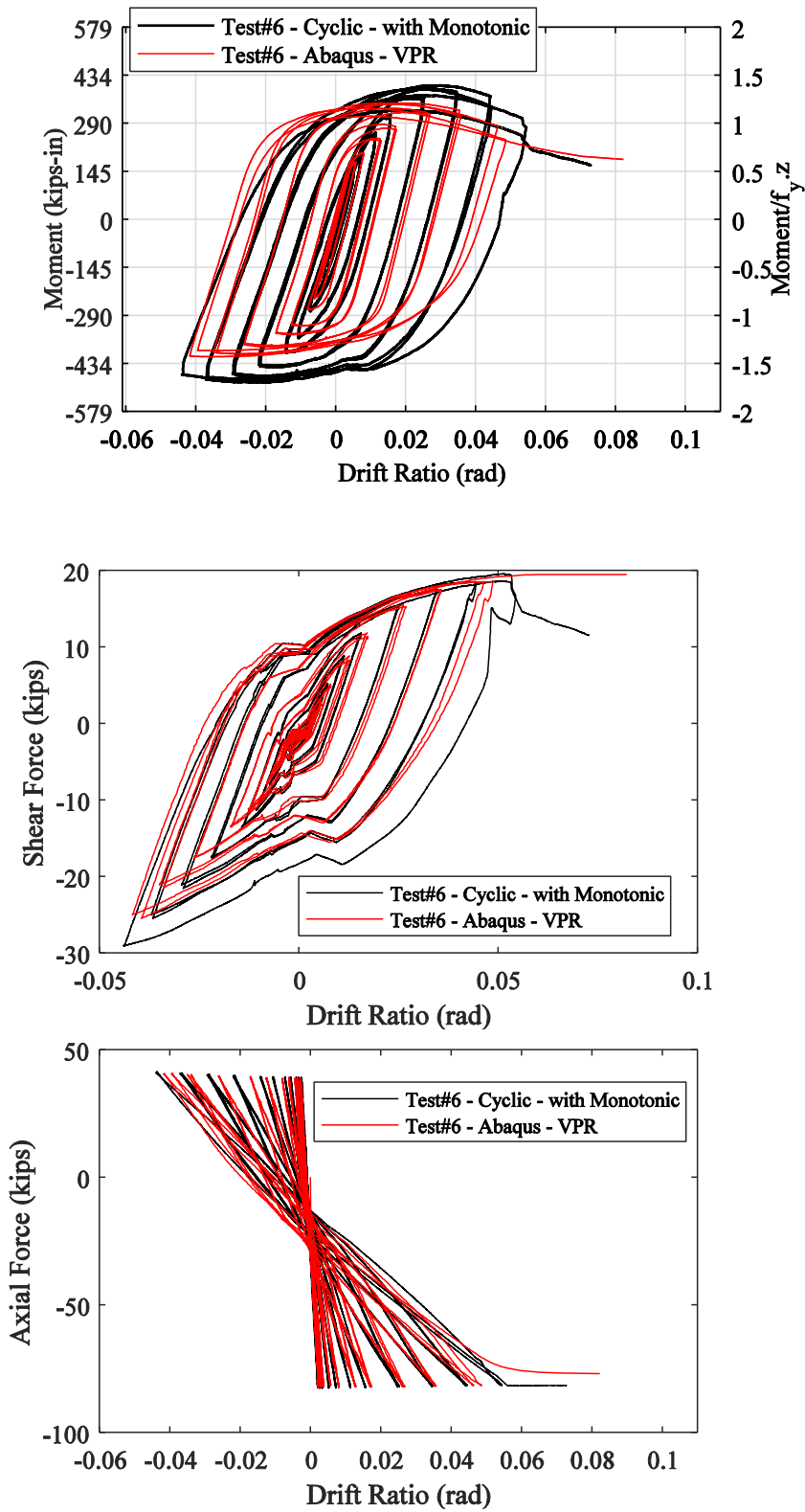
Figure 6-40. Moment, shear, axial at the base vs. drift ratio of the Monotonic-Constant Experiment and Abaqus (Test 6)
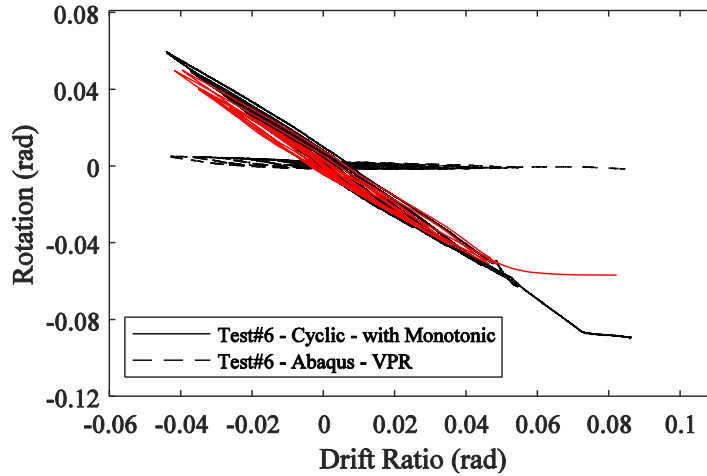
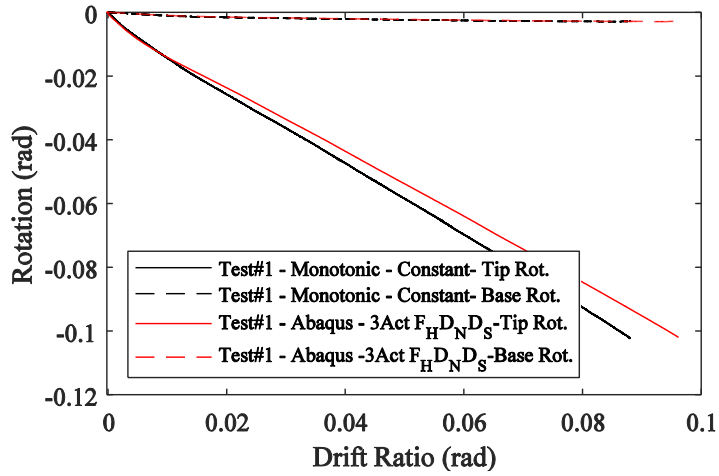Figure 6-41. Rotation of the tip and base vs. drift ratio of the Cyclic-with Monotonic experiment and Abaqus (Test 6)
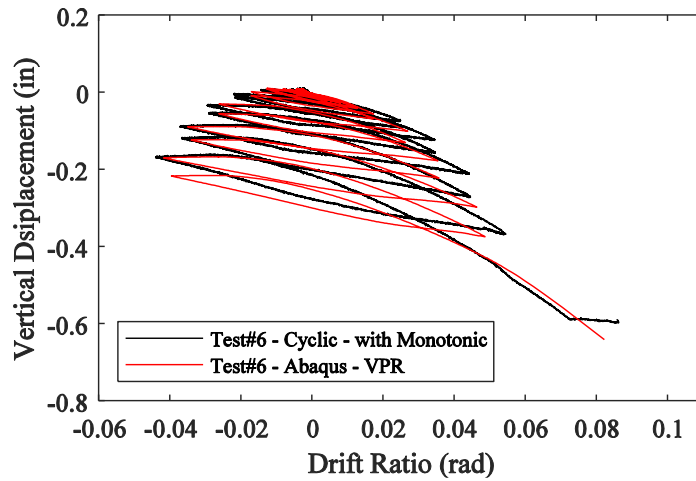
Figure 6-42. Vertical displacement of the tip vs. drift ratio of the Cyclic-with Monotonic experiment and Abaqus (Test 6)
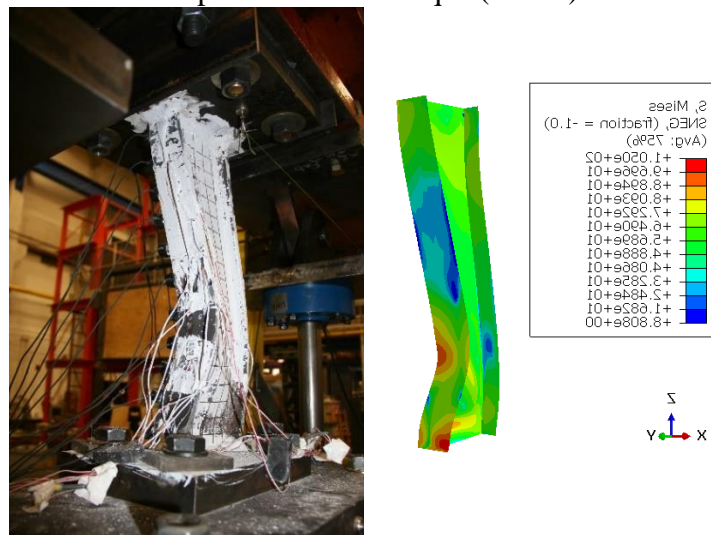
Figure 6-43. Von Mises stress distribution and deflected shape of Test 6 numerical model and experiment at the end of the loading protocol

200

- Modified collapse test, Test 8

In this simulation, the numerical column is subjected to the loading, displacement and rotational histories measured and calculated during the second hybrid experiment. In order to study the effect of loading histories on the global response, moment at the base of the column shown in Figure 6-44, two other cases are studied. These cases are as follow:

(i)   VPR model; shear (V), axial (P) and rotation (R) loading histories

(ii) D_LPR model; lateral displacement (D_L), axial (P), and rotation (R) at the tip loading histories

(iii) $D_L D_V$R model; lateral displacement (D_L), vertical displacement (D_V), and rotation (R) at the tip loading histories

In Figure 6-44, the slopes of the loading and unloading moment-drift ratio, rotational stiffness, of the simulated column in the elastic region is consistent with experimental results. However, with the initiation of yielding in which the material enters the strain hardening zone, the numerical simulation does not reach the same strength level as the experiment in all the studied cases. The numerical column under VPR loading histories experiences larger drift ratios with respect to the experiment. The axial load-drift ratio for the displacement control case ($D_L D_V$R), Figure 6-44, exhibits the same trend with departure in magnitude in larger drift ratios with respect to the experiment. The tip and base rotational loading history is consistent for all the numerical cases, Figure 6-45.

The plastic rotation capacities (θ_p) were estimated as 0.034 rad and 0.04 rad for both experiment and numerical model (VPR) of the cyclic followed by a monotonic loading history, respectively (Figure 6-44).

The post-capping rotations for constant axial load (θ_{pc}) were estimated as 0.027 rad and 0.031 rad for the experiment and numerical model, respectively.

In Figure 6-46, the numerical simulation predicts similar trends for the vertical displacement of the column with respect to the experiment. As shown in Figure 6-47, the overall deflected shape of the column does match the experiment as well, and experiences the same failure mode of web and lateral torsional buckling.
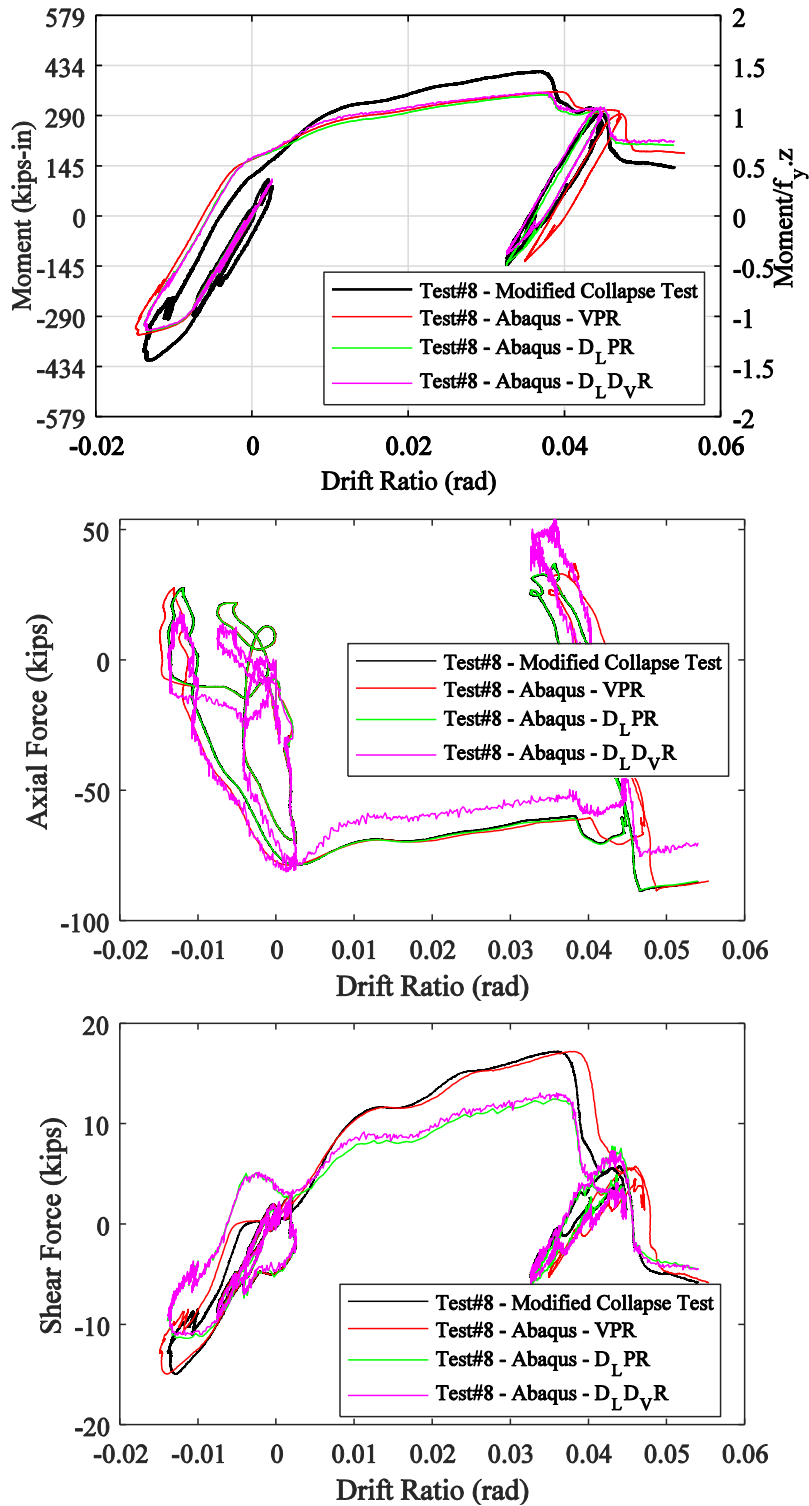
Figure 6-44. Moment, axial force, shear force at the base of the column vs. drift ratio of the modified collapse test (Test 8), Abaqus model cases VPR, D_LPR, and D_LD_VR
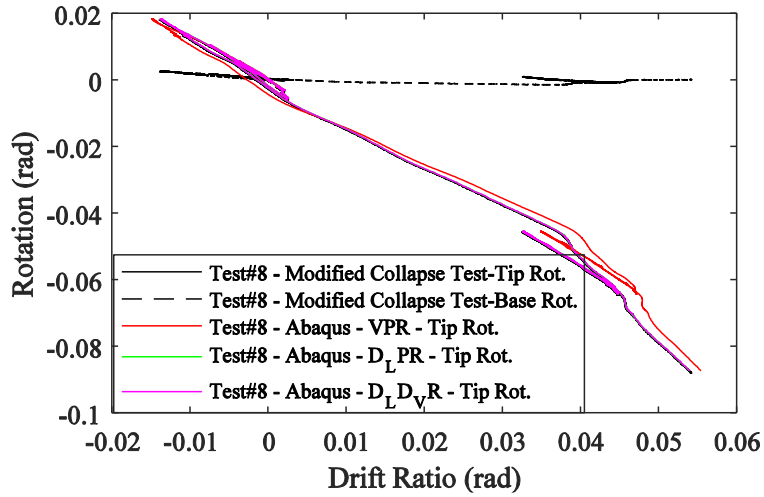
Figure 6-45. Rotation at base and tip of the column vs. drift ratio of the modified collapse test (Test 8), Abaqus model cases VPR, D_LPR, and D_LD_VR
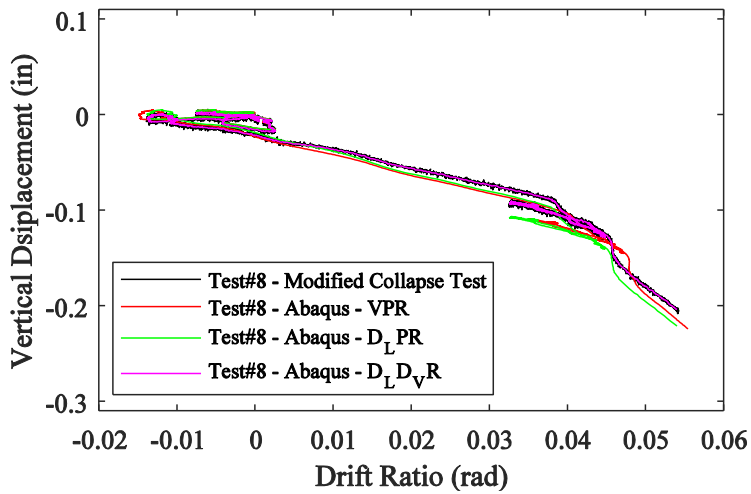
Figure 6-46. Vertical displacement at the tip of the column vs. drift ratio of the modified collapse test (Test 8), Abaqus model cases VPR, D_LPR, and D_LD_VR
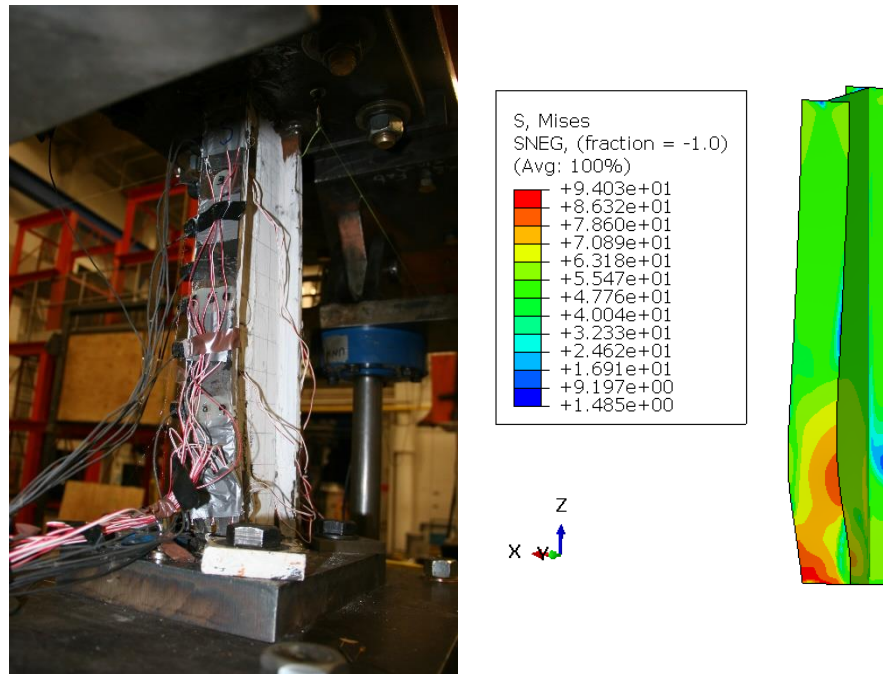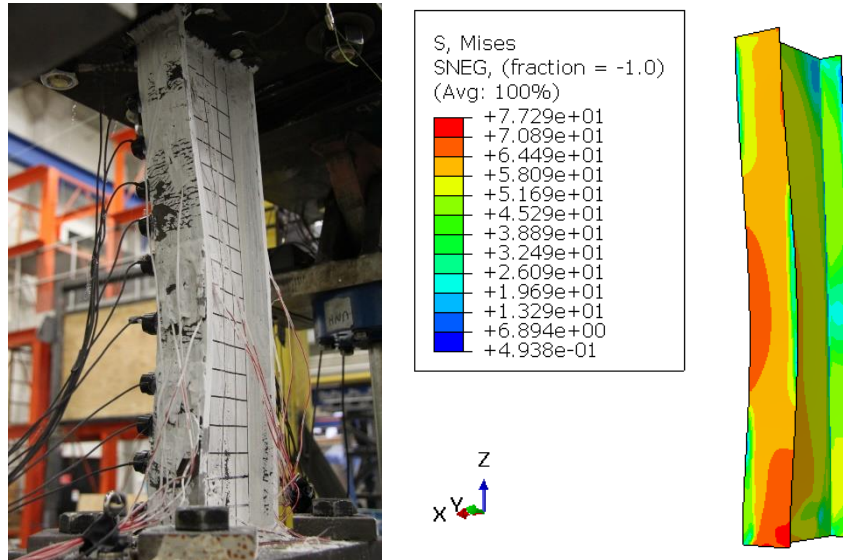
Figure 6-47. Von Mises stress distribution and deflected shape of Test 6 numerical model and experiment at the end of the loading protocol

6.8. Numerical Simulation of the Beam Experiments (@UNH)

For these experiments, a different setup was designed and the specimens were tested. In order to calibrate the numerical models for each experiment, the corresponding loading and boundary conditions are considered, which is described in more detail in the following.

- **Test 1**

In this experiment, the rotation at the base of the beam was calculated using the displacement of the top of the bracket using the LVDT measurements. Therefore, in the numerical model the rotation about the X-axis is imposed (strong axis), and the rest of the degrees of freedom at the base are restrained. The boundary conditions are applied at the tip and base of the beam to reference points, RP-1 and RP-2, respectively. The reference point is coupled to the end surface of the flanges and web edges. At the tip of the column, the vertical (lateral for the beam section), out-of-plane displacements and tip rotation along the longitudinal axis, respectively in the direction of Y, X and Z axes, are applied. The boundary conditions are depicted in Figure 6-48.

205
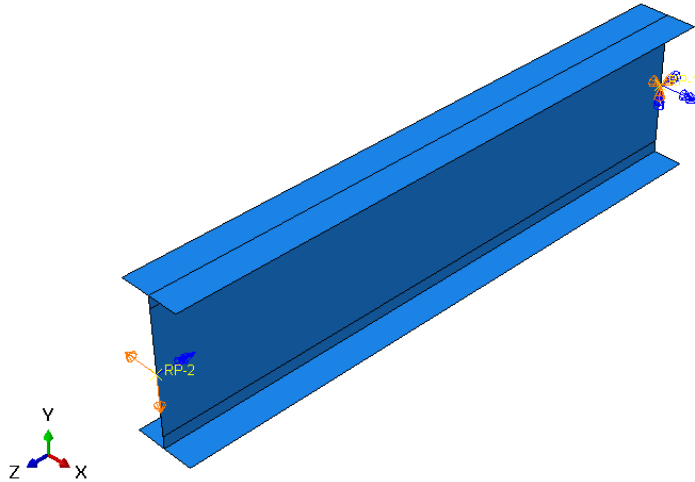
Figure 6-48. Boundary condition defined for the beam simulations for Test 1

The shear and moment at the base of the column obtained from the numerical simulation and experiment for Test 1 are presented in Figure 6-49. The numerical model results is in an excellent agreement with the experiment. For further investigation, the strain data of the strain gauges at different location are evaluated with the numerical simulation, as an example, shown in Figure 6-50. The plastic rotation capacities (θ_p) were estimated as 0.04 rad and 0.044 rad for the experiment and numerical model (Figure 6-49). The post-capping rotations for constant axial load (θ_{pc}) were estimated as 0.05 rad and 0.02 rad for the experiment and numerical model, respectively. The overall deflected shape of the column did match the experiment as well, and experiences the same failure mode of lateral torsional buckling.
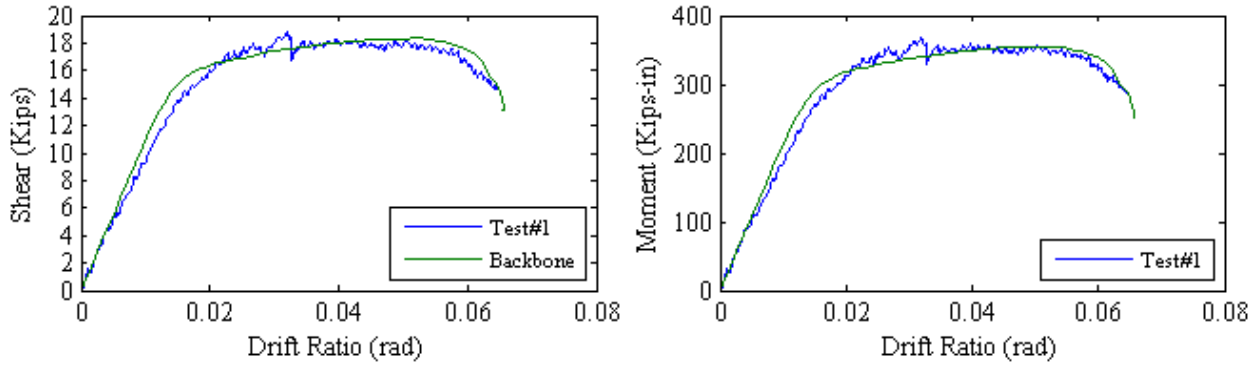
Figure 6-49. Experimental and numerical shear (left) and moment (right) drift ratio at the base of the beam for Test #1
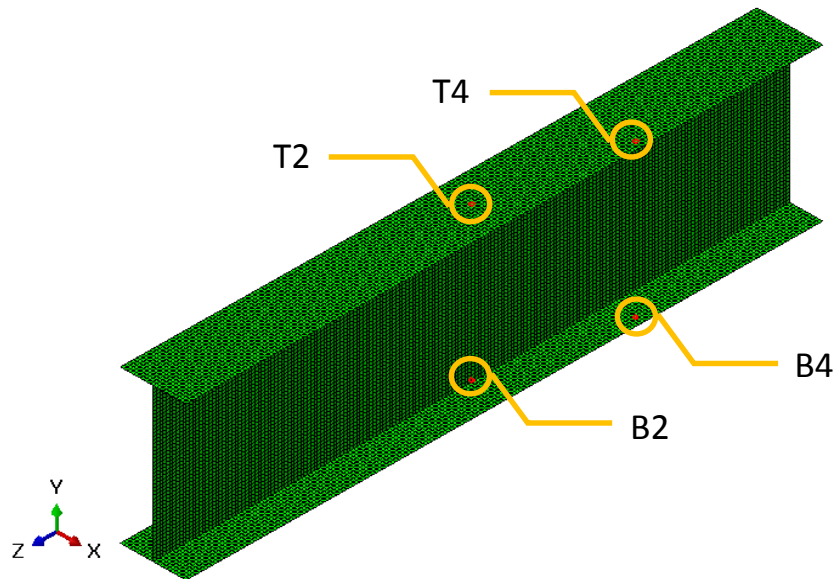
Figure 6-50. Location of selected elements to compare the strains with the strain gauges in the experiment
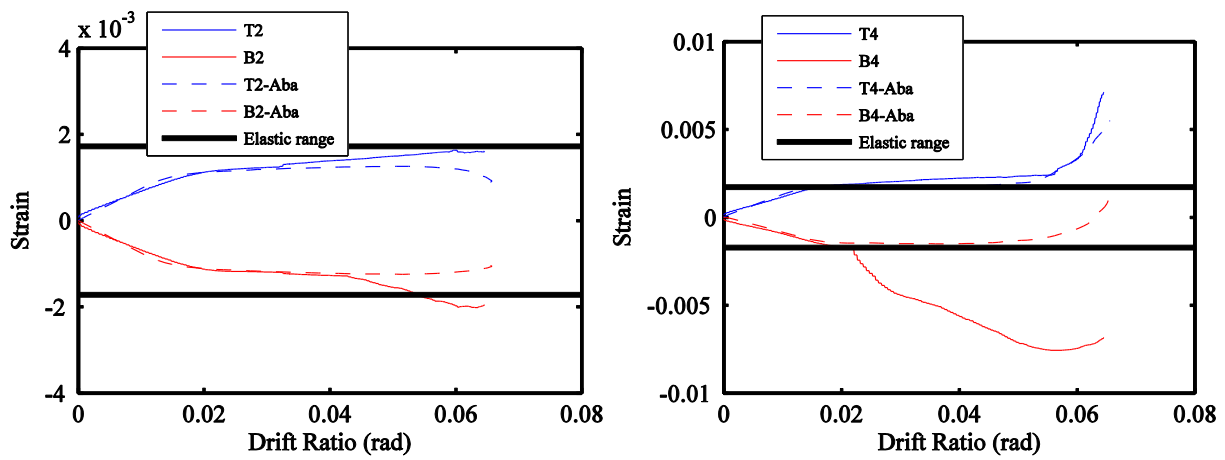
Figure 6-51. Experimental and numerical strain time history, Test 1

- **Test 2**

In this experiment, the rotation at the base of the beam was calculated using the displacement of the top of the bracket using the LVDT measurements. Therefore, in the numerical model the rotation about the X-axis is imposed (strong axis), and the rest of the degrees of freedom at the base are restrained. The boundary conditions are applied at the tip and base of the beam to reference points, RP-1 and RP-2, respectively. The reference point is coupled to the end surface of the flanges and web edges. At the tip of the column, the vertical (lateral for the beam section) and out-of-plane tip displacement, respectively in the direction of Y and X axes, are applied. The boundary conditions are depicted in Figure 6-52.

The shear and moment at the base of the column obtained from the numerical simulation and experiment for Test 2 are presented in Figure 6-49. The shear and moment do match the initial slope up to 0.02 rad; however, the numerical model under predicts the moment capacity for larger drift ratios. The maximum moment capacity of the experiment and numerical model are 1.68 and 1.37 times the estimated plastic moment capacity ($f_y.z$), respectively.

The plastic rotation capacities (θ_p) were estimated as 0.04 rad and 0.044 rad for the experiment and numerical model (Figure 6-49). The post-capping rotations for constant axial load (θ_{pc}) were estimated as 0.05 rad and 0.02 rad for the experiment and numerical model, respectively. The overall deflected shape of the column did match the experiment as well, and experiences the same failure mode of lateral torsional buckling.
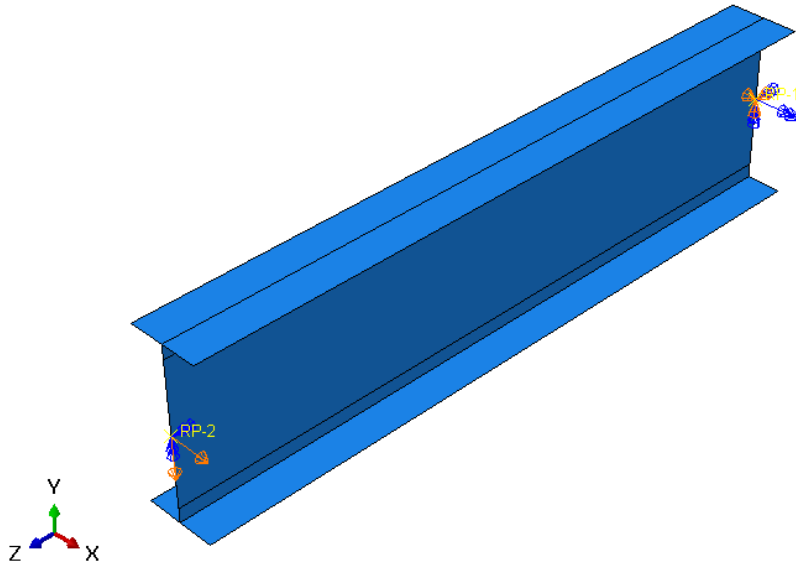
Figure 6-52. Boundary condition defined for the beam simulations for Test 2
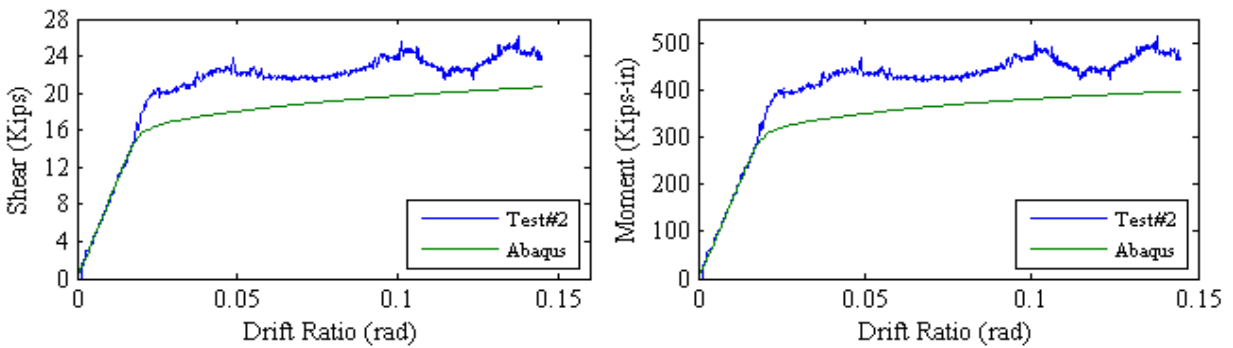
Figure 6-53. Experimental and numerical shear (left) and moment (right) drift ratio at the base of the beam for Test #2
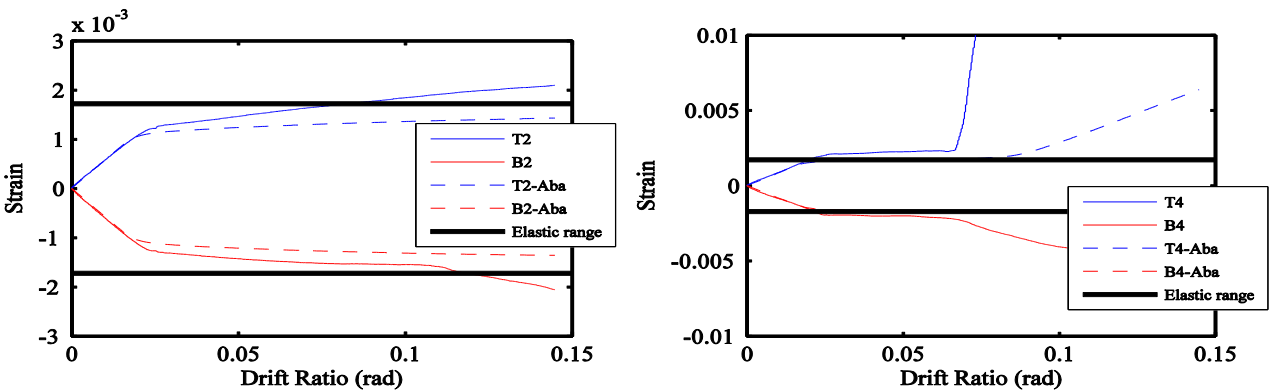
Figure 6-54. Experimental and numerical strain time history, Test 2

6.9.   Summary

In this chapter, numerical models are calibrated utilizing the experimental data (selected experiments that were performed at Buffalo and UNH) obtained in this study. Two modeling approaches are considered. First, "Only Column", in which the column is modeled and the corresponding loading and displacement histories are applied at the boundary conditions. Second, "Three Actuator Setup", in which the entire setup consisting the horizontal and vertical actuators, loading beam, and the column are modeled; and the loading and displacement histories are applied using the actuators (connector elements). The numerical simulations are carried out in the high-fidelity numerical simulation Abaqus software.

The calibrated numerical models captured the overall global response with respect to the experiments. In the elastic range, the moment-drift ratios were compatible with the experimental results. With the initiation of yielding and large drifts, there were discrepancies in the captured strength and stiffness of the numerical models compared to the experiments. This could be due to interaction and control of the horizontal and vertical actuators in the experiment; which for the quasi-static tests they were controlling the lateral displacement, total axial and rotation at the tip of the column (Test 1 to 6), and for the hybrid experiments which they were controlling the lateral displacement, vertical displacement, and tip rotation. The distribution of the forces in the vertical actuators do have a significant effect on the moment at the base of the column.

The plastic rotation capacities and post capping rotations for the column and beam numerical models were slightly larger for some of the calibrated models with respect to the experiments. This could be explained due to the decrease in the captured maximum strength, and increase in the drift magnitudes when the material became inelastic.

The final deflected shape of all the calibrated numerical models were similar to the experiments. In most of the column numerical models (except Test 2 and test 8), the axial shortening in the inelastic range and larger drifts is more pronounce compared to the measured experiment tip vertical displacement.

For the column, the dominant failure modes captured in the numerical models were web buckling and lateral torsional buckling which were consistent with the experiments, and induced strength deterioration and stiffness degradation. For the beams, lateral torsional buckling was observed as the dominant failure mode for both the experiment and numerical model.

6.10. References

ABAQUS. (2013). Dassault Systèmes Corp. (Version 6.13-3).

Abaqus, F. (2017). Abaqus Inc. *Providence, Rhode Island, United States*.

ASTM, A. (2003). 6/A6M-05" Standard Specification for General Requirements for Rolled Structural Steel Bars. *Plates, Shapes, and Sheet Piling*.

Chaboche, J.-L., & Lemaitre, J. (1990). *Mechanics of solid materials*: Cambridge University Press Cambridge.

Committee, A. (2010). Specification for structural steel buildings (ANSI/AISC 360-10). *American Institute of Steel Construction, Chicago-Illinois*.

Elkady, A., & Lignos, D. G. (2015). Analytical investigation of the cyclic behavior and plastic hinge formation in deep wide-flange steel beam-columns. *Bulletin of Earthquake Engineering, 13*(4), 1097-1118.

Fogarty, J., & El-Tawil, S. (2014). COLLAPSE BEHAVIOR OF STEEL COLUMNS UNDER COMBINED AXIAL AND LATERAL LOADING. *Arbor, 1001*, 481059-482125.

Kaufmann, E., Metrovich, B., & Pense, A. (2001). Characterization of cyclic inelastic strain behavior on properties of A572 Gr. 50 and A913 Gr. 50 rolled sections.

Newell, J. D. (2008). *Cyclic behavior and design of steel columns subjected to large drift.* UC San Diego.

Newell, J. D., & Uang, C.-M. (2006). *Cyclic behavior of steel columns with combined high axial load and drift demand*: Department of Structural Engineering, University of California, San Diego.

Ozkula, G. (2017). *Seismic behavior, modeling, and design of deep wide-flange steel columns for special moment frames*: University of California, San Diego.

Simulia, D. (2017). Abaqus 2017 documentation: Dassault Systemes Waltham, MA.

7   SUMMARY AND CONCLUSION

7.1   Summary

In order to conduct reliable numerical simulations to predict collapse, an accurate evaluation of relevant modeling parameters such as plastic rotation capacity and post-capping rotation capacity is critical. First-story exterior columns experience rotation demands at their tip when subjected to seismic events. In the experimental model in order to account for a more realistic representation of the behavior of the column, a rotation was imposed at the tip of the specimen in addition to the lateral and axial loading histories. The result was a better representation of changes in the moment gradient throughout the height of the column.

These experimental results are deemed to be valuable for an enhanced understanding of the behavior of steel columns, as well as an improved calibration of numerical models of deep steel columns that are exposed to significant strength and stiffness degradation considering a set of different loading histories.

One of the main objectives of this research was to evaluate the monotonic and cyclic deterioration characteristics of deep steel column sections, in this case a W36 column section, up to the limit state of collapse. In this study, ten 1:8 scaled W36X652 column sections are tested. The experiments consisted of; (i) two of the specimens being tested as cantilever beam members (without axial load), (ii) six of the column specimens were tested subjected to quasi-static

predefined loading histories with drift ratios and rotations of up to 0.10 and axial load demands of up to 60% of the yield axial load carrying capacity of the column, and (iii) two of the column sections being tested through hybrid simulation.

Numerical models of deep steel column section were calibrated utilizing the experimental data obtained during this study up to limit state of collapse. Two modeling approaches were considered. First, "Column Isolated", in which the column is modeled and the corresponding resultant loading and displacement histories are applied at the boundary conditions. Second, "Three-Actuator Setup", in which the entire setup consisting of horizontal and vertical actuators, the loading beam, and the column are modeled. The loading and displacement histories are applied to the experimental setup using the actuators (connector elements).

7.2   Conclusion

This research consistent of two main parts; experimental data and numerical calibrations. For the experimental part, the tests were performed at NEES@ Buffalo laboratory and HighBay Laboratory @ University of New Hampshire. The existing experimental setups at both Laboratories were evaluated, designed and fabricated to withstand the large deformations and high level loads expected for the test specimens to undergo during the tests. Monotonic and cyclic loading protocols were developed by conducting nonlinear static and dynamic analyses of a two-dimensional 1:8 scaled moment-resisting frame structure numerical model with a set of 100 recorded horizontal ground motions (50 stations). Furthermore, in order to perform the hybrid experiments, the test setup was built and created at NEES@ Buffalo laboratory. For the numerical calibration part, the data collected during the experiments performed in this research were considered for calibration of the numerical models. The calibration consistent of material model calibrations, effect of residual stresses, and boundary conditions.

The main outcomes of this research are presented in the following:

- In all the experiments, the bending moment capacity at the base of the column was higher than the estimated plastic moment capacity $(f_y.z)$. Monotonic tests demonstrated that the spread of inelasticity and its associated strain hardening produced a bending moment capacity at the base of the column on the order of 1.9 times the estimated plastic moment capacity $(f_y.z)$ for a constant axial load of 31% of the axial load carrying capacity of the specimen $(f_y.A)$; and 1.2 times the estimated plastic moment capacity $(f_y.z)$ for a variable axial load with values varied from 15% to 57% of the axial load carrying capacity of the column, respectively. The bending moment at the base vs. drift ratio relationship shows an increase in the maximum bending moment of the tests with cyclic loadings compared to the monotonic ones at the similar level of axial force at the initiation of the loading histories, which is caused by cyclic strain hardening ($1.4\ f_y.z$ to $1.6\ f_y.z$.). In addition, the bending moment capacity at the base of the columns tested through hybrid testing reached an order of 1.75 and 1.4 times the plastic moment capacity $(f_y.z)$ for two separate hybrid experiments with different earthquake intensities.

- The bending moment capacity at the base of the of the cantilever beam with the same geometry as the tested columns, showed an increase of 1.2 and 1.7 times the plastic moment capacity $(f_y.z)$. The difference in the results were due to loss of lateral restraint at the tip of the beam. These experiments showcase the importance of boundary conditions (rotation at the tip) on the response of members.

- Strength and stiffness deterioration after the onset of lateral torsional buckling occurs more rapidly during cyclic loading on the compression side.

- The plastic rotation capacities and post-capping rotation values obtained from the experimental testing indicate that they are strongly dependent on the magnitude of drift ratios, the number of loading cycles, the levels of axial load and the loading histories (symmetrical and unsymmetrical).

- The estimated plastic rotation capacities (θ_p) for the columns were in the range of 0.015 to 0.08 rad for loading histories considered in this study. The plastic rotation capacities for this column member calculated based on ASCE-SEI 41-06 and ASCE-SEI 41-13, estimates a plastic rotation capacity of 0.009 rad when the axial force is 31% of the available axial strength and negligible plastic rotation capacity for an axial load of 57% of the available axial strength, which significantly underestimate the values obtained from the tests. However, in ASCE-SEI 41-17 the modeling parameters for plastic hinges for the column have been modified. These parameters are based on the constant gravity load to axial yield capacity (axial strength). The calculated plastic rotation capacity is 0.02 rad.

- The range of estimated post-capping rotation values (θ_{pc}) were from 0.08 to 0.37 radians for the experiments performed subjected to different loading histories.

- For the tested columns, the dominant failure modes were web buckling and lateral torsional buckling, which induced strength deterioration and stiffness degradation. The inelasticity spreads out up (from the bottom) to about 75% of the length of the column, which the length of inelasticity depends on the moment gradient in the member and the imposed loading history.

- Testing the columns by using the hybrid testing method, provided column responses consistent with realistic loading histories. The hybrid simulation results showed that the hybrid substructuring technique and displacement-control approach were successful in tracing the behavior of a tall steel structure until the onset of global instability was approached. Further,

217

it was demonstrated that hybrid simulations through collapse can be very sensitive to the properties assigned to the numerical portion of the structure. During hybrid testing, variable shear force, axial load, and bending moment demands were imposed at the tip of the column, which allowed for a more accurate simulation of changes in the bending moment gradient of an exterior column that is part of moment-resisting frame. These results are deemed to be valuable for an enhanced understanding of the behavior of steel columns, as well as an improved calibration of numerical models of deep steel columns that are exposed to significant strength and stiffness degradation in the presence of variable axial load demands.

- The bending moment at the base vs. drift ratio relationship shows an increase in the maximum bending moment of the columns tested through hybrid testing on the order of 1.75 and 1.4 times the plastic moment capacity ($f_y \cdot z$) for two separate hybrid experiments with different earthquake intensities. Further, the estimated plastic rotation capacities of 0.07 rad and 0.034 rad were obtained for each of the columns (original and modified tests). One of the column specimens did not experience a noticeable loss of strength at the end of the experiment (original test). In the modified hybrid test, the post-capping rotation was estimated as 0.027 rad, in which there is significant reduction in the post-capping rotation with respect to quasi-static monotonic (0.37 rad and 0.18) and cyclic (0.9 rad and 0.11 rad) tests due to a higher axial load and a consequence of lateral torsional buckling. These results indicate that for a deep steel column such as the W36X652, the plastic rotation capacity is strongly influenced by the loading history and the level of axial load.

- Numerical models were calibrated based on the performed experimental tests to provide a model for performance prediction of deep steel column sections near the limit state of collapse. The calibrated numerical models predicted the overall global response similar to that of the

experimental tests. In the elastic range, the moment-drift ratios are compatible with the experimental results. With the initiation of yielding and large drifts, in some of the experimental tests there were discrepancies in the captured strength of the numerical models compared to the experiments. This could be due to the interaction and control of the horizontal and vertical actuators. In the setup @buffalo, all three actuators are attached to the loading beam with an eccentricity with respect to the tip of the column. Any interaction between the actuators and resulting in a small redistricution of the forces among them will results in a considerable moment at the tip of the column due to the eccentricity and larg difformtions.

- More general conclusions of deep steel column behavior relevant for numerical model calibration will necessitate additional experiments with columns of various sizes and scales that are exposed to biaxial bending moment demands, as well as ground motions with various intensities, durations, and frequency contents. The results from these tests should be interpreted within the conditions and assumptions used to conduct them. The quasi-static tests conducted with these columns as well as the hybrid tests presented herein are just initial steps geared toward characterizing the behavior of deep steel column sections more accurately.

7.3   Future Work

In every research program, there is room for improvement and expansion which can be considered for future work. The following is a list of recommendations and ideas:

- Testing a full scale $W36 \times 652$ column steel section and other deep steel column sections using the loading protocols developed during this research program.

- Further investigation with a broader range of column sizes and scales including the effect of biaxial bending moment demands with variable axial load on deep steel column sections needs to be conducted experimentally and numerically. In addition, results using different loading protocols would be beneficial in order to evaluate and calibrate numerical models to facilitate a more reliable prediction of column behavior till the limit state of collapse is approached.

- Utilizing the numerical updating approach for the hybrid simulation method in which the properties of the numerical model can be updated during the analysis based on the knowledge obtained from the response of the experimentally tested physical specimen.

- Including a customized load cell at the base of the column that can directly measure shear, axial load and moment at the base of the column in the experimental setup.

- Developing a numerical procedure for the three-actuator setup to control the rotation and total axial load simultaneously.

A1. Appendix 1

A2.   Appendix 2

An estimated average moment of inertia value is used to model the section of the girder that spans from the face of the steel column to the center of the RBS section.

Table A 2-1. Parameters of the reduced beam sections (RBS)

Floor	Beam	a (in)	b (in)	L=a+b/2 (in)	c (in)	I (in^4)	I$_{avg}$ (in^4)
R	W24X94	4.75	16	12.75	2	2700	2215
20	W24X103	4.75	16	12.75	2	3000	2452
18, 19	W30X148	5.5	20	15.5	2.25	6680	5481
16, 17	W36X182	6.25	24	18.25	2.75	11300	9190
14, 15	W36X194	6.25	24.5	18.5	2.75	12100	9818
12, 13	W36X232	6.25	24.5	18.5	2.75	15000	12109
8 thru11	W36X256	6.25	24.5	18.5	2.75	16800	13589
6, 7	W36X262	8.5	24.5	20.75	3.75	17900	14604
2 thru 5	W36X282	8.5	24.5	20.75	3.75	19600	15992

The section plastic modulus at the center of the RBS is shown in **Error! Reference source not found.**.

Table A 2-2. Section plastic modulus of reduced beam sections (RBS)

Floor	Beam	c (in)	Depth (in)	d (in)	h (t$_f$) (in)	4*(h*c)	Z (in³)	Z$_{RBS}$ (in³)
R	W24X94	2	24.30	11.71	0.875	7	254	172
20	W24X103	2	24.50	11.76	0.98	7.84	280	188
18, 19	W30X148	2.25	30.70	14.76	1.18	10.62	500	343
16, 17	W36X182	2.75	36.30	17.56	1.18	12.98	718	490
14, 15	W36X194	2.75	36.50	17.62	1.26	13.86	767	523
12, 13	W36X232	2.75	37.10	17.77	1.57	17.27	936	629
8 thru11	W36X256	2.75	37.40	17.84	1.73	19.03	1040	701
6, 7	W36X262	3.75	36.90	17.73	1.44	21.6	1100	717

1 thru 5	W36X282	3.75	37.10	17.77	1.57	23.55	1190	772		

Table A 2-3. Rotational spring stiffness of beam sections

STORY	BEAM SECTION	Length from face to face of columns (in)		length from center of RBS to center of RBS (in)		E (ksi)	I (in^4)	I_e (in^4)	Rotational Spring Stiffness, K_s (kip/in)	
		Exterior beams	Interior beams	Exterior beams	Interior beams				Exterior beams	Interior beams
21	W24X94	323.5	323.5	298	298	29000	2700	2970	17341611	17341611
20	W24X103	323.5	323.5	298	298	29000	3000	3300	19268456	19268456
19	W36X148	323.5	323.5	292.5	292.5	29000	6680	7348	43711179	43711179
18	W36X148	323.5	323.5	292.5	292.5	29000	6680	7348	43711179	43711179
17	W36X182	323.4	323.3	286.9	286.8	29000	11300	12430	75385849	75412134
16	W36X182	323.4	323.3	286.9	286.8	29000	11300	12430	75385849	75412134
15	W36X194	322.9	322.7	285.9	285.7	29000	12100	13310	81005247	81061953
14	W36X194	322.9	322.7	285.9	285.7	29000	12100	13310	81005247	81061953
13	W36X232	322.5	322.3	285.5	285.3	29000	15000	16500	100560420	100630915
12	W36X232	322.5	322.3	285.5	285.3	29000	15000	16500	100560420	100630915
11	W36X256	321.8	321.6	284.8	284.6	29000	16800	18480	112904494	112983837
10	W36X256	321.8	321.6	284.8	284.6	29000	16800	18480	112904494	112983837
9	W36X256	321.6	321.6	284.6	284.6	29000	16800	18480	112983837	112983837
8	W36X256	321.6	321.6	284.6	284.6	29000	16800	18480	112983837	112983837
7	W36X262	320.65	321.1	279.15	279.6	29000	17900	19690	122731865	122554335
6	W36X262	320.65	321.1	279.15	279.6	29000	17900	19690	122731865	122554335
5	W36X282	320.45	320.7	278.95	279.2	29000	19600	21560	134484316	134363897
4	W36X282	320.45	320.7	278.95	279.2	29000	19600	21560	134484316	134363897
3	W36X282	319.8	320.7	278.3	279.2	29000	19600	21560	134798419	134363897
2	W36X282	319.8	320.7	278.3	279.2	29000	19600	21560	134798419	134363897

Table A 2-4. Rotational stiffness of exterior columns springs

Story	Section	L (in)	E (ksi)	I (in^4)	I$_e$ (in^4)	K$_s$ (kip/in)
20	W36X231	131.6	29000	15600	17160	226887538
	W36X231		29000	15600	17160	
19	W36X231	128.4	29000	15600	17160	232542056
	W36X231		29000	15600	17160	
18	W36X231	125.3	29000	15600	17160	238295291
	W36X231		29000	15600	17160	
17	W36X231	122.5	29000	15600	17160	243742041
	W36X231		29000	15600	17160	
16	W36X231	119.7	29000	15600	17160	249443609
	W36X231		29000	15600	17160	
15	W36X231	71.6	29000	15600	17160	417016760
	W36X262	48	29000	17900	19690	713762500
14	W36X262	119.5	29000	17900	19690	286699582
	W36X262		29000	17900	19690	
13	W36X262	71.2	29000	17900	19690	481188202
	W36X302	48	29000	21100	23210	841362500
12	W36X302	118.9	29000	21100	23210	339658537
	W36X302		29000	21100	23210	
11	W36X302	70.75	29000	21100	23210	570818375
	W36X361	48	29000	25700	28270	1024787500
10	W36X361	118.6	29000	25700	28270	414753794
	W36X361		29000	25700	28270	
9	W36X361	70.6	29000	25700	28270	696739377
	W36X395	48	29000	28500	31350	1136437500
8	W36X395	118.6	29000	28500	31350	459940978
	W36X395		29000	28500	31350	
7	W36X395	70.85	29000	28500	31350	769922371
	W36X487	48	29000	36000	39600	1435500000
6	W36X487	119.1	29000	36000	39600	578539043
	W36X487		29000	36000	39600	
5	W36X487	71	29000	36000	39600	970478873
	W36X529	48	29000	39600	43560	1579050000
4	W36X529	118.9	29000	39600	43560	637463415
	W36X529		29000	39600	43560	
3	W36X529	70.9	29000	39600	43560	1069032440
	W36X652	48	29000	50600	55660	2017675000
2	W36X652	118.9	29000	50600	55660	814536585
	W36X652		29000	50600	55660	
1	W36X652	136.65	29000	50600	55660	708733260
	W36X652		29000	50600	55660	

Table A 2-5. Rotational stiffness of interior columns springs

Story	Section	L (in)	E (ksi)	I (in^4)	I$_e$ (in^4)	K$_s$ (kip/in)
20	W36X231	131.6	29000	15600	17160	226887538
	W36X231		29000	15600	17160	
19	W36X231	128.4	29000	15600	17160	232542056
	W36X231		29000	15600	17160	
18	W36X231	125.3	29000	15600	17160	238295291
	W36X231		29000	15600	17160	
17	W36X231	74.5	29000	15600	17160	400783893
	W36X247	48	29000	16700	18370	665912500
16	W36X247	119.7	29000	16700	18370	267032581
	W36X247		29000	16700	18370	
15	W36X247	71.6	29000	16700	18370	446421788
	W36X302	48	29000	21100	23210	841362500
14	W36X302	119.5	29000	21100	23210	337953138
	W36X302		29000	21100	23210	
13	W36X302	71.2	29000	21100	23210	567210674
	W36X330	48	29000	23300	25630	929087500
12	W36X330	118.9	29000	23300	25630	375073171
	W36X330		29000	23300	25630	
11	W36X330	70.75	29000	23300	25630	630334982
	W36X395	48	29000	28500	31350	1136437500
10	W36X395	118.6	29000	28500	31350	459940978
	W36X395		29000	28500	31350	
9	W36X395	118.6	29000	28500	31350	459940978
	W36X395		29000	28500	31350	
8	W36X395	118.6	29000	28500	31350	459940978
	W36X395		29000	28500	31350	
7	W36X395	70.85	29000	28500	31350	769922371
	W36X441	48	29000	32100	35310	1279987500
6	W36X441	119.1	29000	32100	35310	515863980
	W36X441		29000	32100	35310	
5	W36X441	71	29000	32100	35310	865343662
	W36X487	48	29000	36000	39600	1435500000
4	W36X487	118.9	29000	36000	39600	579512195
	W36X487		29000	36000	39600	
3	W36X487	118.9	29000	36000	39600	579512195
	W36X487		29000	36000	39600	
2	W36X487	118.9	29000	36000	39600	579512195
	W36X487		29000	36000	39600	
1	W36X487	136.65	29000	36000	39600	504237102
	W36X487		29000	36000	39600	

Table A 2-6. Point loads and desitributed loads on columns and girders

Floor	Load = 1.05D + 0.25L		
	Ext. Point Loads (kips)	Int. Column Point Load (Kips)	Distributed Load (Kip/in) on beam
R	15.6	26.7	0.085
20	23.5	30.7	0.191
19	23.5	30.7	0.195
18	23.5	30.7	0.195
17	23.5	30.7	0.198
16	23.5	30.7	0.198
15	23.5	30.7	0.199
14	23.5	30.7	0.199
13	23.5	30.7	0.203
12	23.5	30.7	0.203
11	23.5	30.7	0.205
10	23.5	30.7	0.205
9	23.5	30.7	0.205
8	23.5	30.7	0.205
7	23.5	30.7	0.205
6	23.5	30.7	0.205
5	23.5	30.7	0.207
4	23.5	30.7	0.207
3	23.5	30.7	0.207
2	23.5	30.7	0.207

A3. Appendix 3

GENERAL NOTES:

CONTACT INFORMATION :
DR. RICARDO MEDINA,
University of New Hampshire Department of Civil Engineering,
Kingsbury Hall Room W137, 33 Academic Way, Durham, NH 03824
PHONE: (603) 866-4726

DELIVERY INFORMATION :
ALL PIECES SHOULD BE DELIVERED TO NEES BUFFALO LABORATORY,
DUANE KOZLOWSKI
KETTER HALL, BUFFALO, NY 14260
PHONE: (716) 645-2217

1. FOR CONDITIONS NOT CLEARLY UNDERSTOOD SUBMIT SKETCHES AND/OR REQUEST FOR
   INFORMATION TO THE DESIGN ENGINEER FOR RESOLUTION.

2. OMISSIONS, CONFLICTS OR MISUNDERSTANDINGS BETWEEN THE VARIOUS ELEMENTS OF THE
   CONTRACT DOCUMENTS, IF ANY, SHALL BE BROUGHT TO THE ATTENTION OF THE DESIGN
   ENGINEER FOR RESOLUTION BEFORE PROCEEDING WITH THE WORK.

3. VISUAL WELDING INSPECTION:
   VISUAL INSPECTION BY A QUALIFIED INSPECTOR PRIOR TO, DURING AND AFTER WELDING SHOULD
   BE PERFORMED AS THE PRIMARY METHOD TO EVALUATE THE CONFORMANCE OF WELDED JOINTS
   TO THE APPLICABLE QUALITY REQUIREMENTS. THE VISUAL INSPECTION SHOULD INCLUDE JOINTS
   EXAMINATION PRIOR TO THE COMMENCEMENT OF WELDING, PREPARATION, GAPS, ALIGNMENT AND
   OTHER VARIABLES; ADHERENCE TO THE WELDING PROCEDURE SPECIFICATION (WPS); SATISFACTORY
   TO THE COMPLETED WELD TO AWS D1.1.

4. STRUCTURAL STEEL:

4.1. STRUCTURAL STEEL SHALL BE SUPPLIED, DETAILED AND ERECTED IN ACCORDANCE WITH A.I.S.C SPECIFICATIONS LATEST EDITIONS.

4.2. MEMBER/ELEMENT SPECIFICATION
   a. W Shapes   ASTM A992 GR 50
      FABRICATORS (ARCELORMITTAL INTERNATIONAL, GARDAU AMERISTEEL, NUCOR BERKELEY, NUCOR-YAMATO STEEL CO., STEEL DYNAMICS)

   b. CHANNELS   ASTM A36
      FABRICATORS (GARDAU AMERISTEEL, NUCOR BAR MILLS)

   c. ALL PLATES   ASTM A572 GR 50

5. CONNECTION

5.1. BOLTS:
   SHALL NOT BE PROVIDED BY THE FABRICATOR AND WILL BE BOUGHT INDEPENDENTLY.

5.2. ALL HOLES ARE STANDARD HOLE SIZE.

   FOR 1" BOLTS THE HOLE DIAMETER IS $1\frac{1}{16}$"
   FOR $\frac{3}{4}$" BOLTS THE HOLE DIAMETER IS $\frac{13}{16}$"

5.3. WELDING ELECTRODES   E70XX

5.4. ALL WELDING FILLER METAL SHALL HAVE A MINIMUM CHARPY V-NOTCH TOUGHNESS OF 20
   FT-LBS AT MINUS 20 DEGREES F.; SHALL ALSO MEET THE SUPPLEMENTAL TOUGHNESS
   REQUIREMENTS FOR WELD FILLER METAL PER APPENDIX A AND C OF FEMA-353.

5.6. BUTT WELDS SHALL BE COMPLETE PENETRATION WELDS AND THEY ARE INCLUDED IN THE BUILT UP COLUMN.

5.5. WELDING SHALL CONFIRM TO A.W.S. SPECIFICATIONS AND BE PERFORMED BY CERTIFIED
   WELDERS.

6. ERECTION SHALL BE DONE BY UNIVERSITY OF BUFFALO LAB PERSONAL AND GRADUATE
   STUDENTS.

TABLE OF MATERIALS

Item number	Specimen				
	Specification		Drawing #	QTY	Weight (lb)
1	Column (Test specimen)	W8x24x19.4 (scaled)	S-1	8	310
2	Base plate (bottom)	PL12x8x1.5	S-1	8	327
3	Base plate (top)	PL13.5x9.5x1.5	S-1	8	436
	To modify small bearing machine				
4	Diagonals	C5x9x48.076	S-3 , S-4	4	144
5	Attachment plates of diagonals(Hor.)	PL13x16.5x1.0	S-3 , S-4	2	122
6	Attachment plates of diagonals (Ver.)	PL 14x16x1.0	S-3 , S-4	2	127
7	Plate over white pedestal	PL 24x16x1.5	S-2	1	163

LEGEND

-FILLET WELD WITH LEG SIZE a

-COMPLETE-JOINT-PENETRATION GROOVE WELD
(SQUARE GROOVE WELD, BUTT JOINT)

- ILLUSTRATES THE THREAD INFORMATION N x D"-B THRD, RH
"N" IS THE NUMBER OF HOLES
"D" IS THE NOMINAL SIZE OF THE BOLT
"B" IS THE NO. OF THREADS PER INCH
"THRD" MEANS THREAD
"RH" RIGHT HAND THREAD

-ELEVATION   ELEV.

NEES HYBRID TESTING

SINGLE COLUMN TEST SETUP

	NAME	DATE
DESIGNED	Dr. MEDINA	
CHECKED		
REVISION		
DESCRIPTION		DATE

TITLE:
GENERAL NOTES & BOM Table

SIZE: B
DWG. NO.: S-0
REV:
COMMENTS:
SCALE: -   UNIT: INCHES   SHEET 1 OF 9

HORIZONTAL ACTUATOR
(55 kips, +/- 6.00")

REACTION FRAME

LOADING BEAM (ORANGE BEAM)

W14 X 257 (EXISTING)

2 x LATERAL FRAME
(YELLOW FRAME/EXISTING)

2 x VERTICAL ACTUATOR
(70 kips, +/- 2.00")

W14x159
(EXISTING)

W14 X 145
(EXISTING)

W8 X 31
(EXISTING)

BOTTOM BEAM (RED BEAM)

W14 X 257 (EXISTING)

W14 X 145

(EXISTING)

NOTE: FOR GENERAL NOTES SEE DRAWING S-0

	NAME	DATE	NEES HYBRID TESTING
			SINGLE COLUMN TEST SETUP
DESIGNED	Dr. MEDINA		TITLE:
CHECKED			
REVISION			Modified small bearing machine layout
DESCRIPTION		DATE	

SIZE	DWG. NO.		REV
B	S-A		

COMMENTS:

SCALE: 1:25 | UNIT: INCHES | SHEET 2 OF 9

Modified W8X24

DETAIL A

QTY=8

$6\frac{1}{2}$"

$2\frac{1}{4}$" $2\frac{1}{4}$"

$7\frac{5}{16}$"

$2\frac{3}{8}$"

W8X24

W8X24

Original Section, the hatch parts should be cut in order to fabricate the scaled column section.

SCALE 1:5

DETAIL O

QTY=8

2"

$8\frac{7}{10}$"

$5\frac{9}{16}$"

$\frac{1}{4}$"

Modified W8X24

Modified W8x24

TEST SPECIMEN   SCALE 1:5

E70 $1\frac{1}{2}$in

E70 $\frac{3}{8}$ in

Modified W8X24

DETAIL W

The web and the K region should be welded with $\frac{3}{8}$ in and the rest is welded with $\frac{1}{2}$ in weld

$9\frac{1}{2}$"

$4\frac{3}{4}$" $4\frac{3}{4}$"

$1'-1\frac{1}{2}$"

$6\frac{3}{4}$"

$6\frac{3}{4}$"

SEE DETAIL W

SECTION B-B

$9\frac{1}{2}$"

$1\frac{3}{4}$" $1\frac{3}{4}$"

$1'-1\frac{1}{2}$"

$1\frac{3}{4}$"

$1\frac{3}{4}$"

4x∅ 1" BOLTS
4x∅ $1\frac{1}{16}$" HOLES

DETAIL M

QTY=8

1'

6"   6"

8"

4"   4"

SEE DETAIL W

SECTION A-A

1'

$1\frac{3}{4}$" $1\frac{3}{4}$"

8"

$1\frac{3}{4}$"

$4\frac{1}{2}$"

$1\frac{3}{4}$"

4x∅ 1" BOLTS
4x∅ $1\frac{1}{16}$" HOLES

DETAIL N

QTY=8

NOTE: FOR GENERAL NOTES SEE DRAWING S-0

	NEES HYBRID TESTING		
	NAME	**DATE**	SINGLE COLUMN TEST SETUP
DESIGNED	Dr. MEDINA		
CHECKED			TITLE:
REVISION			Column (Test specimen) Attachment to BP and sections
DESCRIPTION		**DATE**	QTY=8
			SIZE **B** / DWG. NO. **S-1** / REV
COMMENTS:			SCALE: 1:10 / UNIT: INCHES / SHEET 3 OF 9

PL 24X16 (NEW)
THICK.= $1\frac{1}{2}$"

N

C

D

F
S-3

W14x159
(EXISTING)

G
S-4

2 C5x9 (NEW)

63°

2 C5x9 (NEW)

A   A

B   B

1'-10$\frac{1}{2}$"

1'-10$\frac{1}{2}$"

2'-6"

2'-6"

N

$5\frac{5}{8}$" $5\frac{5}{8}$"

7"

E70 $\frac{1}{4}$ in

J
S-3

N

$5\frac{5}{8}$" $5\frac{5}{8}$"

7"

E70 $\frac{1}{4}$ in

K
S-4

3'-8"

SECTION C-C

SECTION D-D

H
S-3

$6\frac{3}{4}$" $6\frac{1}{4}$"

1'-4$\frac{1}{2}$"

$5\frac{5}{8}$" $5\frac{5}{8}$"

$\frac{1}{4}$ in E70

I
S-4

$6\frac{1}{4}$" $6\frac{3}{4}$"

1'-4$\frac{1}{2}$"

E70 $\frac{1}{4}$ in

SECTION A-A

SECTION B-B

2'

$7\frac{3}{4}$" $7\frac{3}{4}$"

$2\frac{1}{2}$" $2\frac{1}{2}$"

2"

$5\frac{3}{4}$"

1'-4"

1'

$5\frac{3}{4}$"

2"

PL 24X16
THICK.= $1\frac{1}{2}$"

4x∅ 1" BOLTS
4x1"-8 THRD, RH

4x∅ 1" BOLTS
4x∅ $1\frac{1}{16}$" HOLES

NOTE: THE THREADED HOLES SHOULD GO ALL
THE WAY DOWN THE THICKNESS OF THE PLATE

DETAIL N
QTY=1 SCALE 1:10

NOTE: FOR GENERAL NOTES SEE DRAWING S-0

NEES HYBRID TESTING		
	NAME	DATE
DESIGNED	Dr. MEDINA	
CHECKED		
REVISION		
DESCRIPTION		DATE

SINGLE COLUMN TEST SETUP

TITLE:
Pedestal and diagonals
attachment layout

SIZE	DWG. NO.	REV
B	S-2	

COMMENTS:

SCALE: 1:20 | UNIT: INCHES | SHEET 4 OF 9

DETAIL F

J
—

L
—

H
—

1'-9½"

3'-7"

2 C5x9
(NEW)

63°

DETAIL J

1'-4"

4½"   7"   4½"

2"

4⅛"

1'-2"

5¹³⁄₁₆"

2⅜"

4"   8"   4"

PL14X16
THICK.=1"

6xØ 1" BOLTS
6xØ 1¹⁄₁₆" HOLES

4⁹⁄₁₆"   6⅞"   4⅝"

DETAIL   J
QTY=1

DETAIL H

1'-1"

2¹⁄₁₆"   9³⁄₁₆"   1¾"

1'-4½"

1¾"

3⅜"

6"

3⅜"

1¾"

PL13X16.5
THICK.=1"

6xØ 1" BOLTS
6xØ 1¹⁄₁₆" HOLES

DETAIL   H
QTY=1

DETAIL L

10"

5"

2 C5x9
(NEW)

2½"

5"

4'-6⁵⁄₁₆"

DETAIL   L
QTY=2

NOTE: FOR GENERAL NOTES SEE DRAWING S−0

	NAME	DATE	NEES HYBRID TESTING
			SINGLE COLUMN TEST SETUP
DESIGNED	Dr. MEDINA		TITLE:
CHECKED			Left diagonal
REVISION			Detail F
DESCRIPTION		DATE	

SIZE: B   DWG. NO. S-3   REV

COMMENTS:

SCALE: 1:10   UNIT: INCHES   SHEET 5 OF 9

8 7 6 5 4 3 2 1

K
—

M
—

I
—

1'-9½"

3'-7"

2 C5x9
(NEW)

DETAIL G

QTY=1

1'-4"

4½" 7" 4½"

1'-2"

1¾"
4"
4"
4"
4½"

6xø 1" BOLTS
6xø 1¹/₁₆" HOLES

PL14X16
THICK.=1"

DETAIL K

QTY=1

1'-1"

1¹¹/₁₆" 9³/₁₆" 2⅛"

PL13X16.5
THICK.=1"

1¾" 1¾"
3½"
6¹/₁₆"
3½"
1¾"

1'-4½"

2³/₁₆"

6xø 1" BOLTS
6xø 1¹/₁₆" HOLES

DETAIL I

QTY=1

2½"

10"

5"

2 C5x9

5"

4'-6⁵/₁₆"

DETAIL M

QTY=2

NOTE: FOR GENERAL NOTES SEE DRAWING S−0

	NEES HYBRID TESTING	
	NAME	DATE
DESIGNED	Dr. MEDINA	
CHECKED		

SINGLE COLUMN TEST SETUP

TITLE:

Right Diagonal

Detail G

REVISION	
DESCRIPTION	DATE

SIZE **B** | DWG. NO. **S-4** | REV

SCALE: 1:10 | UNIT: INCHES | SHEET 6 OF 9

COMMENTS:

WEB STIFFENER
12.0 x 3.0 in

WEB STIFFENER
12.0 x 3.0 in

WEB STIFFENER
12.0 x 3.0 in

WEB STIFFENER
12.0 x 3.0 in

WEB STIFFENER
12.0 x 3.0 in

W 14 x 257

Loading beam (Orange beam)

70 Kip actuator
Swivel (16inX16in)

70 Kip actuator
Swivel (16inX16in)

SECTION A-A

$6\frac{3}{4}$" 1' $2'-2\frac{1}{4}$" 1' $2'-2$" 1' $2'-2\frac{1}{4}$" 1' $8\frac{3}{4}$"

2"

12'

LOADING BEAM (ORANGE BEAM), SIDE VIEW
W14 X 257 (EXISTING)

Drill 8xØ $\frac{13}{16}$" new holes for $\frac{3}{4}$" diameter bolts
for attaching the 70 kip actuator swivels

$10\frac{1}{2}$" 1' 1' $10\frac{1}{2}$"

Existing holes
for attaching the Top base plate of the column
Hatched holes are the the existing holes that are going to be used for attaching the columns Top base plate and vertical actuators swivels

HOLE PATTERN ON THE LOADING BEAM, BOTTOM VIEW

70 Kip actuator
Swivel

M
S-1

70 Kip actuator
Swivel

ATTACHED PLATES AND SECTIONS ON THE LOADING BEAM, BOTTOM VIEW

DETAIL C

NOTE: FOR GENERAL NOTES SEE DRAWING S-0

		NEES HYBRID TESTING	
	NAME	DATE	SINGLE COLUMN TEST SETUP
DESIGNED	Dr. MEDINA		
CHECKED			TITLE:
REVISION			Loading beam (Top Beam)
DESCRIPTION		DATE	

SIZE **B** | DWG. NO. **S-5** | REV

SCALE: 1:20 | UNIT: INCHES | SHEET 7 OF 9

8   7   6   5   4   3   2   1

70 Kip actuator
Swivel (9inX16in)

WEB STIFFENER
12.0 x 3.0 in

W 14 x 257

70 Kip actuator
Swivel (9inX16in)

WEB STIFFENER
12.0 x 3.0 in

WEB STIFFENER
12.0 x 3.0 in

WEB STIFFENER
12.0 x 3.0 in

WEB STIFFENER
12.0 x 3.0 in

Bottom beam (Red beam)

SECTION A-A

7" 1' 2'-2¼" 1' 2'-2" 1' 2'-2¼" 1' 9⅛"

12'-0⅛"
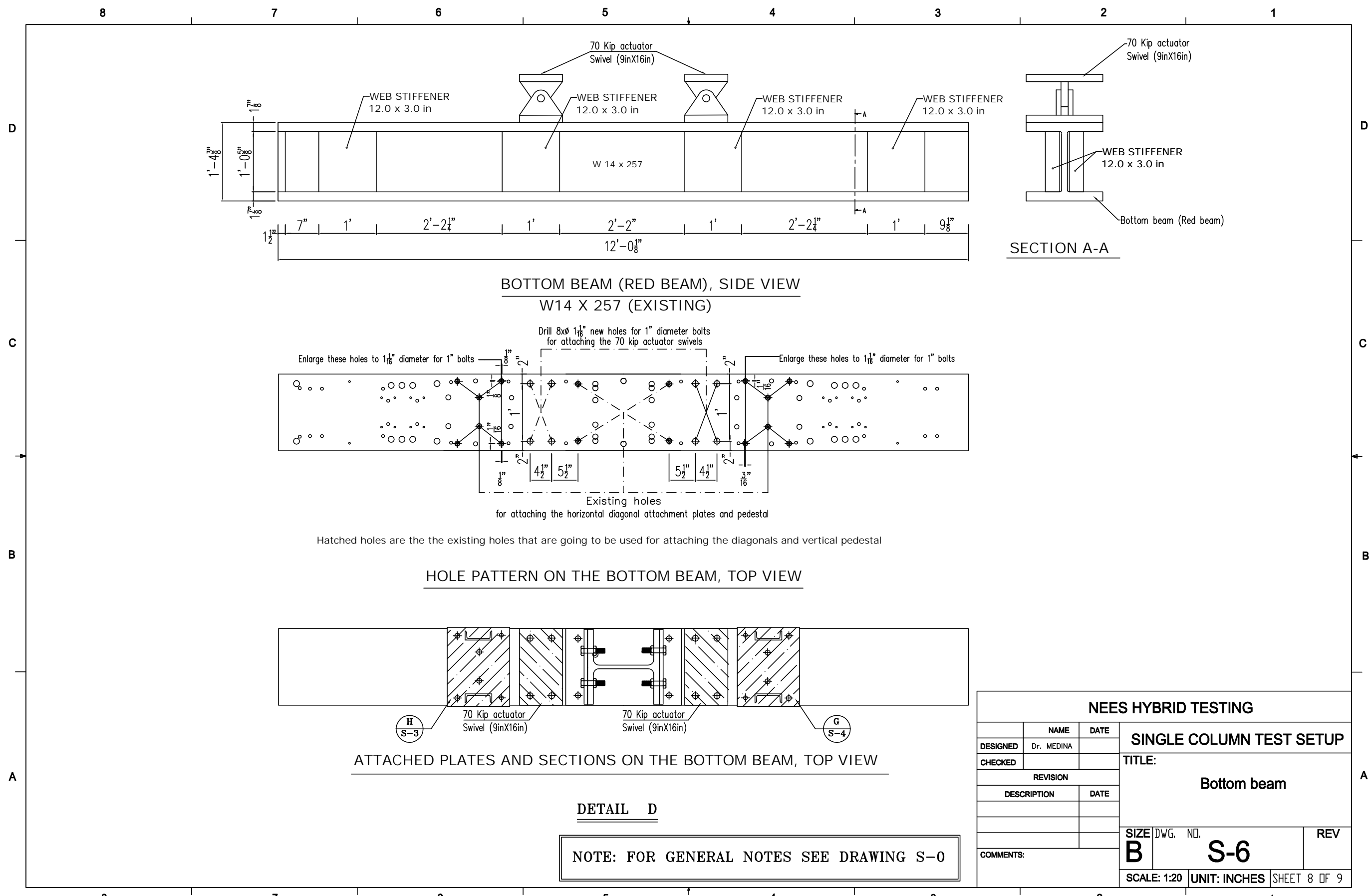
BOTTOM BEAM (RED BEAM), SIDE VIEW
W14 X 257 (EXISTING)

Drill 8xØ 1¹⁄₁₆" new holes for 1" diameter bolts
for attaching the 70 kip actuator swivels

Enlarge these holes to 1¹⁄₁₆" diameter for 1" bolts

Enlarge these holes to 1¹⁄₁₆" diameter for 1" bolts

4½" 5½" 5½" 4½"

Existing holes
for attaching the horizontal diagonal attachment plates and pedestal

Hatched holes are the the existing holes that are going to be used for attaching the diagonals and vertical pedestal
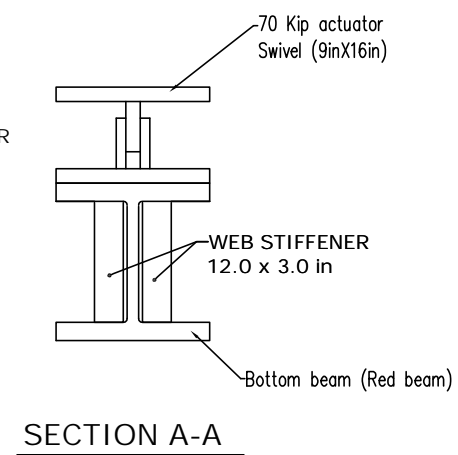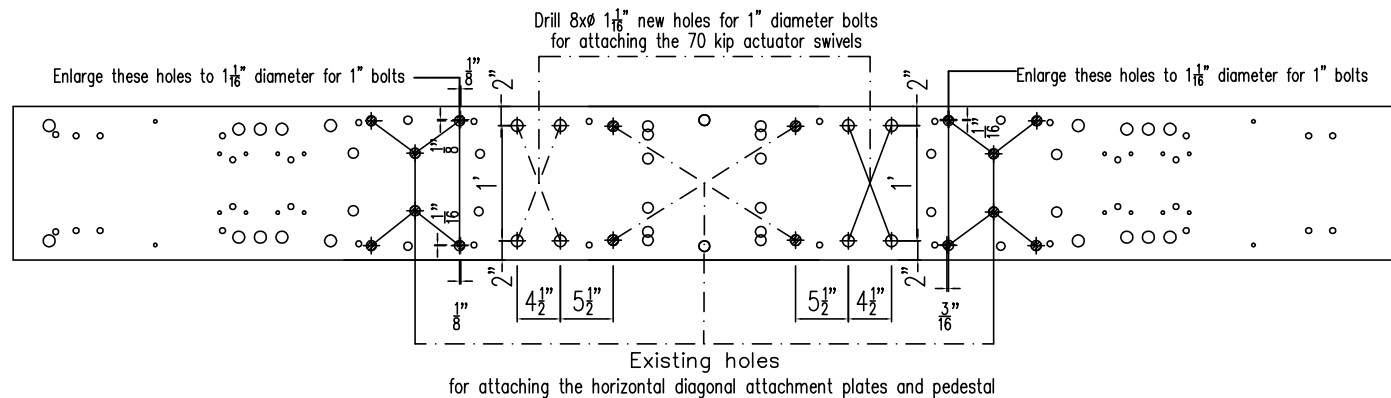
HOLE PATTERN ON THE BOTTOM BEAM, TOP VIEW

70 Kip actuator
Swivel (9inX16in)

70 Kip actuator
Swivel (9inX16in)

H / S-3

G / S-4
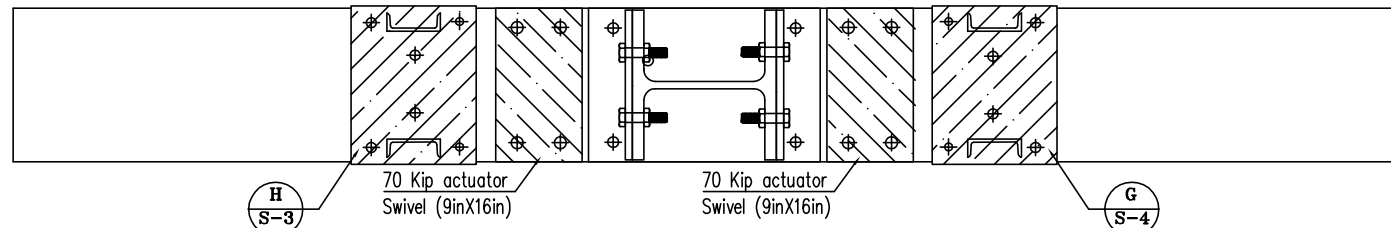
ATTACHED PLATES AND SECTIONS ON THE BOTTOM BEAM, TOP VIEW

DETAIL   D

NOTE: FOR GENERAL NOTES SEE DRAWING S-0

	NEES HYBRID TESTING		
	NAME	DATE	SINGLE COLUMN TEST SETUP
DESIGNED	Dr. MEDINA		
CHECKED			TITLE:
REVISION			Bottom beam
DESCRIPTION		DATE	
COMMENTS:			SIZE **B**	DWG. NO. **S-6**	REV
			SCALE: 1:20	UNIT: INCHES	SHEET 8 OF 9

2 TRANSFER BALLS ON EACH LEG OF LATERAL FRAME

ATTACHED PLATE TO THE BEAM

LOADING BEAM
(TOP BEAM)

LATERAL FRAME
(YELLOW FRAME)

ATTACHED PLATE
TO THE TRANSFER
BALLS

DETAIL E

2 TRANSFER BALLS ON EACH LEG OF LATERAL FRAME

ATTACHED PLATE TO THE BEAM

STIFFENERS

ELEV. 7'−1$\frac{1}{8}$"
FROM TOP OF
THE BOT. BEAM'S
FLANGE

ATTACHED PLATE
TO THE TRANSFER
BALLS

LOADING BEAM
(TOP BEAM)

LATERAL FRAME
(YELLOW FRAME)

SIDE VIEW
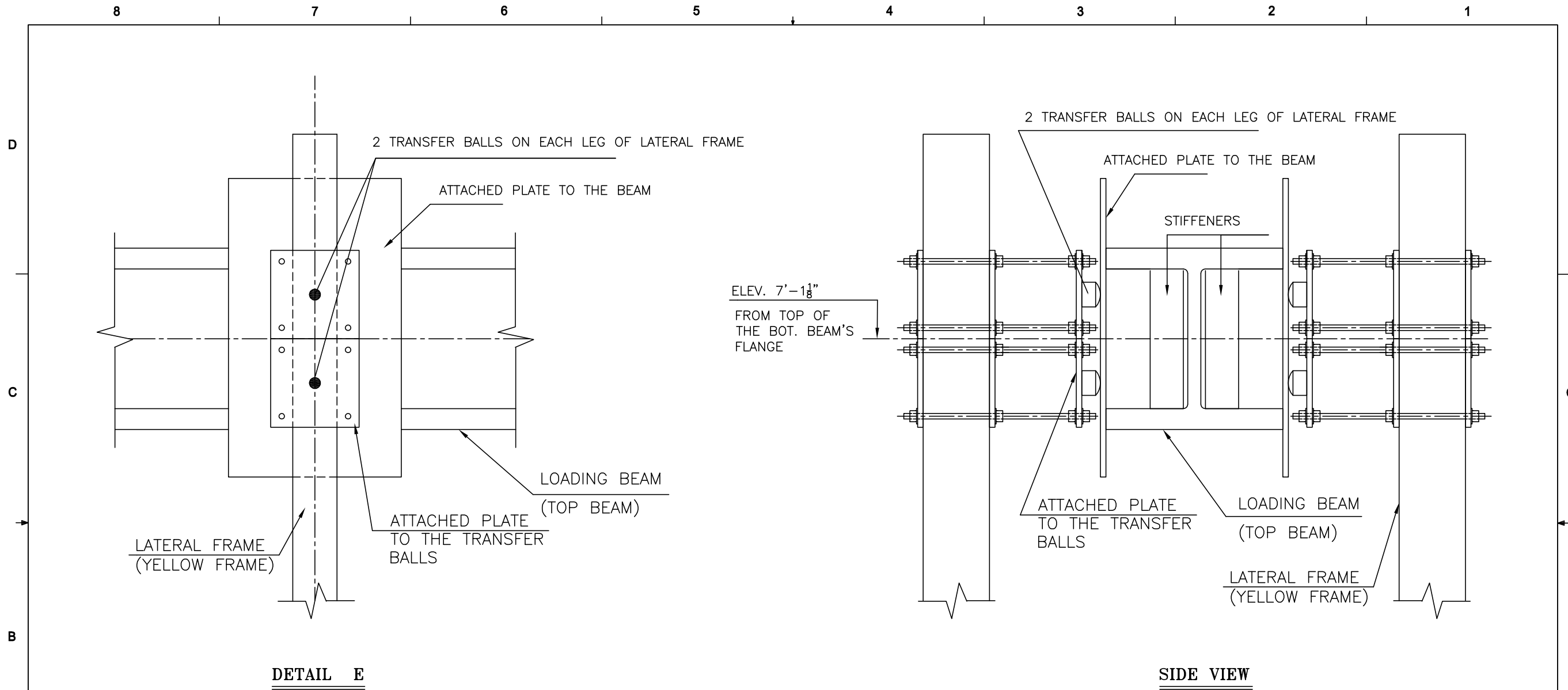
Note: The position of transfer balls should be adjusted to the loading beam's (top beam). The lower level of the upper transfer ball attached plate, should be positioned along the mid height of the loading beam, and the upper level of the lower transfer ball attached plate, should be positioned along the mid height of the loading beam.

NOTE: FOR GENERAL NOTES SEE DRAWING S−0

	NEES HYBRID TESTING	
	SINGLE COLUMN TEST SETUP	

	NAME	DATE
DESIGNED	Dr. MEDINA	
CHECKED		
REVISION		
DESCRIPTION		DATE

TITLE:
Transfer Balls Position

SIZE	DWG. NO.	REV
B	**S-7**	

SCALE: 1:10 | UNIT: INCHES | SHEET 4 OF 15

COMMENTS:

A4. Appendix 4

A5. Appendix 5

Loading Beam

Sleeve

Hydraulic Piston

Load Cell

Semi-Spher bearing

Modified W8X24

Bracket

Exciting Beams

Plan View

Test Setup

B

Loading Beam

Hydraulic Piston

Sleeve

Load Cell

Modified W8X24

Semi-Spher bearing

Bracket

Exciting Beams

Section A-A

A

Loading Beam

Hydraulic Piston

Sleeve

Load Cell

Semi-Spher bearing

Lateral Frame
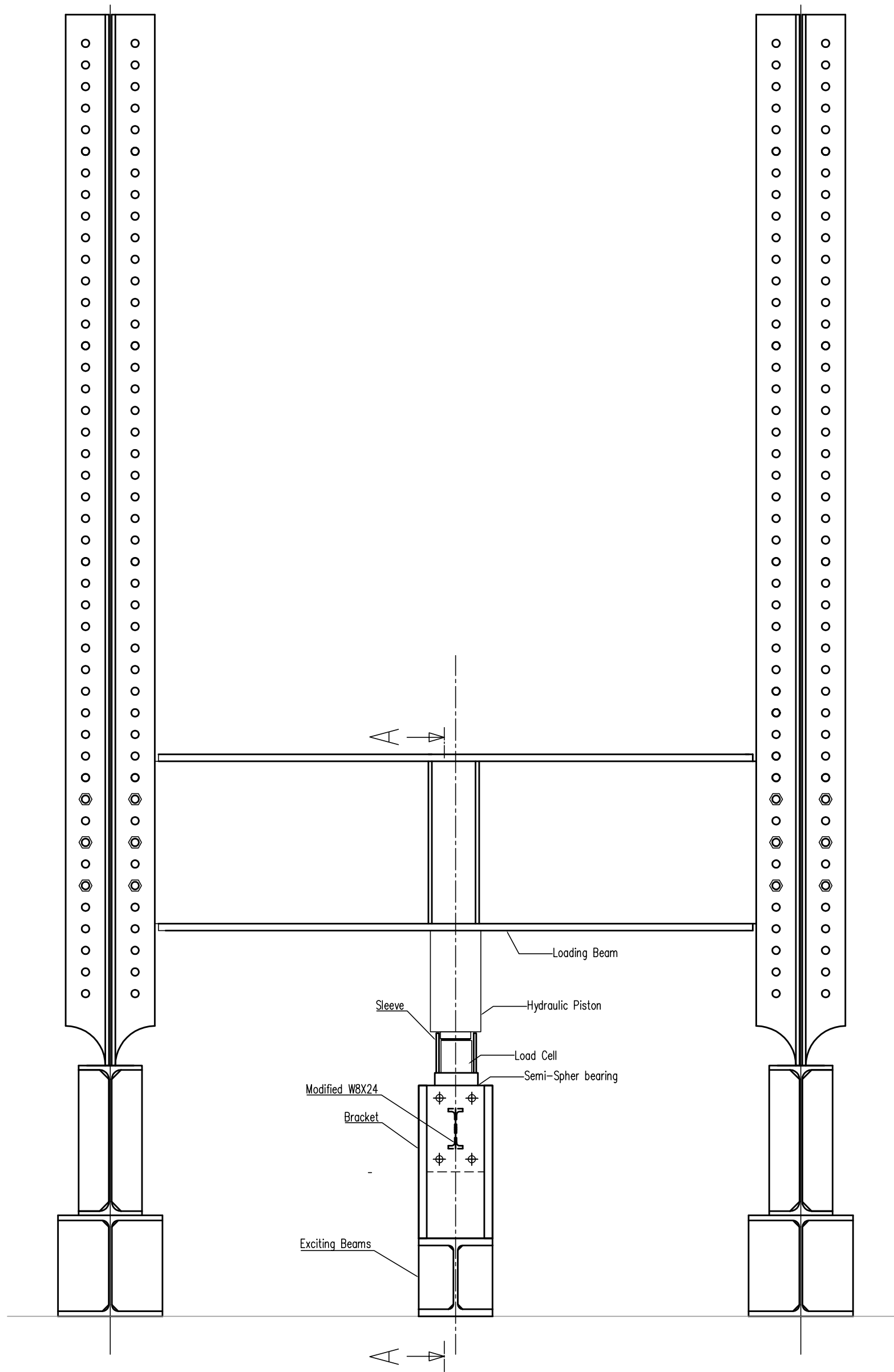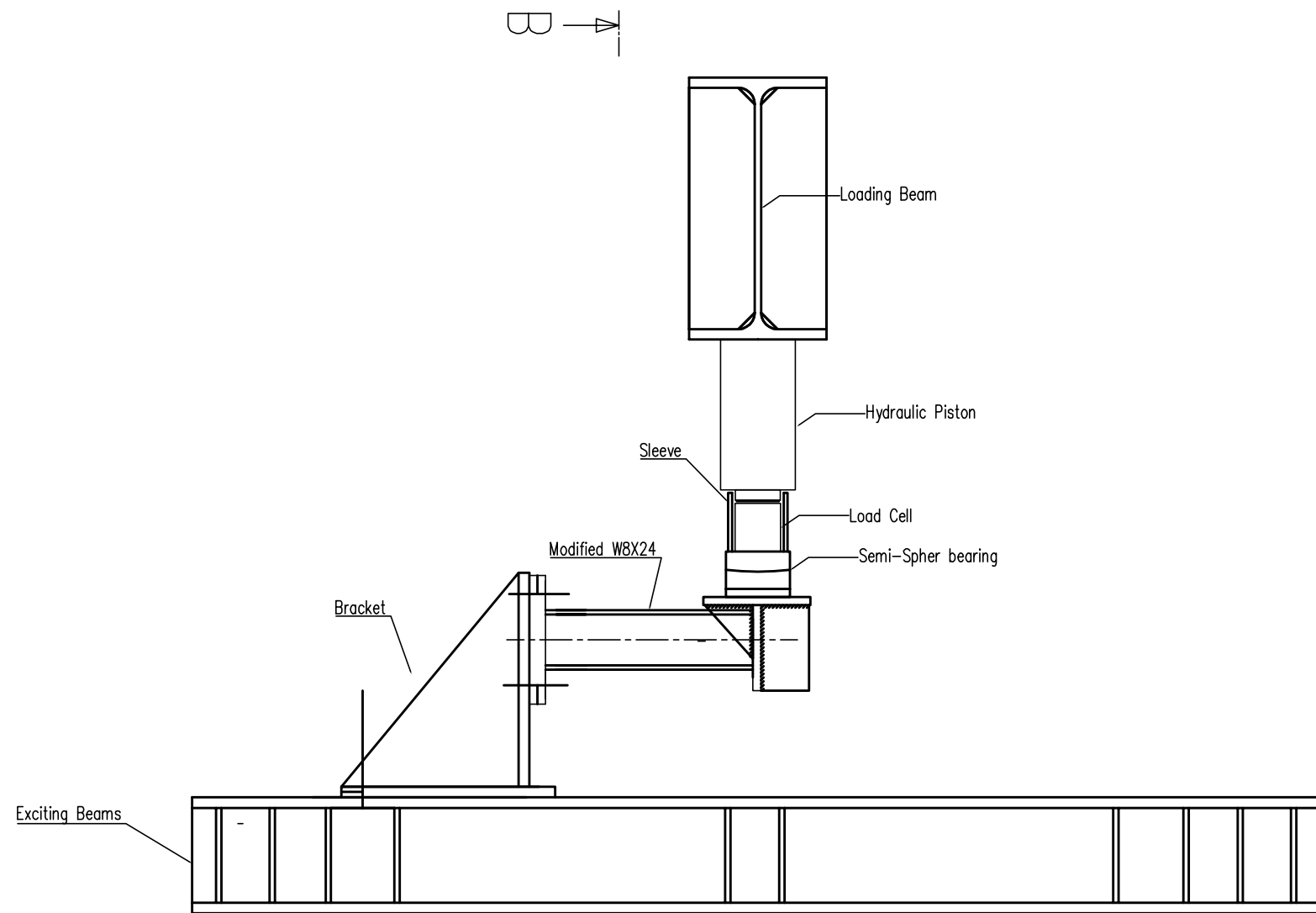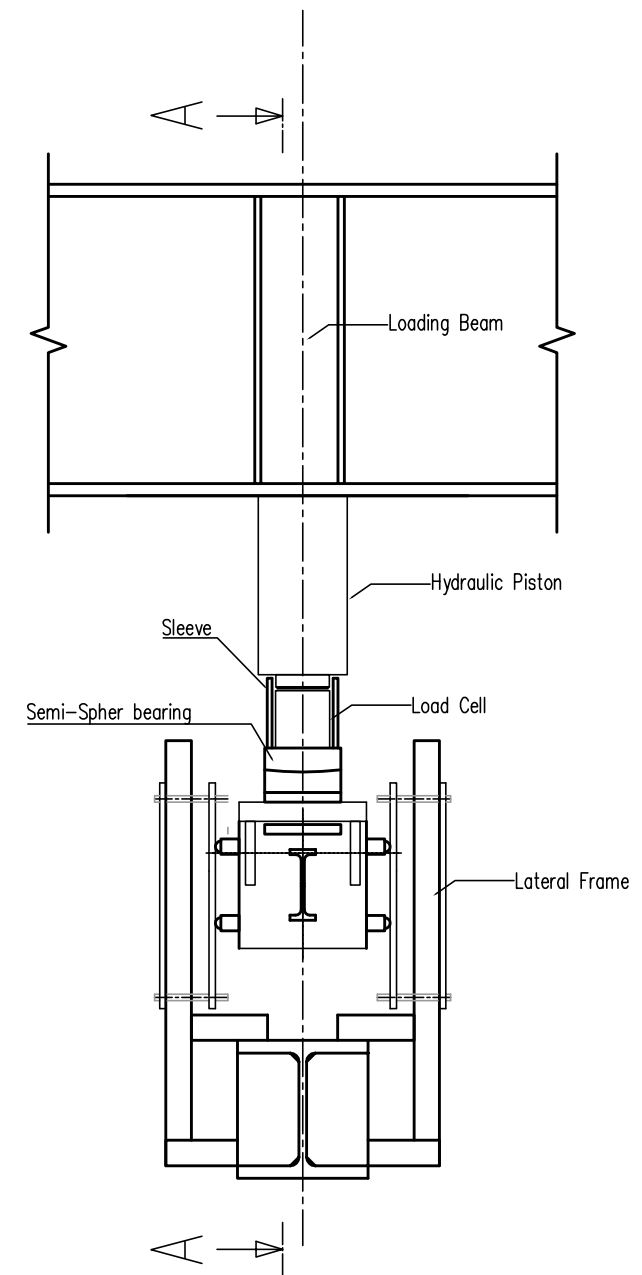
A

Section B-B

Test Setup

GENERAL NOTES:

CONTACT INFORMATION :
Shokoufeh Zargar
University of New Hampshire Department of Civil Engineering,
Kingsbury Hall Room N141, 33 Academic Way, Durham, NH 03824
PHONE: (603) 913-4578

DELIVERY INFORMATION :
ALL PIECES SHOULD BE DELIVERED TO Kingsbury Hall, High Bay Lab, 33 Academic Way, Durham, NH 03824
PHONE: (603) 913-4578

1. FOR CONDITIONS NOT CLEARLY UNDERSTOOD SUBMIT SKETCHES AND/OR REQUEST FOR INFORMATION TO THE DESIGN ENGINEER FOR RESOLUTION.

2. OMISSIONS, CONFLICTS OR MISUNDERSTANDINGS BETWEEN THE VARIOUS ELEMENTS OF THE CONTRACT DOCUMENTS, IF ANY, SHALL BE BROUGHT TO THE ATTENTION OF THE DESIGN ENGINEER FOR RESOLUTION BEFORE PROCEEDING WITH THE WORK.

3. VISUAL WELDING INSPECTION:
VISUAL INSPECTION BY A QUALIFIED INSPECTOR PRIOR TO, DURING AND AFTER WELDING SHOULD BE PERFORMED AS THE PRIMARY METHOD TO EVALUATE THE CONFORMANCE OF WELDED JOINTS TO THE APPLICABLE QUALITY REQUIREMENTS. THE VISUAL INSPECTION SHOULD INCLUDE JOINTS EXAMINATION PRIOR TO THE COMMENCEMENT OF WELDING, PREPARATION, GAPS, ALIGNMENT AND OTHER VARIABLES; ADHERENCE TO THE WELDING PROCEDURE SPECIFICATION (WPS); SATISFACTORY TO THE COMPLETED WELD TO AWS D1.1.

4. STRUCTURAL STEEL:

4.1. STRUCTURAL STEEL SHALL BE SUPPLIED, DETAILED AND ERECTED IN ACCORDANCE WITH A.I.S.C SPECIFICATIONS LATEST EDITIONS.

4.2. MEMBER/ELEMENT SPECIFICATION
  a. W Shapes   ASTM A992 GR 50
     FABRICATORS (ARCELORMITTAL INTERNATIONAL, GARDAU AMERISTEEL, NUCOR BERKELEY, NUCOR-YAMATO STEEL CO., STEEL DYNAMICS)

  b. CHANNELS   ASTM A36
     FABRICATORS (GARDAU AMERISTEEL, NUCOR BAR MILLS)

  c. ALL PLATES   ASTM A572 GR 50

5. CONNECTION

5.1. BOLTS:
SHALL NOT BE PROVIDED BY THE FABRICATOR AND WILL BE BOUGHT INDEPENDENTLY.

5.2. ALL HOLES ARE STANDARD HOLE SIZE.

    FOR 1" BOLTS THE HOLE DIAMETER IS $1\frac{1}{16}$"
    FOR $\frac{3}{4}$" BOLTS THE HOLE DIAMETER IS $\frac{13}{16}$"

5.3. WELDING ELECTRODES   E70XX

5.4. ALL WELDING FILLER METAL SHALL HAVE A MINIMUM CHARPY V-NOTCH TOUGHNESS OF 20 FT-LBS AT MINUS 20 DEGREES F.; SHALL ALSO MEET THE SUPPLEMENTAL TOUGHNESS REQUIREMENTS FOR WELD FILLER METAL PER APPENDIX A AND C OF FEMA-353.

5.6. BUTT WELDS SHALL BE COMPLETE PENETRATION WELDS AND THEY ARE INCLUDED IN THE BUILT UP COLUMN.

5.5. WELDING SHALL CONFIRM TO A.W.S. SPECIFICATIONS AND BE PERFORMED BY CERTIFIED WELDERS.

6. ERECTION SHALL BE DONE BY UNIVERSITY OF NEW HAMPSHIRE LAB PERSONAL AND GRADUATE STUDENTS.

TABLE OF MATERIALS

Item number	Specimen		Drawing #	QTY
	Specification			
1	Column (Test Specimen)	W8x24x19.4 (scaled)	S-1	2
2	base plate (bottom)	PL12x8x1.5	S-1	2
3	base plate (top)	PL8x10x0.75	S-2	2
4	top plate in tip	PL10x10x0.75	S-2	2
5	triangular stiffener in tip	PL 4.5x5x0.5	S-2	4
6	rectangular stiffener in tip	PL 4.5x8x0.5	S-2	4
7	pedestal (vertical plate)	PL 10.5x22x1	S-3	1
8	pedestal (horizontal plate)	PL 10.5x19x1	S-3	1
9	pedestal (stiffeners)	PL 19x21x0.5	S-3	2
10	lateral frame(Ver. Support)	HSS 3x2x0.25	S-4	2
11	lateral frame (Hor. Attachment)	L 2x2x0.25 (L=6 in)	S-4	4
12	lateral frame (threaded rods)	threaded rod 3/8" (L=10 in)	S-4	8
13	lateral frame (contact area)	PL 8x16x0.5	S-4	2
14	lateral frame (plate washers)	PL 8x2x0.25	S-4	8
15	lateral frame (diagonal bar)	1" Bar (L~10 in)	S-4	2

LEGEND

-FILLET WELD WITH LEG SIZE a

-COMPLETE-JOINT-PENETRATION GROOVE WELD (SQUARE GROOVE WELD, BUTT JOINT)

- ILLUSTRATES THE THREAD INFORMATION N x D"-B THRD, RH
"N" IS THE NUMBER OF HOLES
"D" IS THE NOMINAL SIZE OF THE BOLT
"B" IS THE NO. OF THREADS PER INCH
"THRD" MEANS THREAD
"RH" RIGHT HAND THREAD

-ELEVATION   ELEV.

ADVANCED STEEL PROJECT

	NAME	DATE	SINGLE COLUMN TEST SETUP
DESIGNED			
CHECKED			TITLE:
REVISION			GENERAL NOTES & BOM Table
DESCRIPTION		DATE	
COMMENTS:			

SIZE	DWG. NO.	REV
B	S-0	

SCALE: - | UNIT: INCHES | SHEET 1 OF 5

DETAIL A
QTY=2

Modified W8X24

SECTION A-A

W8X24

Original Section, the hatch parts
should be cut in order to fabricate
the scaled column section.

SCALE 1:5

DETAIL O
QTY=2

Modified W8x24

TEST SPECIMEN SCALE 1:5

DETAIL W

The web and the K region should
be welded with $\frac{3}{8}$ in and the rest
is welded with $\frac{1}{2}$ in weld

E70

DETAIL N
QTY=2

4xØ 1" BOLTS
4xØ 1$\frac{1}{16}$" HOLES

SEE DETAIL W
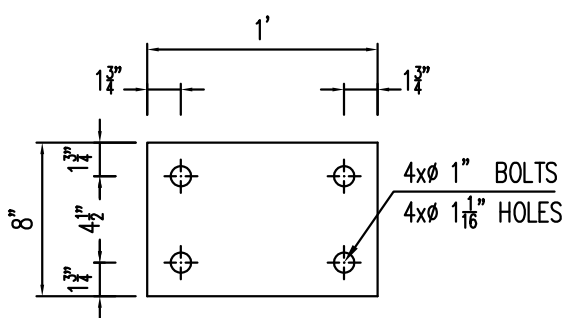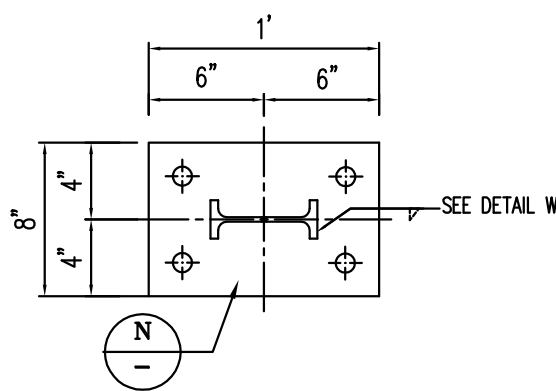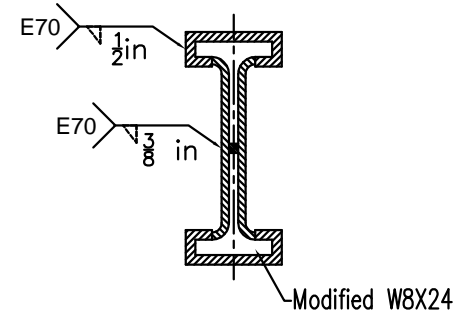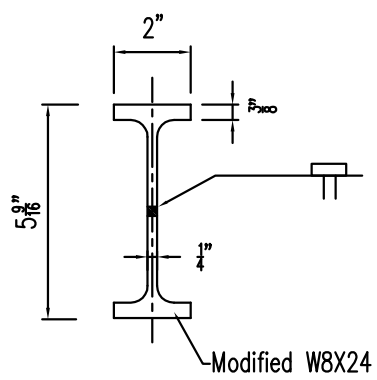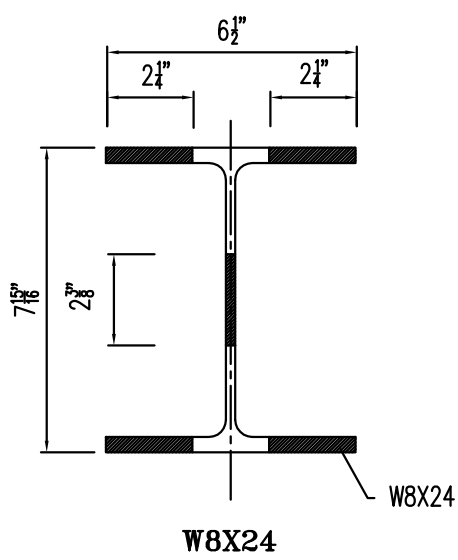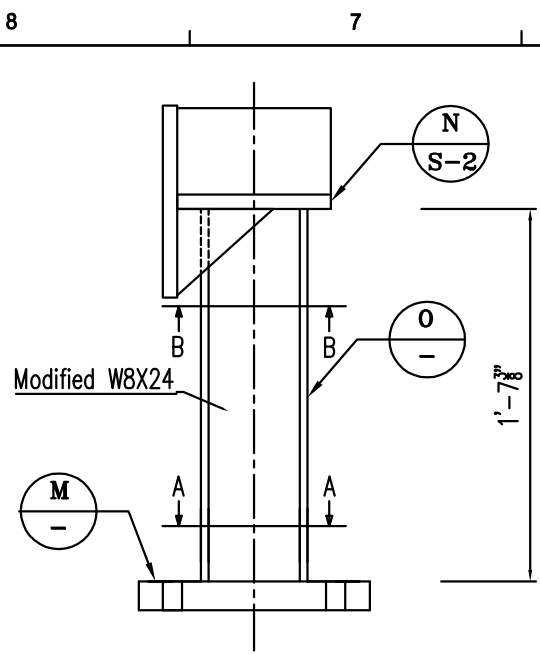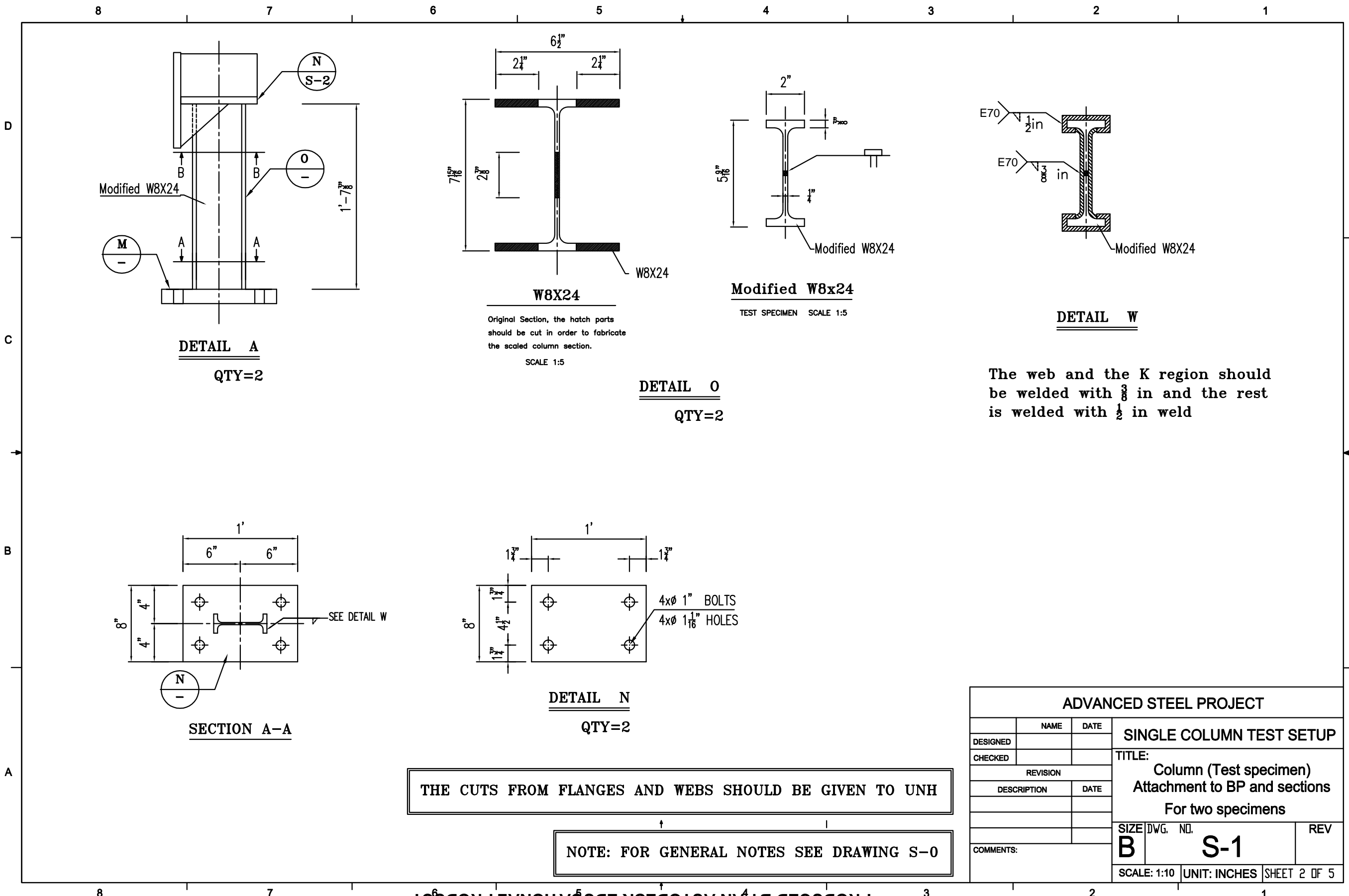
THE CUTS FROM FLANGES AND WEBS SHOULD BE GIVEN TO UNH

NOTE: FOR GENERAL NOTES SEE DRAWING S-0

ADVANCED STEEL PROJECT		
	NAME	DATE
DESIGNED		
CHECKED		

SINGLE COLUMN TEST SETUP

TITLE:
Column (Test specimen)
Attachment to BP and sections
For two specimens

	REVISION	
DESCRIPTION		DATE

COMMENTS:

SIZE: B | DWG. NO. S-1 | REV

SCALE: 1:10 | UNIT: INCHES | SHEET 2 OF 5

SECTION B—B

SEE DETAIL W

SECTION C—C

PL8"X10"

THICK.=$\frac{3}{4}$ "

DETAIL N

QTY=2

PL8"X10"

THICK.=$\frac{3}{4}$ "

DETAIL   P

QTY=2

PL4$\frac{1}{2}$"X5"

THICK.=$\frac{1}{2}$"

DETAIL   Q

QTY=4

PL4$\frac{1}{2}$"X8"

THICK.=$\frac{1}{2}$"

DETAIL   R

QTY=4

NOTE: FOR GENERAL NOTES SEE DRAWING S-0

ADVANCED STEEL PROJECT		
	NAME	DATE
DESIGNED		
CHECKED		
REVISION		
DESCRIPTION		DATE
COMMENTS:		

SINGLE COLUMN TEST SETUP

TITLE:
Column (Test specimen)
Attachment to BP and sections
For two specimens

SIZE: B   DWG. NO.: S-2   REV

SCALE: 1:10   UNIT: INCHES   SHEET 3 OF 5

DETAIL F

K

H
—

E70 ◁ $\frac{1}{4}$ in

G
—

1'-8"

E70 $\frac{1}{2}$in

1'-8"

SECTION D-D

$\frac{1}{2}$"   9$\frac{1}{2}$" $\frac{1}{2}$"

H
—

E70 ◁ $\frac{1}{4}$ in

E70 $\frac{1}{2}$in

DETAIL K
QTY=1

3"   4$\frac{1}{2}$"   3"

2"

8$\frac{1}{2}$"

1'-8"

4xØ 1 $\frac{1}{16}$ " HOLES (TYPE)

PL10 $\frac{1}{2}$" X20"
THICK.=1"

10$\frac{1}{2}$"

DETAIL G
QTY=1

2"

2xØ 1 $\frac{1}{16}$ " HOLES

10$\frac{1}{2}$"

3$\frac{3}{8}$"

4$\frac{1}{4}$"

3$\frac{3}{8}$"

PL20" X10 $\frac{1}{2}$"
THICK.=1"

1'-8"

DETAIL K
QTY=2

2"

2 PL16.5X20
THICK.= $\frac{1}{2}$ "

1'-7"

90°

1'-3$\frac{1}{2}$" 1" 1"

NOTE: FOR GENERAL NOTES SEE DRAWING S-0

	NAME	DATE	ADVANCED STEEL PROJECT	
DESIGNED			SINGLE COLUMN TEST SETUP	
CHECKED			TITLE:	
REVISION			BRACKET	
DESCRIPTION		DATE		
			QTY=1	

SIZE: B   DWG. NO.: S-3   REV

COMMENTS:

SCALE: 1:10   UNIT: INCHES   SHEET 4 OF 5

3"

3"

K
—

K
—

L
—

L
—

2'-8"

6"

1"   1"

2"

8"

PL10 8" X2"

THICK.=$\frac{1}{4}$"

9$\frac{7}{8}$"

$\frac{1}{4}$in   E70

E70 $\frac{1}{4}$in

9$\frac{7}{8}$"

DETAIL   L

DETAIL   I

1"

1"

L 2"X2"x1/4"

L=6"
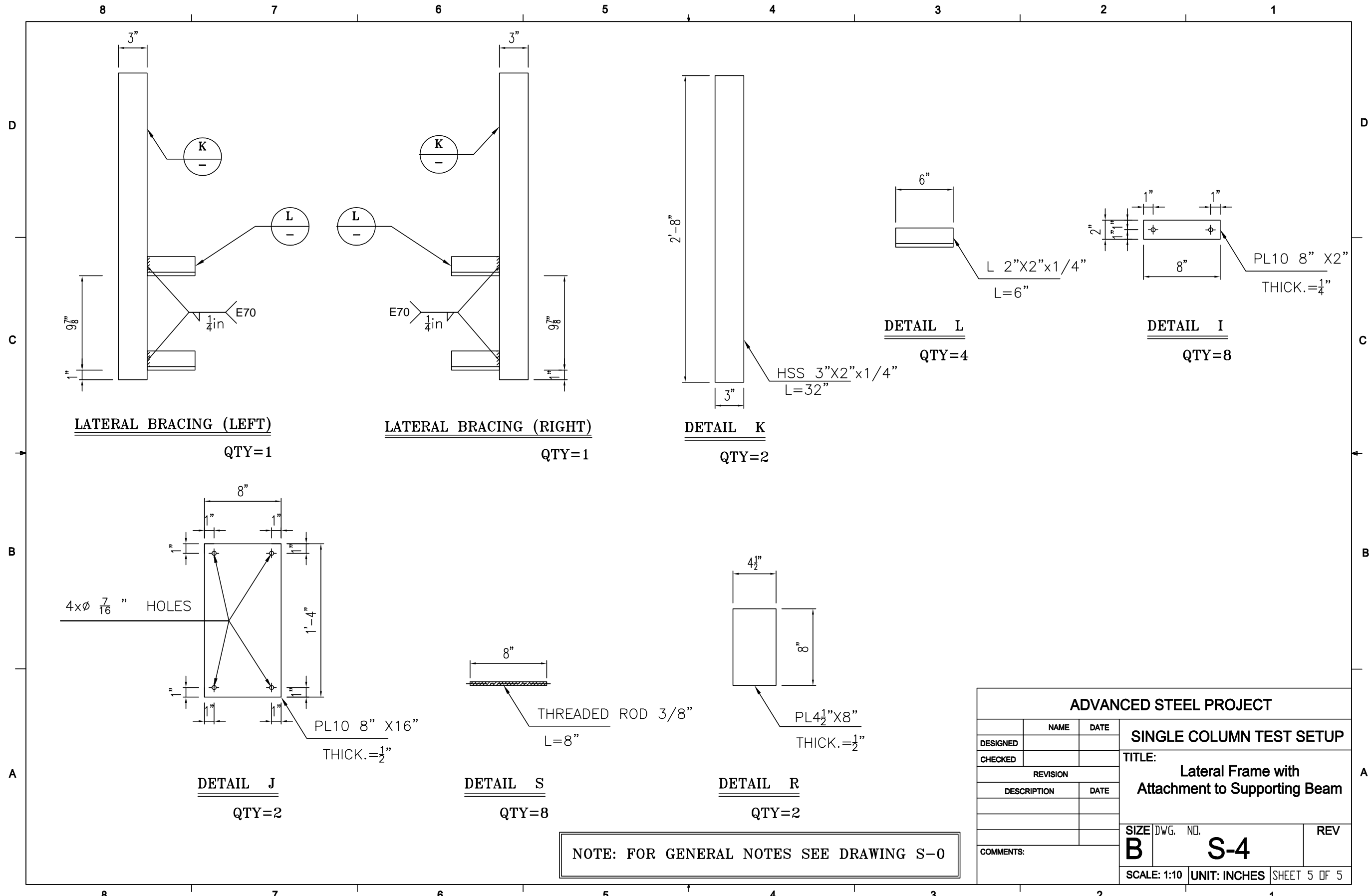
QTY=4

QTY=8

LATERAL BRACING (LEFT)

LATERAL BRACING (RIGHT)

3"

HSS 3"X2"x1/4"
L=32"

QTY=1

QTY=1

DETAIL   K

QTY=2

8"

1"   1"

1"

1"

4$\frac{1}{2}$"

4x∅ $\frac{7}{16}$ "   HOLES

1'-4"

8"

8"

1"

1"

8"

PL4$\frac{1}{2}$"X8"

1"   1"

PL10 8" X16"

THREADED ROD 3/8"

THICK.=$\frac{1}{2}$"

THICK.=$\frac{1}{2}$"

L=8"

DETAIL   J

DETAIL   S
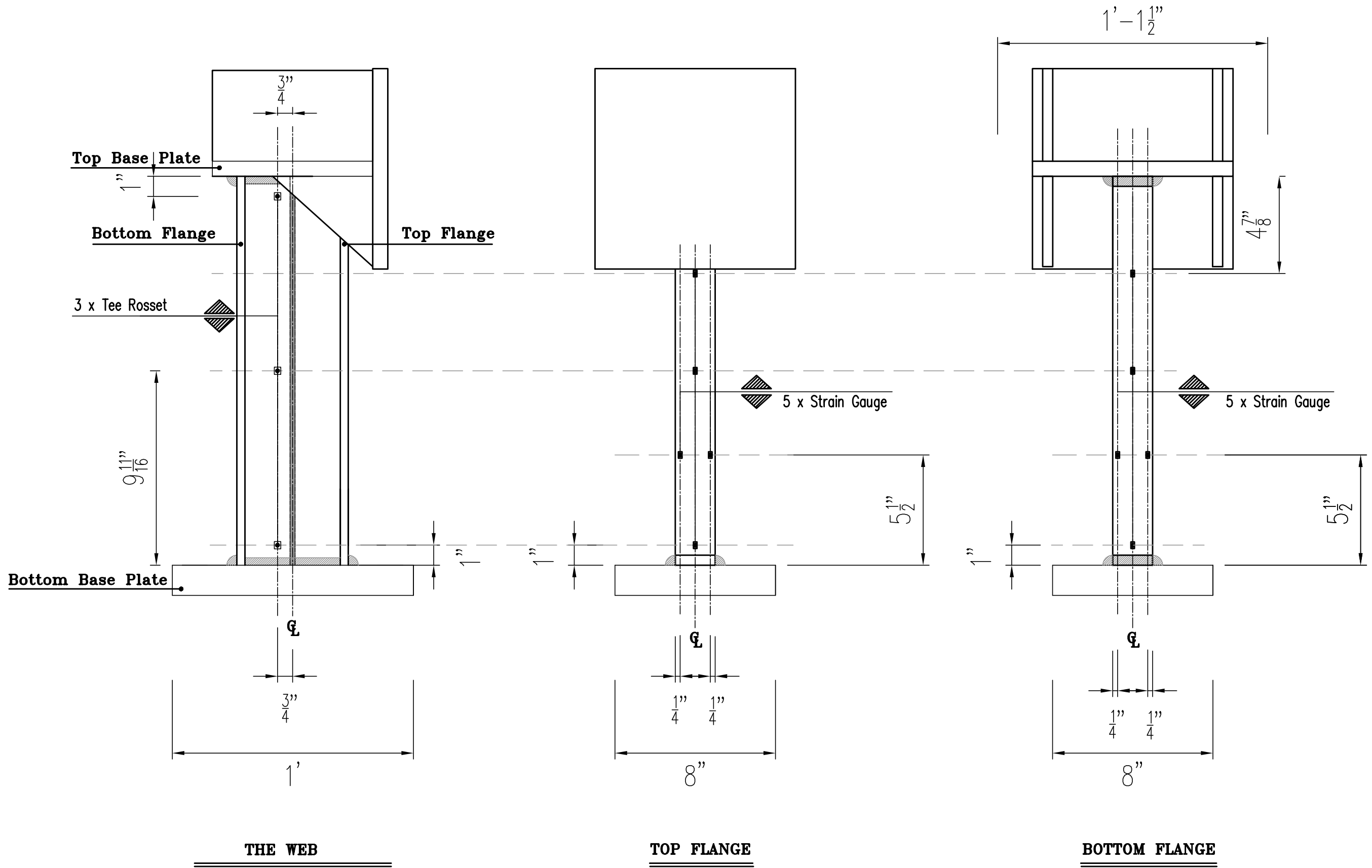
DETAIL   R

QTY=2

QTY=8

QTY=2

NOTE: FOR GENERAL NOTES SEE DRAWING S-0

ADVANCED STEEL PROJECT

	NAME	DATE	SINGLE COLUMN TEST SETUP
DESIGNED			TITLE:
CHECKED			Lateral Frame with
REVISION			Attachment to Supporting Beam
DESCRIPTION		DATE	

SIZE DWG. NO.

REV

B   S-4

COMMENTS:

SCALE: 1:10   UNIT: INCHES   SHEET 5 OF 5

THE WEB

TOP FLANGE

BOTTOM FLANGE

Top Base Plate

Bottom Flange

Top Flange

3 x Tee Rosset

5 x Strain Gauge

5 x Strain Gauge

Bottom Base Plate

Test #1— strain Gauge Locations

THE WEB

H1
V1
H2
V2
H3
V3

TOP FLANGE

T1
T2
T4   T3
T5

BOTTOM FLANGE

B1
B2
B3   B4
B5

Web Side
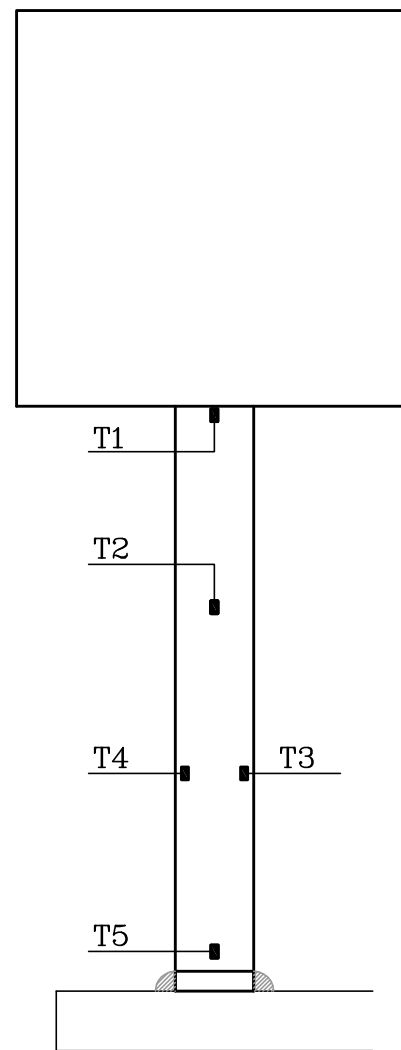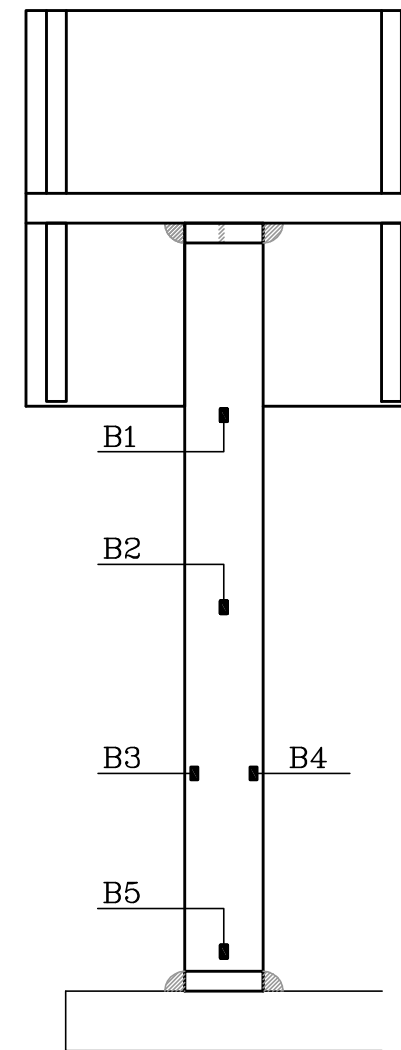
Top Flange   Bottom Flange
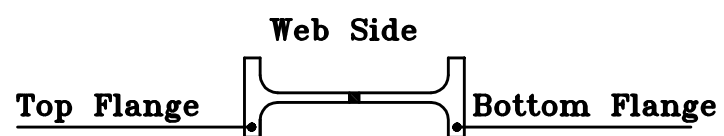
Test #1- strain Gauge Layout

A6.   Appendix 6

17.0   17.0   62.0   69.0

HORIZONTAL ACTUATOR
(55 kips, +/- 6.00")

REACTION FRAME

E / S-7

LOADING BEAM (ORANGE BEAM)

W14 X 257 (EXISTING)

13.2

C / S-5

A / S-1

B / S-2

66.9

2 x LATERAL FRAME
(YELLOW FRAME/EXISTING)

2 x VERTICAL ACTUATOR
(TENSION 50 kips, COMPRESSION 70 kips, +/- 2.00")

W14x159
(EXISTING)

W14 X 145
(EXISTING)

W8 X 31
(EXISTING)

2 C5x9
(NEW)

2 C5x9
(NEW)

D / S-6

BOTTOM BEAM (RED BEAM)

W14 X 257 (EXISTING)

W14 X 145
(EXISTING)

NOTE: FOR GENERAL NOTES SEE DRAWING S-0